



UNIVERSITY OF SOUTHERN QUEENSLAND

INTEGRATED RADIAL BASIS FUNCTION  
METHODS FOR STRUCTURAL, FLUID FLOW AND  
FLUID-STRUCTURE INTERACTION ANALYSES

A dissertation submitted by

**DUC NGO-CONG**

B.Eng., Ho-Chi-Minh City University of Technology, Vietnam, 2006

M.Eng. (Hon.), Gyeongsang National University, South Korea, 2008

For the award of the degree of

**Doctor of Philosophy**

February 2012

# Dedication

*To my family.*

# Certification of Dissertation

I certify that the ideas, experimental work, results and analyses, software and conclusions reported in this dissertation are entirely my own effort, except where otherwise acknowledged. I also certify that the work is original and has not been previously submitted for any other award.

---

Duc Ngo-Cong, Candidate	Date
-------------------------	------

## ENDORSEMENT

---

Prof. Thanh Tran-Cong, Principal supervisor	Date
---	------

---

A/Prof. Warna Karunasena, Co-supervisor	Date
---	------

---

Prof. Nam Mai-Duy, Co-supervisor	Date
----------------------------------	------

# Acknowledgments

The research reported in this thesis was carried out at the Computational Engineering and Science Research Centre (CESRC) and the Centre of Excellence in Engineered Fibre Composites (CEEFC), USQ.

Firstly, I would like to express my deepest gratitude to Prof. Thanh Tran-Cong, my principal supervisor, for his invaluable guidance and useful suggestions. Without his continuous support, this thesis would not have been completed.

I would like to thank A/Prof. Karu Karunasena and Prof. Nam Mai-Duy, my co-supervisors, for their instructive discussions during my PhD research.

I would like to thank to A/Prof. Armando A. Apan, Ms. Katrina Hall, Prof. David Buttsworth, Mrs. Juanita Ryan, and Mr. Martin Geach for their kind support.

I gratefully acknowledge the financial support provided by the USQ through a USQ Postgraduate Research Scholarship and a CESRC supplement.

Also, I would like to thank my dearest friends for their help over the past years.

Finally, I would like to dedicate this work to my parents, my brothers and Lucy Ha. I am greatly indebted to them for their unconditional support, love and encouragement.

# Notes to Readers

Attached to this thesis is a CD-ROM containing the following files:

1. thesis.pdf: An electronic version of this thesis;
2. Square\_BR\_1\_2\_Re\_160\_streamlines.wmv, Square\_BR\_1\_4\_Re\_160\_streamlines.wmv, Square\_BR\_1\_8\_Re\_090\_streamlines.wmv, and Square\_BR\_1\_8\_Re\_160\_streamlines.wmv: Animations showing the evolution of streamlines around a square cylinder in a channel for different blockage ratios and Reynolds numbers (Chapter 5, Example 2);
3. Square\_BR\_1\_2\_Re\_160\_vorticity.wmv, Square\_BR\_1\_4\_Re\_160\_vorticity.wmv, Square\_BR\_1\_8\_Re\_090\_vorticity.wmv, and Square\_BR\_1\_8\_Re\_160\_vorticity.wmv: Animations showing the evolution of vorticity field around a square cylinder in a channel for different blockage ratios and Reynolds numbers (Chapter 5, Example 2);
4. Circular\_Re\_100\_streamlines.wmv: An animation showing the evolution of streamlines around a circular cylinder (Chapter 5, Example 3);
5. Circular\_Re\_100\_vorticity.wmv: An animation showing the evolution of vorticity field around a circular cylinder (Chapter 5, Example 3);
6. Cavity\_prescribed\_flexible\_bottom\_case1.wmv and Cavity\_prescribed\_flexible\_bottom\_case2.wmv: Animations showing the evolution of streamlines inside a lid-driven open-cavity with a prescribed bottom wall motion for Case 1 and Case 2. (Chapter 6, Example 2);

7. `Cavity_fsi_simply_supported_bottom.wmv`: An animation showing the evolution of streamlines inside a lid-driven open-cavity with a simply supported bottom wall. (Chapter 6, Example 4); and
8. `Cavity_fsi_clamped_bottom.wmv`: An animation showing the evolution of streamlines inside a lid-driven open-cavity with a clamped bottom wall. (Chapter 6, Example 4).

# Abstract

The present research is concerned with the development of new numerical methods based on integrated radial basis function network (IRBFN) and collocation techniques for solving structural, fluid-flow and fluid-structure-interaction problems. Simply and multiply-connected domains with rectangular or non-rectangular shapes are discretised by means of Cartesian grids.

An effective one-dimensional integrated radial basis function network collocation technique, namely 1D-IRBFN, is developed for the free vibration analysis of laminated composite plates using the first order shear deformation theory (FSDT). Instead of using conventional differentiated RBF networks, 1D-IRBF networks are employed on grid lines to approximate the field variables. A number of examples concerning various thickness-to-span ratios, material properties and boundary conditions of the composite plates are investigated.

A novel local moving least square - one-dimensional integrated radial basis function network method, namely LMLS-1D-IRBFN, is proposed for solving incompressible viscous flow problems. The method is demonstrated with the analyses of lid-driven cavity flow and flow past a circular cylinder using stream-function - vorticity formulation. In this approach, the partition of unity method is employed as a framework to incorporate the moving least square (MLS) and 1D-IRBFN techniques. The major advantages of the proposed method include: (i) a banded sparse system matrix which helps reduce the computational cost; (ii) the Kronecker- $\delta$  property of the constructed shape functions, which helps impose the essential boundary conditions in an exact manner; and (iii) high

accuracy and fast convergence rate owing to the use of integration instead of conventional differentiation to construct the local RBF approximations.

The LMLS-1D-IRBFN method is then developed to study natural convection flows in multiply-connected domains in terms of stream function, vorticity and temperature. The unknown stream function value on the inner boundary is determined by using the single-valued pressure condition (Lewis, 1979). The LMLS-1D-IRBFN method is further extended and applied to solve time dependent problems such as Burgers' equation, unsteady flow past a square cylinder in a horizontal channel and unsteady flow past a circular cylinder. For fluid flow problems, the diffusion terms are discretised by using LMLS-1D-IRBFN method, while the convection terms are explicitly calculated by using 1D-IRBFN method. The present numerical procedure is combined with a domain decomposition technique to handle large-scale problems. Flow parameters such as drag coefficient, length of recirculation zone, Strouhal number and the effect of blockage ratio on the behaviour of the flow field behind the cylinder are investigated.

A numerical procedure based on 1D-IRBFN and local MLS-1D-IRBFN methods is proposed for solutions of fluid-structure interaction problems. A combination of Chorin's method and pseudo-time subiterative technique is presented for a transient solution of 2-D Navier-Stokes equations for incompressible viscous flow in terms of primitive variables. The fluid solver is first verified through a solution of mixed convection in a lid-driven cavity with a hot-temperature lid and a cold-temperature bottom wall. The FSI numerical procedure is then applied to simulate flows in a lid-driven open-cavity with a flexible bottom wall. The Newmark's method is employed for structural analysis of the flexible bottom wall based on the Euler-Bernoulli theory.

Numerical results obtained in the present research are compared with corresponding analytical solutions, where possible, and numerical results by other techniques in the literature.

# Papers Resulting from the Research

## Journal Papers

1. D. Ngo-Cong, N. Mai-Duy, K. Karunasena and T. Tran-Cong (2011). Free Vibration Analysis of Laminated Composite Plates based on FSDT using One-Dimensional IRBFN Method, *Computers and Structures*, **89**: 1-13.
2. D. Ngo-Cong, N. Mai-Duy, K. Karunasena and T. Tran-Cong (2012). Local Moving Least Square - One-Dimensional IRBFN Technique for Incompressible Viscous Flows, *International Journal for Numerical Methods in Fluids*, published online 9/Jan/2012 DOI: 10.1002/flid.3640.
3. D. Ngo-Cong, N. Mai-Duy, K. Karunasena and T. Tran-Cong (2012). Local Moving Least Square - One-Dimensional IRBFN Technique: Part I - Natural Convection Flows in Concentric and Eccentric Annuli, *CMES: Computer Modeling in Engineering & Science*, **83 (3)**: 275-310.
4. D. Ngo-Cong, N. Mai-Duy, K. Karunasena and T. Tran-Cong (2012). Local Moving Least Square - One-Dimensional IRBFN Technique: Part II - Unsteady Incompressible Viscous Flows, *CMES: Computer Modeling in Engineering & Science*, **83 (3)**: 311-351.
5. D. Ngo-Cong, N. Mai-Duy, K. Karunasena and T. Tran-Cong (2012). A numerical procedure based on 1D-IRBFN and local MLS-1D-IRBFN

methods for fluid-structure interaction analysis, *CMES: Computer Modeling in Engineering & Science*, **83 (5)**: 459-498.

### Conference Papers

1. D. Ngo-Cong, N. Mai-Duy, K. Karunasena and T. Tran-Cong (2010). Integrated-RBF network method for free vibration analysis of laminated composite plates. In *9<sup>th</sup> World Congress on Computational Mechanics (WCCM) and 4<sup>th</sup> Asian Pacific Congress on Computational Mechanics (APCOM)*, 19-23/Jul/2010, Sydney, Australia. IOP Conference Series: Materials Science and Engineering, Vol. 10, Paper No. 012236, 9 pages.
2. D.-A. An-Vo, D. Ngo-Cong, B.H.P. Le, N. Mai-Duy and T. Tran-Cong (2010). Local integrated-radial-basis-function discretisation schemes. In *International Conference on Computational & Experimental Engineering and Sciences (ICCES-MM'10)*, 17-21/Aug/2010, Busan, Korea Republic, 7 pages.
3. D. Ngo-Cong, N. Mai-Duy, K. Karunasena and T. Tran-Cong (2011). Moving Least Square - One Dimensional Integrated Radial Basis Function Networks for Time Dependent Problems. In *Boundary Elements and other Mesh Reduction Methods XXXIII*, 28-30/Jun/2011, The New Forest, United Kingdom, pp 309-320.

# Contents

Dedication	i
Certification of Dissertation	ii
Acknowledgments	iii
Notes to Readers	iv
Abstract	vi
Papers Resulting from the Research	viii
Acronyms & Abbreviations	xvii
List of Tables	xviii
List of Figures	xxvi

---

<b>Chapter 1 Introduction</b>	<b>1</b>
1.1 Motivation . . . . .	1
1.2 Governing equations for fluid, structure and fluid-structure interaction . . . . .	3
1.3 A brief review of traditional numerical methods . . . . .	6
1.4 A brief review of structural, fluid and fluid-structure interaction analyses . . . . .	8
1.5 Radial basis function networks . . . . .	11
1.6 Discussion and objectives of the present research . . . . .	13
1.7 Outline of the present research . . . . .	15
<b>Chapter 2 1D-IRBFN method for free vibration of laminated composite plates</b>	<b>17</b>
2.1 Introduction . . . . .	18
2.2 Governing equations . . . . .	23
2.2.1 First-order shear deformation theory . . . . .	23
2.2.2 Boundary conditions . . . . .	26
2.3 One-dimensional indirect/integrated radial basis function networks	28
2.3.1 IRBFN expressions on a grid line (1D-IRBFN scheme) . . . . .	28

2.3.2	1D-IRBFN expressions over the whole computational domain . . . . .	33
2.4	One-dimensional IRBFN discretisation of laminated composite plates . . . . .	35
2.5	Numerical results and discussion . . . . .	37
2.5.1	Example 1: Rectangular laminated plates . . . . .	38
2.5.2	Example 2: Circular laminated plates . . . . .	48
2.5.3	Example 3: Square isotropic plate with a square hole . . . . .	51
2.6	Concluding remarks . . . . .	53

**Chapter 3 Local MLS-1D-IRBFN method for steady incompressible viscous flows** **54**

3.1	Introduction . . . . .	55
3.2	Notations . . . . .	60
3.3	Moving least square approximation . . . . .	60
3.4	Local moving least square - one dimensional integrated radial basis function network technique . . . . .	63
3.4.1	One-dimensional IRBFN . . . . .	64
3.4.2	Incorporation of MLS and 1D-IRBFN into the partition of unity framework . . . . .	68

3.5	Governing equations for two-dimensional incompressible viscous flows . . . . .	71
3.6	LMLS-1D-IRBFN discretisation of governing equations for incompressible viscous flows . . . . .	71
3.7	Numerical results and discussion . . . . .	73
3.7.1	Example 1: Two-dimensional Poisson equation in a square domain . . . . .	73
3.7.2	Example 2: Two-dimensional Poisson equation in a square domain with a circular hole . . . . .	79
3.7.3	Example 3: Lid-driven cavity flow . . . . .	83
3.7.4	Example 4: Flow past a circular cylinder . . . . .	91
3.8	Concluding remarks . . . . .	102

**Chapter 4 Local MLS-1D-IRBFN method for natural convection in multiply-connected domains 103**

4.1	Introduction . . . . .	104
4.2	Local moving least square - one dimensional integrated radial basis function network technique . . . . .	109
4.3	Governing equations for natural convection flows . . . . .	110
4.4	Numerical results and discussion . . . . .	112

4.4.1	Example 1: Two-dimensional Poisson equation in a square domain with a circular hole . . . . .	113
4.4.2	Example 2: Concentric annulus between two circular cylinders . . . . .	116
4.4.3	Example 3: Concentric annulus between a square outer cylinder and a circular inner cylinder . . . . .	121
4.4.4	Example 4: Eccentric annulus between a square outer cylinder and a circular inner cylinder . . . . .	124
4.5	Concluding remarks . . . . .	133

**Chapter 5 Local MLS-1D-IRBFN method for unsteady incompressible viscous flows 134**

5.1	Introduction . . . . .	135
5.2	Local moving least square - one dimensional integrated radial basis function network technique . . . . .	140
5.3	Governing equations for 2-D unsteady incompressible viscous flows	141
5.4	Numerical results and discussion . . . . .	143
5.4.1	Example 1: Burgers' equation . . . . .	143
5.4.2	Example 2: Steady and unsteady flows past a square cylinder in a horizontal channel . . . . .	149
5.4.3	Example 3: Unsteady flows past a circular cylinder . . . . .	167

5.5 Concluding remarks . . . . . 173

**Chapter 6 A numerical procedure based on 1D-IRBFN and local  
MLS-1D-IRBFN methods for fluid-structure interaction anal-  
ysis 174**

6.1 Introduction . . . . . 175

6.2 1D-IRBFN and local MLS-1D-IRBFN methods . . . . . 179

6.2.1 1D-IRBFN methods . . . . . 179

6.2.2 Local moving least square - one dimensional integrated  
radial basis function network technique . . . . . 181

6.3 Governing equations for fluid, structure and fluid-structure in-  
teraction . . . . . 183

6.3.1 Governing equations for forced vibration of a beam . . . 183

6.3.2 Governing equations for 2-D incompressible viscous flows 184

6.3.3 Coupled equations for fluid-structure interaction . . . . . 185

6.4 Numerical procedures . . . . . 185

6.4.1 Fractional-step projection method (Chorin’s method) . . 186

6.4.2 Combination of fractional-step projection method and subit-  
erative technique . . . . . 189

6.4.3 Determine variable values at “freshly cleared” nodes . . . 192

6.4.4	Sequential staggered fluid-structure interaction algorithm	193
6.5	Numerical results and discussion . . . . .	196
6.5.1	Example 1: Mixed convection in a lid-driven cavity . . .	196
6.5.2	Example 2: Flow in a lid-driven open-cavity with a pre- scribed bottom wall motion . . . . .	204
6.5.3	Example 3: Forced vibration of a simply supported beam	212
6.5.4	Example 4: Fluid-structure interaction in a lid-driven open-cavity flow with a flexible bottom wall . . . . .	214
6.6	Concluding remarks . . . . .	218
<b>Chapter 7 Conclusions</b>		<b>219</b>
<b>Appendix A Basis Functions Used in One-Dimensional Integrated Radial Basis Function Networks Schemes</b>		<b>223</b>
<b>References</b>		<b>225</b>

# Acronyms & Abbreviations

1D-IRBFN	One-dimensional Indirect/Integrated Radial Basis Function Network
BEM	Boundary Element Method
CFD	Computational Fluid Dynamics
DRBFN	Direct Radial Basis Function Network
FDM	Finite Difference Method
FEM	Finite Element Method
FVM	Finite Volume Method
FSI	Fluid Structure Interaction
IRBFN	Indirect/Integrated Radial Basis Function Network
LHS	Left Hand Side
LMLS-1D-IRBFN	Local Moving Least Square - One-dimensional Indirect/Integrated Radial Basis Function Network
MLPG	Meshless Local Petrov-Galerkin method
MLS	Moving Least Square
MQ	Multiquadric
ODE	Ordinary Differential Equation
PDE	Partial Differential Equation
RBF	Radial Basis Function
RBFN	Radial Basis Function Network
RHS	Right Hand Side
SVD	Singular Value Decomposition

# List of Tables

- 2.1 Simply supported three-ply  $[0^\circ/90^\circ/0^\circ]$  square laminated plate: convergence study of nondimensionalised natural frequencies  $\bar{\omega} = \omega (b^2/\pi^2) \sqrt{\rho h/D_0}$  by two approaches,  $t/b = 0.2$ . Here *cond* denotes the condition number. . . . . 39
- 2.2 Simply supported three-ply  $[0^\circ/90^\circ/0^\circ]$  rectangular laminated plate: convergence study of nondimensionalised natural frequencies  $\bar{\omega} = \omega (b^2/\pi^2) \sqrt{\rho h/D_0}$  using Approach 1. Note that Ferreira and Fasshauer (2007) used 19x19 grid. . . . . 40
- 2.3 Clamped three-ply  $[0^\circ/90^\circ/0^\circ]$  rectangular laminated plate: convergence study of nondimensionalised natural frequencies  $\bar{\omega} = \omega (b^2/\pi^2) \sqrt{\rho h/D_0}$  using Approach 1. Note that Ferreira and Fasshauer (2007) used 19x19 grid. . . . . 40
- 2.4 Simply supported four-ply  $[0^\circ/90^\circ/90^\circ/0^\circ]$  square laminated plate: effect of thickness-to-length ratio on the nondimensionalised fundamental frequency  $\bar{\omega} = \omega (b^2/\pi^2) \sqrt{\rho h/D_0}$  in comparison with other published results, using Approach 1 and a grid of  $13 \times 13$ . 41

- 2.5 Three-ply  $[0^\circ/90^\circ/0^\circ]$  rectangular laminated plates with various boundary conditions: effect of thickness-to-length ratio on nondimensionalised natural frequencies  $\bar{\omega} = \omega (b^2/\pi^2) \sqrt{\rho h/D_0}$ , using Approach 1 and a grid of  $13 \times 13$ . . . . . 43
- 2.6 Four-ply  $[0^\circ/90^\circ/90^\circ/0^\circ]$  rectangular laminated plates with various boundary conditions: effect of thickness-to-length ratio on nondimensionalised natural frequency  $\bar{\omega} = \omega (b^2/\pi^2) \sqrt{\rho h/D_0}$ , using Approach 1 and a grid of  $13 \times 13$ . . . . . 44
- 2.7 Simply supported four-ply  $[0^\circ/90^\circ/90^\circ/0^\circ]$  square laminated plate: effect of modulus ratio  $E_1/E_2$  on the accuracy of nondimensionalised fundamental frequency  $\bar{\omega} = (\omega b^2/h) \sqrt{\rho/E_2}$ ,  $t/b = 0.2$ , using Approach 1 and a grid of  $13 \times 13$ ,  $K_s = 5/6$ . . . . . 47
- 2.8 Simply supported four-ply  $[\beta^\circ / -\beta^\circ / -\beta^\circ / \beta^\circ]$  circular laminated plate: convergence study of nondimensionalised natural frequencies for various mode number  $\bar{\omega} = (\omega b^2/h) \sqrt{\rho/E_2}$ ,  $t/b = 0.1$ ,  $E_1/E_2 = 40$ . 49
- 2.9 Clamped four-ply  $[\beta^\circ / -\beta^\circ / -\beta^\circ / \beta^\circ]$  circular laminated plate: convergence study of nondimensionalised natural frequencies for various mode number  $\left(\bar{\omega} = (\omega b^2/h) \sqrt{\rho/E_2}, t/b = 0.1, E_1/E_2 = 40\right)$ . 50
- 2.10 Clamped four-ply  $[\beta^\circ / -\beta^\circ / -\beta^\circ / \beta^\circ]$  circular laminated plate: effect of thickness-to-diameter ratio on nondimensionalised natural frequencies for various mode numbers,  $\bar{\omega} = (\omega b^2/h) \sqrt{\rho/E_2}$ ,  $E_1/E_2 = 40$ , using a grid of  $15 \times 15$ . . . . . 50
- 2.11 Simply supported square isotropic plate: Comparison of nondimensionalised natural frequencies among 1D-IRBF, Strand7 and exact results,  $\bar{\omega} = (\omega b^2/h) \sqrt{\rho/E_2}$ ,  $t/b = 0.1$ ,  $K_s = 5/6$ . . . . . 52

2.12	Simply supported square isotropic plate with a square hole: Comparison of nondimensionalised natural frequencies between 1D-IRBF and Strand7 results, $\bar{\omega} = (\omega b^2/h) \sqrt{\rho/E_2}$ , $t/b = 0.1$ , $K_s = 5/6$ . . . . .	52
3.1	Poisson equation in a square domain subject to Dirichlet boundary conditions: comparisons (with FDM and 1D-IRBFN) of the number of nonzero elements per row of the system matrix ( $N_{nzpr}$ ) and condition number ( $cond$ ). The system matrix is stored in a sparse matrix format. . . . .	77
3.2	Poisson equation in a square domain subject to Dirichlet boundary conditions: comparison (with FDM and 1D-IRBFN) of CPU time and percentage of nonzero elements of the system matrix ( $\epsilon$ ). Note that for a given grid size the present Approach 2 is slower than the FDM. However, the present Approach 2 achieves a given level of accuracy with a coarser grid and hence more efficient. For example, as shown in Figure 3.3, the present Approach 2 with grid= $21 \times 21$ yields better accuracy ( $Ne = 6.88e - 6$ ) in 0.88 seconds than the FDM with grid= $121 \times 121$ ( $Ne = 3.49e - 5$ ) in 1.74 seconds. . . . .	78
3.3	Poisson equation in a square domain subject to Dirichlet and Neumann boundary conditions: comparison condition number ( $cond$ ). . . . .	79
3.4	Poisson equation in a square domain with a circular hole subject to Dirichlet boundary conditions: comparison of relative error norm ( $Ne$ ) and condition number ( $cond$ ). . . . .	81

3.5	Poisson equation in a square domain with a circular hole subject to Dirichlet boundary conditions: comparison of CPU time and percentage of nonzero elements of the system matrix ( $\epsilon$ ). . . . .	81
3.6	Lid-driven cavity flow, $Re = 1000$ : the grid convergence study and comparison of extrema of velocity profiles along the center lines. The convection terms are calculated using LMLS-1D-IRBFN technique. Note that “Error” is relative to a Benchmark solution. . . . .	86
3.7	Lid-driven cavity flow, $Re = 1000$ : comparisons of the number of nonzero elements per row of the system matrix ( $N_{nzpr}$ ), number of iterations ( $N_{iteration}$ ) and total CPU time ( $T_{total}$ ) required to obtain the converged solution with $TOL = 10^{-12}$ . The time step $\Delta t$ is set to be $5 \times 10^{-3}$ for all cases. Note that for a given grid size the present approach is slower than the FDM. However, the present approach achieves a given level of accuracy with a coarser grid and hence more efficient. For example, as shown in Table 3.6, the present approach with grid= $81 \times 81$ yields better accuracy in 1559.77 seconds than the FDM with grid= $129 \times 129$ in 1733.02 seconds. . . . .	87
3.8	Lid-driven cavity flow, $Re = 1000$ : the grid convergence study and comparison of extrema of horizontal and vertical velocity profiles along the center lines. The convection terms are calculated using 1D-IRBFN technique. Note that “Error” is relative to a Benchmark solution. . . . .	88
3.9	Flow past a circular cylinder: comparison of the wake length ( $L_{sep}$ ), the separation angle ( $\theta_{sep}$ ) and the drag coefficient ( $C_D$ ) for $Re = 5, 10, 20$ and $40$ , using a grid of $151 \times 151$ . . . . .	98

4.1	Poisson equation in a square domain with a circular hole subject to Dirichlet boundary conditions: comparison of relative error norm ( $Ne$ ), condition number ( $cond$ ) and percentage of nonzero elements of the system matrix ( $\varepsilon$ ), using $\beta = 1$ for 1D-IRBFN and $\beta = 6$ for the present method (LMLS-1D-IRBFN). . . . .	114
4.2	Concentric annulus between two circular cylinders: Grid convergence study of the average equivalent conductivity on the outer and inner cylinders, $k_{eqo}$ and $k_{eqi}$ , respectively, for different Rayleigh numbers. . . . .	117
4.3	Concentric annulus between a square outer cylinder and a circular inner cylinder: Grid convergence study of the average Nusselt number on the inner and outer cylinders, $Nu_i$ and $Nu_o$ , respectively, for different Rayleigh numbers. . . . .	122
4.4	Eccentric annulus between a square outer cylinder and a circular inner cylinder: Comparison of the maximum stream-function values $\psi_{max}$ for different values of $\varepsilon_0$ and $\varphi$ . . . . .	126
4.5	Eccentric annulus between a square outer cylinder and a circular inner cylinder: Comparison of the stream-function values on the inner cylinder $\psi_{wall}$ for different values of $\varepsilon_0$ and $\varphi$ . . . . .	126
4.6	Eccentric annulus between a square outer cylinder and a circular inner cylinder: Comparison of the average Nusselt number $Nu$ for different values of $\varepsilon_0$ and $\varphi$ . . . . .	127
5.1	Burgers' equations, approximation of shock wave propagation: comparison of numerical results and exact solution at $t = 1.0$ for $Re = 100$ and several time step sizes, using a grid of 61. (1) 1D-IRBFN, (2) LMLS-1D-IRBFN . . . . .	145

5.2	Burgers' equations, approximation of shock wave propagation: grid convergence study of numerical results for $Re = 100, t = 1.0$ , and $\Delta t = 10^{-3}$ . (1) 1D-IRBFN, (2) LMLS-1D-IRBFN . . . . .	146
5.3	Burgers' equations, sinusoidal initial condition: comparison among the numerical results of LMLS-1D-IRBFN and Local-RBF (Hosseini and Hashemi, 2011) and the analytical solution for $Re = 10, \Delta t = 10^{-3}$ . . . . .	147
5.4	Burgers' equations, sinusoidal initial condition: comparison among the numerical results of LMLS-1D-IRBFN and Local-RBF (Hosseini and Hashemi, 2011) and the analytical solution for $Re = 100, \Delta t = 10^{-3}$ . . . . .	147
5.5	Burgers' equations, sinusoidal initial condition: comparison among numerical results and exact solution for $Re = 10000, \Delta t = 10^{-4}$ , using a grid of 301. . . . .	148
5.6	Burgers' equations, sinusoidal initial condition: comparison of numerical results for $Re = 10000, \Delta t = 10^{-4}$ , using a grid of 301.	148
5.7	Steady flow past a square cylinder in a channel: grid convergence study of recirculation length $L_r$ and drag coefficient $C_D$ for $Re = 40$ .	154
5.8	Steady flow past a square cylinder in a channel: comparison of recirculation length $L_r$ and drag coefficient $C_D$ , using a grid of $571 \times 351$ . . . . .	154
5.9	Unsteady flow past a square cylinder in a channel: Strouhal number $St$ and time-averaged drag coefficient $C_{Dm}$ for different blockage ratios $\beta_0 = 1/2, 1/4$ and $1/8$ , using grids of $645 \times 191, 645 \times 271$ and $645 \times 367$ , respectively. Note that in the case of $\beta_0 = 1/2, 1/4$ , the flow is still steady for $Re = 60, 80$ . . . . .	163

---

5.10	Unsteady flow past a circular cylinder: Strouhal number $St$ for different Reynolds number $Re = 80, 100$ and $200$ . . . . .	169
5.11	Unsteady flow past a circular cylinder: Drag coefficient $C_D$ for different Reynolds number $Re = 80, 100$ and $200$ . . . . .	169
5.12	Unsteady flow past a circular cylinder: Lift coefficient $C_L$ for different Reynolds number $Re = 80, 100$ and $200$ . . . . .	169
6.1	Mixed convection in a lid-driven cavity: grid convergence study and comparison of the average Nusselt number ( $Nu$ ) at the top wall for the Grashof number $Gr = 10^2$ , and several Reynolds numbers $Re = 100, 400$ and $1000$ , using the 1D-IRBFN method (Approach 1) and the numerical procedure based on the 1D-IRBFN and local MLS-1D-IRBFN methods (Approach 2). . . .	198
6.2	Mixed convection in a lid-driven cavity: grid convergence study and comparison of the average Nusselt number ( $Nu$ ) at the top wall for the Grashof number $Gr = 10^4$ , and several Reynolds numbers $Re = 100, 400$ and $1000$ , using the 1D-IRBFN method (Approach 1) and the numerical procedure based on the 1D-IRBFN and local MLS-1D-IRBFN methods (Approach 2). . . .	198
6.3	Mixed convection in a lid-driven cavity: grid convergence study and comparison of the average Nusselt number ( $Nu$ ) at the top wall for the Grashof number $Gr = 10^6$ , and several Reynolds numbers $Re = 100, 400$ and $1000$ , using the 1D-IRBFN method (Approach 1) and the numerical procedure based on the 1D-IRBFN and local MLS-1D-IRBFN methods (Approach 2). . . .	199

6.4	Forced vibration of a simply supported beam: Relative error norms of deflection $Ne(u)$ and velocity $Ne(v)$ at time $t = 14s$ , using several time steps. . . . .	213
-----	--	-----

# List of Figures

2.1	Cartesian grid. . . . .	29
2.2	Simply supported four-ply $[0^\circ/90^\circ/90^\circ/0^\circ]$ square laminated plate: errors of nondimensionalised fundamental frequency ( $\epsilon = (\bar{\omega} - \bar{\omega}_E)/\bar{\omega}_E$ ) with respect to thickness-to-length ratios $t/b$ . . . . .	42
2.3	Mode shapes for simply supported three-ply $[0^\circ/90^\circ/0^\circ]$ square laminated plate with $t/b = 0.2$ and grid of $15 \times 15$ . . . . .	45
2.4	Mode shapes for simply supported three-ply $[0^\circ/90^\circ/0^\circ]$ rectan- gular laminated plate with $a/b = 2$ , $t/b = 0.2$ and grid of $15 \times 15$ . . . . .	45
2.5	Mode shapes for clamped three-ply $[0^\circ/90^\circ/0^\circ]$ square laminated plate with $t/b = 0.2$ and grid of $15 \times 15$ . . . . .	46
2.6	Simply supported four-ply square laminated plate $[0^\circ/90^\circ/90^\circ/0^\circ]$ : errors of nondimensionalised fundamental frequency ( $\epsilon = (\bar{\omega} - \bar{\omega}_E)/\bar{\omega}_E$ ) with respect to modulus ratio $E_1/E_2$ , $t/b = 0.2$ . . . . .	47
2.7	Computational domain of four-ply $[\beta^\circ / -\beta^\circ / -\beta^\circ / \beta^\circ]$ circular laminated plate. . . . .	48
2.8	Mode shapes for simply supported four-ply $[45^\circ / -45^\circ / -45^\circ / 45^\circ]$ circular laminated plate, $t/b = 0.1$ , grid of $19 \times 19$ . . . . .	49

---

2.9	Mode shapes of simply supported square isotropic plate with a square hole, $t/b = 0.1$ , using a grid of $17 \times 17$ . . . . .	52
3.1	Cartesian grid discretisation. . . . .	61
3.2	LMLS-1D-IRBFN-3-node scheme, $\square$ a typical $[j]$ node. . . . .	64
3.3	Poisson equation in a square domain subject to Dirichlet boundary conditions: convergence study for 1D-IRBFN, Approach 1 with $\beta = 10$ and Approach 2 with $\beta = 15$ . FDM (central difference) results are included for comparison. . . . .	75
3.4	Poisson equation in a square domain subject to Dirichlet and Neumann boundary conditions: convergence study for 1D-IRBFN, Approach 1 with $\beta = 10$ and Approach 2 with $\beta = 5$ . . . . .	76
3.5	A square domain with a circular hole. . . . .	80
3.6	Poisson equation in a square domain with a circular hole subject to Dirichlet boundary conditions: convergence study for 1D-IRBFN and the present method (LMLS-1D-IRBFN-5-node) with $\beta = 15$ . . . . .	82
3.7	Lid-driven cavity flow: problem geometry and boundary conditions. . . . .	83
3.8	Lid-driven cavity flow: contours of stream function (left) and vorticity (right) for different Reynolds numbers $Re = 1000, 3200$ and $7500$ , using grids of $101 \times 101$ , $121 \times 121$ , and $151 \times 151$ , respectively. . . . .	89

---

3.9	Lid-driven cavity flow: comparison of profiles of vertical and horizontal velocities along the horizontal and vertical center lines of the cavity for different Reynolds numbers $Re = 1000, 3200$ and $7500$ , using grids of $101 \times 101$ , $121 \times 121$ , and $151 \times 151$ , respectively.	90
3.10	Flow past a circular cylinder: problem geometry and boundary conditions. . . . .	91
3.11	Circular cylinder and associated coordinate systems. . . . .	92
3.12	Non-overlapping partition of the domain $\Omega$ into two subdomains $\Omega_1$ and $\Omega_2$ . . . . .	95
3.13	Flow past a circular cylinder: grid configuration. . . . .	99
3.14	Flow past a circular cylinder: grid convergence study, $Re = 40$ . . . . .	99
3.15	Flow past a circular cylinder: comparison of vorticity on the circular cylinder in the cases of $Re = 5, 10, 20$ and $40$ , using a grid of $151 \times 151$ . . . . .	100
3.16	Flow past a circular cylinder: comparison of pressure coefficient on the circular cylinder in the cases of $Re = 5, 10, 20$ and $40$ , using a grid of $151 \times 151$ . . . . .	100
3.17	Flow past a circular cylinder: contours of stream function (left) and vorticity (right) for the cases of $Re = 5, 10, 20$ and $40$ , from top to bottom, using a grid of $151 \times 151$ . . . . .	101
4.1	LMLS-1D-IRBFN scheme, $\square$ a typical $[j]$ node. . . . .	110
4.2	A square domain with a circular hole. . . . .	113

- 
- 4.3 Poisson equation in a square domain with a circular hole subject to Dirichlet boundary conditions:  $\beta$ -adaptivity study for the present method (LMLS-1D-IRBFN). . . . . 115
- 4.4 Concentric annulus between two circular cylinders: problem geometry and boundary conditions. Angular positions are measured clockwise from the positive  $y$ -axis. Note that computational boundary conditions for vorticity are determined by Equations (4.10)-(4.14). . . . . 116
- 4.5 Concentric annulus between two circular cylinders: influence of Rayleigh number on local and average equivalent conductivities on the inner cylinders. . . . . 118
- 4.6 Concentric annulus between two circular cylinders: influence of Rayleigh number on local and average equivalent conductivities on the outer cylinders. . . . . 118
- 4.7 Concentric annulus between two circular cylinders: contours of temperature (left) and stream function (right) for different Rayleigh numbers  $Ra = 10^2, 10^3, 3 \times 10^3$  and  $6 \times 10^3$ , from top to bottom, using a grid of  $61 \times 61$ . Each plot contains 21 contour levels varying linearly from the minimum value to the maximum value. 119
- 4.8 Concentric annulus between two circular cylinders: contours of temperature (left) and stream function (right) for different Rayleigh numbers  $Ra = 10^4, 5 \times 10^4$  and  $7 \times 10^4$ , from top to bottom, using a grid of  $61 \times 61$ . Each plot contains 21 contour levels varying linearly from the minimum value to the maximum value. . . . . 120

- 
- 4.9 Concentric annulus between a square outer cylinder and a circular inner cylinder: problem geometry and boundary conditions. Note that computational boundary conditions for vorticity are determined by Equations (4.10)-(4.14). . . . . 121
- 4.10 Concentric annulus between a square outer cylinder and a circular inner cylinder: contours of temperature (left), stream function (middle) and vorticity (right) for different Rayleigh numbers  $Ra = 5 \times 10^4, 10^5, 5 \times 10^5$  and  $10^6$ , from top to bottom, using a grid of  $63 \times 63$ . Each plot contains 21 contour levels varying linearly from the minimum value to the maximum value. . . . . 123
- 4.11 Eccentric annulus between a square outer cylinder and a circular inner cylinder: problem geometry and boundary conditions. The angular position  $\varphi$  of the center of the inner cylinder is measured counterclockwise from the positive  $x$ -axis. Note that computational boundary conditions for vorticity are determined by Equations (4.10)-(4.14). . . . . 125
- 4.12 Eccentric annulus between a square outer cylinder and a circular inner cylinder: contours of temperature (left), stream function (middle) and vorticity (right) for the cases of  $\varepsilon_0 = 0.25, 0.50, 0.75$  and  $0.95$ , from top to bottom,  $Ra = 3 \times 10^5, L/2R = 2.6, \varphi = -45^\circ$ , using a grid of  $82 \times 82$ . Each plot contains 21 contour levels varying linearly from the minimum value to the maximum value. . . . . 128

- 4.13 Eccentric annulus between a square outer cylinder and a circular inner cylinder: contours of temperature (left), stream function (middle) and vorticity (right) for the cases of  $\varepsilon_0 = 0.25, 0.50$  and  $0.75$ , from top to bottom,  $Ra = 3 \times 10^5, L/2R = 2.6, \varphi = 0^\circ$ , using a grid of  $108 \times 108$  for the case  $\varepsilon_0 = 0.75$  and a grid of  $82 \times 82$  for the others. Each plot contains 21 contour levels varying linearly from the minimum value to the maximum value. 129
- 4.14 Eccentric annulus between a square outer cylinder and a circular inner cylinder: contours of temperature (left), stream function (middle) and vorticity (right) for the cases of  $\varepsilon_0 = 0.25, 0.50, 0.75$  and  $0.95$ , from top to bottom,  $Ra = 3 \times 10^5, L/2R = 2.6, \varphi = 45^\circ$ , using a grid of  $82 \times 82$ . Each plot contains 21 contour levels varying linearly from the minimum value to the maximum value. 130
- 4.15 Eccentric annulus between a square outer cylinder and a circular inner cylinder: contours of temperature (left), stream function (middle) and vorticity (right) for the cases of  $\varepsilon_0 = 0.75, 0.50$  and  $0.25$ , from top to bottom,  $Ra = 3 \times 10^5, L/2R = 2.6, \varphi = 90^\circ$ , using a grid of  $108 \times 108$  for the case  $\varepsilon_0 = 0.75$  and a grid of  $82 \times 82$  for the others. Each plot contains 21 contour levels varying linearly from the minimum value to the maximum value. 131
- 4.16 Eccentric annulus between a square outer cylinder and a circular inner cylinder: contours of temperature (left), stream function (middle) and vorticity (right) for the cases of  $\varepsilon_0 = 0.25, 0.50$  and  $0.75$ , from top to bottom,  $Ra = 3 \times 10^5, L/2R = 2.6, \varphi = -90^\circ$ , using a grid of  $108 \times 108$  for the case  $\varepsilon_0 = 0.75$  and a grid of  $82 \times 82$  for the others. Each plot contains 21 contour levels varying linearly from the minimum value to the maximum value. 132
- 5.1 LMLS-1D-IRBFN scheme,  $\square$  a typical  $[j]$  node. . . . . 141

---

5.2	Flow past a square cylinder in a channel: geometry and boundary conditions. The blockage ratio is defined as $\beta_0 = D/H$ . Note that computational boundary conditions for vorticity are determined by Equation (5.9). . . . .	149
5.3	Flow past a square cylinder in a channel: grid configuration. . .	150
5.4	Pressure and shear stress acting on the surface of a square cylinder.	153
5.5	Steady flow past a square cylinder in a channel: grid convergence study of recirculation length $L_r$ for $Re = 40$ . . . . .	155
5.6	Steady flow past a square cylinder in a channel: grid convergence study of drag coefficient $C_D$ for $Re = 40$ . . . . .	155
5.7	Steady flow past a square cylinder in a channel: contours of stream function for different Reynolds numbers, using a grid of $571 \times 351$ . . . . .	156
5.8	Unsteady flow past a square cylinder in a channel (blockage ratio $\beta_0 = 1/8$ ): variation of Strouhal number $St$ with respect to Reynolds number $Re$ , using different grids of $547 \times 331$ , $571 \times 351$ and $645 \times 367$ ; FVM (Breuer et al., 2000) using a non-uniform grid of $560 \times 340$ ; LBA (Breuer et al., 2000) using a uniform grid of $2000 \times 320$ ; STAM (Berrone and Marro, 2009); CVFEM (Bouaziz et al., 2010) using a non-uniform grid of $249 \times 197$ . . .	159

- 
- 5.9 Unsteady flow past a square cylinder in a channel (blockage ratio  $\beta_0 = 1/8$ ): variation of time-averaged drag coefficient  $C_{Dm}$  with respect to Reynolds number  $Re$ , using different grids of  $547 \times 331$ ,  $571 \times 351$  and  $645 \times 367$ ; FVM (Breuer et al., 2000) using a non-uniform grid of  $560 \times 340$ ; LBA (Breuer et al., 2000) using a uniform grid of  $2000 \times 320$ ; STAM (Berrone and Marro, 2009); CVFEM (Bouaziz et al., 2010) using a non-uniform grid of  $249 \times 197$ . . . . . 159
- 5.10 Unsteady flow past a square cylinder in a channel (blockage ratio  $\beta_0 = 1/8$ ): variation of drag coefficient  $C_D$  and lift coefficient  $C_L$  with respect to time  $t$  for the case of  $Re = 90$ , using a grid of  $571 \times 351$ . . . . . 160
- 5.11 Unsteady flow past a square cylinder in a channel (blockage ratio  $\beta_0 = 1/8$ ): Contours of stream function for different Reynolds numbers, using a grid of  $645 \times 367$ . . . . . 161
- 5.12 Unsteady flow past a square cylinder in a channel (blockage ratio  $\beta_0 = 1/8$ ): Contours of vorticity for different Reynolds numbers, using a grid of  $645 \times 367$ . . . . . 162
- 5.13 Unsteady flow past a square cylinder in a channel: variation of time-averaged drag coefficient  $C_{Dm}$  with respect to Reynolds number  $Re$  for blockage ratios  $\beta_0 = 1/2$  and  $1/4$ , using grids of  $645 \times 191$  and  $645 \times 271$ , respectively; . . . . . 164
- 5.14 Unsteady flow past a square cylinder in a channel: variation of time-averaged drag coefficient  $C_{Dm}$  with respect to Reynolds number  $Re$  for blockage ratios  $\beta_0 = 1/2$  and  $1/4$ , using grids of  $645 \times 191$  and  $645 \times 271$ , respectively; . . . . . 164

---

5.15	Unsteady flow past a square cylinder in a channel: Contours of stream function for different Reynolds numbers ( $\beta_0 = 1/4$ , grid = $645 \times 271$ ). . . . .	165
5.16	Unsteady flow past a square cylinder in a channel: Contours of vorticity for different Reynolds numbers ( $\beta_0 = 1/4$ , grid = $645 \times 271$ ). . . . .	165
5.17	Unsteady flow past a square cylinder in a channel: Contours of stream function for different Reynolds numbers ( $\beta_0 = 1/2$ , grid = $645 \times 191$ ). . . . .	166
5.18	Unsteady flow past a square cylinder in a channel: Contours of vorticity for different Reynolds numbers ( $\beta_0 = 1/2$ , grid = $645 \times 191$ ). . . . .	166
5.19	Unsteady flow past a circular cylinder: geometry and boundary conditions. Note that computational boundary conditions for vorticity are determined by Equations (5.9)-(5.13). . . . .	168
5.20	Unsteady flow past a circular cylinder: grid configuration. . . . .	170
5.21	Unsteady flow past a stationary cylinder: drag and lift coefficients $C_D$ and $C_L$ with respect to time for $Re = 100$ , using a grid of $548 \times 379$ . . . . .	170
5.22	Unsteady flow past a circular cylinder: contours of stream function for different Reynolds numbers $Re = 80, 100$ and $200$ , using grids of $548 \times 379$ , $548 \times 379$ and $640 \times 379$ , respectively. . . . .	171
5.23	Unsteady flow past a circular cylinder: contours of vorticity for different Reynolds numbers $Re = 80, 100$ and $200$ , using grids of $548 \times 379$ , $548 \times 379$ and $640 \times 379$ , respectively. . . . .	172

---

6.1	Cartesian grid discretisation. . . . .	180
6.2	LMLS-1D-IRBFN scheme, $\square$ a typical $[j]$ node. . . . .	182
6.3	Configuration to determine $v^*$ at nodes on a curved boundary. . . . .	188
6.4	Configuration to determine initial values at "freshly cleared" nodes. . . . .	193
6.5	Flowchart of the FSI analysis procedure. . . . .	195
6.6	Mixed convection in a lid-driven cavity: geometry and boundary conditions. . . . .	197
6.7	Mixed convection in a lid-driven cavity: isothermal lines (left) and streamlines (right) of the flow at $Gr = 10^2$ , and several Reynolds numbers $Re = 100, 400$ and $1000$ , using grids of $61 \times 61$ , $81 \times 81$ and $101 \times 101$ , respectively. The isothermal values are 25 uniformly distributed values in the range $[T_C, T_H]$ . The contour values of stream function used here are taken to be the same as those in (Ghia et al., 1982). . . . .	201
6.8	Mixed convection in a lid-driven cavity: isothermal lines (left) and streamlines (right) of the flow at $Gr = 10^4$ , and several Reynolds numbers $Re = 100, 400$ and $1000$ , using grids of $61 \times 61$ , $81 \times 81$ and $101 \times 101$ , respectively. The isothermal values are 25 uniformly distributed values in the range $[T_C, T_H]$ . The contour values of stream function used here are taken to be the same as those in (Ghia et al., 1982). . . . .	202

- 
- 6.9 Mixed convection in a lid-driven cavity: isothermal lines (left) and streamlines (right) of the flow at  $Gr = 10^6$ , and several Reynolds numbers  $Re = 100, 400$  and  $1000$ , using grids of  $61 \times 61$ ,  $81 \times 81$  and  $101 \times 101$ , respectively. The isothermal values are 25 uniformly distributed values in the range  $[T_C, T_H]$ . The contour values of stream function used here are taken to be the same as those in (Ghia et al., 1982). . . . . 203
- 6.10 Flow in a lid-driven open-cavity with a prescribed bottom wall motion: geometry and boundary conditions. . . . . 204
- 6.11 Flow in a lid-driven open-cavity with a stationary bottom wall: Grid convergence study of vertical and horizontal velocity profiles along the horizontal and vertical center lines, and static pressure distribution along the bottom wall for  $Re = 200$ . . . . . 206
- 6.12 Flow in a lid-driven open-cavity with a stationary bottom wall: contours of stream function (left), velocity magnitude (middle) and static pressure (right) of the flow in the cavity for  $Re = 200$ , using a grid of  $61 \times 61$ . Each plot contains 50 contour levels varying linearly from the minimum value to the maximum value. 207
- 6.13 Strategy for spatial discretisation using 1D-IRBFN and LMLS-1D-IRBFN methods. . . . . 207
- 6.14 Flow in a lid-driven open-cavity with a prescribed bottom wall motion (Case 1): static pressure at the mid-point of the bottom wall with respect to time  $t$ , using a Cartesian grid with a grid spacing of  $1/60$ . . . . . 208

- 
- 6.15 Flow in a lid-driven open-cavity with a prescribed bottom wall motion (Case 1): contours of stream function (left), velocity magnitude (middle) and static pressure (right) of the flow for several times  $t = 51.5, 52.0, 52.5$  and  $53.0s$ , from top to bottom, using a Cartesian grid with a grid spacing of  $1/60$ . . . . . 209
- 6.16 Flow in a lid-driven open-cavity with a prescribed bottom wall motion (Case 2): static pressure at the mid-point of the bottom wall with respect to time  $t$ , using a Cartesian grid with a grid spacing of  $1/60$ . . . . . 210
- 6.17 Flow in a lid-driven open-cavity with a prescribed bottom wall motion (Case 2): contours of stream function (left), velocity magnitude (middle) and static pressure (right) of the flow for several times  $t = 51.5, 52.0, 52.5$  and  $53.0s$ , from top to bottom, using a Cartesian grid with a grid spacing of  $1/60$ . . . . . 211
- 6.18 Forced vibration of a simply supported beam. . . . . 212
- 6.19 Forced vibration of a simply supported beam: steady state response of the mid-point of a simply supported beam, using a uniform grid of 61 and  $\Delta t = 0.1s$ . . . . . 213
- 6.20 Flow in a lid-driven open-cavity with a simply supported flexible bottom wall: deflection of the mid-point of the bottom wall with respect to time  $t$  between two different approaches of predictors, using a Cartesian grid with a grid spacing of  $1/60$ . . . . . 215
- 6.21 Flow in a lid-driven open-cavity with a flexible bottom wall: deflection of the mid-point of the clamped bottom wall with respect to time  $t$  in comparison with the case of simply supported bottom wall, using a Cartesian grid with a grid spacing of  $1/60$ . . . . . 216

- 
- 6.22 Flow in a lid-driven open-cavity with a simply supported flexible bottom wall (Case 1): contours of stream function (left), velocity magnitude (middle) and static pressure (right) of the flow at time  $t = 92.5s$ , using a Cartesian grid with a grid spacing of  $1/60$ . Each plot contains 50 contour levels varying linearly from the minimum value to the maximum value. . . . . 217
- 6.23 Flow in a lid-driven open-cavity with a clamped flexible bottom wall (Case 2): contours of stream function (left), velocity magnitude (middle) and static pressure (right) of the flow at time  $t = 92.5s$ , using a Cartesian grid with a grid spacing of  $1/60$ . Each plot contains 50 contour levels varying linearly from the minimum value to the maximum value. . . . . 217

# Chapter 1

## Introduction

This chapter starts with the motivation for the present research. Then, we presents an overview of the governing equations for fluid, structure and fluid-structure interaction (FSI). A review of numerical methods for solving fluid mechanics, solid mechanics and FSI problems is followed. Finally, the outline of the dissertation is described.

### 1.1 Motivation

Fluid-Structure Interaction (FSI) plays a central role in several engineering problems such as flow-induced vibration (Liew et al., 2007), aircraft wing flutter (Rendall and Allen, 2008), bridge flutter (Ge and Xiang, 2008), ocean wave energy extraction device (Agamloh et al., 2008), blood flow in heart valves (Vierendeels et al., 2005), design of helicopter rotors (Xiong and Yu, 2007), and sailing boat (Parolini and Quarteroni, 2005). Therefore, FSI is a very interesting topic and FSI analysis is the key for resolving those kinds of problems. FSI is also a challenge for numerical modelling.

So far, finite element method (FEM), finite difference method (FDM), finite vol-

ume method (FVM) have been usually used for analysis of FSI problems (Guruswamy and Byun, 1995; Garcia and Guruswamy, 1999; Vierendeels et al., 2005; Liew et al., 2007). However, the FEM, FDM and FVM have difficulties in handling fluid flow problems with free surface and moving boundary conditions (Liu, 2003). This research project is concerned with the development of a new numerical procedure that can handle FSI and moving boundary problems with ease and high accuracy. The proposed approach is based on (i) global one-dimensional integrated radial basis function network collocation method (1D-IRBFN) and (ii) local moving least square - one-dimensional integrated radial basis function network method (LMLS-1D-IRBFN). It is expected that the outcome of the project will be a more advanced approach for solving engineering problems involving FSI phenomena.

In the framework of continuum mechanics, fluid and solid behaviours are usually modelled by a set of partial differential equations (PDEs) and a set of boundary conditions. The governing equations for fluid flow are derived from the application of four basic laws (i) conservation of mass (continuity); (ii) conservation of momentum (Newton's second law of motion); (iii) conservation of energy (first law of thermodynamics); and (iv) second law of thermodynamics. In addition, for each material, a constitutive law is required for closure. In the case of Newtonian fluids (e.g. water, air) under iso-thermal condition, the continuity equation, the momentum equation and the constitutive relation can be combined to obtain the well known Navier-Stokes equations. For solid mechanics problems, one has strain-displacement equations, motion equations and constitutive equations (stress-strain relations). To solve FSI problems, one needs to consider both the geometrical compatibility and the equilibrium conditions of the interfaces between fluid and structure domains. Structural behaviour presents complicated boundary conditions for fluid flow analysis, thus in some cases the boundaries are assumed to be rigid. Some FSI behaviours can converge to a steady state solution, others can be oscillatory or even unstable.

## 1.2 Governing equations for fluid, structure and fluid-structure interaction

### Governing equations for structure

Let  $R_s(t)$  be the spatial domain of a structure with the boundary  $\partial R_s(t)$  at time  $t$ . Here, the subscript  $s$  stands for the structural component. Let  $x$  be a position vector of a point of a structure. The equilibrium equation for the structure is

$$\rho_s \frac{\partial^2 \mathbf{u}_s}{\partial t^2} = \nabla \cdot \sigma_s + \rho_s \mathbf{f} \quad \forall x \in R_s(t), \quad (1.1)$$

where  $\rho_s$  is the mass density of the structure;  $\mathbf{u}_s$  the structural displacement vector;  $\nabla$  the vector differential operator;  $\sigma_s$  the stress tensor of the structure; and  $\mathbf{f}$  the body force vector (measured per unit mass) acting on the structure. The boundary conditions include

- Dirichlet boundary condition

$$\mathbf{u}_s = \mathbf{u}_B \quad \forall x \in \partial R_s^{\mathbf{u}}, \quad (1.2)$$

- Neumann boundary condition

$$\sigma_s \cdot \mathbf{n} = \mathbf{h}_B \quad \forall x \in \partial R_s^{\mathbf{h}}, \quad (1.3)$$

where  $\partial R_s^{\mathbf{u}}$  and  $\partial R_s^{\mathbf{h}}$  represent the parts of the boundary with prescribed displacements  $\mathbf{u}_B$  and traction  $\mathbf{h}_B$ , respectively; and  $\mathbf{n}$  is the unit outward vector normal to the boundary  $\partial R_s^{\mathbf{h}}$  at  $x$ .

### Governing equations for fluid

In the present research, we limit the analysis to 2-D problems and the di-

mensional conservative form of the Navier-Stokes equations of incompressible viscous flow in terms of primitive variables is written in  $xy$ -Cartesian system as

$$\frac{\partial u}{\partial x} + \frac{\partial v}{\partial y} = 0, \quad (1.4)$$

$$\rho_f \frac{\partial u}{\partial t} + \rho_f \frac{\partial u^2}{\partial x} + \rho_f \frac{\partial uv}{\partial y} = -\frac{\partial p}{\partial x} + \mu \left[ \frac{\partial^2 u}{\partial x^2} + \frac{\partial^2 u}{\partial y^2} \right], \quad (1.5)$$

$$\rho_f \frac{\partial v}{\partial t} + \rho_f \frac{\partial uv}{\partial x} + \rho_f \frac{\partial v^2}{\partial y} = -\frac{\partial p}{\partial y} + \mu \left[ \frac{\partial^2 v}{\partial x^2} + \frac{\partial^2 v}{\partial y^2} \right], \quad (1.6)$$

where  $u$ ,  $v$  and  $p$  are velocity components and static pressure of the fluid, respectively; and  $\rho_f$  and  $\mu$  the density and dynamic viscosity of the fluid, respectively.

The dimensionless form of the above system of equations is given by

$$\frac{\partial U}{\partial X} + \frac{\partial V}{\partial Y} = 0, \quad (1.7)$$

$$\frac{\partial U}{\partial t'} + \frac{\partial U^2}{\partial X} + \frac{\partial UV}{\partial Y} = -\frac{\partial P}{\partial X} + \frac{1}{Re} \left[ \frac{\partial^2 U}{\partial X^2} + \frac{\partial^2 U}{\partial Y^2} \right], \quad (1.8)$$

$$\frac{\partial V}{\partial t'} + \frac{\partial UV}{\partial X} + \frac{\partial V^2}{\partial Y} = -\frac{\partial P}{\partial Y} + \frac{1}{Re} \left[ \frac{\partial^2 V}{\partial X^2} + \frac{\partial^2 V}{\partial Y^2} \right]. \quad (1.9)$$

The non-dimensionalisation is as follows.

$$t' = \frac{t}{H/U_0}, \quad X = \frac{x}{H}, \quad Y = \frac{y}{H},$$

$$U = \frac{u}{U_0}, \quad V = \frac{v}{U_0}, \quad P = \frac{p}{\rho_f U_0^2},$$

where  $H$  is a characteristic length; and  $U_0$  reference velocity. The Reynolds number is defined by  $Re = U_0 H / \nu$ , in which  $\nu$  is the kinematic viscosity of the fluid ( $\nu = \mu / \rho_f$ ).

The 2-D Navier-Stokes equations of incompressible viscous flow can be written

in terms of stream function  $\psi$  and vorticity  $\omega$  as follows.

$$\frac{\partial^2 \psi}{\partial x^2} + \frac{\partial^2 \psi}{\partial y^2} = -\omega, \quad (1.10)$$

$$\frac{1}{Re} \left( \frac{\partial^2 \omega}{\partial x^2} + \frac{\partial^2 \omega}{\partial y^2} \right) = \frac{\partial \omega}{\partial t} + \left( \frac{\partial \psi}{\partial y} \frac{\partial \omega}{\partial x} - \frac{\partial \psi}{\partial x} \frac{\partial \omega}{\partial y} \right), \quad (1.11)$$

where the  $x$  and  $y$  components of the velocity vector can be defined in terms of the stream function as

$$u = \frac{\partial \psi}{\partial y}, \quad (1.12)$$

$$v = -\frac{\partial \psi}{\partial x}. \quad (1.13)$$

### Coupled equations for fluid-structure interaction

The geometrical compatibility conditions at the interface  $\Gamma$  between the fluid and structural domains are given by

$$\mathbf{r}_f^\Gamma(t) = \mathbf{u}_s^\Gamma(t), \quad (1.14)$$

$$\dot{\mathbf{r}}_f^\Gamma(t) = \dot{\mathbf{u}}_s^\Gamma(t), \quad (1.15)$$

where  $\mathbf{r}_f^\Gamma$  and  $\mathbf{u}_s^\Gamma$  are the displacement vectors of the fluid and structure at the interface  $\Gamma$ , respectively; and  $\dot{\mathbf{r}}_f^\Gamma$  and  $\dot{\mathbf{u}}_s^\Gamma$  the velocity vectors of the fluid and structure at the interface  $\Gamma$ , respectively.

The equilibrium conditions can be described as follows.

$$\mathbf{h}_f^\Gamma(t) + \mathbf{h}_s^\Gamma(t) = \mathbf{0}, \quad (1.16)$$

where  $\mathbf{h}_f^\Gamma$  and  $\mathbf{h}_s^\Gamma$  are the traction vectors acting on the fluid and structure at interface  $\Gamma$ , respectively.

## 1.3 A brief review of traditional numerical methods

Numerical simulation plays a crucial role in design and manufacturing of products in several fields such as aerospace, biomedical, civil, mechanical and electrical engineering. In general, due to the lack of analytical solutions to practical problems with irregular domains, complex material constitution and high non-linearity, numerical methods become a useful alternative to find approximate solutions to these problems. By using numerical methods, one can investigate the effects of problem parameters on the behaviour of the products, which is much cheaper than using experiments for obtaining the same level of understanding. The fundamental concept of numerical methods is based on the approximation of the partial derivatives by algebraic expressions. After approximating the PDEs by algebraic equations, they can be solved numerically by using the aid of a computer. A brief review of some traditional numerical methods including finite difference method (FDM), finite volume method (FVM), finite element method (FEM) and boundary element method (BEM) is described as follows.

In FDMs, the spatial discretisation is performed in conjunction with structured grids, while FVMs and FEMs can be employed in conjunction with both structured and unstructured grids. The FDMs are most efficiently solved in rectangular domains with equal grid spacings. When dealing with nonrectangular domains, it is necessary to transform the nonrectangular physical domain into a rectangular computational domain with uniform grid spacings. The representations of the partial derivatives in the governing equations of the problem are obtained from Taylor series expansions at each grid point. Even if a coordinate transformation is available, when dealing with highly irregular domains using the FDMs, there can be some serious difficulties in accuracy and convergence of the solution. The reader is referred to (Roache, 1998; Hoffmann and Chiang, 2000) for more details.

In FVMs and FEMs, the original differential equations are integrated on the physical domain and then solved numerically. Therefore, the grid system for FVM and FEM are generated directly within the physical space. The physical domains can be discretised using structured and unstructured grids. The main advantage of the unstructured grid is that it can be used to easily discretise irregular and multiply-connected domains. Therefore, the FVMs and FEMs have advantages over the FDMs when dealing with complicated irregular domain problems. However, if the physical domain can be discretised into a smooth structured grid, FDMs could be a better choice owing to its efficiency over that of FVMs and FEMs.

FVM is a common approach for solving problems of fluid mechanics. The conservation laws of fluid motion can be expressed in either differential form or integral form. When using FVMs, the domain of interest is divided into small volumes, namely control volumes. Subsequently, the conservation laws in integral form are applied to these control volumes. For 2-D analysis, the Green's theorem is applied to convert area integrals to line integrals. For 3-D analysis, the divergence theorem is used to convert volume integrals (that contain a divergence term) to surface integrals. These terms are then evaluated as fluxes at the surfaces of each control volume. The reader is referred to (Hoffmann and Chiang, 2000; Toro, 2009) for more details.

Historically, FEM was developed for solving solid mechanics problems. In recent decades, it has been extended for many other fields including fluid mechanics and heat transfer. In FEMs, the physical domain is represented as a collection of simple subdomains, called finite elements. The approximate forms of the solution over each element are constructed systematically by using variational (energy) method or weighted-residual methods (e.g., the collocation method, the least-square method, the Galerkin method, and the Petrov-Galerkin method). These functions, representing approximate problem solutions, are often algebraic polynomials that are derived using interpolation theory. Assembly of

elements is usually based on continuity of the solution and balance of internal fluxes. Once the governing equations have been discretised, the resulting set of linear algebraic equations is solved using a digital computer. The reader is referred to (Reddy, 2006) for more details.

In BEM, the governing partial differential equations are transformed into equivalent boundary integral equations by using the Green's identities. The boundary of solution domain is represented by a set of boundary elements and the boundary integrals are approximated over the boundary elements. For linear problems, the dimensionality of the problem in BEM is reduced by one, which is considered as an advantage of the BEM over spatial domain methods such as FDM, FVM and FEM. However, while BEM is suitable for linear and mildly nonlinear problems, it does not work well with highly nonlinear problems. The reader is referred to (Tanner, 1985; Phan-Thien and Kim, 1994; Tran-Cong, 1989; Pozrikidis, 2002) for more details.

## **1.4 A brief review of structural, fluid and fluid-structure interaction analyses**

It is highly desirable to develop an efficient numerical method to investigate and optimize the mechanical behaviour of composite structure instead of using experimental testing which is usually time-consuming and costly. Because of the limitations of analytical methods in practical applications, numerical methods are becoming the most effective tools to solve many industrial problems. Finite Element Method (FEM) is a powerful method used to solve most linear and nonlinear practical engineering problems in solid mechanics. However, FEM has some limitations which include time-consuming task of mesh generation, low accuracy when solving large deformation problems due to element distortions, difficulty in simulating problems with strain localization and shear band

formation due to discontinuities that may not coincide with some of the original nodal lines (Liu, 2003).

Grid or mesh based numerical methods such as FDM, FVM, and FEM have been applied to solve various problems of computational fluid dynamics. These methods are very useful to solve PDEs that govern the fluid flow problems. While FDM (Chung, 2002) is suitable for problems with simple geometries, FVM (Toro, 2009) and FEM (Reddy, 1993) are flexible in handling problems with complex geometries and complicated boundary conditions. These methods have achieved remarkable results and are currently the most popular methods in numerical analyses of both fluid and solid mechanics. However, they have limitations in dealing with several types of complicated problems. The drawbacks have resulted from the use of meshes which can cause various difficulties in handling problems with free surface and moving boundary.

Meshfree methods have great potential to overcome those challenges and have become a major research focus for both solid and fluid mechanics problems over the last few decades. Nayroles et al. (1992) introduced the diffuse element method (DEM), a first meshless method using moving least square (MLS) approximations to construct the shape function. The finite element mesh is totally unnecessary in this method. Belytschko et al. (1994) proposed an element-free Galerkin (EFG) method based on the DEM with modifications in the implementation to increase the accuracy and the rate of convergence. In their work, Lagrange multipliers were used to impose essential boundary conditions. Liu and Gu (2001) developed a point interpolation method (PIM) to construct polynomial interpolation functions with  $\delta$ -function property so the essential boundary conditions can be imposed with ease as done in the conventional FEM. However, the problem of singular moment matrix can occur, resulting in termination of the computation. A point interpolation method based on radial basis function (RPIM) was proposed by Wang and Liu (2002) to produce a non-singular moment matrix. In the PIM and RPIM, the compatibility characteristics is not

ensured so the field function approximated could be discontinuous when nodes enter or leave the moving support domain. Liu et al. (2005) suggested a linearly conforming point interpolation method (LC-PIM) with a simple scheme for local supporting node selection, and a linearly conforming radial point interpolation method (LC-RPIM) (Liu et al., 2006) to overcome the singular moment matrix issue and ensure the compatibility of the displacement.

Meshfree methods can be categorised into two main groups with respect to their approximation techniques. Group one methods are based on strong form formulation such as the meshfree collocation method in which the numerical solution satisfies the governing equation at the collocation points (Mai-Duy and Tran-Cong, 2009b; Le-Cao et al., 2009). The other group consists of weak-form methods based on an integration technique in which the final numerical equations are generated by substituting the approximation functions into a Galerkin integration equation. This formulation can produce a stable system of algebraic equations and gives a discretised system of equations that yields much more accurate results (Mai-Duy and Tran-Cong, 2009a; Ho-Minh et al., 2009). However, the major drawback of weak-form methods is highly expensive computational cost due to the numerical integration.

In the fluid-structure interaction (FSI) analysis, a coupling strategy to satisfy both the geometrical compatibility and the equilibrium conditions of the interface is a key issue. There are two main approaches for solving FSI problems, namely monolithic methods (Rugonyi and Bathe, 2001; Heil, 2004; Liew et al., 2007) and partitioned methods (Farhat and Lesoinne, 1998; Piperno, 1997). Partitioned procedures are usually preferred when the interaction between the fluid and the structure is weak while the monolithic solution procedure is chosen to be effective for solving problems with a strong FSI dependence. In the monolithic approach, the fluid and structural equations are tightly coupled and solved simultaneously. This approach may lead to two drawbacks (i) an increase in the number of degrees of freedom (DOFs) and (ii) an ill-conditioned system

matrix. In the partitioned approach, the fluid and structure fields are solved separately and the solution variables are transferred at the interface. By using this approach, it is flexible to choose different solvers for each field. However, the approach introduces a time delay which translates as non-physical energy dissipation (Farhat and Lesoinne, 1998).

## 1.5 Radial basis function networks

Kansa (1990a) proposed a collocation scheme based on multiquadric (MQ) radial basis functions (RBF) for the numerical solution of PDEs. Their numerical results showed that MQ scheme yielded an excellent interpolation and partial derivative estimates for a variety of two-dimensional functions over both gridded and scattered data. The main drawback of RBF-based methods is the lack of mathematical theories for finding the appropriate values of network parameters. For example, the RBF width, which strongly affects the performance of RBF networks, has still been chosen either by empirical approaches or by optimization techniques. Kansa's approach is here referred to as the conventional differentiated radial basis function network (DRBFN) method. Radial basis function networks (RBFN) are capable of universal approximation based on meshfree discretisation (Park and Sandberg, 1991). Approximants based on some RBFs such as multiquadric and Gaussian functions can offer an exponential rate of convergence (Madych and Nelson, 1989).

In contrast to the advantages of no mesh generation, global meshfree methods are not suitable for simulating large-scale problems because they produce very dense system matrices (Zerroukat et al., 2000; Šarler and Perko, 2004). Sparse system matrices can be generated by the use of compactly supported RBFs (Wendland, 1995), and the accuracy of such an approach can be improved by a multilevel technique (Chen et al., 2002). Atluri and Zhu (1998) presented a meshless local Petrov-Galerkin (MLPG) approach based on a local

symmetric weak form and the MLS approximation, which is a truly meshless method. One of the possible ways to avoid the fully dense matrix problem is to employ a domain decomposition technique (Mai-Duy and Tran-Cong, 2002). Lee et al. (2003) proposed local multiquadric (LMQ) and local inverse multiquadric (LIMQ) approximation methods for solving boundary value problems. Their numerical results indicated that the methods are highly efficient and able to yield accurate solutions for a wide range of values of the RBF width. Wright and Fornberg (2006) presented local RBF-based finite difference schemes for solving differential equations. Šarler and Vertnik (2006) presented an explicit local RBF collocation method for diffusion problems. The method appeared efficient, because it does not require a solution of a large system of equations like the original RBF collocation method (Kansa, 1990b). Divo and Kassab (2007) developed a localized RBF meshless method for a solution of coupled viscous fluid flow and conjugate heat transfer problems. In their work, a domain decomposition technique is used to accelerate the computation speed by distributing the computational load over multiple processors. Stevens, Power and Morvan (2009) proposed a local Hermitian interpolation (LHI) method for steady and unsteady solutions of linear convection-diffusion-reaction problems. The method was then extended by using interpolation functions which themselves satisfy the governing equations, resulting in an improvement of the solution accuracy (Stevens, Power, Lees and Morvan, 2009).

As an alternative to the DRBFN, Mai-Duy and Tran-Cong (2001a) proposed the use of integration to construct the RBFN expressions (the IRBFN method) for the approximation of a function and its derivatives and for the solution of PDEs. The use of integration instead of conventional differentiation to construct the RBF approximations significantly improved the stability and accuracy of the numerical solution. The improvement is attributable to the fact that integration is a smoothing operation and is more numerically stable. The numerical results showed that the IRBFN method achieves superior accuracy (Mai-Duy and Tran-Cong, 2001a, 2003a). A one-dimensional integrated radial basis func-

tion network (1D-IRBFN) collocation method for the solution of second- and fourth-order PDEs was presented by Mai-Duy and Tanner (2007). Along grid lines, 1D-IRBFN are constructed to satisfy the governing DEs together with boundary conditions in an exact manner. The 1D-IRBFN method is much more efficient than the original IRBFN method reported by Mai-Duy and Tran-Cong (2001a).

## 1.6 Discussion and objectives of the present research

From the literature review above, it can be seen that FEM has limitations when handling structural analysis problems with large deformation due to element distortions. Meshfree and Cartesian-based methods have great capabilities to overcome these problems. The 1D-IRBFN method with the use of integration instead of conventional differentiation to construct the RBF approximations significantly improved the accuracy and stability of numerical solution. The method is employed to perform structural analyses in the present research (Ngo-Cong et al., 2011).

Babuška and Melenk (1997) presented the partition of unity method (PUM) with attractive features. In the PUM, if analytic knowledge about the local behaviour of the problem solution is known, local approximation can be done with functions better suited than polynomials as in the classical FEM. In this research, the PU concept is employed as a framework to incorporate MLS and 1D-IRBFN techniques in an approach, namely local MLS-1D-IRBFN or LMLS-1D-IRBFN. The approximation is locally supported, which leads to sparse system matrices and requires less computational effort than the case of using 1D-IRBFN method alone, while the order of accuracy remains high as in the case of 1D-IRBFN. Unlike conventional MLS-based methods, the LMLS-1D-

IRBFN shape functions satisfy the Kronecker- $\delta$  property and thus the essential boundary conditions can be imposed in an exact manner. Therefore, the proposed method can be used to solve large-scale problems with less computational effort and high accuracy.

In the literature, different strategies have been proposed to simulate FSI, and the selection of the most effective method strongly depends on the characteristics of the given problem. In this study, a numerical procedure based on the 1D-IRBFN and local MLS-1D-IRBFN methods in conjunction with a sequentially staggered algorithm is developed for solving FSI problems.

In short, we propose the 1D-IRBFN, local MLS-1D-IRBFN methods and a novel numerical procedure based on the 1D-IRBFN and local MLS-1D-IRBFN methods for an accurate and efficient solution to solid mechanics, fluid mechanics and FSI problems. The high level of accuracy and efficiency are achieved by means of the following main characteristics.

- RBF network is a high-order approximation.
- The use of integration instead of conventional differentiation to construct the RBF approximations significantly improves the stability and accuracy of the numerical solution. The improvement is attributable to the fact that integration is a smoothing operation and is more numerically stable.
- The constants of integration in the IRBF formulation are used for the purpose of imposing Neumann boundary conditions in an exact manner.
- Cartesian grids are used to discretise the problem domains. It is clear that generating a Cartesian grid is much simpler and easier than generating a finite element mesh.
- The local MLS-1D-IRBFN approximation is locally supported, which leads to sparse system matrices and requires less computational effort than the

case of using 1D-IRBFN method alone, while the order of accuracy remains high as in the case of 1D-IRBFN. Therefore, it can be used to solve large-scale problems with less computational effort.

- Unlike conventional MLS-based methods, the LMLS-1D-IRBFN shape functions satisfy the Kronecker- $\delta$  property and thus the essential boundary conditions can be imposed in an exact manner.

## 1.7 Outline of the present research

In this dissertation, each chapter is structured in a self-explanatory manner as follows.

Chapter 2 presents a 1D-IRBFN collocation technique for the free vibration analysis of laminated composite plates using the first order shear deformation theory. The rectangular and non-rectangular plates are simply discretised by means of Cartesian grids. A number of examples concerning various thickness-to-span ratios, material properties and boundary conditions are considered.

Chapter 3 reports a novel local moving least square - one-dimensional integrated radial basis function network (LMLS-1D-IRBFN) method for solving incompressible viscous flow problems using stream function-vorticity formulation. The LMLS-1D-IRBFN method yields the same level of accuracy as that of the 1D-IRBFN method while reduces the computational cost significantly owing to its banded sparse system matrix. The proposed method is verified through problems of flow in a lid-driven cavity and steady flow past a circular cylinder.

Chapter 4 reports the LMLS-1D-IRBFN method for multiply-connected-domain problems. The proposed numerical procedure is verified through simulations of natural convection flows in concentric and eccentric annuli in terms of stream

function, vorticity and temperature. The stream function value on the inner boundary of the eccentric annulus is unknown and determined by using the single-valued pressure condition (Lewis, 1979).

Chapter 5 presents a further development of the LMLS-1D-IRBFN method for a solution of time-dependent problems such as Burgers' equation, unsteady flow past a square cylinder in a horizontal channel and unsteady flow past a circular cylinder. The present numerical method is combined with a domain decomposition technique to handle large-scale problems. Flow parameters such as drag coefficient, length of recirculation zone, Strouhal number and the effect of blockage ratio on the behaviour of the flow field behind the cylinder are investigated.

Chapter 6 presents a new numerical procedure based on the 1D-IRBFN and local MLS-1D-IRBFN methods for fluid-structure interaction analysis. A combination of Chorin's method and pseudo-time subiterative technique is presented for a transient solution of 2-D incompressible viscous Navier-Stokes equations in terms of primitive variables. The fluid solver is first verified through a solution of mixed convection in a lid-driven cavity with a hot lid and a cold bottom wall. The structural solver is verified with an analytical solution of forced vibration of a beam. The FSI numerical procedure is then applied to simulate flows in a lid-driven open-cavity with a flexible bottom wall.

Chapter 7 gives some concluding remarks from the present research.

## Chapter 2

# 1D-IRBFN method for free vibration of laminated composite plates

This chapter presents an effective radial basis function (RBF) collocation technique for free vibration analysis of laminated composite plates using the first order shear deformation theory (FSDT). The plates, which can be rectangular or non-rectangular, are simply discretised by means of Cartesian grids. Instead of using conventional differentiated RBF networks, one-dimensional integrated RBF networks (1D-IRBFN) are employed on grid lines to approximate the field variables. Several examples are chosen to investigate the effect of thickness-to-span ratios, material properties and boundary conditions. Results obtained are compared with available analytical solutions and numerical results by other techniques in the literature to assess the performance of the proposed method. In Chapters 3-5 we will report methods for fluid flows and finally in Chapter 6 the combination of methods developed in Chapters 2-5 in a new approach for FSI analysis is demonstrated.

## 2.1 Introduction

Free vibration analysis of laminated composite plates has been an important problem in the design of mechanical, civil and aerospace applications. Vibration can waste energy and create unwanted noise in the motions of engines, motors, or any mechanical devices in operation. When a system operates at the system natural frequency, resonance can happen causing large deformations and even catastrophic failure in improperly constructed structures. Careful designs can minimize those unwanted vibrations.

The lamination scheme and material properties of individual lamina provide an added flexibility to designers to tailor the stiffness and strength of composite laminates to match the structural requirements. The significant difference between the classical plate theory (CLPT) and the first order shear deformation theory (FSDT) is the effect of including transverse shear deformation on the predicted deflections and frequencies. The CLPT underpredicts deflections and overpredicts frequencies for plates with thickness-to-length ratios larger than 0.05 (Reddy, 2004) while the FSDT has been the most commonly used in the vibration analysis of moderately thick composite plates with thickness-to-length ratio less than 0.2 (Noor and Burton, 1973). The FSDT is an approximate theory with some assumptions on the deformation of a plate which reduce the dimensions of the plate problem from three to two and greatly simplify the governing equations. However, these assumptions inherently result in errors which can be significant when the thickness-to-length ratio increases.

Using the theory of elasticity, Srinivas and Rao (1970) developed an exact three-dimensional (3-D) solution for bending, vibration and buckling of simply supported thick orthotropic rectangular plates. Their results have been widely used as benchmark solutions by many researchers. Liew et al. (1993) developed a continuum 3-D Ritz formulation based on the 3-D elasticity theory and the Ritz minimum energy principle for the vibration analysis of homogeneous,

thick, rectangular plates with arbitrary combination of boundary constraints. The formulation was employed to study the effects of geometric parameters on the overall normal mode characteristics of simply supported plates, and the effects of in-plane inertia on the vibration frequencies of plates with different thicknesses (Liew et al., 1994). This formulation was also applied specifically to investigate the effects of boundary constraints and thickness ratios on the vibration responses of plates (Liew et al., 1995). Liew and Teo (1999) employed the differential quadrature (DQ) method for the vibration analysis of 3-D elasticity plates with a high degree of accuracy.

When dealing with highly orthotropic composite plates, the higher-order shear deformation theories (HSDT) is more favourable than the FSDT because the former can yield highly accurate results without the need for a shear correction factor. Reddy and Phan (1985) employed the HSDT (Reddy, 1984) to determine the natural frequencies and buckling loads of elastic plates. Their exact solutions obtained were more accurate than those of the FSDT and CLPT when compared with the exact solutions by 3-D elasticity theory. Lim et al. (1998a,b) developed an energy-based higher-order plate theory in association with geometrically oriented shape function to investigate the free vibration of thick shear deformable, rectangular plates with arbitrary combinations of boundary constraints. This method required considerably less memory than the direct 3-D elasticity analysis while maintaining the same level of accuracy. Their numerical results showed that for transverse-dominant vibration modes, an increase in thickness results in higher frequency while for inplane-dominant vibration modes, the effects of variation in thickness is insignificant.

Finite element method (FEM) is a powerful method used to solve most linear and nonlinear practical engineering problems in solid and fluid mechanics. However, FEM has some limitations which include time-consuming task of mesh generation, low accuracy when solving large deformation problems due to element distortions, difficulty in simulating problems with strain localization and

shear band formation due to discontinuities that may not coincide with some of the original nodal lines (Liu, 2003). Meshless method has great potential to overcome those challenges. Nayroles et al. (1992) introduced the diffuse element method (DEM), a first meshless method using moving least square (MLS) approximations to construct the shape function. The finite element mesh is totally unnecessary in this method. Belytschko et al. (1994) proposed an element-free Galerkin (EFG) method based on the DEM with modifications in the implementation to increase the accuracy and the rate of convergence. Liu and Gu (2001) developed a point interpolation method (PIM) to construct polynomial interpolation functions with delta function property so the essential boundary conditions can be imposed as done in the conventional FEM with ease. Liew and Chen (2004) and Liew, Chen and Reddy (2004) proposed a numerical algorithm based on the RPIM for the buckling analysis of rectangular, circular, trapezoidal and skew Mindlin plates that are subjected to non-uniformly distributed in-plane edge loads.

In 1990, Kansa proposed a collocation scheme based on multiquadric (MQ) radial basis functions for the numerical solution of partial differential equations (PDEs) (Kansa, 1990a,b). Their numerical results showed that MQ scheme yielded an excellent interpolation and partial derivative estimates for a variety of two-dimensional functions over both gridded and scattered data. The main drawback of RBF based methods is the lack of mathematical theories for finding the appropriate values of network parameters. For example, the RBF width, which strongly affects the performance of RBF networks, has still been chosen either by empirical approaches or by optimization techniques. The use of RBF based method for the free vibration analysis of laminated composite plates has been previously studied by numerous authors. The MQ-RBF procedure was used to predict the free vibration behaviour of moderately thick symmetrically laminated composite plates by Ferreira et al. (2005). The free vibration analysis of Timoshenko beams and Mindlin plates using Kansa's non-symmetric RBF collocation method was performed by Ferreira and Fasshauer

(2005). Ferreira and Fasshauer (2007) showed that the combination of RBF and pseudospectral methods produces highly accurate results for free vibration analysis of symmetric composite plates. Liew (1996) proposed a p-Ritz method with high accuracy, but, it is difficult to choose the appropriate trial functions for complicated problems. Karunasena et al. (1996) and Karunasena and Kiti-pornchai (1997) investigated natural frequencies of thick arbitrary quadrilateral plates and shear-deformable general triangular plates with arbitrary combinations of boundary conditions using the pb-2 Rayleigh-Ritz method in conjunction with the FSDT. Liew et al. (2002) proposed the harmonic reproducing kernel particle method for the free vibration analysis of rotating cylindrical shells. This technique provides ease of enforcing various types of boundary conditions and concurrently is able to capture the travelling modes. Zhao et al. (2004) employed the reproducing kernel particle estimation in hybridized form with harmonic functions to study the frequency characteristics of cylindrical panels. Liew, Wang, Tan and Rajendran (2004) presented a meshfree kernel particle Ritz method (kp-Ritz) for the geometrically nonlinear analysis of laminated composite plates with large deformations, which is based on the FSDT and the total Lagrangian formulation. Liew et al. (2003) adopted a moving least squares differential quadrature (MLSDQ) method for predicting the free vibration behaviour of square, circular and skew plates with various boundary conditions. A meshfree method based on the reproducing kernel particle approximate for the free vibration and buckling analyses of shear-deformation plates was conducted by Liew, Wang, Ng and Tan (2004). In this method, the essential boundary conditions were enforced by a transformation technique.

As an alternative to the conventional differentiated radial basis function network (DRBFN) method Kansa (1990b), Mai-Duy and Tran-Cong (2001b) proposed the use of integration to construct the RBFN expressions (the IRBFN method) for the approximation of a function and its derivatives and for the solution of PDEs. The use of integration instead of conventional differentiation to construct the RBF approximations significantly improved the stability and accuracy of

the numerical solution. The improvement is attributable to the fact that integration is a smoothing operation and is more numerically stable. The numerical results showed that the IRBFN method achieves superior accuracy (Mai-Duy and Tran-Cong, 2001b, 2003a). Mai-Duy and Tran-Cong (2003b) presented a mesh-free IRBFN method using Thin Plate Splines (TPSs) for numerical solution of differential equations (DEs) in rectangular and curvilinear coordinates. The IRBFN was also used to simulate the static analysis of moderately-thick laminated composite plates using the FSDT (Mai-Duy et al., 2007).

A one-dimensional integrated radial basis function network (1D-IRBFN) collocation method for the solution of second- and fourth-order PDEs was presented by Mai-Duy and Tanner (2007). Along grid lines, 1D-IRBFN are constructed to satisfy the governing DEs together with boundary conditions in an exact manner. The 1D-IRBFN method was further developed for the simulation of fluid flow problems. In the present chapter, the 1D-IRBFN method is extended to the case of free vibration of composite laminates based on FSDT. A number of examples are considered to investigate the effects of various plate shapes, length-to-width ratios, thickness-to-span ratios, material properties and boundary conditions on natural frequencies of composite laminated plates. The results obtained are compared with available published results from different methods.

The chapter is organised as follows. Section 2.2 describes the governing equations based on FSDT and boundary conditions for the free vibration of laminated composite plates. The 1D-IRBFN-based Cartesian-grid technique is presented in Section 2.3. The discretisation of the governing equations and boundary conditions is described in Section 2.4. The proposed technique is then validated through several test examples in Section 2.5. Section 2.6 concludes the chapter.

## 2.2 Governing equations

### 2.2.1 First-order shear deformation theory

In the FSDT (Reddy, 2004), the transverse normals do not remain perpendicular to the mid-surface after deformation due to the effects of transverse shear strains. The inextensibility of transverse normals requires  $w$  not to be a function of the thickness coordinate  $z$ . The displacement field of the FSDT at time  $t$  is of the form

$$u(x, y, z, t) = u_0(x, y, t) + z\phi_x(x, y, t), \quad (2.1)$$

$$v(x, y, z, t) = v_0(x, y, t) + z\phi_y(x, y, t), \quad (2.2)$$

$$w(x, y, z, t) = w_0(x, y, t), \quad (2.3)$$

where  $(x, y, z)$  denotes the vector of problem coordinate;  $(u_0, v_0, w_0)$  the vector of displacement of a point on the plane  $z = 0$ ; and  $\phi_x$  and  $\phi_y$  are, respectively, the rotations of a transverse normal about the  $y$ - and  $x$ -axes.

Since the transverse shear strains are assumed to be constant through the laminate thickness, it follows that the transverse shear stresses will also be constant. However, in practice, the transverse shear stresses vary at least quadratically through layer thickness. This discrepancy between the actual stress state and the constant stress state predicted by the FSDT is often corrected by a parameter  $K_s$ , called the shear correction coefficient. It is noted that the natural frequencies of the plate are affected by the factor  $K_s$  and the rotary inertia (RI). The smaller the values of  $K_s$  and RI, the smaller the frequencies will be.

In this chapter we consider a symmetrically laminated plate with the coordinate system originated at the midplane of the laminate, where each layer of the laminate is orthotropic with respect to the  $x$ - and  $y$ -axes and all layers are of equal thickness. For symmetric laminates, the displacements  $u_0$  and  $v_0$  can be disregarded due to the uncoupling between extension and bending actions.

The equations of motion for the free vibration of symmetric cross-ply laminated plates can be expressed by the dynamic version of the principle of virtual displacements as

$$K_s A_{55} \left( \frac{\partial^2 w}{\partial x^2} + \frac{\partial \phi_x}{\partial x} \right) + K_s A_{44} \left( \frac{\partial^2 w}{\partial y^2} + \frac{\partial \phi_y}{\partial y} \right) = I_0 \frac{\partial^2 w}{\partial t^2}, \quad (2.4)$$

$$D_{11} \frac{\partial^2 w}{\partial x^2} + D_{12} \frac{\partial^2 \phi_y}{\partial x \partial y} + D_{66} \left( \frac{\partial^2 \phi_x}{\partial y^2} + \frac{\partial^2 \phi_y}{\partial x \partial y} \right) - K_s A_{55} \left( \frac{\partial w}{\partial x} + \phi_x \right) = I_2 \frac{\partial^2 \phi_x}{\partial t^2}, \quad (2.5)$$

$$D_{66} \left( \frac{\partial^2 \phi_x}{\partial x \partial y} + \frac{\partial^2 \phi_y}{\partial x^2} \right) + D_{12} \frac{\partial^2 \phi_x}{\partial y^2} + D_{22} \frac{\partial^2 \phi_y}{\partial y^2} - K_s A_{44} \left( \frac{\partial w}{\partial y} + \phi_y \right) = I_2 \frac{\partial^2 \phi_y}{\partial t^2}, \quad (2.6)$$

where  $I_0$  and  $I_2$  are the mass inertia tensor components defined as

$$I_0 = \rho h, \quad (2.7)$$

$$I_2 = \frac{\rho h^3}{12}, \quad (2.8)$$

in which  $\rho$  and  $h$  denote the density and the total thickness of the composite plate, respectively; and  $A_{ij}$  and  $D_{ij}$  are the extensional and bending stiffnesses given by

$$A_{ij} = \sum_{k=1}^N \bar{Q}_{ij}^{(k)} (z_{k+1} - z_k), \quad (2.9)$$

$$D_{ij} = \frac{1}{3} \sum_{k=1}^N \bar{Q}_{ij}^{(k)} (z_{k+1}^3 - z_k^3), \quad (2.10)$$

in which  $\bar{Q}_{ij}^{(k)}$  is the transformed material plane stress-reduced stiffness matrix of the layer  $k$ .

Let  $(x_1, x_2, x_3)$  be the principal material coordinates of a typical layer in the laminate. The  $x_1$ -axis is taken to be parallel to the fibre, the  $x_2$ -axis transverse to the fibre direction in the plane of the lamina, and the  $x_3$ -axis is perpendicular to the plane of the lamina. In (2.9) and (2.10), the matrix  $\bar{Q}_{ij}^{(k)}$  can be obtained

through

$$\bar{\mathbf{Q}} = \mathbf{T}\mathbf{Q}_m\mathbf{T}^T, \quad (2.11)$$

where  $\mathbf{T}$  is the transformation matrix given by

$$\mathbf{T} = \begin{bmatrix} \cos^2 \theta & \sin^2 \theta & 0 & 0 & -\sin 2\theta \\ \sin^2 \theta & \cos^2 \theta & 0 & 0 & \sin 2\theta \\ 0 & 0 & \cos \theta & \sin \theta & 0 \\ 0 & 0 & -\sin \theta & \cos \theta & 0 \\ \sin \theta \cos \theta & -\sin \theta \cos \theta & 0 & 0 & \cos^2 \theta - \sin^2 \theta \end{bmatrix}; \quad (2.12)$$

and  $\mathbf{Q}_m$  is the material plane stress-reduced stiffness

$$\mathbf{Q}_m = \begin{bmatrix} E_1/(1 - \nu_{12}\nu_{21}) & \nu_{12}E_2/(1 - \nu_{12}\nu_{21}) & 0 & 0 & 0 \\ \nu_{12}E_2/(1 - \nu_{12}\nu_{21}) & E_2/(1 - \nu_{12}\nu_{21}) & 0 & 0 & 0 \\ 0 & 0 & G_{23} & 0 & 0 \\ 0 & 0 & 0 & G_{13} & 0 \\ 0 & 0 & 0 & 0 & G_{12} \end{bmatrix}, \quad (2.13)$$

in which  $\theta$  is the angle measured from the global  $x$ -axis to the fibre direction which is positive if measured clockwise, and negative if measured anti-clockwise;  $E_1$  and  $E_2$  the Young's moduli for a layer parallel to fibres and perpendicular to fibres, respectively;  $\nu_{12}$  and  $\nu_{21}$  Poisson's ratios; and  $G_{23}$ ,  $G_{13}$ , and  $G_{12}$  shear moduli in the  $x_2x_3$ ,  $x_1x_3$ , and  $x_1x_2$  planes, respectively.

Expressing the variables  $w$ ,  $\phi_x$ , and  $\phi_y$  in the following harmonic forms

$$w(x, y, t) = W(x, y)e^{i\omega t}, \quad (2.14)$$

$$\phi_x(x, y, t) = \Psi_x(x, y)e^{i\omega t}, \quad (2.15)$$

$$\phi_y(x, y, t) = \Psi_y(x, y)e^{i\omega t}, \quad (2.16)$$

the equations of motion (2.4)-(2.6) become

$$K_s A_{55} \left( \frac{\partial^2 W}{\partial x^2} + \frac{\partial \Psi_x}{\partial x} \right) + K_s A_{44} \left( \frac{\partial^2 W}{\partial y^2} + \frac{\partial \Psi_y}{\partial y} \right) = -I_0 \omega^2 W, \quad (2.17)$$

$$D_{11} \frac{\partial^2 W}{\partial x^2} + D_{12} \frac{\partial^2 \Psi_y}{\partial x \partial y} + D_{66} \left( \frac{\partial^2 \Psi_x}{\partial y^2} + \frac{\partial^2 \Psi_y}{\partial x \partial y} \right) - K_s A_{55} \left( \frac{\partial W}{\partial x} + \Psi_x \right) = -I_2 \omega^2 \Psi_x, \quad (2.18)$$

$$D_{66} \left( \frac{\partial^2 \Psi_x}{\partial x \partial y} + \frac{\partial^2 \Psi_y}{\partial x^2} \right) + D_{12} \frac{\partial^2 \Psi_x}{\partial y^2} + D_{22} \frac{\partial^2 \Psi_y}{\partial y^2} - K_s A_{44} \left( \frac{\partial W}{\partial y} + \Psi_y \right) = -I_2 \omega^2 \Psi_y, \quad (2.19)$$

where  $\omega$  is the frequency of natural vibration.

## 2.2.2 Boundary conditions

The boundary conditions for a simply supported or clamped edge can be described as follows.

- Simply supported case: There are two kinds of simply support boundary conditions for the FSDT plate models.

- The first kind is the soft simple support (SS1)

$$w = 0; M_{ns} = 0; M_n = 0. \quad (2.20)$$

- The second kind is the hard simple support (SS2)

$$w = 0; \phi_s = 0; M_n = 0. \quad (2.21)$$

The hard simple support is considered in this chapter. From (2.21), we

have the following relations

$$w = 0, \quad \text{on } \Gamma, \quad (2.22)$$

$$n_x \phi_y - n_y \phi_x = 0, \quad \text{on } \Gamma, \quad (2.23)$$

$$n_x^2 M_{xx} + 2n_x n_y M_{xy} + n_y^2 M_{yy} = 0, \quad \text{on } \Gamma, \quad (2.24)$$

in which  $n_x$  and  $n_y$  are the direction cosines of a unit normal vector at a point on the plate boundary  $\Gamma$ .

Equation (2.24) can be expressed as

$$(n_x^2 D_{11} + n_y^2 D_{12}) \frac{\partial \phi_x}{\partial x} + 2n_x n_y D_{66} \left( \frac{\partial \phi_x}{\partial y} + \frac{\partial \phi_y}{\partial x} \right) + (n_x^2 D_{12} + n_y^2 D_{22}) \frac{\partial \phi_y}{\partial y} = 0. \quad (2.25)$$

- Clamped case:

$$w = 0; \quad \phi_n = 0; \quad \phi_s = 0. \quad (2.26)$$

Clamped boundary conditions (2.26) can be described as follows.

$$w = 0, \quad \text{on } \Gamma, \quad (2.27)$$

$$\phi_x = 0, \quad \text{on } \Gamma, \quad (2.28)$$

$$\phi_y = 0, \quad \text{on } \Gamma. \quad (2.29)$$

In (2.20), (2.21) and (2.26), the  $n$  and  $s$  represent the normal and tangential directions of the edge, respectively;  $M_n$  and  $M_{ns}$  denote the normal bending moment and twisting moment, respectively; and  $\phi_n$  and  $\phi_s$  are rotations about the tangential and normal coordinates on the laminate edge.

## 2.3 One-dimensional indirect/integrated radial basis function networks

In the remainder of the chapter, we use

- the notation  $\widehat{[\ ]}$  for a vector/matrix  $[\ ]$  that is associated with a grid line,
- the notation  $\widetilde{[\ ]}$  for a vector/matrix  $[\ ]$  that is associated with the whole set of grid lines,
- the notation  $[\ ]_{(\eta,\theta)}$  to denote selected rows  $\eta$  and columns  $\theta$  of the matrix  $[\ ]$ ,
- the notation  $[\ ]_{(\eta)}$  to denote selected components  $\eta$  of the vector  $[\ ]$ ,
- the notation  $[\ ]_{(:,\theta)}$  to denote all rows and selected columns  $\theta$  of the matrix  $[\ ]$ , and
- the notation  $[\ ]_{(\eta,:)}$  to denote all columns and selected rows  $\eta$  of the matrix  $[\ ]$ .

The domain of interest is discretised using a Cartesian grid, i.e. an array of straight lines that run parallel to the  $x$ - and  $y$ -axes. The dependent variable  $u$  and its derivatives on each grid line are approximated using an IRBF interpolation scheme as described in the remainder of this section.

### 2.3.1 IRBFN expressions on a grid line (1D-IRBFN scheme)

Consider an  $x$ -grid line, e.g.  $[j]$ , as shown in Figure 2.1. The variation of  $u$  along this line is sought in the IRBF form. The second-order derivative of  $u$  is decomposed into RBFs; the RBF network is then integrated once and twice

to obtain the expressions for the first-order derivative of  $u$  and the solution  $u$  itself,

$$\frac{\partial^2 u(x)}{\partial x^2} = \sum_{i=1}^{N_x^{[j]}} w^{(i)} G^{(i)}(x) = \sum_{i=1}^{N_x^{[j]}} w^{(i)} H_{[2]}^{(i)}(x), \quad (2.30)$$

$$\frac{\partial u(x)}{\partial x} = \sum_{i=1}^{N_x^{[j]}} w^{(i)} H_{[1]}^{(i)}(x) + c_1, \quad (2.31)$$

$$u(x) = \sum_{i=1}^{N_x^{[j]}} w^{(i)} H_{[0]}^{(i)}(x) + c_1 x + c_2, \quad (2.32)$$

where  $N_x^{[j]}$  is the number of nodes on the grid line  $[j]$ ;  $\{w^{(i)}\}_{i=1}^{N_x^{[j]}}$  RBF weights to be determined;  $\{G^{(i)}(x)\}_{i=1}^{N_x^{[j]}} = \{H_{[2]}^{(i)}(x)\}_{i=1}^{N_x^{[j]}}$  known RBFs;  $H_{[1]}^{(i)}(x) = \int H_{[2]}^{(i)}(x) dx$ ;  $H_{[0]}^{(i)}(x) = \int H_{[1]}^{(i)}(x) dx$ ; and  $c_1$  and  $c_2$  integration constants which are also unknown. An example of RBF, used in this work, is the multiquadrics  $G^{(i)}(x) = \sqrt{(x - x^{(i)})^2 + a^{(i)2}}$ ,  $a^{(i)}$  - the RBF width determined as  $a^{(i)} = \beta d^{(i)}$ ,  $\beta$  a positive factor, and  $d^{(i)}$  the distance from the  $i^{th}$  center to its nearest neighbour.

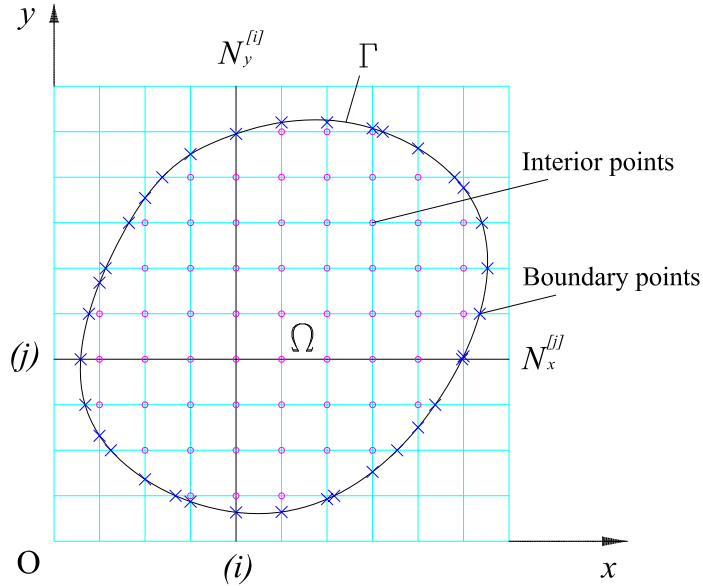


Figure 2.1: Cartesian grid.

It is more convenient to work in the physical space than in the network-weight space. The RBF coefficients including two integration constants can be trans-

formed into the physically meaningful nodal variable values through the following relation

$$\hat{u} = \hat{\mathbf{H}} \begin{pmatrix} \hat{w} \\ \hat{c} \end{pmatrix}, \quad (2.33)$$

where  $\hat{\mathbf{H}}$  is an  $N_x^{[j]} \times (N_x^{[j]} + 2)$  matrix and defined by

$$\hat{\mathbf{H}} = \begin{bmatrix} H_{[0]}^{(1)}(x^{(1)}) & H_{[0]}^{(2)}(x^{(1)}) & \dots & H_{[0]}^{(N_x^{[j]})}(x^{(1)}) & x^{(1)} & 1 \\ H_{[0]}^{(1)}(x^{(2)}) & H_{[0]}^{(2)}(x^{(2)}) & \dots & H_{[0]}^{(N_x^{[j]})}(x^{(2)}) & x^{(2)} & 1 \\ \dots & \dots & \dots & \dots & \dots & \dots \\ H_{[0]}^{(1)}(x^{(N_x^{[j]})}) & H_{[0]}^{(2)}(x^{(N_x^{[j]})}) & \dots & H_{[0]}^{(N_x^{[j]})}(x^{(N_x^{[j]})}) & x^{(N_x^{[j]})} & 1 \end{bmatrix};$$

$\hat{u} = (u^{(1)}, u^{(2)}, \dots, u^{(N_x^{[j]})})^T$ ;  $\hat{w} = (w^{(1)}, w^{(2)}, \dots, w^{(N_x^{[j]})})^T$  and  $\hat{c} = (c_1, c_2)^T$ . There are two possible transformation cases.

Non-square conversion matrix (NSCM): The direct use of (2.33) leads to an underdetermined system of equations

$$\hat{u} = \hat{\mathbf{H}} \begin{pmatrix} \hat{w} \\ \hat{c} \end{pmatrix} = \hat{\mathbf{C}} \begin{pmatrix} \hat{w} \\ \hat{c} \end{pmatrix}, \quad (2.34)$$

or

$$\begin{pmatrix} \hat{w} \\ \hat{c} \end{pmatrix} = \hat{\mathbf{C}}^{-1} \hat{u}, \quad (2.35)$$

where  $\hat{\mathbf{C}} = \hat{\mathbf{H}}$  is the conversion matrix whose inverse can be found using the singular value decomposition (SVD) technique.

Square conversion matrix (SCM): Due to the presence of  $c_1$  and  $c_2$ , one can add

two additional equations of the form

$$\hat{f} = \hat{\mathbf{K}} \begin{pmatrix} \hat{w} \\ \hat{c} \end{pmatrix} \quad (2.36)$$

to equation system (2.34). For example, in the case of Neumann boundary conditions, this subsystem can be used to impose derivative boundary values

$$\hat{f} = \begin{pmatrix} \frac{\partial u}{\partial x}(x^{(1)}) \\ \frac{\partial u}{\partial x}(x^{(N_x^{[j]})}) \end{pmatrix}, \quad (2.37)$$

$$\hat{\mathbf{K}} = \begin{bmatrix} H_{[1]}^{(1)}(x^{(1)}) & H_{[1]}^{(2)}(x^{(1)}) & \dots & H_{[1]}^{(N_x^{[j]})}(x^{(1)}) & 1 & 0 \\ H_{[1]}^{(1)}(x^{(N_x^{[j]})}) & H_{[1]}^{(2)}(x^{(N_x^{[j]})}) & \dots & H_{[1]}^{(N_x^{[j]})}(x^{(N_x^{[j]})}) & 1 & 0 \end{bmatrix}. \quad (2.38)$$

The conversion system can be written as

$$\begin{pmatrix} \hat{u} \\ \hat{f} \end{pmatrix} = \begin{bmatrix} \hat{\mathbf{H}} \\ \hat{\mathbf{K}} \end{bmatrix} \begin{pmatrix} \hat{w} \\ \hat{c} \end{pmatrix} = \hat{\mathbf{C}} \begin{pmatrix} \hat{w} \\ \hat{c} \end{pmatrix}, \quad (2.39)$$

or

$$\begin{pmatrix} \hat{w} \\ \hat{c} \end{pmatrix} = \hat{\mathbf{C}}^{-1} \begin{pmatrix} \hat{u} \\ \hat{f} \end{pmatrix}. \quad (2.40)$$

It can be seen that (2.35) is a special case of (2.40), where  $\hat{f}$  is simply set to null. By substituting Equation (2.40) into Equations (2.30) and (2.31), the second- and first-order derivatives of the variable  $u$  are expressed in

$$\frac{\partial^2 u(x)}{\partial x^2} = \left( H_{[2]}^{(1)}(x), H_{[2]}^{(2)}(x), \dots, H_{[2]}^{(N_x^{[j]})}(x), 0, 0 \right) \hat{\mathbf{C}}^{-1} \begin{pmatrix} \hat{u} \\ \hat{f} \end{pmatrix}, \quad (2.41)$$

$$\frac{\partial u(x)}{\partial x} = \left( H_{[1]}^{(1)}(x), H_{[1]}^{(2)}(x), \dots, H_{[1]}^{(N_x^{[j]})}(x), 1, 0 \right) \hat{\mathbf{C}}^{-1} \begin{pmatrix} \hat{u} \\ \hat{f} \end{pmatrix}, \quad (2.42)$$

or

$$\frac{\partial^2 u(x)}{\partial x^2} = \bar{D}_{2x} \hat{u} + k_{2x}(x), \quad (2.43)$$

$$\frac{\partial u(x)}{\partial x} = \bar{D}_{1x} \hat{u} + k_{1x}(x), \quad (2.44)$$

where  $k_{1x}$  and  $k_{2x}$  are scalars whose values depend on  $x$ ,  $f_1$  and  $f_2$ ; and  $\bar{D}_{1x}$  and  $\bar{D}_{2x}$  known vectors of length  $N_x^{[j]}$ .

Application of Equations (2.43) and (2.44) to boundary and interior points on the grid line  $[j]$  yields

$$\widehat{\frac{\partial^2 u^{[j]}}{\partial x^2}} = \hat{\mathbf{D}}_{2x}^{[j]} \hat{u} + \hat{k}_{2x}^{[j]}, \quad (2.45)$$

$$\widehat{\frac{\partial u^{[j]}}{\partial x}} = \hat{\mathbf{D}}_{1x}^{[j]} \hat{u} + \hat{k}_{1x}^{[j]}, \quad (2.46)$$

where  $\hat{\mathbf{D}}_{1x}^{[j]}$  and  $\hat{\mathbf{D}}_{2x}^{[j]}$  are known matrices of dimension  $N_x^{[j]} \times N_x^{[j]}$ ; and  $\hat{k}_{1x}^{[j]}$  and  $\hat{k}_{2x}^{[j]}$  known vectors of length  $N_x^{[j]}$ .

Similarly, along a vertical line  $[j]$  parallel to the  $y$ -axis, the values of the second- and first-order derivatives of  $u$  with respect to  $y$  at the nodal points can be given by

$$\widehat{\frac{\partial^2 u^{[j]}}{\partial y^2}} = \hat{\mathbf{D}}_{2y}^{[j]} \hat{u} + \hat{k}_{2y}^{[j]}, \quad (2.47)$$

$$\widehat{\frac{\partial u^{[j]}}{\partial y}} = \hat{\mathbf{D}}_{1y}^{[j]} \hat{u} + \hat{k}_{1y}^{[j]}. \quad (2.48)$$

### 2.3.2 1D-IRBFN expressions over the whole computational domain

The values of the second- and first-order derivatives of  $u$  with respect to  $x$  at the nodal points over the problem domain can be given by

$$\frac{\widetilde{\partial^2 u}}{\partial x^2} = \tilde{\mathbf{D}}_{2x} \tilde{u} + \tilde{k}_{2x}, \quad (2.49)$$

$$\frac{\widetilde{\partial u}}{\partial x} = \tilde{\mathbf{D}}_{1x} \tilde{u} + \tilde{k}_{1x}, \quad (2.50)$$

where

$$\tilde{u} = (u^{(1)}, u^{(2)}, \dots, u^{(N)})^T; \quad (2.51)$$

$$\frac{\widetilde{\partial^2 u}}{\partial x^2} = \left( \frac{\partial^2 u^{(1)}}{\partial x^2}, \frac{\partial^2 u^{(2)}}{\partial x^2}, \dots, \frac{\partial^2 u^{(N)}}{\partial x^2} \right)^T; \quad (2.52)$$

$$\frac{\widetilde{\partial u}}{\partial x} = \left( \frac{\partial u^{(1)}}{\partial x}, \frac{\partial u^{(2)}}{\partial x}, \dots, \frac{\partial u^{(N)}}{\partial x} \right)^T; \quad (2.53)$$

and  $\tilde{\mathbf{D}}_{1x}$  and  $\tilde{\mathbf{D}}_{2x}$  are known matrices of dimension  $N \times N$ ;  $\tilde{k}_{1x}$  and  $\tilde{k}_{2x}$  known vectors of length  $N$ ; and  $N$  the total number of nodal points. The matrices  $\tilde{\mathbf{D}}_{1x}$  and  $\tilde{\mathbf{D}}_{2x}$  and the vectors  $\tilde{k}_{1x}$  and  $\tilde{k}_{2x}$  are formed as follows.

$$\tilde{\mathbf{D}}_{2x(idj, idj)} = \hat{\mathbf{D}}_{2x}^{[j]}, \quad (2.54)$$

$$\tilde{\mathbf{D}}_{1x(idj, idj)} = \hat{\mathbf{D}}_{1x}^{[j]}, \quad (2.55)$$

$$\tilde{k}_{2x(idj)} = \hat{k}_{2x}^{[j]}, \quad (2.56)$$

$$\tilde{k}_{1x(idj)} = \hat{k}_{1x}^{[j]}, \quad (2.57)$$

where  $idj$  is the index vector indicating the location of nodes on the  $[j]$  grid line over the whole grid.

Similarly, the values of the second- and first-order derivatives of  $u$  with respect

to  $y$  at the nodal points over the problem domain can be given by

$$\frac{\widetilde{\partial^2 u}}{\partial y^2} = \tilde{\mathbf{D}}_{2y} \tilde{u} + \tilde{k}_{2y}, \quad (2.58)$$

$$\frac{\widetilde{\partial u}}{\partial y} = \tilde{\mathbf{D}}_{1y} \tilde{u} + \tilde{k}_{1y}. \quad (2.59)$$

The mixed partial derivative of  $\tilde{u}$  can be given by

$$\frac{\partial^2 \tilde{u}}{\partial x \partial y} = \frac{1}{2} \left( \tilde{\mathbf{D}}_{1x} \tilde{\mathbf{D}}_{1y} + \tilde{\mathbf{D}}_{1y} \tilde{\mathbf{D}}_{1x} \right) \tilde{u} + \tilde{k}_{2xy} = \tilde{\mathbf{D}}_{2xy} \tilde{u} + \tilde{k}_{2xy}, \quad (2.60)$$

where  $\tilde{k}_{2xy}$  is a known vector of length  $N$ .

In the special case of a rectangular domain and NSCM, the nodal values of the derivatives of  $u$  over the whole domain can be simply computed by means of Kronecker tensor products as follows.

$$\frac{\widetilde{\partial^2 u}}{\partial x^2} = \left( \hat{\mathbf{D}}_{2x} \otimes \mathbf{I}_y \right) \hat{u} = \tilde{\mathbf{D}}_{2x} \hat{u}, \quad (2.61)$$

$$\frac{\widetilde{\partial u}}{\partial x} = \left( \hat{\mathbf{D}}_{1x} \otimes \mathbf{I}_y \right) \hat{u} = \tilde{\mathbf{D}}_{1x} \hat{u}, \quad (2.62)$$

$$\frac{\widetilde{\partial^2 u}}{\partial y^2} = \left( \hat{\mathbf{D}}_{2y} \otimes \mathbf{I}_x \right) \hat{u} = \tilde{\mathbf{D}}_{2y} \hat{u}, \quad (2.63)$$

$$\frac{\widetilde{\partial u}}{\partial y} = \left( \hat{\mathbf{D}}_{1y} \otimes \mathbf{I}_x \right) \hat{u} = \tilde{\mathbf{D}}_{1y} \hat{u}, \quad (2.64)$$

where  $\mathbf{I}_x$  and  $\mathbf{I}_y$  are the identity matrices of dimension  $N_x \times N_x$  and  $N_y \times N_y$ , respectively;  $\hat{\mathbf{D}}_{1x}$  and  $\hat{\mathbf{D}}_{2x}$  known matrices of dimension  $N_x \times N_x$ ;  $\hat{\mathbf{D}}_{1y}$  and  $\hat{\mathbf{D}}_{2y}$  known matrices of dimension  $N_y \times N_y$ ;  $\tilde{\mathbf{D}}_{2x}$ ,  $\tilde{\mathbf{D}}_{1x}$ ,  $\tilde{\mathbf{D}}_{2y}$  and  $\tilde{\mathbf{D}}_{1y}$  known matrices of dimension  $N_x N_y \times N_x N_y$ ;  $\tilde{u} = (u^{(1)}, u^{(2)}, \dots, u^{(N_x N_y)})^T$ ; and  $N_x$  and  $N_y$  the number of nodes in the  $x$ - and  $y$ -axes, respectively.

## 2.4 One-dimensional IRBFN discretisation of laminated composite plates

Let the subscripts  $bp$  and  $ip$  represent the location indices of boundary and interior points,  $N_{bp}$  the number of boundary points and  $N_{ip}$  the number of interior points.

Making use of (2.49), (2.50), (2.58), (2.59) and (2.60) and collocating the governing equations (2.17), (2.18) and (2.19) at the interior points result in

$$\left[ \tilde{\mathbf{R}} - \lambda \tilde{\mathbf{S}} \right] \tilde{\phi} = \mathbf{0}, \quad (2.65)$$

where

$$\lambda = \omega^2; \quad (2.66)$$

$$\tilde{\mathbf{R}} = \begin{bmatrix} \begin{pmatrix} kA_{55}\tilde{\mathbf{D}}_{2x(ip,:)}^W \\ +kA_{44}\tilde{\mathbf{D}}_{2y(ip,:)}^W \end{pmatrix} & kA_{55}\tilde{\mathbf{D}}_{1x(ip,:)}^{\Psi_x} & kA_{44}\tilde{\mathbf{D}}_{1y(ip,:)}^{\Psi_y} \\ -kA_{55}\tilde{\mathbf{D}}_{1x(ip,:)}^W & \begin{pmatrix} D_{11}\tilde{\mathbf{D}}_{2x(ip,:)}^{\Psi_x} \\ +D_{66}\tilde{\mathbf{D}}_{2y(ip,:)}^{\Psi_x} - kA_{55}\mathbf{I} \end{pmatrix} & (D_{12} + D_{66})\tilde{\mathbf{D}}_{2xy(ip,:)}^{\Psi_y} \\ kA_{44}\tilde{\mathbf{D}}_{1y(ip,:)}^W & D_{66}\tilde{\mathbf{D}}_{2xy(ip,:)}^{\Psi_x} + D_{12}\tilde{\mathbf{D}}_{2y(ip,:)}^{\Psi_x} & \begin{pmatrix} D_{66}\tilde{\mathbf{D}}_{2x(ip,:)}^{\Psi_y} \\ +D_{22}\tilde{\mathbf{D}}_{2y(ip,:)}^{\Psi_y} - kA_{44}\mathbf{I} \end{pmatrix} \end{bmatrix}; \quad (2.67)$$

$$\tilde{\mathbf{S}} = \begin{bmatrix} I_0\mathbf{I} & \mathbf{0} & \mathbf{0} \\ \mathbf{0} & I_2\mathbf{I} & \mathbf{0} \\ \mathbf{0} & \mathbf{0} & I_2\mathbf{I} \end{bmatrix}; \quad (2.68)$$

$$\tilde{\phi} = \begin{bmatrix} \tilde{W} \\ \tilde{\psi}_x \\ \tilde{\psi}_y \end{bmatrix}; \quad (2.69)$$

and  $\mathbf{I}$  and  $\mathbf{0}$  are identity and zero matrices of dimensions  $N_{ip} \times N$ , respectively.

The system (2.65) can be expressed as

$$\tilde{\mathbf{L}}_G \tilde{\phi} = \lambda \tilde{\phi}, \quad (2.70)$$

where

$$\tilde{\mathbf{L}}_G = \tilde{\mathbf{S}}^{-1} \tilde{\mathbf{R}}. \quad (2.71)$$

Making use of (2.50) and (2.59) and collocating the expressions (2.22), (2.23) and (2.25) at the boundary points on  $\Gamma$  yield

$$\tilde{\mathbf{L}}_B \tilde{\phi} = \mathbf{0}, \quad (2.72)$$

where

$$\tilde{\mathbf{L}}_B = \begin{bmatrix} \mathbf{I} & \mathbf{0} & \mathbf{0} \\ \mathbf{0} & -n_y \mathbf{I} & n_x \mathbf{I} \\ \mathbf{0} & \begin{pmatrix} (n_x^2 D_{11} + n_y^2 D_{12}) \tilde{\mathbf{D}}_{1x(ip,:)} \\ + 2n_x n_y D_{66} \tilde{\mathbf{D}}_{1y(ip,:)} \end{pmatrix} & \begin{pmatrix} (n_x^2 D_{12} + n_y^2 D_{22}) \tilde{\mathbf{D}}_{1y(ip,:)} \\ + 2n_x n_y D_{66} \tilde{\mathbf{D}}_{1x(ip,:)} \end{pmatrix} \end{bmatrix}. \quad (2.73)$$

By combining (2.70) and (2.72), one is able to obtain the discrete form of 1D-IRBFN for laminated composite plates

$$\tilde{\mathbf{L}}_G \tilde{\phi} = \lambda \tilde{\phi}, \quad (2.74)$$

$$\tilde{\mathbf{L}}_B \tilde{\phi} = \mathbf{0}, \quad (2.75)$$

or

$$\begin{bmatrix} \tilde{\mathbf{L}}_{G(:,ip)} & \tilde{\mathbf{L}}_{G(:,bp)} \end{bmatrix} \begin{pmatrix} \tilde{\phi}(ip) \\ \tilde{\phi}(bp) \end{pmatrix} = \lambda \tilde{\phi}(ip), \quad (2.76)$$

$$\begin{bmatrix} \tilde{\mathbf{L}}_{B(:,ip)} & \tilde{\mathbf{L}}_{B(:,bp)} \end{bmatrix} \begin{pmatrix} \tilde{\phi}(ip) \\ \tilde{\phi}(bp) \end{pmatrix} = \mathbf{0}. \quad (2.77)$$

Solving (2.77) gives

$$\tilde{\phi}_{(bp)} = -\tilde{\mathbf{L}}_{B(:,bp)}^{-1} \tilde{\mathbf{L}}_{B(:,ip)} \tilde{\phi}_{(ip)}. \quad (2.78)$$

Substitution of (2.78) into (2.76) leads to the following system

$$\tilde{\mathbf{L}} \tilde{\phi}_{(ip)} = \lambda \tilde{\phi}_{(ip)}, \quad (2.79)$$

where  $\tilde{\mathbf{L}}$  is a matrix of dimensions  $N_{ip} \times N_{ip}$ , defined as

$$\tilde{\mathbf{L}} = \tilde{\mathbf{L}}_{G(:,ip)} - \tilde{\mathbf{L}}_{G(:,bp)} \tilde{\mathbf{L}}_{B(:,bp)}^{-1} \tilde{\mathbf{L}}_{B(:,ip)}, \quad (2.80)$$

from which the natural frequencies and mode shapes of laminated composite plates can be obtained.

## 2.5 Numerical results and discussion

Three examples are considered here to study the performance of the present method. Unless otherwise stated, all layers of the laminate are assumed to be of the same thickness, density and made of the same linearly elastic composite material. The material parameters of a layer used here are:  $E_1/E_2 = 40$ ;  $G_{12} = G_{13} = 0.6E_2$ ;  $G_{23} = 0.5E_2$ ;  $\nu_{12} = 0.25$ , where the subscripts 1 and 2 denote the directions parallel and perpendicular to the fibre direction in a layer. The ply angle of each layer measured from the global  $x$ -axis to the fibre direction is positive if measured clockwise, and negative if measured anti-clockwise. The eigenproblem (2.79) is solved using MATLAB to obtain the natural frequencies and mode shapes of laminated composite plates. In order to compare with the published results of Ferreira and Fasshauer (2007), Liew (1996), Liew et al. (2003) and Nguyen-Van et al. (2008), the same shear correction factors and nondimensionalised natural frequencies are also employed here:

- Case 1: Shear correction factor  $K_s = \pi^2/12$ .  
Nondimensionalised natural frequency:  $\bar{\omega} = \omega (b^2/\pi^2) \sqrt{\rho h/D_0}$  with  $D_0 = E_2 h^3/12(1 - \nu_{12}\nu_{21})$ .
- Case 2: Shear correction factor  $K_s = 5/6$ .  
Nondimensionalised natural frequency:  $\bar{\omega} = (\omega b^2/h) \sqrt{\rho/E_2}$ ,

where  $b$  is the length of the vertical edges of square/rectangular plates or the diameter of circular plates.

Boundary conditions can be imposed in the following ways:

- Approach 1: through the conversion process (2.39).
- Approach 2: by the algorithm (2.72) - (2.80).

### 2.5.1 Example 1: Rectangular laminated plates

This example investigates the characteristics of free vibration of rectangular cross-ply laminated plates with various thickness-to-length ratios, boundary conditions, lay-up stacking sequences and material properties. Both Approach 1 and Approach 2 are applied here to implement the boundary conditions.

#### Convergence study

Table 2.1 shows the convergence study of nondimensionalised natural frequencies. It can be seen that results by Approach 1 are slightly more accurate than those of Approach 2. The condition numbers in Approach 1 are smaller than those in Approach 2.

Table 2.2 presents the convergence study of nondimensionalised natural frequencies for simply supported three-ply  $[0^\circ/90^\circ/0^\circ]$  rectangular laminated plates for

two cases of thickness to span ratios  $t/b = 0.001$  and  $0.2$  by using Approach 1, while the corresponding convergence study for clamped laminated plates is presented in Table 2.3. Table 2.2 shows that faster convergence can be obtained for higher  $t/b$  ratios irrespective of  $a/b$  ratios. It can be seen that accuracy of the current results is generally higher than that of Ferreira and Fasshauer (2007) who used RBF-pseudospectral method (RBF-PS) and nearly equal to that of Liew (1996) in the case of  $t/b = 0.2$ . For the thin plate case  $t/b = 0.001$ , the p-Ritz method results are more accurate than RBF-PS ones and the IRBF ones in comparison with the exact solution. Specifically, the IRBF results of nondimensionalised fundamental natural frequency deviate by 0.32% from the exact solution for the simply supported plate, and by 0.05% from the p-Ritz method results for the clamped plate in the cases of  $t/b = 0.001$  and  $a/b = 1$ .

Table 2.1: Simply supported three-ply  $[0^\circ/90^\circ/0^\circ]$  square laminated plate: convergence study of nondimensionalised natural frequencies  $\bar{\omega} = \omega (b^2/\pi^2) \sqrt{\rho h/D_0}$  by two approaches,  $t/b = 0.2$ . Here *cond* denotes the condition number.

		Mode sequence number								
	Grid	1	2	3	4	5	6	7	8	<i>cond</i>
App. 1	$11 \times 11$	3.5939	5.7708	7.3982	8.6896	9.1665	11.2222	11.2406	12.1306	1.36E+05
	$13 \times 13$	3.5939	5.7696	7.3974	8.6881	9.1520	11.2125	11.2283	12.1209	2.43E+05
	$15 \times 15$	3.5939	5.7693	7.3972	8.6878	9.1478	11.2097	11.2248	12.1182	3.95E+05
	$17 \times 17$	3.5939	5.7692	7.3971	8.6876	9.1463	11.2087	11.2235	12.1173	5.65E+05
App. 2	$11 \times 11$	3.5932	5.7649	7.3968	8.6851	9.1299	11.2111	11.2184	12.1252	2.60E+05
	$13 \times 13$	3.5935	5.7667	7.3967	8.6860	9.1371	11.2108	11.2162	12.1186	9.21E+05
	$15 \times 15$	3.5937	5.7676	7.3968	8.6865	9.1402	11.2088	11.2186	12.1169	2.45E+06
	$17 \times 17$	3.5937	5.7681	7.3969	8.6868	9.1418	11.2082	11.2199	12.1165	5.12E+06
Exact <sup>a</sup>		3.5939	5.7691	7.3972	8.6876	9.1451	11.2080	11.2230	12.1170	

<sup>a</sup> (Reddy, 2004)

Table 2.2: Simply supported three-ply  $[0^\circ/90^\circ/0^\circ]$  rectangular laminated plate: convergence study of nondimensionalised natural frequencies  $\bar{\omega} = \omega (b^2/\pi^2) \sqrt{\rho h/D_0}$  using Approach 1. Note that Ferreira and Fasshauer (2007) used 19x19 grid.

a/b	t/b	Grid	Mode sequence number								
			1	2	3	4	5	6	7	8	
1	0.001	11 × 11	6.6542	9.4811	15.9414	24.983	26.3037	26.3794	30.0499	37.4233	
		13 × 13	6.6427	9.4708	16.0981	25.0024	26.2019	26.3967	30.1587	37.3711	
		15 × 15	6.6592	9.4715	16.1697	24.9665	26.3591	26.4214	30.1662	37.5117	
		17 × 17	6.6464	9.466	16.2146	24.8845	26.2837	26.534	30.1281	37.5459	
		RBF-PS <sup>a</sup>	6.618	9.4368	16.2192	25.1131	26.4938	26.6667	30.2983	37.785	
		p-Ritz <sup>b</sup>	6.6252	9.447	16.2051	25.1146	26.82	26.6572	30.3139	37.7854	
		Exact <sup>c</sup>	6.6252	9.447	16.205	25.115	26.498	26.657	30.314	37.785	
		0.2	11 × 11	3.5939	5.7708	7.3982	8.6896	9.1665	11.2222	11.2406	12.1306
			13 × 13	3.5939	5.7696	7.3974	8.6881	9.152	11.2125	11.2283	12.1209
			15 × 15	3.5939	5.7693	7.3972	8.6878	9.1478	11.2097	11.2248	12.1182
17 × 17	3.5939		5.7692	7.3971	8.6876	9.1463	11.2087	11.2235	12.1173		
RBF-PS <sup>a</sup>	3.5934		5.7683	7.3968	8.867	9.1444	11.2078	11.2218	12.1162		
p-Ritz <sup>b</sup>	3.5939		5.7691	7.3972	8.6876	9.1451	11.208	11.2225	12.1166		
Exact <sup>c</sup>	3.5939		5.7691	7.3972	8.6876	9.1451	11.208	11.223	12.117		
2	0.001	11 × 11	2.3728	6.6869	6.7991	8.3924	9.6042	13.9864	14.0793	15.8732	
		13 × 13	2.3866	6.7419	6.7685	9.599	14.393	14.533	16.2707	16.3855	
		15 × 15	2.3855	6.7206	6.7569	9.575	14.4173	14.5091	16.2875	16.354	
		17 × 17	2.3641	6.6461	6.671	9.4658	14.2607	14.386	16.1137	16.2146	
		RBF-PS <sup>a</sup>	2.367	6.6331	6.6691	9.4676	14.2921	14.3915	16.1009	16.1009	
		p-Ritz <sup>b</sup>	2.3618	6.6252	6.6845	9.447	14.2869	16.3846	16.1347	16.2051	
		Exact <sup>c</sup>	2.3618	6.6252	6.6645	9.447	14.287	14.3846	16.1347	16.2051	
	0.2	11 × 11	1.9393	3.5945	4.8775	5.4933	5.7712	7.125	7.457	8.6202	
		13 × 13	1.9393	3.594	4.8761	5.488	5.7697	7.12	7.4118	8.6047	
		15 × 15	1.9393	3.5939	4.8757	5.4864	5.7693	7.1186	7.4022	8.6003	
		17 × 17	1.9393	3.5939	4.8756	5.4859	5.7692	7.1181	7.3992	8.5987	
		RBF-PS <sup>a</sup>	1.9387	3.5934	4.875	5.4851	5.7683	7.117	7.3968	8.5969	
		p-Ritz <sup>b</sup>	1.9393	3.5939	4.8755	5.4855	5.7691	7.1177	7.3972	8.5973	
		Exact <sup>c</sup>	1.9393	3.5939	4.8755	5.4855	5.7691	7.1177	7.3972	8.5973	

<sup>a</sup> (Ferreira and Fasshauer, 2007)

<sup>b</sup> (Liew, 1996)

<sup>c</sup> (Reddy, 2004)

Table 2.3: Clamped three-ply  $[0^\circ/90^\circ/0^\circ]$  rectangular laminated plate: convergence study of nondimensionalised natural frequencies  $\bar{\omega} = \omega (b^2/\pi^2) \sqrt{\rho h/D_0}$  using Approach 1. Note that Ferreira and Fasshauer (2007) used 19x19 grid.

a/b	t/b	Grid	Mode sequence number								
			1	2	3	4	5	6	7	8	
1	0.001	11 × 11	14.6844	17.6511	24.1628	33.6225	39.0914	40.7855	44.6870	51.2194	
		13 × 13	14.6791	17.6539	24.3897	34.7431	39.1978	40.8591	44.8533	47.8648	
		15 × 15	14.6774	17.6470	24.4898	35.2604	39.2082	40.8519	44.8829	48.8046	
		17 × 17	14.6722	17.6383	24.5238	35.4471	39.2005	40.8349	44.8746	49.5902	
		RBF-PS <sup>a</sup>	14.8138	17.6138	24.5114	35.5318	39.1572	40.7685	44.7865	50.3226	
		p-Ritz <sup>b</sup>	14.6655	17.6138	24.5114	35.5318	39.1572	40.7685	44.7865	50.3226	
		0.2	11 × 11	4.4466	6.6433	7.7006	9.1870	9.7502	11.4125	11.6550	12.4789
			13 × 13	4.4466	6.6423	7.6998	9.1856	9.7417	11.4033	11.6473	12.4698
			15 × 15	4.4466	6.6420	7.6996	9.1853	9.7393	11.4007	11.6452	12.4673
			17 × 17	4.4466	6.6419	7.6996	9.1852	9.7384	11.3998	11.6444	12.4664
RBF-PS <sup>a</sup>	4.4463		6.6419	7.6995	9.1839	9.7376	11.3994	11.6420	12.4651		
p-Ritz <sup>b</sup>	4.4468		6.6419	7.6996	9.1852	9.7378	11.3991	11.6439	12.4658		
2	0.001		11 × 11	5.1181	10.5213	10.5731	14.3641	19.1429	19.1845	21.8532	21.8669
		13 × 13	5.1140	10.5488	10.6073	14.3851	19.4334	19.4949	22.0916	22.1203	
		15 × 15	5.1140	10.5491	10.6086	14.3748	19.5293	19.6364	22.1586	22.2252	
		17 × 17	5.1092	10.5447	10.6042	14.3642	19.5622	19.6912	22.1764	22.2607	
		p-Ritz <sup>b</sup>	5.1051	10.5265	10.5828	14.3241	19.5674	19.7011	22.1483	22.2368	
		0.2	11 × 11	3.0454	4.2489	5.7933	5.9109	6.5371	7.7354	7.7434	9.1903
			13 × 13	3.0454	4.2485	5.7921	5.9066	6.5358	7.7016	7.7311	9.1813
	15 × 15		3.0454	4.2484	5.7918	5.9054	6.5354	7.6927	7.7300	9.1787	
	17 × 17		3.0453	4.2484	5.7917	5.9050	6.5353	7.6900	7.7295	9.1778	
	p-Ritz <sup>b</sup>		3.0453	4.2484	5.7918	5.9047	6.5354	7.6881	7.7293	9.1762	

<sup>a</sup> (Ferreira and Fasshauer, 2007)

<sup>b</sup> (Liew, 1996)

### Thickness-to-length ratios

Table 2.4 shows the effect of thickness-to-length ratio  $t/b$  on nondimensionalised fundamental frequency of the simply supported four-ply  $[0^\circ/90^\circ/90^\circ/0^\circ]$  square laminated plate in comparison with other published results. It can be seen that the fundamental frequency decreases with increasing  $t/b$  ratios. The numerical results obtained are in good agreement with the published results of Liew (1996) and Ferreira and Fasshauer (2007) and the exact solution derived from the FSDT plate model (Reddy, 2004). Figure 2.2 describes errors of nondimensionalised fundamental frequency  $\varepsilon = (\bar{\omega} - \bar{\omega}_E)/\bar{\omega}_E$  ( $\bar{\omega}_E$ : nondimensionalised value of the exact fundamental frequency) with respect to thickness-to-span ratios  $t/b$  for the simply supported four-ply  $[0^\circ/90^\circ/90^\circ/0^\circ]$  square laminated plate in comparison with available published results. This figure shows that the accuracy of the present method is higher than that of the others for  $t/b$  ratios larger than 0.04. The errors reduce with increasing  $t/b$  ratios for IRBFN and RBF-PS methods, indicating that these methods are more accurate for thick plates than for thin plates. When the  $t/b$  ratio is smaller than 0.04, the accuracy of p-Ritz method is higher than that of IRBF and RBF-PS methods.

Table 2.4: Simply supported four-ply  $[0^\circ/90^\circ/90^\circ/0^\circ]$  square laminated plate: effect of thickness-to-length ratio on the nondimensionalised fundamental frequency  $\bar{\omega} = \omega (b^2/\pi^2) \sqrt{\rho h/D_0}$  in comparison with other published results, using Approach 1 and a grid of  $13 \times 13$ .

$t/b$	0.01	0.0200	0.04	0.05	0.08	0.1	0.2	0.25
IRBFN	6.6069	6.5464	6.3378	6.1882	5.6675	5.2991	3.7918	3.2806
RBF-PS <sup>a</sup>	6.6012	6.5438	6.3300	6.1844	5.6641	5.2960	3.7903	3.2796
p-Ritz <sup>b</sup>	6.6060	6.5490	6.3380	6.1930	5.6770	5.3110	3.8070	3.2950
Exact <sup>c</sup>	6.6059	6.5483	6.3342	6.1885	5.6675	5.2991	3.7918	3.2806

<sup>a</sup> (Ferreira and Fasshauer, 2007)

<sup>b</sup> (Liew, 1996)

<sup>c</sup> (Reddy, 2004)

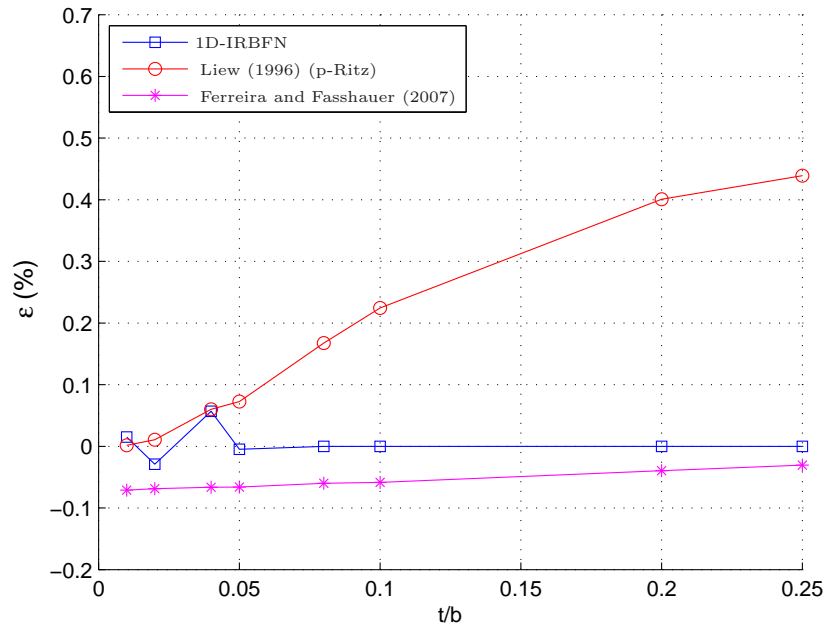


Figure 2.2: Simply supported four-ply  $[0^\circ/90^\circ/90^\circ/0^\circ]$  square laminated plate: errors of nondimensionalised fundamental frequency ( $\epsilon = (\bar{\omega} - \bar{\omega}_E)/\bar{\omega}_E$ ) with respect to thickness-to-length ratios  $t/b$ .

### Boundary conditions

Tables 2.5 and 2.6 show the effect of  $t/b$  ratio on nondimensionalised natural frequencies of three-ply  $[0^\circ/90^\circ/0^\circ]$  and four-ply  $[0^\circ/90^\circ/90^\circ/0^\circ]$  rectangular laminated plates with boundary conditions SSSS, CCCC and SCSC. The first eight nondimensionalised natural frequencies are reported in these tables. It can be seen that the nondimensionalised natural frequencies reduce with increasing  $t/b$  ratios due to the effects of shear deformation and rotary inertia. These effects are more pronounced in higher modes. The effect of boundary conditions on the natural frequencies can also be seen in these tables. The higher constraints at the edges result in higher natural frequencies for the laminated plates as shown in Tables 2.5 and 2.6, i.e., the nondimensionalised natural frequency of SCSC plates is higher than that of SSSS plates, but lower than that of CCCC plates. Figures 2.3-2.5 show mode shapes of a simply supported three-ply  $[0^\circ/90^\circ/0^\circ]$  square laminated plate, a simply supported three-ply  $[0^\circ/90^\circ/0^\circ]$

rectangular with  $a/b = 2$  laminated plate, and a clamped three-ply  $[0^\circ/90^\circ/0^\circ]$  square laminated plate, respectively, in the case of  $t/b = 0.2$  and using a grid of  $15 \times 15$ . The current results are fairly reasonable in comparison with available published results (Ferreira and Fasshauer, 2007).

Table 2.5: Three-ply  $[0^\circ/90^\circ/0^\circ]$  rectangular laminated plates with various boundary conditions: effect of thickness-to-length ratio on nondimensionalised natural frequencies  $\bar{\omega} = \omega (b^2/\pi^2) \sqrt{\rho h/D_0}$ , using Approach 1 and a grid of  $13 \times 13$ .

B.C.	$a/b$	$t/b$	Mode sequence number									
			1	2	3	4	5	6	7	8		
SSSS	1	0.001	6.6427	9.4708	16.0981	25.0024	26.2019	26.3967	30.1587	37.3711		
		0.050	6.1379	10.4509	12.2686	12.2686	14.9902	19.3564	20.7612	24.2701		
		0.100	5.1662	7.7586	12.9473	13.0492	14.3770	17.8115	19.6232	21.0611		
		0.150	4.2748	6.6678	9.4883	10.8246	10.8377	13.8136	14.6715	15.5964		
	2	0.200	3.5939	5.7696	7.3974	8.6881	9.1520	11.2125	11.2283	12.1209		
		0.001	2.3866	6.7419	6.7685	9.5990	14.3930	14.5330	16.2707	16.3855		
		0.050	2.3251	6.1374	6.5306	8.9272	11.4203	12.1885	13.4651	14.0131		
		0.100	2.2213	5.1659	6.0163	7.7562	9.0282	10.8012	11.8844	12.9471		
		0.150	2.0855	4.2751	5.4445	6.6679	6.8725	8.5997	9.5089	10.0955		
		0.200	1.9393	3.5940	4.8761	5.4880	5.7697	7.1200	7.4118	8.6047		
		CCCC	1	0.001	14.6791	17.6539	24.3897	34.7431	39.1978	40.8591	44.8533	47.8648
				0.050	10.9532	14.0298	20.3988	23.1977	24.9817	29.2481	29.4098	36.3054
0.100	7.4108			10.3935	13.9134	15.4372	15.8068	19.5792	21.4976	21.6743		
0.150	5.5482			8.1470	9.9044	11.6223	12.0305	14.6493	14.9165	16.1288		
2	0.200		4.4466	6.6423	7.6998	9.1856	9.7417	11.4033	11.6473	12.4698		
	0.001		5.1140	10.5488	10.6073	14.3851	19.4334	19.4949	22.0916	22.1203		
	0.050		4.7791	8.8414	9.8490	12.5142	14.7127	17.3115	17.6840	19.4410		
	0.100		4.1412	6.6172	8.3548	9.8967	9.9710	12.4472	13.6882	14.1293		
	0.150		3.5397	5.1819	6.9271	7.4270	7.9371	9.5807	9.8737	11.2359		
	0.200		3.0454	4.2485	5.7921	5.9066	6.5358	7.7016	7.7311	9.1813		
	SCSC		1	0.001	7.4203	12.1879	20.6756	25.2643	27.6224	32.1561	33.0467	42.0340
				0.050	6.8909	11.2486	18.6756	19.6220	21.8062	26.7027	28.3039	34.3921
0.100		5.8707		9.4551	13.3411	14.8865	15.3416	19.2365	21.2412	21.3301		
0.150		4.9054		7.7815	9.7801	11.5266	11.8206	14.5809	14.8557	16.0790		
2		0.200	4.1370	6.4758	7.6655	9.1608	9.6559	11.3907	11.6364	12.4619		
		0.001	3.9926	7.4338	10.0811	12.1967	14.5705	17.8531	19.1850	20.6813		
		0.050	3.8663	6.8929	9.4403	11.2497	12.5959	15.6065	17.4616	18.6763		
		0.100	3.5695	5.8712	8.1101	9.4478	9.4554	12.0675	13.3765	14.0007		
		0.150	3.2017	4.9056	6.7853	7.2757	7.7816	9.4780	9.8001	11.1627		
		0.200	2.8400	4.1370	5.7076	5.8509	6.4748	7.6786	7.6951	9.1385		

Table 2.6: Four-ply  $[0^\circ/90^\circ/90^\circ/0^\circ]$  rectangular laminated plates with various boundary conditions: effect of thickness-to-length ratio on nondimensionalised natural frequency  $\bar{\omega} = \omega (b^2/\pi^2) \sqrt{\rho h/D_0}$ , using Approach 1 and a grid of  $13 \times 13$ .

B.C.	$a/b$	$t/b$	Mode sequence number							
			1	2	3	4	5	6	7	8
SSSS	1	0.001	6.7059	12.0397	18.5141	22.0534	23.3726	30.9024	40.5234	46.2463
		0.050	6.1882	11.1007	18.8131	20.7977	21.2014	27.7936	33.4569	34.3564
		0.100	5.2991	9.5066	12.8655	15.1686	16.3195	20.1927	20.7286	22.2630
		0.150	4.4572	7.9529	9.4381	11.5313	12.8403	14.5062	15.3210	15.9592
	2	0.200	3.7918	6.6928	7.4020	9.2365	10.3860	11.1171	12.1797	12.4176
		0.001	2.9712	6.6541	9.9919	11.9088	13.6687	17.1813	21.8132	22.9920
		0.050	2.9126	6.1904	9.4342	11.1019	11.8981	15.2281	18.9543	19.8146
		0.100	2.7737	5.2996	8.2610	8.9588	9.5069	11.9952	12.9014	15.1988
		0.150	2.5834	4.4575	6.9071	7.0351	7.9531	9.4582	9.5600	11.5477
		0.200	2.3764	3.7920	5.5656	5.9910	6.6929	7.4160	7.8395	9.2477
CCCC	1	0.001	14.6792	20.6910	32.9201	37.6858	40.8607	48.8204	50.1301	62.4002
		0.050	11.3126	16.7726	22.9297	26.2097	26.2696	33.2400	37.0230	38.2915
		0.100	7.8902	12.1365	13.9783	16.8124	18.3066	21.3197	21.7360	23.3033
		0.150	5.9351	9.1657	9.9964	12.2341	13.5791	14.8417	15.8326	16.4452
	2	0.200	4.7214	7.2800	7.7663	9.5679	10.7005	11.3499	12.3791	12.6607
		0.001	6.5340	10.9786	15.6695	18.2386	19.0696	24.2980	29.7601	29.9145
		0.050	6.0569	9.3919	13.6991	14.7711	15.5837	19.4157	21.3104	24.3658
		0.100	5.1020	7.1586	10.2158	10.5241	11.7065	13.7411	13.8243	16.6254
		0.150	4.1965	5.5887	7.6416	8.1429	8.9674	9.9607	10.3876	12.2071
		0.200	3.4843	4.5283	6.0592	6.5421	7.1725	7.7662	8.2341	9.5683
SCSC	1	0.001	8.3209	16.7088	24.5146	29.0185	30.5059	39.2791	48.5199	53.3015
		0.050	7.7027	14.6439	19.3708	23.2436	25.0077	31.0304	34.6669	37.0746
		0.100	8.2781	16.5860	24.2823	28.7169	30.3815	38.9510	48.8953	52.1464
		0.150	8.2468	16.4639	24.0415	28.4167	30.0368	38.4583	48.1057	49.8091
	2	0.200	4.4165	7.1096	7.7278	9.5387	10.5949	11.3260	12.3570	12.6413
		0.001	5.7766	8.3309	14.5915	15.3473	16.7142	20.8753	24.1291	28.6815
		0.050	5.4215	7.7045	12.7571	13.4298	14.6448	17.9696	19.5078	23.3567
		0.100	4.6716	6.4819	9.6960	10.3349	11.3299	13.4182	13.4679	16.3745
		0.150	3.9187	5.3244	7.4861	8.0180	8.8189	9.8824	10.2831	12.1477
		0.200	3.3028	4.4166	6.0005	6.4606	7.1096	7.7412	8.1954	9.5496

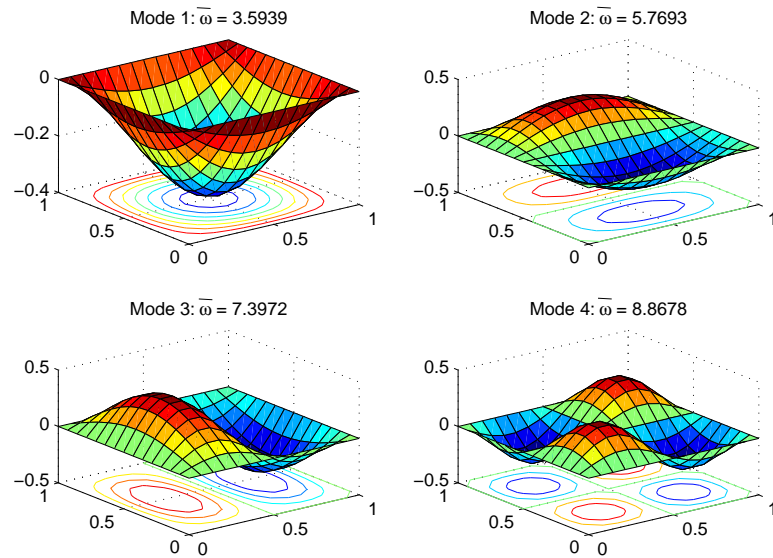


Figure 2.3: Mode shapes for simply supported three-ply  $[0^\circ/90^\circ/0^\circ]$  square laminated plate with  $t/b = 0.2$  and grid of  $15 \times 15$ .

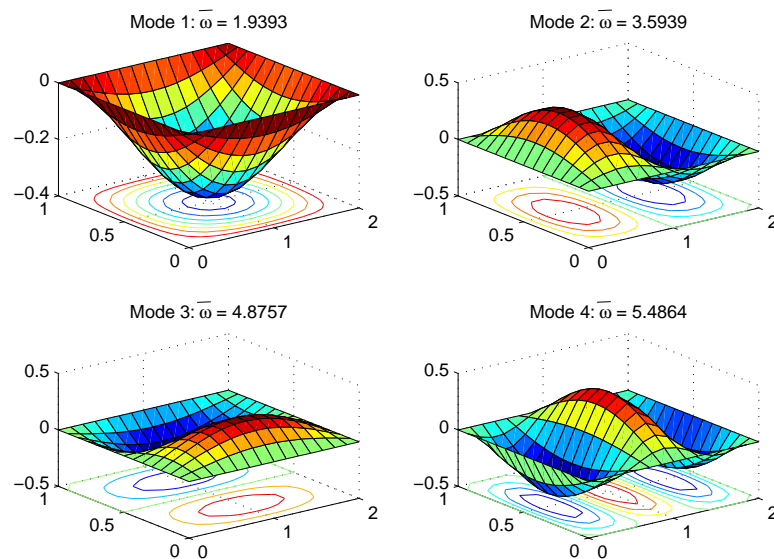


Figure 2.4: Mode shapes for simply supported three-ply  $[0^\circ/90^\circ/0^\circ]$  rectangular laminated plate with  $a/b = 2$ ,  $t/b = 0.2$  and grid of  $15 \times 15$ .

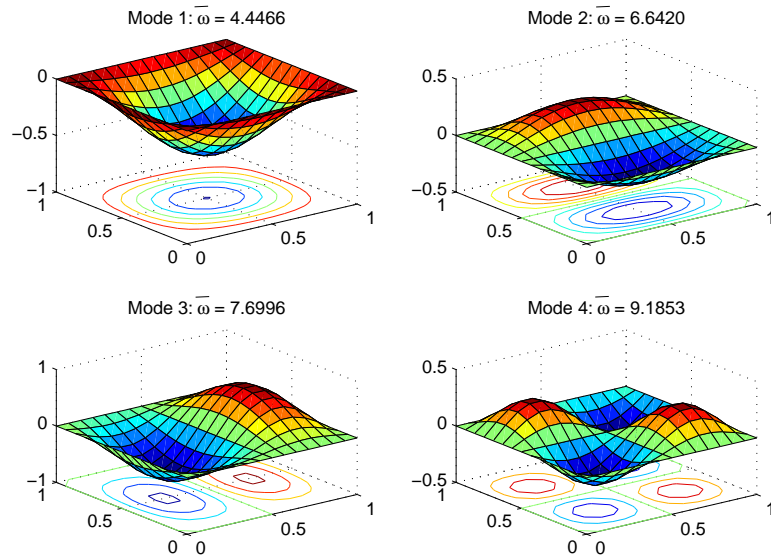


Figure 2.5: Mode shapes for clamped three-ply  $[0^\circ/90^\circ/0^\circ]$  square laminated plate with  $t/b = 0.2$  and grid of  $15 \times 15$ .

### Material property

Table 2.7 presents the effect of modulus ratio  $E_1/E_2$  on the nondimensionalised fundamental frequency of the simply supported four-ply  $[0^\circ/90^\circ/90^\circ/0^\circ]$  square laminated plate. In order to compare with the available published results, the shear correction factor of  $5/6$  and thickness-to-length ratio of  $0.2$  are used in this example. It can be seen that the fundamental frequency increases with increasing modulus ratio. Figure 2.6 shows the errors of nondimensionalised fundamental frequency ( $\varepsilon = (\bar{\omega} - \bar{\omega}_E)/\bar{\omega}_E$ ) with respect to modulus ratio  $E_1/E_2$  for the simply supported four-ply laminated square plate  $[0^\circ/90^\circ/90^\circ/0^\circ]$  in comparison with existing published results. The accuracy of current method is not only fairly high but also very stable in a wide range of  $E_1/E_2$  ratios as shown in this figure.

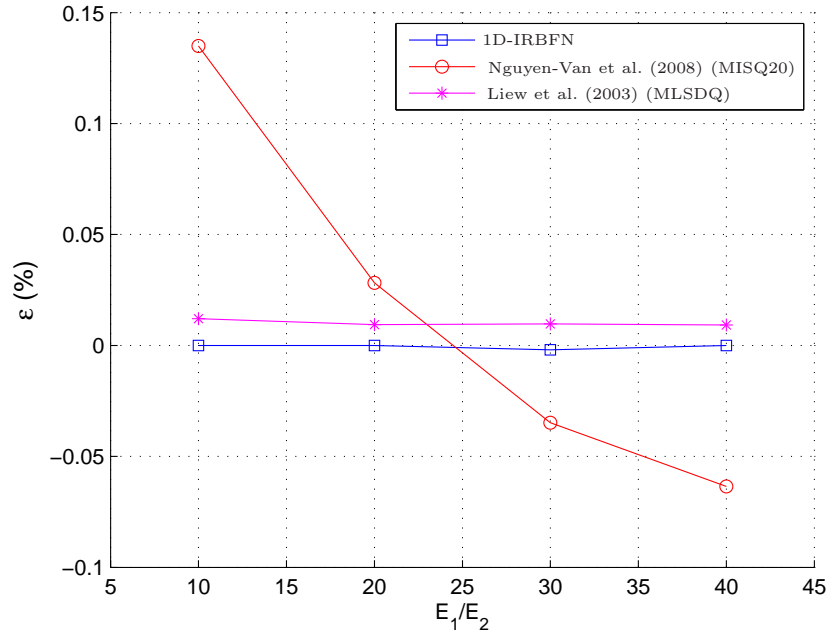


Figure 2.6: Simply supported four-ply square laminated plate  $[0^\circ/90^\circ/90^\circ/0^\circ]$ : errors of nondimensionalised fundamental frequency ( $\epsilon = (\bar{\omega} - \bar{\omega}_E)/\bar{\omega}_E$ ) with respect to modulus ratio  $E_1/E_2$ ,  $t/b = 0.2$ .

Table 2.7: Simply supported four-ply  $[0^\circ/90^\circ/90^\circ/0^\circ]$  square laminated plate: effect of modulus ratio  $E_1/E_2$  on the accuracy of nondimensionalised fundamental frequency  $\bar{\omega} = (\omega b^2/h) \sqrt{\rho/E_2}$ ,  $t/b = 0.2$ , using Approach 1 and a grid of  $13 \times 13$ ,  $K_s = 5/6$ .

	$E_1/E_2$			
	10	20	30	40
IRBFN	8.2982	9.5671	10.3258	10.8540
MISQ20 (Nguyen-Van et al., 2008)	8.3094	9.5698	10.3224	10.8471
MLSDQ (Liew et al., 2003)	8.2992	9.5680	10.3270	10.8550
Exact (Reddy, 2004)	8.2982	9.5671	10.3260	10.8540

### 2.5.2 Example 2: Circular laminated plates

Free vibration analysis for  $[\beta^\circ / -\beta^\circ / -\beta^\circ / \beta^\circ]$  circular laminated plates with diameter  $b$  and thickness  $t$  shown in Figure 2.7 is studied in this section. Boundary conditions are imposed with Approach 2. The thickness-to-diameter ratio  $t/b$  of 0.1, various fibre orientation angles with  $\beta = 0^\circ$  and  $45^\circ$ , and modulus ratio ( $E_1/E_2$ ) of 40 are considered. Table 2.8 presents the convergence study of nondimensionalised natural frequencies for various mode numbers for the simply supported four-ply  $[\beta^\circ / -\beta^\circ / -\beta^\circ / \beta^\circ]$  circular laminated plate in comparison with other published results, while the corresponding convergence study for a clamped four-ply  $[\beta^\circ / -\beta^\circ / -\beta^\circ / \beta^\circ]$  circular laminated plate is given in Table 2.9. It can be seen that the current results are in good agreement with those of Liew et al. (2003) who used a moving least squares differential quadrature method (MLSDQ). The numerical solution converges faster for the clamped circular plate than for the simply supported one. Table 2.10 shows the effect of thickness-to-diameter ratio on the nondimensionalised frequencies for various modes of the clamped four ply  $[\beta^\circ / -\beta^\circ / -\beta^\circ / \beta^\circ]$  circular laminated plate. A grid is taken to be  $15 \times 15$  in this computation. Figure 2.8 presents the mode shapes of the simply supported four-ply  $[45^\circ / -45^\circ / -45^\circ / 45^\circ]$  circular laminated plate with  $t/b = 0.1$ .

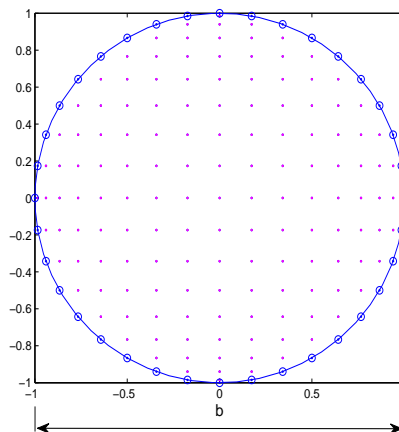


Figure 2.7: Computational domain of four-ply  $[\beta^\circ / -\beta^\circ / -\beta^\circ / \beta^\circ]$  circular laminated plate.

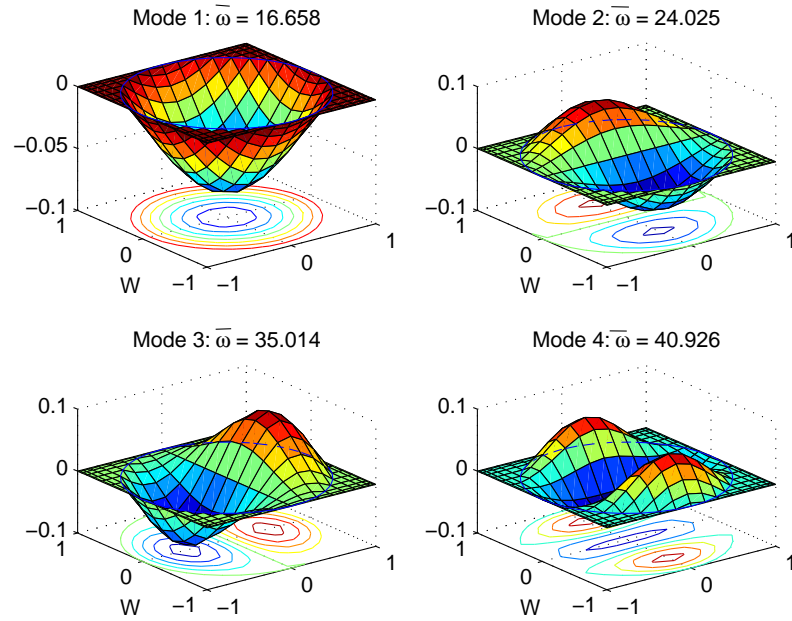


Figure 2.8: Mode shapes for simply supported four-ply  $[45^\circ / -45^\circ / -45^\circ / 45^\circ]$  circular laminated plate,  $t/b = 0.1$ , grid of  $19 \times 19$ .

Table 2.8: Simply supported four-ply  $[\beta^\circ / -\beta^\circ / -\beta^\circ / \beta^\circ]$  circular laminated plate: convergence study of nondimensionalised natural frequencies for various mode number  $\bar{\omega} = (\omega b^2/h) \sqrt{\rho/E_2}$ ,  $t/b = 0.1$ ,  $E_1/E_2 = 40$ .

$\beta$	Grid	Mode sequence number							
		1	2	3	4	5	6	7	8
$0^\circ$	$11 \times 11$	16.720	24.339	36.233	41.031	49.048	52.850	60.710	65.304
	$13 \times 13$	16.690	24.157	35.490	40.980	48.803	50.483	59.661	65.091
	$15 \times 15$	16.673	24.083	35.215	40.952	48.707	49.640	59.293	64.959
	$17 \times 17$	16.664	24.046	35.084	40.936	48.659	49.254	59.124	64.833
	$19 \times 19$	16.658	24.025	35.014	40.926	48.631	49.056	59.032	64.709
	$25 \times 25$	16.648	23.999	34.931	40.910	48.592	48.838	58.919	64.473
	$31 \times 31$	16.645	23.990	34.904	40.904	48.576	48.774	58.878	64.384
	MISQ20 <sup>a</sup>	16.168	-	-	-	-	-	-	-
	(MLSDQ, $N_c = 3$ ) <sup>b</sup>	16.512	-	-	-	-	-	-	-
	(MLSDQ, $N_c = 4$ ) <sup>b</sup>	16.359	-	-	-	-	-	-	-
(MLSDQ, $N_c = 5$ ) <sup>b</sup>	16.278	-	-	-	-	-	-	-	
$45^\circ$	$11 \times 11$	17.653	32.175	40.886	52.412	53.679	64.551	71.124	72.677
	$13 \times 13$	17.643	32.128	40.861	52.116	53.683	64.376	70.979	72.288
	$15 \times 15$	17.637	32.111	40.847	51.997	53.682	64.304	70.898	72.055
	$17 \times 17$	17.634	32.103	40.839	51.939	53.679	64.267	70.852	71.926
	$19 \times 19$	17.631	32.098	40.833	51.907	53.677	64.246	70.824	71.853
	$25 \times 25$	17.627	32.090	40.824	51.866	53.670	64.218	70.784	71.762
	$31 \times 31$	17.625	32.087	40.819	51.850	53.665	64.208	70.767	71.732
	MISQ20 <sup>a</sup>	17.162	-	-	-	-	-	-	-
	(MLSDQ, $N_c = 3$ ) <sup>b</sup>	17.147	-	-	-	-	-	-	-
	(MLSDQ, $N_c = 4$ ) <sup>b</sup>	17.781	-	-	-	-	-	-	-
(MLSDQ, $N_c = 5$ ) <sup>b</sup>	17.141	-	-	-	-	-	-	-	

<sup>a</sup> (Nguyen-Van et al., 2008)

<sup>b</sup> (Liew et al., 2003)

Table 2.9: Clamped four-ply  $[\beta^\circ / -\beta^\circ / -\beta^\circ / \beta^\circ]$  circular laminated plate: convergence study of nondimensionalised natural frequencies for various mode number ( $\bar{\omega} = (\omega b^2/h) \sqrt{\rho/E_2}$ ,  $t/b = 0.1$ ,  $E_1/E_2 = 40$ ).

		Mode sequence number							
$\beta$	Grid	1	2	3	4	5	6	7	8
$0^\circ$	$11 \times 11$	22.198	29.658	40.987	42.764	50.582	55.075	61.568	65.849
	$13 \times 13$	22.195	29.647	40.929	42.754	50.521	54.906	61.299	65.793
	$15 \times 15$	22.198	29.646	40.921	42.759	50.526	54.876	61.312	65.787
	$17 \times 17$	22.198	29.644	40.918	42.761	50.523	54.865	61.304	65.786
	MISQ20 <sup>a</sup>	22.123	29.768	41.726	42.805	50.756	56.950	-	-
	(MLSDQ, $N_c = 3$ ) <sup>b</sup>	22.211	29.651	41.101	42.635	50.309	54.553	60.719	64.989
	(MLSDQ, $N_c = 4$ ) <sup>b</sup>	22.219	-	-	-	-	-	-	-
	(MLSDQ, $N_c = 5$ ) <sup>b</sup>	22.199	-	-	-	-	-	-	-
$45^\circ$	$11 \times 11$	24.737	39.112	43.638	57.190	57.254	65.693	74.254	75.149
	$13 \times 13$	24.737	39.101	43.630	57.135	57.194	65.640	74.029	74.854
	$15 \times 15$	24.737	39.099	43.630	57.138	57.185	65.630	74.035	74.823
	$17 \times 17$	24.737	39.099	43.630	57.136	57.181	65.627	74.029	74.810
	MISQ20 <sup>a</sup>	24.766	39.441	43.817	57.907	57.945	66.297	-	-
	(MLSDQ, $N_c = 3$ ) <sup>b</sup>	24.752	39.181	43.607	56.759	56.967	65.571	73.525	74.208
	(MLSDQ, $N_c = 4$ ) <sup>b</sup>	24.744	-	-	-	-	-	-	-
	(MLSDQ, $N_c = 5$ ) <sup>b</sup>	24.734	-	-	-	-	-	-	-

<sup>a</sup> (Nguyen-Van et al., 2008)

<sup>b</sup> (Liew et al., 2003)

Table 2.10: Clamped four-ply  $[\beta^\circ / -\beta^\circ / -\beta^\circ / \beta^\circ]$  circular laminated plate: effect of thickness-to-diameter ratio on nondimensionalised natural frequencies for various mode numbers,  $\bar{\omega} = (\omega b^2/h) \sqrt{\rho/E_2}$ ,  $E_1/E_2 = 40$ , using a grid of  $15 \times 15$ .

		Mode sequence number							
$\beta$	$t/b$	1	2	3	4	5	6	7	8
$0^\circ$	0.001	45.245	56.510	72.646	93.440	118.647	119.399	134.972	146.804
	0.050	33.401	42.190	55.649	70.957	73.602	80.909	94.742	95.602
	0.100	22.198	29.646	40.921	42.759	50.526	54.876	61.312	65.787
	0.150	16.424	23.040	30.528	32.359	37.045	43.081	45.728	45.907
	0.200	13.111	18.923	23.801	26.641	29.339	35.109	35.246	36.465
$45^\circ$	0.001	46.435	70.615	110.019	115.873	143.115	163.166	184.000	218.970
	0.050	35.506	55.366	70.743	84.208	89.932	112.326	117.096	117.614
	0.100	24.737	39.099	43.630	57.138	57.185	65.630	74.035	74.823
	0.150	18.580	29.222	31.328	41.286	41.855	46.084	53.062	53.211
	0.200	14.754	23.093	24.359	32.151	32.686	35.454	41.023	41.079

### 2.5.3 Example 3: Square isotropic plate with a square hole

Before investigating the free vibration of a square isotropic plate with a square hole for which there is currently no exact solution, a simply supported square isotropic plate is considered to validate the results of both 1D-IRBF method and Strand7 (Finite element analysis system). The results by the 1D-IRBF for complete geometries can then be compared with those obtained by Strand7. Approach 1 is employed here to implement the boundary conditions. Table 2.11 presents the comparison of nondimensionalised natural frequencies between 1D-IRBF, Strand7 and exact results for the simply supported square isotropic plate with thickness to length ratio  $t/b$  of 0.1. Converged solutions are obtained on a grid of  $15 \times 15$  for the IRBF method and of  $21 \times 21$  for Strand7. This table shows that the IRBF result is more accurate than Strand7's in comparison with the exact solution of Reddy (2004). Next, the methods are used to analyse the simply supported square isotropic plate with a square hole. All edges of the hole are also subjected to the simply supported boundary condition. Table 2.12 shows the nondimensionalised natural frequencies for various mode numbers of the simply supported square isotropic plate with a square hole. In this computation, the grid is taken to be  $17 \times 17$  for the IRBF method and  $41 \times 41$  for Strand7 to obtain the converged solutions. It can be seen that good agreement between the 1D-IRBF and Strand7 results is obtained for various mode numbers. Figure 2.9 shows the first four mode shapes of the simply supported square isotropic plate with a square hole.

Table 2.11: Simply supported square isotropic plate: Comparison of nondimensionalised natural frequencies among 1D-IRBF, Strand7 and exact results,  $\bar{\omega} = (\omega b^2/h) \sqrt{\rho/E_2}$ ,  $t/b = 0.1$ ,  $K_s = 5/6$ .

Mode	IRBF ( $15 \times 15$ )	Strand7 ( $21 \times 21$ )	Exact (Reddy, 2004)
1	5.769	5.809	5.769
2	13.765	13.970	13.764
3	21.122	21.569	21.121
4	25.780	26.278	25.734
5	32.319	33.129	32.284

Table 2.12: Simply supported square isotropic plate with a square hole: Comparison of nondimensionalised natural frequencies between 1D-IRBF and Strand7 results,  $\bar{\omega} = (\omega b^2/h) \sqrt{\rho/E_2}$ ,  $t/b = 0.1$ ,  $K_s = 5/6$ .

Mode	IRBF ( $17 \times 17$ )	Strand7 ( $41 \times 41$ )
1	38.931	38.856
2	39.959	39.805
3	42.503	41.805
4	42.886	44.142
5	46.890	47.964

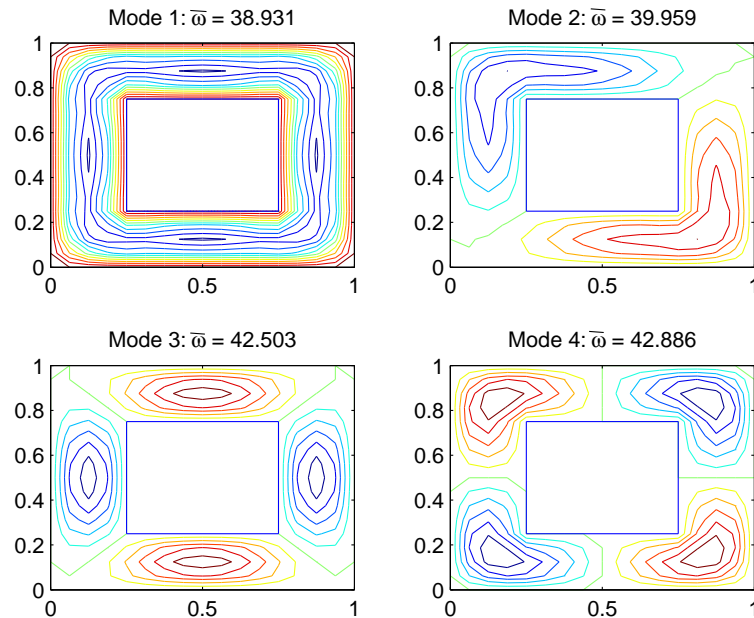


Figure 2.9: Mode shapes of simply supported square isotropic plate with a square hole,  $t/b = 0.1$ , using a grid of  $17 \times 17$ .

## 2.6 Concluding remarks

Free vibration analysis of laminated composite plates using FSDT and 1D-IRBFN method is presented. Unlike DRBFNs, IRBFNs are constructed through integration rather than differentiation, which helps to stabilise a numerical solution and provide an effective way to implement derivative boundary conditions. Cartesian grids are used to discretise both rectangular and non-rectangular plates. The laminated composite plates with various boundary conditions, length-to-width ratios  $a/b$ , thickness-to-length ratios  $t/b$ , and material properties are considered. The obtained numerical results are in good agreement with the available published results and exact solutions. Convergence study shows that faster rates are obtained for higher  $t/b$  ratios irrespective of  $a/b$  ratios of the rectangular plates. The effects of boundary conditions on the natural frequencies are also numerically investigated, which indicates that higher constraints at the edges yield higher natural frequencies. It is also found that the present method is not only highly accurate but also very stable for a wide range of modulus ratios.

# Chapter 3

## Local MLS-1D-IRBFN method for steady incompressible viscous flows

In the previous chapter, the 1D-IRBFN method has been successfully developed for free vibration analysis of laminated composite plates. In the present chapter, we propose a novel local moving least square - one-dimensional integrated radial basis function network (LMLS-1D-IRBFN) method for solving incompressible viscous flow problems using stream function-vorticity formulation. In this method, the partition of unity method is employed as a framework to incorporate the moving least square (MLS) and one-dimensional integrated radial basis function network (1D-IRBFN) techniques. The major advantages of the proposed method include: (i) a banded sparse system matrix which helps reduce the computational cost; (ii) the Kronecker- $\delta$  property of the constructed shape function which helps impose the essential boundary condition in an exact manner; and (iii) high accuracy and fast convergence rate owing to the use of integration instead of conventional differentiation to construct the local RBF approximations. Several examples including two-dimensional Poisson problems,

lid-driven cavity flow and flow past a circular cylinder are considered and the present results are compared with exact solutions and numerical results from other methods in the literature to demonstrate the attractiveness of the proposed method.

### 3.1 Introduction

Two-dimensional (2D) incompressible viscous flows governed by Navier-Stokes equations have been extensively studied to verify new numerical methods. The main issues for a successful numerical solver for this kind of problems are the proper treatments of the nonlinear convection term and incompressibility. For the first issue, the presence of the convection term causes serious numerical difficulties in the form of oscillatory solutions or numerical divergence when Reynolds ( $Re$ ) number or Peclet ( $Pe$ ) number is high. To deal with this, schemes related to upwinding have been developed to stabilize the FDM, FEM, and FVM (Ghia et al., 1982; Leonard, 1979; Brooks and Hughes, 1982). Brooks and Hughes (1982) developed a Streamline Upwind/Petrov-Galerkin (SUPG) method for convection-dominated flows, which has the robustness of an upwind method and the accuracy associated with the wiggle-free Galerkin solutions. In their method, an additional stability term was added in the upwind direction and several different treatments of incompressibility are incorporated into the formulation. The upwind concept is also needed in the meshfree methods in order to obtain a good accuracy for convection-dominated flows. Lin and Atluri (2000) proposed the meshless local Petrov-Galerkin (MLPG) method with two upwinding schemes for solving convection-diffusion problems. They skewed the weight function opposite to the streamline direction in the first scheme and shifted the local subdomain opposite to the streamline direction in the second scheme. Their numerical results indicated that the MLPG with the second scheme yielded better solutions than SUPG. This method was extended to solve the incompressible Navier-Stokes equations in (Lin and Atluri, 2001).

For the second issue, i.e. treatment for incompressibility, incompressible flows can be solved through the stream function and vorticity formulation. This approach can satisfy the incompressibility condition automatically, and the pressure term is eliminated. However, this formulation experiences other type of difficulty arising from the computation of the vorticity boundary condition on the wall, especially the curved ones. For three-dimensional problems, the incompressible Navier-Stokes equations are usually based on primitive variables (pressure and velocity) as the stream function and vorticity formulation are not applicable. In order to impose the incompressibility constraint, mixed formulations are considered by introducing another variable, the Lagrange multiplier. There are so-called inf-sup (or Ladyzenskaya-Babuška-Brezzi) stability conditions for this kind of formulations (Babuška, 1971). If these conditions are not satisfied, spurious pressure solutions may be obtained.

In 1990, Kansa proposed a collocation scheme based on multiquadric (MQ) radial basis functions for the numerical solution of partial differential equations (PDEs) (Kansa, 1990b). Their numerical results showed that MQ scheme yielded an excellent interpolation and partial derivative estimates for a variety of two-dimensional functions over both gridded and scattered data. Since this original work, a number of meshfree methods have been developed and used to solve fluid-flow problems. Park and Youn (2001) proposed the first-order least-squares method (LSMFM) to solve Laplace equations. Unlike the Galerkin method, the least-square formulation did not make use of the divergence theorem to convert the domain integral into a boundary integral. Therefore, the solution accuracy is less sensitive to the integration accuracy. However, the first-order least squares formulation requires more unknowns than the Galerkin formulation since the dual variables are employed as unknowns in addition to the primary variables, thereby increasing the computational cost. Zhang et al. (2005) employed the LSMFM based on the first-order velocity-pressure-vorticity formulation to investigate the 2D steady incompressible viscous flow problems. Their numerical results showed that the least-squares method based on the min-

imization of the squared residuals can reduce oscillations and instability of the solutions in comparison with the behaviour of methods based on Galerkin formulation. In their approach, the penalty method was used to enforce the essential boundary conditions. It is well-known that the larger the penalty parameter, the more accurate the numerical solution will be, but large penalty parameters can affect the conditioning of the system matrix adversely (Hetherington and Askes, 2009). Arzani and Afshar (2006) developed discrete least-squares meshless (DLSM) method for the solution of convection-dominated problems. A fractional step method in conjunction with DLSM method was proposed to solve the steady-state incompressible Navier-Stokes equations in primitive form using large time steps without having to satisfy the inf-sup condition (Firoozjaee and Afshar, 2011).

In contrast to the advantages of no mesh generation, most of the meshfree methods have difficulty in simulating large-scale problems, because they produce very dense system matrices. Lee et al. (2003) proposed the local multiquadric (LMQ) and the local inverse multiquadric (LIMQ) approximations for solving partial differential equations (PDEs). Their constructed shape functions strictly satisfied the Kronecker- $\delta$  condition which allows an imposition of the essential boundary condition in the same manner as in the standard FEM. Their numerical results showed that the LMQ and LIMQ often outperform their global counterparts, particularly with regard to viability and stability. Šarler and Vertnik (2006) presented an explicit local radial basis function (RBF) collocation method for diffusion problems. The method appeared efficient, because it does not require a solution of a large system of equations like the original RBF collocation method (Kansa, 1990b). Babuška and Melenk (1997) presented the partition of unity method (PUM) with attractive features. In the PUM, if analytic knowledge about the local behaviour of the problem solution is known, local approximation can be done with functions better suited than polynomials as in the classical FEM. The PU framework also provides a powerful approach to model mechanical problems with discontinuities and singularities. Krysl and

Belytschko (2000) proposed an approach to construct linear approximation basis functions for meshless method based on the concept of PU. In their work, the Shepard basis (Shepard, 1968) is used as a PU function. The PUM was also employed by Chen et al. (2008) to combine the reproducing kernel and RBF approximations in an approach that enjoys the exponential convergence of RBF and yields a banded and better-conditioned discrete system matrix. Le et al. (2010) proposed a locally supported moving IRBFN-based meshless method for solving various problems including heat transfer, elasticity of both compressible and incompressible materials, and linear static crack problems.

In the past, lid-driven cavity flow and flow past a circular cylinder have been studied as benchmark problems by many researchers to verify their new numerical methods. In the first problem, the presence of singularities at two of the corners of the cavity, where the velocity is discontinuous, makes it difficult to predict the numerical results accurately. Ghia et al. (1982) presented a FDM with a coupled strongly implicit multigrid method to obtain high- $Re$  fine-mesh flow solutions. Botella and Peyret (1998) introduced a third-order time-accurate Chebyshev projection method with an analytical treatment of the singularities for the lid-driven cavity flow. Their numerical results are widely considered as benchmark solutions in the literature. In the second problem, it is well-known that the flow has a stable pattern with a fixed pair of symmetric vortices behind the cylinder at  $Re$  up to 40. Ding et al. (2004) presented a hybrid approach, which combines the conventional FDM and the meshfree least square-based finite difference (MLSFD) method for simulating the 2D steady and unsteady incompressible flows. In their works, the MLSFD method was adopted to deal with the spatial discretisation in the region with complex geometry and the conventional FDM was applied in the rest of the flow domain to take advantage of its high computational efficiency. Kim et al. (2007) developed a meshfree point collocation method for the stream function-vorticity formulation of 2D incompressible Navier-Stokes equations. The MLS approximation was employed to construct shape functions in conjunction with a point collocation technique.

A one-dimensional integrated radial basis function network (1D-IRBFN) collocation method for the solution of second- and fourth-order PDEs was presented by Mai-Duy and Tanner (2007). In this method, Cartesian grids were used to discretise both rectangular and non-rectangular problem domains. The computational cost associated with the Cartesian grid generation is negligible in comparison with that required for the body-fitted mesh. Along a grid line, IRBFNs are employed to represent the field variable and its relevant derivatives. Such networks are called 1D-IRBFNs. Through integration constants, one can impose derivative boundary conditions and the governing equations at the two end points of a grid line in an exact manner. The 1D-IRBFN method is much more efficient than the original IRBFN method reported in Mai-Duy and Tran-Cong (2001a). Ngo-Cong et al. (2011) extended this method to investigate free vibration of composite laminated plates based on first-order shear deformation theory (Chapter 2). The present work is concerned with the development of a new numerical method to handle 2D incompressible viscous flows at a high  $Re$  number and in large scale problems. The proposed method is based on the PU concept acting as a framework to incorporate MLS and 1D-IRBFN techniques, and from here on is named LMLS-1D-IRBFN, which is a local MLS-1D-IRBFN method. The approximation is locally supported, which leads to sparse system matrices and requires less computational effort than the case of using 1D-IRBFN method alone, while the order of accuracy remains high as in the case of 1D-IRBFN. Unlike conventional MLS-based methods, the LMLS-1D-IRBFN shape functions satisfy the Kronecker- $\delta$  property and thus the essential boundary conditions can be imposed in an exact manner.

The chapter is organised as follows. Section 3.2 describes the notations. Section 3.3 briefly reproduces the MLS approximation technique. The LMLS-1D-IRBFN method is presented in Section 3.4. The governing equations for incompressible viscous flows are given in Section 3.5. The LMLS-1D-IRBFN discretisation of the governing equations is described in Section 3.6. Several numerical examples are investigated using the proposed method in Section 3.7.

Section 3.8 concludes the chapter.

## 3.2 Notations

In the remainder of the chapter, we use

- the notation  $\bar{[]}$  for a vector/matrix  $[]$  that is associated with a segment of a grid line;
- the notation  $\widehat{[]}$  for a vector/matrix  $[]$  that is associated with a grid line;
- the notation  $\widetilde{[]}$  for a vector/matrix  $[]$  that is associated with the whole set of grid lines;
- the notation  $[]_{(\eta,\theta)}$  to denote selected rows  $\eta$  and columns  $\theta$  of the matrix  $[]$ ;
- the notation  $[]_{(\eta)}$  to denote selected components  $\eta$  of the vector  $[]$ ;
- the notation  $[]_{(:,\theta)}$  to denote all rows and selected columns  $\theta$  of the matrix  $[]$ ; and
- the notation  $[]_{(\eta,:)}$  to denote all columns and selected rows  $\eta$  of the matrix  $[]$ .

## 3.3 Moving least square approximation

The moving least square procedure (Liu, 2003) is briefly described in this section. The domain of interest is discretised using a Cartesian grid as shown in Figure 3.1. On an  $x$ -grid line, e.g.  $[l]$ , consider a nodal point  $x_i$  with its associated support domain, e.g.  $[x_{i-1}, x_{i+1}]$  for the case of 3-node local support. Let

$u^h(x)$  be the approximation of the field variable  $u$  along this support domain and given by

$$u^h(x) = \sum_{j=0}^m p_j(x) a_j(x) = \bar{p}^T(x) \bar{a}(x), \quad (3.1)$$

where  $m$  is the number of terms of monomials;  $\bar{a}(x)$  a vector of coefficients; and  $\bar{p}^T(x)$  a complete polynomial basis, given by

$$\bar{a}(x) = \left( a_0(x) \quad a_1(x) \quad \dots \quad a_m(x) \right)^T, \quad (3.2)$$

$$\bar{p}(x) = \left( p_0(x) \quad p_1(x) \quad \dots \quad p_m(x) \right)^T = \left( 1 \quad x \quad x^2 \quad \dots \quad x^m \right)^T. \quad (3.3)$$

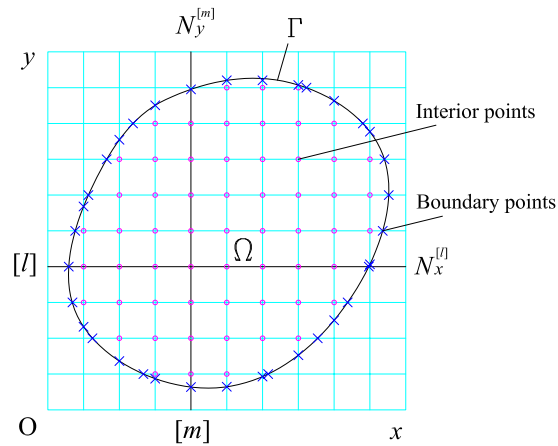


Figure 3.1: Cartesian grid discretisation.

The expression for  $\bar{a}(x)$  can be obtained at each point  $x$  by minimizing the following weighted residual

$$J = \sum_{I=1}^n W(x - x_I) \left[ \bar{p}^T(x_I) \bar{a}(x) - u^{(I)} \right]^2, \quad (3.4)$$

where  $u^{(I)}$  is the nodal value of the field variable  $u$  at  $x = x_I$ ; and  $n$  the number of nodes in the support domain of  $x$  where the weight function  $W(x - x_I) \neq 0$ . In the present chapter, the cubic spline weight function is used to construct

MLS shape functions.

$$W(d) = \begin{cases} \frac{2}{3} - 4d^2 + 4d^3, & d \leq \frac{1}{2} \\ \frac{4}{3} - 4d + 4d^2 - \frac{4}{3}d, & \frac{1}{2} < d \leq 1 \\ 0, & d > 1 \end{cases} \quad (3.5)$$

where  $d = |x - x_I|/d_w$  and  $d_w$  defines the size of the support domain. The minimization of the weighted residual  $J$  results in the following linear equation system

$$\mathbf{A}(x)\bar{a}(x) = \mathbf{B}(x)\bar{u}, \quad (3.6)$$

or

$$\bar{a}(x) = \mathbf{A}(x)^{-1}\mathbf{B}(x)\bar{u}, \quad (3.7)$$

where

$$\bar{u} = \left( u^{(1)} \quad u^{(2)} \quad \dots \quad u^{(n)} \right)^T; \quad (3.8)$$

$$\mathbf{A}(x) = \sum_{I=1}^n W(x - x_I)\bar{p}(x_I)\bar{p}^T(x_I); \quad (3.9)$$

$$\mathbf{B}(x) = \left[ B_1 \quad B_2 \quad \dots \quad B_n \right]; \quad (3.10)$$

in which

$$B_I = W(x - x_I)\bar{p}(x_I). \quad (3.11)$$

Substituting (3.7) into (3.1),  $u^h$  can be expressed as

$$u^h(x) = \bar{\phi}^T(x)\bar{u}, \quad (3.12)$$

where  $\bar{\phi}$  is the vector of MLS shape functions and given by

$$\bar{\phi}(x) = \left( \bar{p}^T \mathbf{A}^{-1} B_1 \quad \bar{p}^T \mathbf{A}^{-1} B_2 \quad \dots \quad \bar{p}^T \mathbf{A}^{-1} B_n \right)^T. \quad (3.13)$$

It should be noted that the MLS shape functions do not satisfy the Kronecker- $\delta$  criterion, but possess a so-called partition of unity properties as follows.

$$\sum_{I=1}^n \bar{\phi}_I(x) = 1. \quad (3.14)$$

A new shape function possessing the Kronecker- $\delta$  function properties is created through a technique as described in the following section.

### 3.4 Local moving least square - one dimensional integrated radial basis function network technique

A schematic outline of the LMLS-1D-IRBFN method is depicted in Figure 3.2. For brevity, the proposed method with 3-node support domains ( $n = 3$ ) and 3-node local 1D-IRBF networks ( $n_s = 3$ ) is presented here. On an  $x$ -grid line  $[l]$ , a global interpolant for the field variable at a grid point  $x_i$  is sought in the form

$$u(x_i) = \sum_{j=1}^n \bar{\phi}_j(x_i) u^{[j]}(x_i), \quad (3.15)$$

where  $\{\bar{\phi}_j\}_{j=1}^n$  is a set of the partition of unity functions constructed using MLS approximants;  $u^{[j]}(x_i)$  the nodal function value obtained from a local interpolant represented by a 1D-IRBF network  $[j]$ ;  $n$  the number of nodes in the support domain of  $x_i$ . In (3.15), MLS approximants are presently based on

linear polynomials, which are defined in terms of 1 and  $x$ . Relevant derivatives of  $u$  at  $x_i$  can be obtained by differentiating (3.15)

$$\frac{\partial u(x_i)}{\partial x} = \sum_{j=1}^n \left( \frac{\partial \bar{\phi}_j(x_i)}{\partial x} u^{[j]}(x_i) + \bar{\phi}_j(x_i) \frac{\partial u^{[j]}(x_i)}{\partial x} \right), \quad (3.16)$$

$$\frac{\partial^2 u(x_i)}{\partial x^2} = \sum_{j=1}^n \left( \frac{\partial^2 \bar{\phi}_j(x_i)}{\partial x^2} u^{[j]}(x_i) + 2 \frac{\partial \bar{\phi}_j(x_i)}{\partial x} \frac{\partial u^{[j]}(x_i)}{\partial x} + \bar{\phi}_j(x_i) \frac{\partial^2 u^{[j]}(x_i)}{\partial x^2} \right), \quad (3.17)$$

where the values  $u^{[j]}(x_i)$ ,  $\partial u^{[j]}(x_i)/\partial x$  and  $\partial^2 u^{[j]}(x_i)/\partial x^2$  are calculated from 1D-IRBFN networks with  $n_s$  nodes.

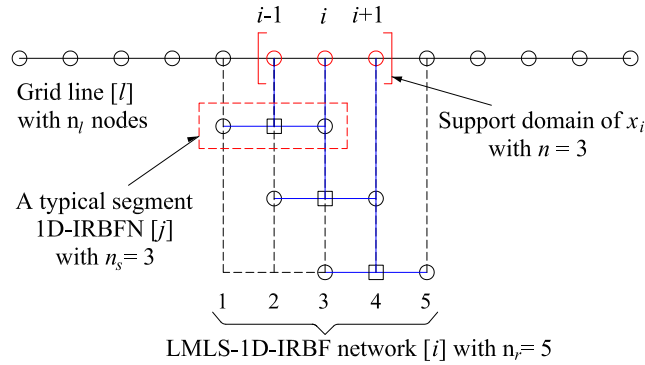


Figure 3.2: LMLS-1D-IRBFN-3-node scheme, □ a typical  $[j]$  node.

### 3.4.1 One-dimensional IRBFN

Consider a segment  $[j]$  with  $n_s$  nodes on an  $x$ -grid line  $[l]$  as shown in Figure 3.2. The variation of the nodal function  $u^{[j]}$  along this segment is sought in the IRBF form. The second-order derivative of  $u^{[j]}$  is decomposed into RBFs; the RBF network is then integrated once and twice to obtain the expressions for the

first-order derivative of  $u^{[j]}$  and the function  $u^{[j]}$  itself as follows.

$$\frac{\partial^2 u^{[j]}(x)}{\partial x^2} = \sum_{k=1}^{n_s} w^{(k)} G^{(k)}(x) = \sum_{k=1}^{n_s} w^{(k)} H_{[2]}^{(k)}(x), \quad (3.18)$$

$$\frac{\partial u^{[j]}(x)}{\partial x} = \sum_{k=1}^{n_s} w^{(k)} H_{[1]}^{(k)}(x) + c_1, \quad (3.19)$$

$$u^{[j]}(x) = \sum_{k=1}^{n_s} w^{(k)} H_{[0]}^{(k)}(x) + c_1 x + c_2, \quad (3.20)$$

where  $\{w^{(k)}\}_{k=1}^{n_s}$  are RBF weights to be determined;  $\{G^{(k)}(x)\}_{k=1}^{n_s} = \{H_{[2]}^{(k)}(x)\}_{k=1}^{n_s}$  known RBFs;  $H_{[1]}^{(k)}(x) = \int H_{[2]}^{(k)}(x) dx$ ;  $H_{[0]}^{(k)}(x) = \int H_{[1]}^{(k)}(x) dx$ ; and  $c_1$  and  $c_2$  integration constants which are also unknown. An example of RBF, used in this work, is the multiquadrics  $G^{(k)}(x) = \sqrt{(x - x^{(k)})^2 + a^{(k)2}}$ ,  $a^{(k)}$  - the RBF width determined as  $a^{(k)} = \beta d^{(k)}$ ,  $\beta$  a positive factor, and  $d^{(k)}$  the distance from the  $k^{th}$  center to its nearest neighbour.

It is more convenient to work in the physical space than in the network-weight space. The RBF coefficients including two integration constants can be transformed into the physically meaningful nodal variable values through the following relation

$$\bar{u}^{[j]} = \bar{\mathbf{H}} \begin{pmatrix} \bar{w} \\ \bar{c} \end{pmatrix}, \quad (3.21)$$

where  $\bar{\mathbf{H}}$  is an  $n_s \times (n_s + 2)$  matrix and given by

$$\mathbf{H} = \begin{bmatrix} H_{[0]}^{(1)}(x_1) & H_{[0]}^{(2)}(x_1) & \dots & H_{[0]}^{(n_s)}(x_1) & x_1 & 1 \\ H_{[0]}^{(1)}(x_2) & H_{[0]}^{(2)}(x_2) & \dots & H_{[0]}^{(n_s)}(x_2) & x_2 & 1 \\ \dots & \dots & \dots & \dots & \dots & \dots \\ H_{[0]}^{(1)}(x_{n_s}) & H_{[0]}^{(2)}(x_{n_s}) & \dots & H_{[0]}^{(n_s)}(x_{n_s}) & x_{n_s} & 1 \end{bmatrix}; \quad (3.22)$$

$\bar{u}^{[j]} = (u^{(1)}, u^{(2)}, \dots, u^{(n_s)})^T$ ;  $\bar{w} = (w^{(1)}, w^{(2)}, \dots, w^{(n_s)})^T$  and  $\bar{c} = (c_1, c_2)^T$ . There are two possible transformation cases.

For a segment  $[j]$  with only interior points: The direct use of (3.21) leads to an underdetermined system of equations

$$\bar{u}^{[j]} = \bar{\mathbf{H}} \begin{pmatrix} \bar{w} \\ \bar{c} \end{pmatrix} = \bar{\mathbf{C}} \begin{pmatrix} \bar{w} \\ \bar{c} \end{pmatrix}, \quad (3.23)$$

or

$$\begin{pmatrix} \bar{w} \\ \bar{c} \end{pmatrix} = \bar{\mathbf{C}}^{-1} \bar{u}^{[j]}, \quad (3.24)$$

where  $\bar{\mathbf{C}} = \bar{\mathbf{H}}$  is the conversion matrix whose inverse can be found using the singular value decomposition (SVD) technique.

For a segment  $[j]$  with interior and boundary points: Owing to the presence of  $c_1$  and  $c_2$ , one can add an additional equation of the form

$$f = \mathbf{K} \begin{pmatrix} \bar{w} \\ \bar{c} \end{pmatrix} \quad (3.25)$$

to equation system (3.21). In the case of Neumann boundary conditions, this subsystem can be used to impose a derivative boundary value at  $x = x_b$

$$f = \frac{\partial u(x_b)}{\partial x}, \quad (3.26)$$

$$\mathbf{K} = \begin{bmatrix} H_{[1]}^{(1)}(x_b) & H_{[1]}^{(2)}(x_b) & \dots & H_{[1]}^{(n_s)}(x_b) & 1 & 0 \end{bmatrix}. \quad (3.27)$$

The conversion system can be written as

$$\begin{pmatrix} \bar{u}^{[j]} \\ f \end{pmatrix} = \begin{bmatrix} \bar{\mathbf{H}} \\ \mathbf{K} \end{bmatrix} \begin{pmatrix} \bar{w} \\ \bar{c} \end{pmatrix} = \bar{\mathbf{C}} \begin{pmatrix} \bar{w} \\ \bar{c} \end{pmatrix}, \quad (3.28)$$

or

$$\begin{pmatrix} \bar{w} \\ \bar{c} \end{pmatrix} = \bar{\mathbf{C}}^{-1} \begin{pmatrix} \bar{u}^{[j]} \\ f \end{pmatrix}. \quad (3.29)$$

It can be seen that (3.24) is a special case of (3.29), where  $f$  is simply set to null. By substituting Equation (3.29) into Equations (3.18)-(3.20), the second- and first-order derivatives and the function of the variable  $u^{[j]}$  are expressed in terms of nodal variable values as

$$\frac{\partial^2 u^{[j]}(x)}{\partial x^2} = \left( H_{[2]}^{(1)}(x), H_{[2]}^{(2)}(x), \dots, H_{[2]}^{(n_s)}(x), 0, 0 \right) \bar{\mathbf{C}}^{-1} \begin{pmatrix} \bar{u}^{[j]} \\ f \end{pmatrix}, \quad (3.30)$$

$$\frac{\partial u^{[j]}(x)}{\partial x} = \left( H_{[1]}^{(1)}(x), H_{[1]}^{(2)}(x), \dots, H_{[1]}^{(n_s)}(x), 1, 0 \right) \bar{\mathbf{C}}^{-1} \begin{pmatrix} \bar{u}^{[j]} \\ f \end{pmatrix}, \quad (3.31)$$

$$u^{[j]}(x) = \left( H_{[0]}^{(1)}(x), H_{[0]}^{(2)}(x), \dots, H_{[0]}^{(n_s)}(x), x, 1 \right) \bar{\mathbf{C}}^{-1} \begin{pmatrix} \bar{u}^{[j]} \\ f \end{pmatrix}, \quad (3.32)$$

or

$$\frac{\partial^2 u^{[j]}(x)}{\partial x^2} = \bar{d}_{2x}^T \bar{u}^{[j]} + k_{2x}(x), \quad (3.33)$$

$$\frac{\partial u^{[j]}(x)}{\partial x} = \bar{d}_{1x}^T \bar{u}^{[j]} + k_{1x}(x), \quad (3.34)$$

$$u^{[j]}(x) = \bar{d}_{0x}^T \bar{u}^{[j]} + k_{0x}(x), \quad (3.35)$$

where  $k_{0x}$ ,  $k_{1x}$  and  $k_{2x}$  are scalars whose values depend on  $x$  and the boundary value  $f$ ; and  $\bar{d}_{0x}$ ,  $\bar{d}_{1x}$  and  $\bar{d}_{2x}$  known vectors of length  $n_s$ .

By application of Equations (3.33) and (3.34) to  $n_s$  nodes on the segment  $[j]$ , the second- and first-order derivatives of  $u^{[j]}$  at node  $x_i$  are determined as

$$\frac{\partial^2 u^{[j]}(x_i)}{\partial x^2} = \bar{\mathbf{D}}_{2x(idk,:)} \bar{u}^{[j]} + \bar{k}_{2x(idk)}, \quad (3.36)$$

$$\frac{\partial u^{[j]}(x_i)}{\partial x} = \bar{\mathbf{D}}_{1x(idk,:)} \bar{u}^{[j]} + \bar{k}_{1x(idk)}, \quad (3.37)$$

$$u^{[j]}(x_i) = \bar{\mathbf{D}}_{0x(idk,:)} \bar{u}^{[j]} + \bar{k}_{0x(idk)} = \bar{\mathbf{I}}_{(idk,:)} \bar{u}^{[j]}, \quad (3.38)$$

where  $\bar{\mathbf{D}}_{1x}$  and  $\bar{\mathbf{D}}_{2x}$  are known matrices of dimension  $n_s \times n_s$ ;  $\bar{k}_{1x}$  and  $\bar{k}_{2x}$  known vectors of length  $n_s$ ; and  $idk$  the index number indicating the location of node  $x_i$  in the local network  $[j]$ . It is noted that  $\bar{\mathbf{D}}_{0x} = \bar{\mathbf{I}}$ , where  $\bar{\mathbf{I}}$  is an identity

matrix of dimension  $n_s \times n_s$  and  $\bar{k}_{0x} = \bar{0}$ . Therefore, the 1D-IRBFN shape function possesses the Kronecker- $\delta$  function properties.

### 3.4.2 Incorporation of MLS and 1D-IRBFN into the partition of unity framework

By substituting Equations (3.36)-(3.38) into Equations (3.15)-(3.17), the function  $u(x_i)$  and its derivatives are expressed as

$$u(x_i) = \sum_{j=1}^n \bar{m}_{0x}^{[j]} \bar{u}^{[j]}, \quad (3.39)$$

$$\frac{\partial u(x_i)}{\partial x} = \sum_{j=1}^n \left( \bar{m}_{1x}^{[j]} \bar{u}^{[j]} + k_{1x}^{[j]} \right), \quad (3.40)$$

$$\frac{\partial^2 u(x_i)}{\partial x^2} = \sum_{j=1}^n \left( \bar{m}_{2x}^{[j]} \bar{u}^{[j]} + k_{2x}^{[j]} \right), \quad (3.41)$$

where

$$\bar{m}_{0x}^{[j]} = \bar{\phi}_j(x_i) \bar{\mathbf{I}}_{(idk, \cdot)}; \quad (3.42)$$

$$\bar{m}_{1x}^{[j]} = \frac{\partial \bar{\phi}_j(x_i)}{\partial x} \bar{\mathbf{I}}_{(idk, \cdot)} + \bar{\phi}_j(x_i) \bar{\mathbf{D}}_{1x(idk, \cdot)}; \quad (3.43)$$

$$\bar{m}_{2x}^{[j]} = \frac{\partial^2 \bar{\phi}_j(x_i)}{\partial x^2} \bar{\mathbf{I}}_{(idk, \cdot)} + 2 \frac{\partial \bar{\phi}_j(x_i)}{\partial x} \bar{\mathbf{D}}_{1x(idk, \cdot)} + \bar{\phi}_j(x_i) \bar{\mathbf{D}}_{2x(idk, \cdot)}; \quad (3.44)$$

$$k_{1x}^{[j]} = \bar{\phi}_j(x_i) \bar{k}_{1x(idk)}; \quad (3.45)$$

$$k_{2x}^{[j]} = 2 \frac{\partial \bar{\phi}_j(x_i)}{\partial x} \bar{k}_{1x(idk)} + \bar{\phi}_j(x_i) \bar{k}_{2x(idk)}. \quad (3.46)$$

From Equations (3.14), (3.39) and (3.42), one can see that the LMLS-1D-IRBFN shape function possesses the Kronecker- $\delta$  function properties.

Equations (3.40) and (3.41) can be expressed as

$$\frac{\partial u(x_i)}{\partial x} = \bar{m}_{1x}^{[i]} \bar{u}^{[i]} + k_{1x}^{[i]}, \quad (3.47)$$

$$\frac{\partial^2 u(x_i)}{\partial x^2} = \bar{m}_{2x}^{[i]} \bar{u}^{[i]} + k_{2x}^{[i]}, \quad (3.48)$$

where  $\bar{u}^{[i]} = (u^{(1)}, u^{(2)}, \dots, u^{(n_r)})^T$ ;  $n_r$  is the number of nodes in the network  $[i]$ ;  $k_{1x}^{[i]}$  and  $k_{2x}^{[i]}$  known scalars; and  $\bar{m}_{1x}^{[i]}$  and  $\bar{m}_{2x}^{[i]}$  known vectors of length  $n_r$ , defined by

$$\bar{m}_{1x(idj)}^{[i]} = \bar{m}_{1x(idj)}^{[i]} + \bar{m}_{1x}^{[j]}, \quad j = 1, 2, \dots, n \quad (3.49)$$

$$\bar{m}_{2x(idj)}^{[i]} = \bar{m}_{2x(idj)}^{[i]} + \bar{m}_{2x}^{[j]}, \quad j = 1, 2, \dots, n \quad (3.50)$$

in which  $idj$  is the index vector mapping the location of nodes of the local network  $[j]$  to that in the LMLS-1D-IRBF network  $[i]$ .

The values of first- and second-order derivatives of  $u$  with respect to  $x$  at the nodal points on the grid line  $[l]$  are given by

$$\frac{\partial \hat{u}}{\partial x} = \hat{\mathbf{M}}_{1x}^{[l]} \hat{u}^{[l]} + \hat{k}_{1x}^{[l]}, \quad (3.51)$$

$$\frac{\partial^2 \hat{u}}{\partial x^2} = \hat{\mathbf{M}}_{2x}^{[l]} \hat{u}^{[l]} + \hat{k}_{2x}^{[l]}, \quad (3.52)$$

where

$$\hat{u} = (u^{(1)}, u^{(2)}, \dots, u^{(n_l)})^T; \quad (3.53)$$

$$\hat{\mathbf{M}}_{1x(i,idi)}^{[l]} = \bar{m}_{1x}^{[i]}, \quad (3.54)$$

$$\hat{\mathbf{M}}_{2x(i,idi)}^{[l]} = \bar{m}_{2x}^{[i]}, \quad (3.55)$$

$$\hat{k}_{1x(i)}^{[l]} = k_{1x}^{[i]}, \quad (3.56)$$

$$\hat{k}_{2x(i)}^{[l]} = k_{2x}^{[i]}, \quad (3.57)$$

in which  $n_l$  is the number of nodes on the grid line  $[l]$ , and  $idi$  the index vector mapping the location of nodes of the local network  $[i]$  to that in the grid line

[ $l$ ].

The values of first- and second-order derivatives of  $u$  with respect to  $x$  at the nodal points over the problem domain are given by

$$\frac{\partial \tilde{u}}{\partial x} = \tilde{\mathbf{M}}_{1x} \tilde{u} + \tilde{k}_{1x}, \quad (3.58)$$

$$\frac{\partial^2 \tilde{u}}{\partial x^2} = \tilde{\mathbf{M}}_{2x} \tilde{u} + \tilde{k}_{2x}, \quad (3.59)$$

where

$$\tilde{u} = (u^{(1)}, u^{(2)}, \dots, u^{(N_{ip})})^T; \quad (3.60)$$

$$\frac{\partial \tilde{u}}{\partial x} = \left( \frac{\partial u^{(1)}}{\partial x}, \frac{\partial u^{(2)}}{\partial x}, \dots, \frac{\partial u^{(N_{ip})}}{\partial x} \right)^T; \quad (3.61)$$

$$\frac{\partial^2 \tilde{u}}{\partial x^2} = \left( \frac{\partial^2 u^{(1)}}{\partial x^2}, \frac{\partial^2 u^{(2)}}{\partial x^2}, \dots, \frac{\partial^2 u^{(N_{ip})}}{\partial x^2} \right)^T; \quad (3.62)$$

and  $\tilde{\mathbf{M}}_{1x}$  and  $\tilde{\mathbf{M}}_{2x}$  are known matrices of dimension  $N_{ip} \times N_{ip}$ ;  $\tilde{k}_{1x}$  and  $\tilde{k}_{2x}$  known vectors of length  $N_{ip}$ ; and  $N_{ip}$  the total number of interior nodal points. The matrices  $\tilde{\mathbf{M}}_{1x}$  and  $\tilde{\mathbf{M}}_{2x}$  and the vectors  $\tilde{k}_{1x}$  and  $\tilde{k}_{2x}$  are formed as follows.

$$\tilde{\mathbf{M}}_{1x(idl, idl)} = \hat{\mathbf{M}}_{1x}^{[l]}, \quad (3.63)$$

$$\tilde{\mathbf{M}}_{2x(idl, idl)} = \hat{\mathbf{M}}_{2x}^{[l]}, \quad (3.64)$$

$$\tilde{k}_{1x(idl)} = \hat{k}_{1x}^{[l]}, \quad (3.65)$$

$$\tilde{k}_{2x(idl)} = \hat{k}_{2x}^{[l]}, \quad (3.66)$$

in which  $idl$  is the index vector mapping the location of nodes on the grid line [ $l$ ] to that in the whole grid.

Similarly, the values of the second- and first-order derivatives of  $u$  with respect

to  $y$  at the nodal points over the problem domain are given by

$$\frac{\partial \tilde{u}}{\partial y} = \tilde{\mathbf{M}}_{1y} \tilde{u} + \tilde{k}_{1y}, \quad (3.67)$$

$$\frac{\partial^2 \tilde{u}}{\partial y^2} = \tilde{\mathbf{M}}_{2y} \tilde{u} + \tilde{k}_{2y}. \quad (3.68)$$

### 3.5 Governing equations for two-dimensional incompressible viscous flows

In this work we limit the analysis to two-dimensional problems and the governing equations for incompressible viscous flows can therefore be written in terms of stream function  $\psi$  and vorticity  $\omega$  as (Glowinski, 2003)

$$\frac{\partial^2 \psi}{\partial x^2} + \frac{\partial^2 \psi}{\partial y^2} = -\omega, \quad (3.69)$$

$$\frac{1}{Re} \left( \frac{\partial^2 \omega}{\partial x^2} + \frac{\partial^2 \omega}{\partial y^2} \right) = \frac{\partial \omega}{\partial t} + \left( \frac{\partial \psi}{\partial y} \frac{\partial \omega}{\partial x} - \frac{\partial \psi}{\partial x} \frac{\partial \omega}{\partial y} \right), \quad (3.70)$$

where  $Re$  is the Reynolds number;  $t$  the time; and  $(x, y)^T$  the position vector. The  $x$  and  $y$  components of the velocity vector can be defined in terms of the stream function as

$$u = \frac{\partial \psi}{\partial y}, \quad (3.71)$$

$$v = -\frac{\partial \psi}{\partial x}. \quad (3.72)$$

### 3.6 LMLS-1D-IRBFN discretisation of governing equations for incompressible viscous flows

The domain of interest is discretised using uniform Cartesian grids. With the backward Euler scheme for time discretisation, Equations (3.69) and (3.70) can

be expressed as

$$\frac{\partial^2 \psi^{(n+1)}}{\partial x^2} + \frac{\partial^2 \psi^{(n+1)}}{\partial y^2} = -\omega^{(n)}, \quad (3.73)$$

$$\frac{\Delta t}{Re} \left( \frac{\partial^2 \omega^{(n+1)}}{\partial x^2} + \frac{\partial^2 \omega^{(n+1)}}{\partial y^2} \right) - \omega^{(n+1)} = -\omega^{(n)} + \Delta t \left( \frac{\partial \psi^{(n)}}{\partial y} \frac{\partial \omega^{(n)}}{\partial x} - \frac{\partial \psi^{(n)}}{\partial x} \frac{\partial \omega^{(n)}}{\partial y} \right), \quad (3.74)$$

where the superscripts  $(n)$  and  $(n+1)$  denote the time levels; and  $\Delta t$  the time discretisation step.

Making use of (3.58), (3.59), (3.67) and (3.68) and collocating the governing equations (3.73) and (3.74) at the interior points result in

$$\tilde{E}_1 \tilde{\psi}^{(n+1)} = RHS_1, \quad (3.75)$$

$$\tilde{E}_2 \tilde{\omega}^{(n+1)} = RHS_2, \quad (3.76)$$

where

$$\tilde{E}_1 = \tilde{\mathbf{M}}_{2x} + \tilde{\mathbf{M}}_{2y}; \quad (3.77)$$

$$RHS_1 = -\omega^{(n)} - \left( \tilde{k}_{2x\psi} + \tilde{k}_{2y\psi} \right); \quad (3.78)$$

$$\tilde{E}_2 = \frac{\Delta t}{Re} \left( \tilde{\mathbf{M}}_{2x} + \tilde{\mathbf{M}}_{2y} - \tilde{\mathbf{I}} \right); \quad (3.79)$$

$$RHS_2 = -\omega^{(n)} - \frac{\Delta t}{Re} \left( \tilde{k}_{2x\omega} + \tilde{k}_{2y\omega} \right) + \Delta t \left[ \left( \tilde{\mathbf{M}}_{1y} \tilde{\psi}^{(n)} + \tilde{k}_{1y\psi}^{(n)} \right) \cdot \left( \tilde{\mathbf{M}}_{1x} \tilde{\omega}^{(n)} + \tilde{k}_{1x\omega}^{(n)} \right) - \left( \tilde{\mathbf{M}}_{1x} \tilde{\psi}^{(n)} + \tilde{k}_{1x\psi}^{(n)} \right) \cdot \left( \tilde{\mathbf{M}}_{1y} \tilde{\omega}^{(n)} + \tilde{k}_{1y\omega}^{(n)} \right) \right]; \quad (3.80)$$

in which  $\tilde{k}_{1x\psi}$ ,  $\tilde{k}_{2x\psi}$ ,  $\tilde{k}_{1y\psi}$ ,  $\tilde{k}_{2y\psi}$ ,  $\tilde{k}_{1x\omega}$ ,  $\tilde{k}_{2x\omega}$ ,  $\tilde{k}_{1y\omega}$  and  $\tilde{k}_{2y\omega}$  are known vectors of length  $N_{ip}$ .

The nonlinear system of equations (3.75) and (3.76) is solved using the pseudo-time stepping procedure as follows:

- Step 1: Guess the initial solution of vorticity  $\omega$ .
- Step 2: Solve (3.75) for  $\psi$ .
- Step 3: Compute the vorticity boundary conditions and the convection

terms explicitly.

- Step 4: Solve (3.76) for  $\omega$ .
- Step 5: Check convergence criterion for  $\omega$

$$\frac{\sqrt{\sum_{i=1}^{Nip} (\omega_i^{(t+1)} - \omega_i^{(t)})^2}}{\sqrt{\sum_{i=1}^{Nip} (\omega_i^{(t+1)})^2}} < TOL, \quad (3.81)$$

where  $TOL$  is a given tolerance and presently set to be  $10^{-12}$ . If not converged, return to step 2. Otherwise, stop.

## 3.7 Numerical results and discussion

Several examples are investigated here to study the performance of the present method. The domains of interest are discretised using Cartesian grids. By using the LMLS-1D-IRBFN method to discretise governing equations and the LU decomposition technique to solve the resultant sparse system of simultaneous equations, the computational cost and data storage requirements are reduced. For the purpose of CPU times comparisons, all related computations are carried out on a single 2.4 GHz processor machine with 4 GB RAM.

### 3.7.1 Example 1: Two-dimensional Poisson equation in a square domain

The present method is first verified through the solution of the following 2D Poisson equation

$$\frac{\partial^2 u}{\partial x^2} + \frac{\partial^2 u}{\partial y^2} = 0, \quad (3.82)$$

defined on a square domain  $0 \leq x, y \leq 1$  and subject to Dirichlet boundary conditions. The problem has the following exact solution

$$u_E = \frac{1}{\sinh(\pi)} \sin(\pi x) \sinh(\pi y). \quad (3.83)$$

A uniform grid of  $N_x \times N_y$  is employed to discretise the problem domain. Two cases of boundary conditions are considered as follows.

- Case 1: Dirichlet boundary conditions are imposed along all four edges.
- Case 2: Dirichlet boundary conditions are imposed along two horizontal edges and Neumann boundary conditions are imposed along two vertical edges.

These boundary conditions can be derived from the exact solution. The proposed LMLS-1D-IRBFN method with the following two approaches is considered.

- Approach 1:  $n = 3$  and  $n_s = 3$ , called LMLS-1D-IRBFN-3-node.
- Approach 2:  $n = 3$  and  $n_s = 5$ , called LMLS-1D-IRBFN-5-node.

Figure 3.3 presents the grid convergence study for Case 1 for the two approaches in comparison with those of FDM with central-difference scheme and the 1D-IRBFN method. The convergence study for Case 2 for the two approaches in comparison with those of the 1D-IRBFN method is shown in Figure 3.4. The convergence behaviours of FDM, 1D-IRBFN, Approach 1 and Approach 2 for Case 1 are  $O(h^{2.05})$ ,  $O(h^{3.16})$ ,  $O(h^{1.78})$  and  $O(h^{2.69})$ , respectively. The convergence behaviour of 1D-IRBFN, Approach 1 and Approach 2 for Case 2 are  $O(h^{1.98})$ ,  $O(h^{1.84})$  and  $O(h^{1.89})$ , respectively. The numerical results show that the LMLS-1D-IRBFN-5-node is much more accurate than FDM and LMLS-1D-IRBFN-3-node, and slightly better than those of its global counterpart, i.e. 1D-IRBFN method.

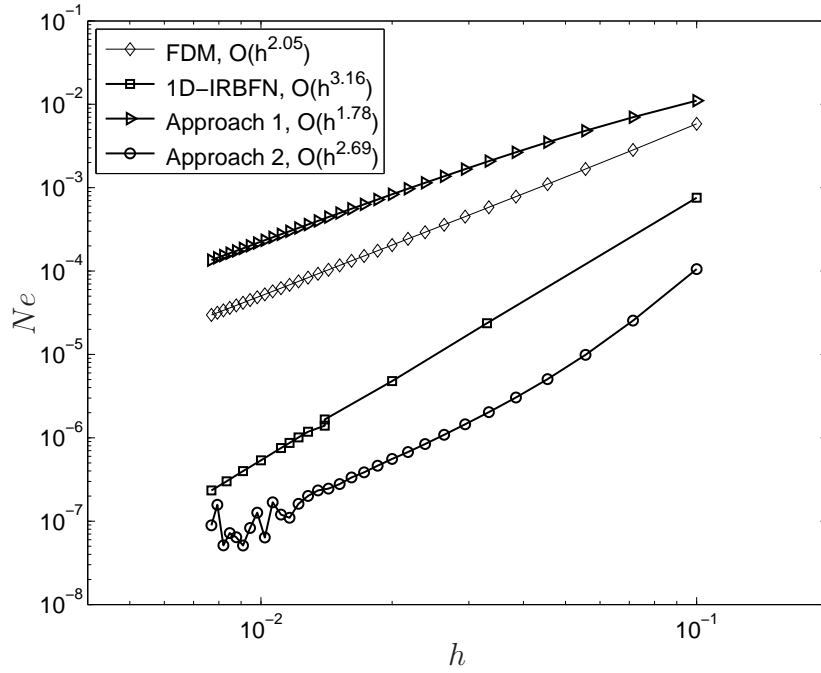


Figure 3.3: Poisson equation in a square domain subject to Dirichlet boundary conditions: convergence study for 1D-IRBFN, Approach 1 with  $\beta = 10$  and Approach 2 with  $\beta = 15$ . FDM (central difference) results are included for comparison.

Table 3.1 presents the comparison of the number of nonzero elements per row of the system matrix ( $N_{nzpr}$ ) and condition number ( $cond$ ) among the FDM, two present approaches and the 1D-IRBFN for Case 1, while Table 3.2 shows the comparison of CPU time and percentage of nonzero elements of the system matrix  $\epsilon = (N_{nz}/N_{total}) \times 100$  ( $N_{nz}$  and  $N_{total}$ : the number of nonzero elements and the total number of elements of the system matrix, respectively) among these methods. The comparison of condition number for Case 2 is given in Table 3.3. The condition numbers of 1D-IRBFN, Approach 1 and Approach 2 are of the same order of magnitude and at most one order of magnitude larger than those of FDM. The number of nonzero elements per row of the system matrix  $N_{nzpr}$  of the FDM with central-difference scheme, LMLS-1D-IRBF-3-node and LMLS-1D-IRBF-5-node methods are 5, 9, and 13, respectively and less than that of the 1D-IRBFN method. Therefore, for a given grid size, the CPU time and memory requirements of Approach 2 are larger than those of Approach

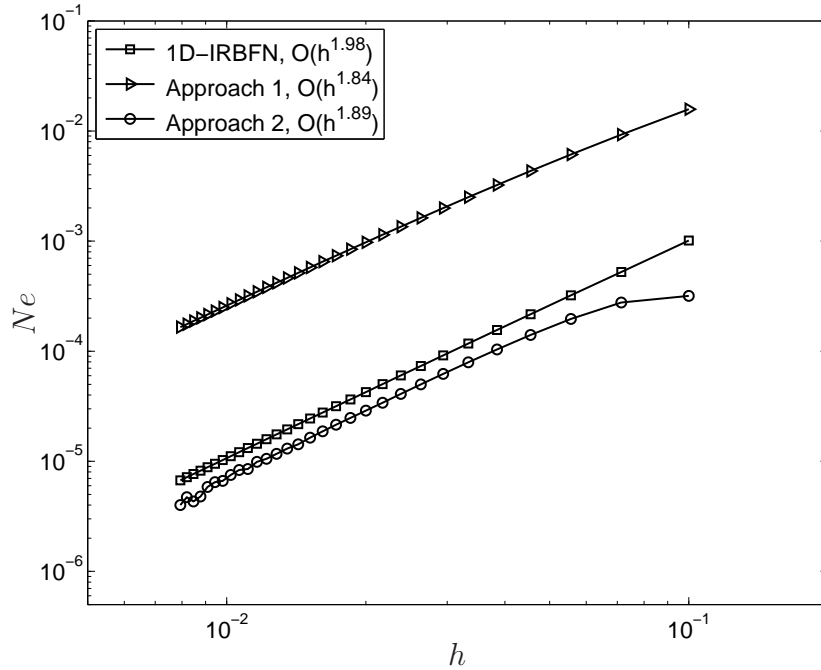


Figure 3.4: Poisson equation in a square domain subject to Dirichlet and Neumann boundary conditions: convergence study for 1D-IRBFN, Approach 1 with  $\beta = 10$  and Approach 2 with  $\beta = 5$ .

1 and FDM, and significantly less than those of the 1D-IRBFN method. For example, for a grid of  $121 \times 121$ , the CPU time and the  $\epsilon$  of Approach 2 are 38.7 times and 2.6 times larger than those of the FDM, respectively, and 89.6 times and 18.5 times less than those of the 1D-IRBFN method, respectively. It is noted that for a given grid size the present Approach 2 is slower than the FDM. However, the present Approach 2 achieves a given level of accuracy with a coarser grid and hence more efficient. For example, as shown in Figure 3.3 and Table 3.2, the present Approach 2 with grid= $21 \times 21$  yields better accuracy ( $Ne = 6.88e - 6$ ) in 0.88 seconds than the FDM with grid= $121 \times 121$  ( $Ne = 3.49e - 5$ ) in 1.74 seconds.

Table 3.1: Poisson equation in a square domain subject to Dirichlet boundary conditions: comparisons (with FDM and 1D-IRBFN) of the number of nonzero elements per row of the system matrix ( $N_{nzpr}$ ) and condition number ( $cond$ ). The system matrix is stored in a sparse matrix format.

Grid	System matrix	$N_{nzpr}$				$cond$			
		FDM	1D-IRBFN	App. 1	App. 2	FDM	1D-IRBFN	App. 1	App. 2
$11 \times 11$	$81 \times 81$	5	21	9	13	5.85E+01	1.59E+02	1.66E+02	1.55E+02
$21 \times 21$	$361 \times 361$	5	41	9	13	2.35E+02	5.85E+02	6.93E+02	6.24E+02
$31 \times 31$	$841 \times 841$	5	61	9	13	5.30E+02	1.32E+03	1.57E+03	1.41E+03
$41 \times 41$	$1521 \times 1521$	5	81	9	13	9.43E+02	2.35E+03	2.80E+03	2.50E+03
$51 \times 51$	$2401 \times 2401$	5	101	9	13	1.47E+03	3.67E+03	4.37E+03	3.91E+03
$61 \times 61$	$3481 \times 3481$	5	121	9	13	2.12E+03	5.28E+03	6.30E+03	5.63E+03
$71 \times 71$	$4761 \times 4761$	5	141	9	13	2.89E+03	7.19E+03	8.58E+03	7.66E+03
$81 \times 81$	$6241 \times 6241$	5	161	9	13	3.77E+03	9.39E+03	1.12E+04	1.00E+04
$91 \times 91$	$7921 \times 7921$	5	181	9	13	4.77E+03	1.19E+04	1.42E+04	1.27E+04
$101 \times 101$	$9801 \times 9801$	5	201	9	13	5.89E+03	1.47E+04	1.75E+04	1.56E+04
$111 \times 111$	$11881 \times 11881$	5	221	9	13	7.13E+03	1.78E+04	2.12E+04	1.89E+04
$121 \times 121$	$14161 \times 14161$	5	241	9	13	8.49E+03	2.11E+04	2.52E+04	2.25E+04

Table 3.2: Poisson equation in a square domain subject to Dirichlet boundary conditions: comparison (with FDM and 1D-IRBFN) of CPU time and percentage of nonzero elements of the system matrix ( $\epsilon$ ). Note that for a given grid size the present Approach 2 is slower than the FDM. However, the present Approach 2 achieves a given level of accuracy with a coarser grid and hence more efficient. For example, as shown in Figure 3.3, the present Approach 2 with grid= $21 \times 21$  yields better accuracy ( $Ne = 6.88e - 6$ ) in 0.88 seconds than the FDM with grid= $121 \times 121$  ( $Ne = 3.49e - 5$ ) in 1.74 seconds.

Grid	CPU time ( <i>seconds</i> ) for all shape functions				Total CPU time ( <i>seconds</i> )				$\epsilon(\%)$			
	FDM	1D-IRBFN	App. 1	App. 2	FDM	1D-IRBFN	App. 1	App. 2	FDM	1D-IRBFN	App. 1	App. 2
$11 \times 11$	0.00	0.03	0.12	0.22	0.00	0.05	0.18	0.23	5.624	20.988	9.465	12.757
$21 \times 21$	0.00	0.06	0.53	0.86	0.01	0.10	0.54	0.88	1.327	10.249	2.318	3.251
$31 \times 31$	0.01	0.39	1.31	2.05	0.02	0.58	1.33	2.08	0.578	6.778	1.021	1.447
$41 \times 41$	0.03	2.12	2.54	3.83	0.05	2.85	2.62	3.97	0.322	5.062	0.571	0.814
$51 \times 51$	0.05	8.58	4.35	6.34	0.09	10.71	4.46	6.58	0.205	4.040	0.365	0.521
$61 \times 61$	0.10	25.98	6.82	9.71	0.16	30.86	6.99	10.00	0.142	3.361	0.253	0.362
$71 \times 71$	0.18	66.68	10.01	14.02	0.25	77.73	10.24	14.49	0.104	2.878	0.185	0.266
$81 \times 81$	0.30	169.14	14.08	19.44	0.40	190.49	14.40	20.14	0.079	2.516	0.142	0.203
$91 \times 91$	0.46	462.68	19.15	26.11	0.62	502.23	19.67	26.90	0.063	2.235	0.112	0.161
$101 \times 101$	0.69	1073.42	25.36	34.27	0.88	1139.92	26.04	35.58	0.051	2.010	0.091	0.130
$111 \times 111$	1.00	2202.37	32.84	43.85	1.25	2308.72	33.61	45.60	0.042	1.826	0.075	0.108
$121 \times 121$	1.43	4959.75	41.74	55.33	1.74	5123.18	42.58	57.37	0.035	1.674	0.063	0.090

Table 3.3: Poisson equation in a square domain subject to Dirichlet and Neumann boundary conditions: comparison condition number (*cond*).

Grid	<i>cond</i>		
	1D-IRBFN	App. 1	App. 2
11 × 11	3.87E+02	3.70E+02	4.55E+02
21 × 21	1.41E+03	1.36E+03	1.63E+03
31 × 31	3.10E+03	2.94E+03	3.53E+03
41 × 41	5.45E+03	5.12E+03	6.14E+03
51 × 51	8.45E+03	7.89E+03	9.47E+03
61 × 61	1.21E+04	1.13E+04	1.35E+04
71 × 71	1.64E+04	1.52E+04	1.83E+04
81 × 81	2.14E+04	1.98E+04	2.37E+04
91 × 91	2.70E+04	2.49E+04	2.99E+04
101 × 101	3.33E+04	3.07E+04	3.68E+04
111 × 111	4.02E+04	3.70E+04	4.45E+04
121 × 121	4.78E+04	4.40E+04	5.28E+04

Approach 2 yields much more accurate results than Approach 1 and FDM with central-difference scheme and is significantly more efficient than 1D-IRBFN in terms of computational cost, as grid density increases. Therefore, the remaining examples will be investigated using Approach 2, i.e. LMLS-1D-IRBFN-5-node.

### 3.7.2 Example 2: Two-dimensional Poisson equation in a square domain with a circular hole

This example is concerned with the following 2D Poisson equation

$$\frac{\partial^2 u}{\partial x^2} + \frac{\partial^2 u}{\partial y^2} = -8\pi^2 \sin(2\pi x) \sin(2\pi y), \quad (3.84)$$

defined on a square domain with a circular hole as shown in Figure 3.5 and subject to Dirichlet boundary conditions. The problem has the following exact solution

$$u_E = \sin(2\pi x) \sin(2\pi y), \quad (3.85)$$

from which the boundary values of  $u$  can be derived.

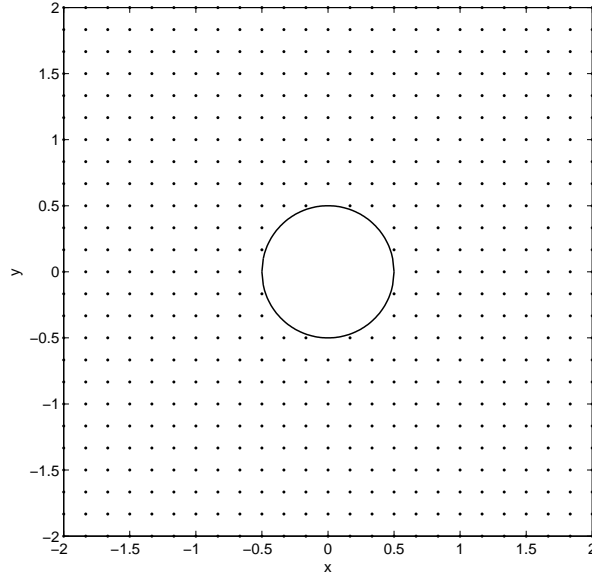


Figure 3.5: A square domain with a circular hole.

The grid convergence study for LMLS-1D-IRBFN and 1D-IRBFN methods is presented in Figure 3.6. Table 3.4 describes the relative error norms ( $Ne$ ) and condition number ( $cond$ ) of the present method in comparison with those of 1D-IRBFN method. The numerical results showed that the present method is not as accurate as the 1D-IRBFN method, but has a higher convergence rate (error norm of  $O(h^{3.70})$ ) than the 1D-IRBFN method (error norm of  $O(h^{3.00})$ ). Table 3.5 presents the comparison of CPU time and percentage of nonzero elements of the system matrix ( $\epsilon$ ) between the 1D-IRBFN and LMLS-1D-IRBFN methods. The present method is much more efficient than the 1D-IRBFN method in terms of CPU time (e.g. 101.3 times for a grid of  $129 \times 129$ ) and memory requirements (e.g. 17.2 times for a grid of  $129 \times 129$ ), thus the grid size can be refined to obtain more accurate solutions as shown in Figure 3.6.

Table 3.4: Poisson equation in a square domain with a circular hole subject to Dirichlet boundary conditions: comparison of relative error norm ( $Ne$ ) and condition number ( $cond$ ).

Grid	$Ne$		$cond$	
	1D-IRBFN	Present	1D-IRBFN	Present
$25 \times 25$	8.62E-03	4.86E-02	4.15E+02	4.28E+02
$33 \times 33$	3.43E-03	2.01E-02	6.20E+02	6.17E+02
$41 \times 41$	1.72E-03	9.12E-03	9.60E+02	8.75E+02
$49 \times 49$	9.95E-04	4.61E-03	1.35E+03	1.21E+03
$57 \times 57$	6.29E-04	2.57E-03	2.19E+03	2.21E+03
$65 \times 65$	4.27E-04	1.54E-03	2.15E+03	2.20E+03
$73 \times 73$	2.98E-04	9.80E-04	3.55E+03	3.58E+03
$81 \times 81$	2.19E-04	6.55E-04	3.58E+03	3.72E+03
$89 \times 89$	1.65E-04	4.55E-04	6.15E+03	6.29E+03
$97 \times 97$	1.28E-04	3.27E-04	6.65E+03	6.74E+03
$105 \times 105$	1.00E-04	2.41E-04	7.83E+03	8.28E+03
$113 \times 113$	8.02E-05	1.83E-04	1.35E+04	1.41E+04
$121 \times 121$	6.53E-05	1.41E-04	1.20E+04	1.28E+04
$129 \times 129$	5.39E-05	1.11E-04	1.47E+04	1.52E+04

Table 3.5: Poisson equation in a square domain with a circular hole subject to Dirichlet boundary conditions: comparison of CPU time and percentage of nonzero elements of the system matrix ( $\epsilon$ ).

Grid	CPU time ( <i>seconds</i> )		$\epsilon$ (%)	
	1D-IRBFN	Present	1D-IRBFN	Present
$25 \times 25$	0.39	1.71	7.579	2.323
$33 \times 33$	0.89	2.71	5.739	1.325
$41 \times 41$	3.18	4.41	4.600	0.851
$49 \times 49$	9.68	6.65	3.824	0.591
$57 \times 57$	24.72	9.49	3.276	0.434
$65 \times 65$	55.88	13.02	2.871	0.333
$73 \times 73$	115.22	17.27	2.548	0.263
$81 \times 81$	222.04	22.56	2.295	0.213
$89 \times 89$	464.42	28.76	2.085	0.176
$97 \times 97$	946.15	35.96	1.913	0.148
$105 \times 105$	1793.67	44.39	1.766	0.126
$113 \times 113$	3153.54	54.16	1.639	0.109
$121 \times 121$	5140.94	65.55	1.530	0.095
$129 \times 129$	7937.85	78.39	1.435	0.083

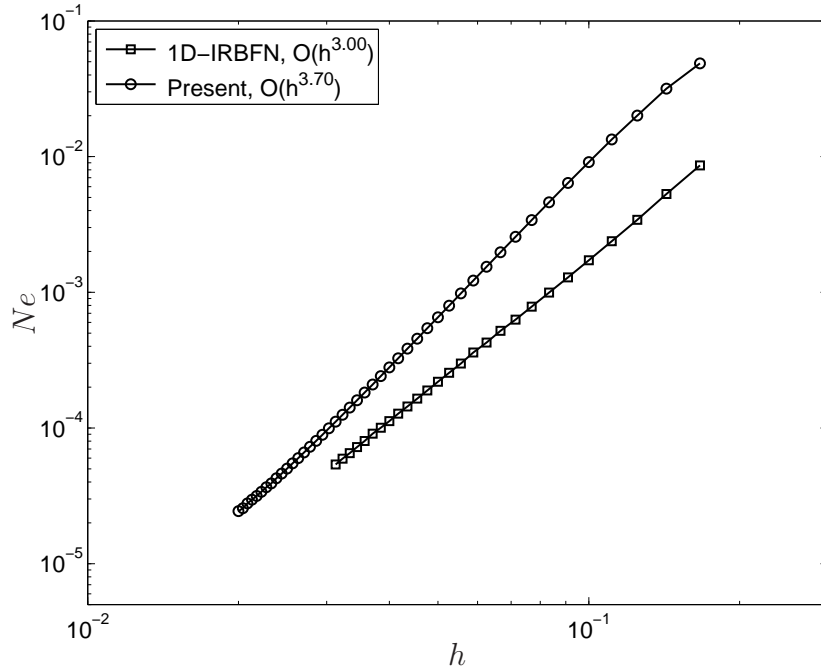


Figure 3.6: Poisson equation in a square domain with a circular hole subject to Dirichlet boundary conditions: convergence study for 1D-IRBFN and the present method (LMLS-1D-IRBFN-5-node) with  $\beta = 15$ .

In comparing the convergence behaviours in Example 1 (homogeneous Poisson equation on simply-connected domain) and Example 2 (non-homogeneous Poisson equation on multiply-connected domain), it is observed that the overall convergence rate of Approach 2 for the former is 2.69 and that for the latter is 3.70. At first glance, the results might seem strange. However, it is observed that to achieve similar accuracy ( $Ne$  of  $O(10^{-5})$ ), the convergence rates are very similar, i.e. 3.72 for Example 1 and 3.70 for Example 2. In Example 1, the shape of solution is relatively simple and the method can achieve even higher accuracy ( $Ne$  of  $O(10^{-7})$ ). However, at this higher level of accuracy, the local convergence rate decreases, causing a lower overall convergence rate as described above.

### 3.7.3 Example 3: Lid-driven cavity flow

The cavity is taken to be a unit square with the lid sliding from left to right at a unit velocity as shown in Figure 3.7. The boundary conditions for stream function  $\psi$  are defined by

$$\psi = 0, \quad \text{on } x = 0, x = 1, y = 0, y = 1, \quad (3.86)$$

$$\frac{\partial \psi}{\partial x} = 0, \quad \text{on } x = 0, x = 1, \quad (3.87)$$

$$\frac{\partial \psi}{\partial y} = 0, \quad \text{on } y = 0, \quad (3.88)$$

$$\frac{\partial \psi}{\partial y} = 1, \quad \text{on } y = 1. \quad (3.89)$$

It is noted that only the Dirichlet boundary conditions (3.86) are used for solving (3.69), while the Neumann boundary conditions (3.87)-(3.89) are used to derive computational vorticity boundary conditions for solving (3.70).

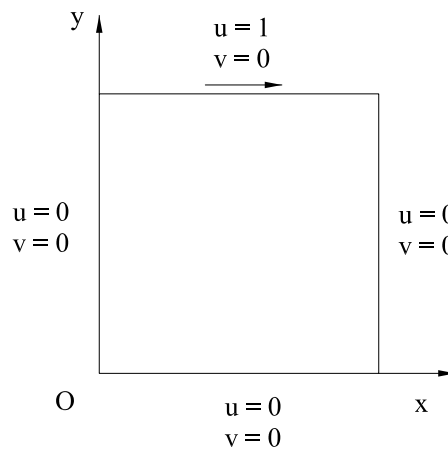


Figure 3.7: Lid-driven cavity flow: problem geometry and boundary conditions.

It is well-known that the major difficulties of lid-driven cavity flow simulation are: (i) the presence of singularities at two of the corners, which makes it difficult to predict the solution accurately; and (ii) the dominant convection terms, when dealing with high  $Re$ , which can cause oscillatory solutions if an improper scheme is used or computational grids are not sufficiently refined. The

grid convergence study is first conducted for the lid-driven cavity flow problem with  $Re$  of 1000 using following two approaches.

- Approach 1: The convection terms are calculated using LMLS-1D-IRBFN technique.
- Approach 2: The convection terms are calculated using 1D-IRBFN technique.

Table 3.6 shows the grid convergence study of the extrema of the horizontal and vertical velocity profiles along the center lines of the cavity for Approach 1 in comparison with the results of FDMs (Ghia et al., 1982; Bruneau and Jouron, 1990), 1D-IRBFN (Mai-Duy and Tran-Cong, 2009b) and spectral benchmark solutions (Botella and Peyret, 1998). The second-order accurate central finite-difference approximation was employed to approximate the linear terms in both FDMs mentioned above (Ghia et al., 1982; Bruneau and Jouron, 1990), while the nonlinear convection terms were discretised by using a first-order accurate upwind difference scheme including its second-order accurate term as a deferred correction in FDM (Ghia et al., 1982) and uncentered second-order differences in FDM (Bruneau and Jouron, 1990). In Table 3.6, the percentage errors ( $\varepsilon = (V_m - V_s) \times 100/V_s$ ) of the extremal velocities ( $V_m$ ) based on the corresponding spectral benchmark solutions ( $V_s$ ) (Botella and Peyret, 1998) are given. It can be seen that these errors reduce with increasing grid densities. The orders of convergence are 2.42, 2.61 and 2.92 for the minimum horizontal velocity  $u_{min}$ , the maximum vertical velocity  $v_{max}$  and the minimum vertical velocity  $v_{min}$  along the center lines, respectively. The present results for a grid of  $101 \times 101$  are more accurate than those of FDMs with more refined grids (Ghia et al., 1982; Bruneau and Jouron, 1990), but less than those of 1D-IRBFN (Mai-Duy and Tran-Cong, 2009b). Table 3.7 describes comparisons of the number of nonzero elements per row of the system matrix ( $N_{nzpr}$ ), number of iterations ( $N_{iteration}$ ) and total CPU time ( $T_{total}$ ) required to obtain the converged solution

with  $TOL = 10^{-12}$ . The time step  $\Delta t$  is set to be  $5 \times 10^{-3}$  for all cases. Note that for a given grid size the present approach is slower than the FDM. However, the present approach achieves a given level of accuracy with a coarser grid and hence more efficient. For example, as shown in Tables 3.6 and 3.7, the present approach with grid= $81 \times 81$  yields better accuracy in 1559.77 seconds than the FDM with grid= $129 \times 129$  in 1733.02 seconds.

The corresponding grid convergence study for Approach 2 is given in Table 3.8. The orders of convergence are 3.80, 3.26 and 4.26 for  $u_{min}$ ,  $v_{max}$  and  $v_{min}$ , respectively. It is interesting to see that Approach 2 yields more accurate results than Approach 1 and the 1D-IRBFN method, and the convergence orders of Approach 2 are higher than those of Approach 1. Approach 2 is employed to study the cases with high Reynolds numbers ( $Re = 3200$  and  $7500$ ). The contours of stream function and vorticity of the flow field inside the cavity at  $Re = 1000, 3200$  and  $7500$  are shown in Figure 3.8. The vertical and horizontal velocities along the horizontal and vertical center lines at  $Re = 1000, 3200$  and  $7500$  are given in Figure 3.9. These figures show that the current results are in good agreement with benchmark solutions of Ghia et al. (1982) and Botella and Peyret (1998).

Table 3.6: Lid-driven cavity flow,  $Re = 1000$ : the grid convergence study and comparison of extrema of velocity profiles along the center lines. The convection terms are calculated using LMLS-1D-IRBFN technique. Note that “Error” is relative to a Benchmark solution.

	Grid	$u_{min}$	Error (%)	$y$	$v_{max}$	Error (%)	$x$	$v_{min}$	Error (%)	$x$
Present	$21 \times 21$	-0.33342	14.193	0.333	0.27403	27.301	0.220	-0.34690	34.184	0.827
	$31 \times 31$	-0.33043	14.962	0.202	0.32097	14.848	0.172	-0.43390	17.678	0.888
	$41 \times 41$	-0.35408	8.876	0.183	0.34304	8.993	0.165	-0.47541	9.804	0.901
	$51 \times 51$	-0.36903	5.029	0.177	0.35730	5.211	0.162	-0.49891	5.345	0.906
	$61 \times 61$	-0.37750	2.848	0.174	0.36561	3.006	0.160	-0.51164	2.930	0.907
	$71 \times 71$	-0.38218	1.644	0.173	0.37027	1.769	0.159	-0.51846	1.635	0.908
	$81 \times 81$	-0.38478	0.976	0.172	0.37290	1.072	0.159	-0.52215	0.935	0.909
	$91 \times 91$	-0.38626	0.595	0.172	0.37441	0.670	0.158	-0.52420	0.547	0.909
	$101 \times 101$	-0.38712	0.373	0.172	0.37531	0.432	0.158	-0.52536	0.326	0.909
1D-IRBFN (Mai-Duy and Tran-Cong, 2009b)	$101 \times 101$	-0.38772	0.218	0.172	0.37601	0.247	0.158	-0.52598	0.208	0.909
FDM ( $\psi - \omega$ ) (Ghia et al., 1982)	$129 \times 129$	-0.38289	1.462	0.172	0.37095	1.589	0.156	-0.51550	2.197	0.906
FDM ( $\mathbf{u} - p$ ) (Bruneau and Jouron, 1990)	$256 \times 256$	-0.37640	3.132	0.160	0.36650	2.770	0.152	-0.52080	1.192	0.910
Benchmark (Botella and Peyret, 1998)		-0.38857		0.172	0.37694		0.158	-0.52708		0.909
Present	Order of convergence		2.42			2.61			2.92	

Table 3.7: Lid-driven cavity flow,  $Re = 1000$ : comparisons of the number of nonzero elements per row of the system matrix ( $N_{nzpr}$ ), number of iterations ( $N_{iteration}$ ) and total CPU time ( $T_{total}$ ) required to obtain the converged solution with  $TOL = 10^{-12}$ . The time step  $\Delta t$  is set to be  $5 \times 10^{-3}$  for all cases. Note that for a given grid size the present approach is slower than the FDM. However, the present approach achieves a given level of accuracy with a coarser grid and hence more efficient. For example, as shown in Table 3.6, the present approach with grid= $81 \times 81$  yields better accuracy in 1559.77 seconds than the FDM with grid= $129 \times 129$  in 1733.02 seconds.

Grid	System matrix	FDM			Present		
		$N_{nzpr}$	$N_{iteration}$	$T_{total}(s)$	$N_{nzpr}$	$N_{iteration}$	$T_{total}(s)$
$21 \times 21$	$361 \times 361$	5	52207	36.46	13	51088	43.66
$31 \times 31$	$841 \times 841$	5	44914	45.67	13	40590	63.48
$41 \times 41$	$1521 \times 1521$	5	41703	68.59	13	43047	220.69
$51 \times 51$	$2401 \times 2401$	5	36467	148.10	13	44513	452.89
$61 \times 61$	$3481 \times 3481$	5	39591	250.27	13	45239	781.17
$71 \times 71$	$4761 \times 4761$	5	41803	354.93	13	45569	884.19
$81 \times 81$	$6241 \times 6241$	5	42893	482.21	13	45714	1559.77
$91 \times 91$	$7921 \times 7921$	5	43568	679.77	13	45779	2356.15
$101 \times 101$	$9801 \times 9801$	5	44028	898.53	13	45807	2964.84
$111 \times 111$	$9801 \times 9801$	5	44360	1207.33	13	-	-
$121 \times 121$	$9801 \times 9801$	5	44608	1433.07	13	-	-
$129 \times 129$	$9801 \times 9801$	5	44764	1733.02	13	-	-

Table 3.8: Lid-driven cavity flow,  $Re = 1000$ : the grid convergence study and comparison of extrema of horizontal and vertical velocity profiles along the center lines. The convection terms are calculated using 1D-IRBFN technique. Note that “Error” is relative to a Benchmark solution.

	Grid	$u_{min}$	Error (%)	$y$	$v_{max}$	Error (%)	$x$	$v_{min}$	Error (%)	$x$
Present	$21 \times 21$	-0.30543	21.397	0.223	0.29460	21.844	0.181	-0.39550	24.963	0.866
	$31 \times 31$	-0.35522	8.583	0.179	0.34326	8.936	0.166	-0.47452	9.971	0.900
	$41 \times 41$	-0.37207	4.245	0.173	0.35938	4.660	0.162	-0.50276	4.615	0.906
	$51 \times 51$	-0.38005	2.193	0.172	0.36744	2.519	0.160	-0.51576	2.147	0.908
	$61 \times 61$	-0.38423	1.117	0.171	0.37183	1.356	0.159	-0.52208	0.949	0.909
	$71 \times 71$	-0.38642	0.552	0.171	0.37421	0.725	0.158	-0.52512	0.371	0.909
	$81 \times 81$	-0.38756	0.259	0.171	0.37549	0.385	0.158	-0.52655	0.100	0.909
	$91 \times 91$	-0.38815	0.108	0.171	0.37618	0.203	0.158	-0.52720	0.022	0.909
	$101 \times 101$	-0.38845	0.032	0.171	0.37655	0.104	0.158	-0.52746	0.073	0.909
1D-IRBFN (Mai-Duy and Tran-Cong, 2009b)	$101 \times 101$	-0.38772	0.218	0.172	0.37601	0.247	0.158	-0.52598	0.208	0.909
FDM ( $\psi - \omega$ ) (Ghia et al., 1982)	$129 \times 129$	-0.38289	1.462	0.172	0.37095	1.589	0.156	-0.51550	2.197	0.906
FDM ( $\mathbf{u} - p$ ) (Bruneau and Jouron, 1990)	$256 \times 256$	-0.37640	3.132	0.160	0.36650	2.770	0.152	-0.52080	1.192	0.910
Benchmark (Botella and Peyret, 1998)		-0.38857		0.172	0.37694		0.158	-0.52708		0.909
Present	Order of convergence		3.80			3.26			4.26	

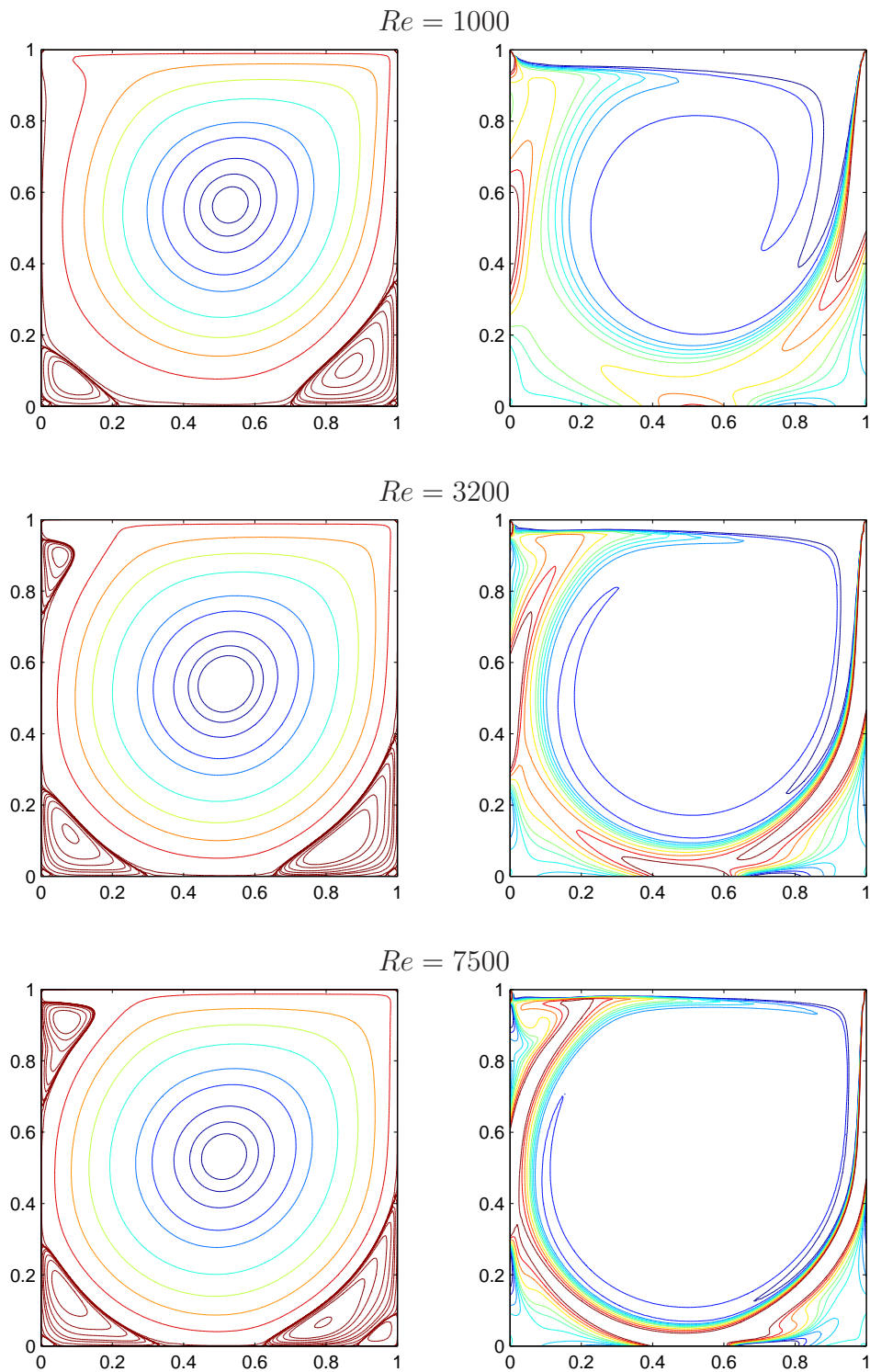


Figure 3.8: Lid-driven cavity flow: contours of stream function (left) and vorticity (right) for different Reynolds numbers  $Re = 1000, 3200$  and  $7500$ , using grids of  $101 \times 101$ ,  $121 \times 121$ , and  $151 \times 151$ , respectively.

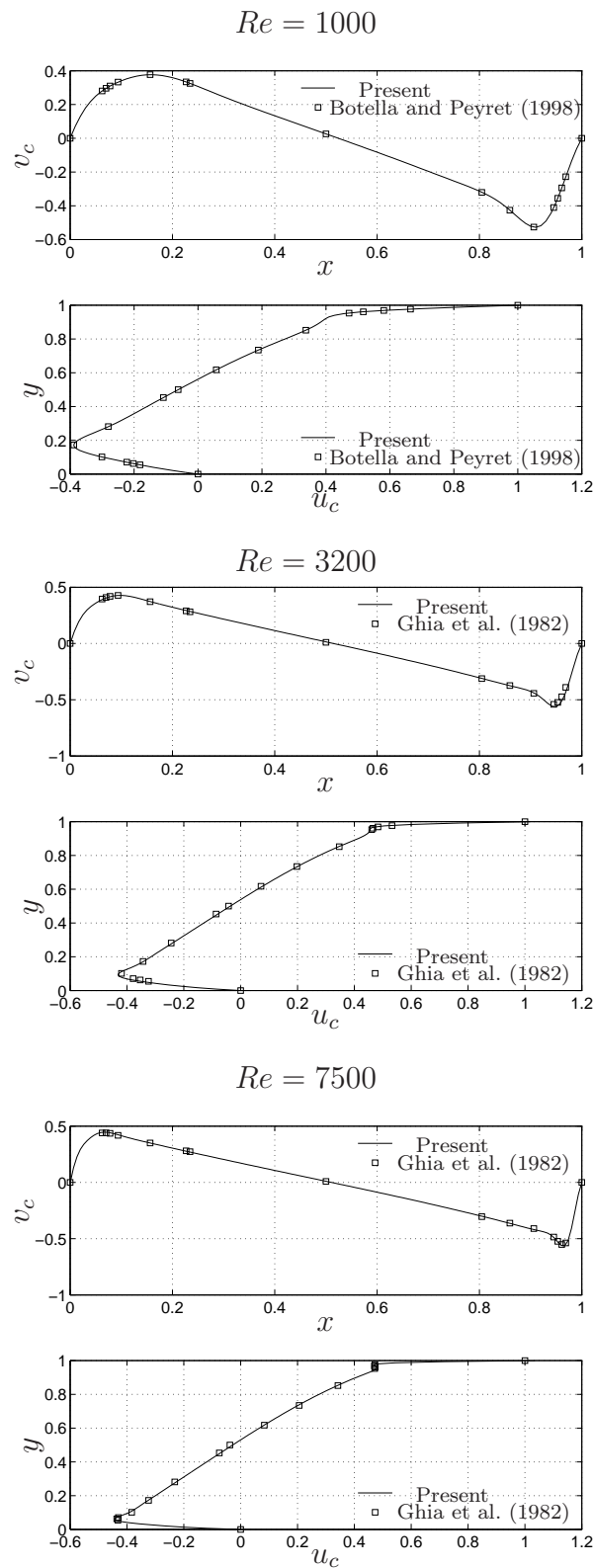


Figure 3.9: Lid-driven cavity flow: comparison of profiles of vertical and horizontal velocities along the horizontal and vertical center lines of the cavity for different Reynolds numbers  $Re = 1000, 3200$  and  $7500$ , using grids of  $101 \times 101$ ,  $121 \times 121$ , and  $151 \times 151$ , respectively.

### 3.7.4 Example 4: Flow past a circular cylinder

The steady flow past a circular cylinder at low  $Re$  numbers are considered in this section, where  $Re = U_0 D / \nu$ ,  $U_0$  is the far-field inlet velocity taken to be 1,  $D$  the diameter of the cylinder taken to be 1,  $\nu$  the kinematic viscosity. The top, bottom, inlet and outlet boundaries are positioned at a distance of  $20D$ ,  $20D$ ,  $10D$  and  $30D$  away from the cylinder, respectively, as shown in Figure 3.10. These distances are large enough to assume that the far-field flow behaves as a potential flow (Kim et al., 2007) and the far-field stream function  $\psi^{far}$  can be defined by

$$\psi^{far} = U_0 y \left( 1 - \frac{D^2}{4(x^2 + y^2)} \right). \quad (3.90)$$

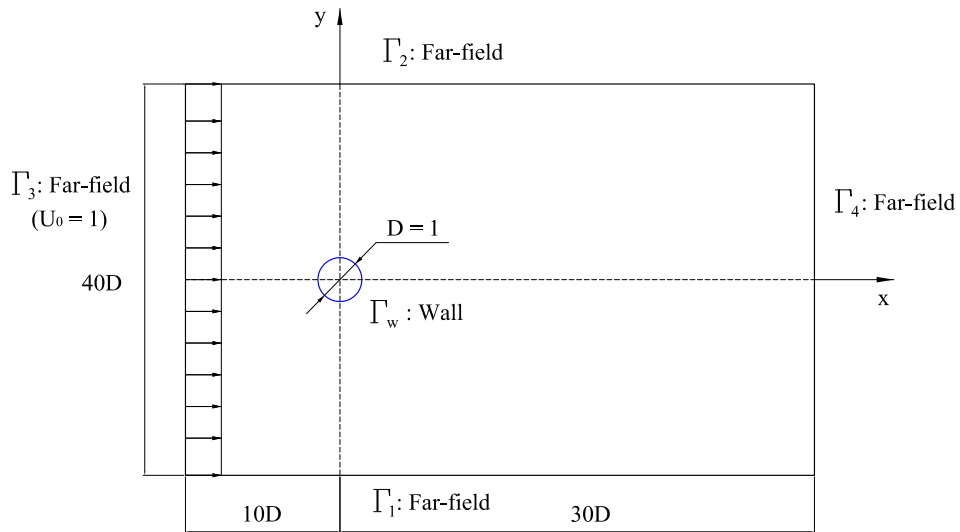


Figure 3.10: Flow past a circular cylinder: problem geometry and boundary conditions.

The boundary conditions for stream function and vorticity are given by

$$\psi = \psi^{far}, \quad \omega = 0, \quad \text{on } \Gamma_1, \Gamma_2, \Gamma_3, \quad (3.91)$$

$$\frac{\partial \psi}{\partial x} = 0, \quad \frac{\partial \omega}{\partial x} = 0, \quad \text{on } \Gamma_4, \quad (3.92)$$

$$\psi = 0, \quad \frac{\partial \psi}{\partial n} = 0, \quad \text{on } \Gamma_w. \quad (3.93)$$

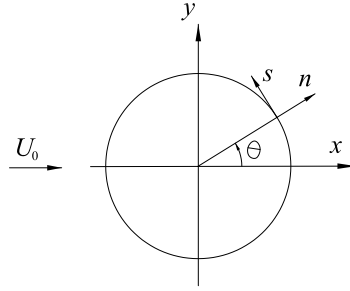


Figure 3.11: Circular cylinder and associated coordinate systems.

where  $n$  is the direction normal to the cylinder surface as shown in Figure 3.11. The values of the vorticity on the circular boundary  $\Gamma_w$  can be computed as

$$\omega_w = - \left( \frac{\partial^2 \psi_w}{\partial x^2} + \frac{\partial^2 \psi_w}{\partial y^2} \right) \quad (3.94)$$

where the subscript  $w$  is used to denote quantities on the circular boundary. A formula of Le-Cao et al. (2009) is employed here to derive the vorticity boundary conditions at boundary points on  $x$ - and  $y$ -grid lines as follows.

$$\omega_w^{(x)} = - \left[ 1 + \left( \frac{t_x}{t_y} \right)^2 \right] \frac{\partial^2 \psi_w}{\partial x^2} - q_y, \quad (3.95)$$

$$\omega_w^{(y)} = - \left[ 1 + \left( \frac{t_y}{t_x} \right)^2 \right] \frac{\partial^2 \psi_w}{\partial y^2} - q_x, \quad (3.96)$$

where  $q_x$  and  $q_y$  are known quantities defined by

$$q_x = - \frac{t_y}{t_x^2} \frac{\partial^2 \psi_w}{\partial y \partial s} + \frac{1}{t_x} \frac{\partial^2 \psi_w}{\partial x \partial s}, \quad (3.97)$$

$$q_y = - \frac{t_x}{t_y^2} \frac{\partial^2 \psi_w}{\partial x \partial s} + \frac{1}{t_y} \frac{\partial^2 \psi_w}{\partial y \partial s}, \quad (3.98)$$

in which  $t_x = \partial x / \partial s$ ,  $t_y = \partial y / \partial s$  and  $s$  is the direction tangential to the cylinder surface (Figure 3.11).

### Calculation of drag and pressure coefficients

For viscous flow, the forces acting on the body come from two sources including pressure and friction. For the case of flow past a circular cylinder, the drag  $F_D$  and its coefficient  $C_D$  can be defined by

$$F_D = R \int_0^{2\pi} \left( \mu R \frac{\partial \omega}{\partial n} - \mu \omega \right) \sin \theta d\theta, \quad (3.99)$$

$$C_D = \frac{F_D}{\rho U_0^2 R}, \quad (3.100)$$

where  $R$  is the radius of the cylinder;  $\rho$  fluid density; and  $\mu$  the dynamic viscosity. The dimensionless pressure coefficient is given by

$$C_p(\theta) = \frac{p(\theta) - p_0}{1/2\rho U_0^2}, \quad (3.101)$$

where  $p_0$  is the far-field inlet pressure; and  $p(\theta)$  the pressure on the cylinder surface at angle  $\theta$ , evaluated as (Muralidhar and Sundararajan, 1995)

$$p(\theta) = (p_0 + 1/2\rho U_0^2) - \int_R^{d_0} \left( \frac{\mu}{r} \frac{\partial \omega}{\partial \theta} \right) \Big|_{\theta=0} dr - R \int_0^\theta \mu \frac{\partial \omega}{\partial n} \Big|_{r=R} d\theta, \quad (3.102)$$

in which  $d_0$  is the distance from the cylinder center to the inlet boundary.

### Non-overlapping domain decomposition technique

As described in Section 3.5, the relevant governing equations are of Poisson type. Thus, consider the following Poisson problem in a domain  $\Omega$  with Dirichlet

boundary condition on the boundary  $\partial\Omega$

$$\Delta u = f(x, y) \quad \text{in } \Omega \quad (3.103)$$

$$u = b \quad \text{on } \partial\Omega \quad (3.104)$$

It is noted that the Neumann boundary conditions (3.92) can be imposed directly through the conversion process (3.26)-(3.29). Therefore, we just need to consider the Poisson problem with Dirichlet boundary condition here.

Without loss of generality, the domain of interest  $\Omega$  is partitioned into just two non-overlapping subdomains  $\Omega_1$  and  $\Omega_2$  as shown in Figure 3.12. The Poisson problem can be reformulated in the equivalent multi-domain form as follows (Quarteroni and Valli, 1999).

$$\Delta u^{[1]} = f^{[1]} \quad \text{in } \Omega_1 \quad (3.105)$$

$$u = b^{[1]} \quad \text{on } \partial\Omega_1 \cap \partial\Omega \quad (3.106)$$

$$\Delta u^{[2]} = f^{[2]} \quad \text{in } \Omega_2 \quad (3.107)$$

$$u = b^{[2]} \quad \text{on } \partial\Omega_2 \cap \partial\Omega \quad (3.108)$$

$$u^{[1]} = u^{[2]} \quad \text{on } \Gamma \quad (3.109)$$

$$\frac{\partial u^{[1]}}{\partial n} = \frac{\partial u^{[2]}}{\partial n} \quad \text{on } \Gamma \quad (3.110)$$

where  $\Gamma$  is the interface between  $\Omega_1$  and  $\Omega_2$ ;  $\partial\Omega_1$  and  $\partial\Omega_2$  the boundaries of the subdomains  $\Omega_1$  and  $\Omega_2$ , respectively; and the superscript  $[\cdot]$  denotes a subdomain. Equations (3.109) and (3.110) are the transmission conditions for  $u^{[1]}$  and  $u^{[2]}$  on the interface  $\Gamma$ . By solving the system of Equations (3.105)-(3.110), one can obtain the interface values  $u_\Gamma$ , and the subdomain solutions  $u^{[1]}$  and  $u^{[2]}$ .

We now describe an algorithm for solving the system of Equations (3.105)-(3.110) as follows. Let the subscripts *ip*, *bp* and *fb* represent the location indices

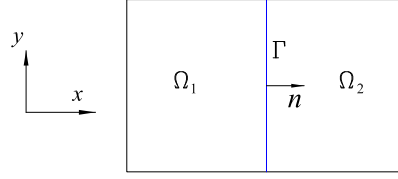


Figure 3.12: Non-overlapping partition of the domain  $\Omega$  into two subdomains  $\Omega_1$  and  $\Omega_2$ .

of interior points, known boundary points and interface points over a subdomain, respectively;  $N$ ,  $N_{ip}$ ,  $N_{bp}$  and  $N_{fp}$  are the total number of points, the number of interior points, known boundary points and interface points of a subdomain, respectively.

System of Equations (3.105)-(3.110) are written in matrix form as follows.

$$\tilde{E}^{[1]}\tilde{u}^{[1]} = RHS^{[1]}, \quad (3.111)$$

$$\tilde{u}_{(bp)}^{[1]} = u_b^{[1]}, \quad (3.112)$$

$$\tilde{E}^{[2]}\tilde{u}^{[2]} = RHS^{[2]}, \quad (3.113)$$

$$\tilde{u}_{(bp)}^{[2]} = u_b^{[2]}, \quad (3.114)$$

$$\tilde{u}_{(fp)}^{[1]} = \tilde{u}_{(fp)}^{[2]} = u_\Gamma, \quad (3.115)$$

$$D^{[1]}\tilde{u}^{[1]} = D^{[2]}\tilde{u}^{[2]}, \quad (3.116)$$

where  $\tilde{E}^{[1]}$  and  $\tilde{E}^{[2]}$  are the known matrices of dimension  $(N_{ip}^{[1]} \times N^{[1]})$  and  $(N_{ip}^{[2]} \times N^{[2]})$ , respectively;  $\tilde{u}^{[1]}$  and  $\tilde{u}^{[2]}$  field variable vectors of length  $N^{[1]}$  and  $N^{[2]}$ , respectively;  $RHS^{[1]}$ ,  $RHS^{[2]}$ ,  $u_b^{[1]}$  and  $u_b^{[2]}$  the known vectors of length  $N_{ip}^{[1]}$ ,  $N_{ip}^{[2]}$ ,  $N_{bp}^{[1]}$  and  $N_{bp}^{[2]}$ , respectively;  $u_\Gamma$  unknown vector of length  $N_{fp}$ ; and  $D^{[1]}$  and  $D^{[2]}$  the known matrices of dimension  $(N_{fp} \times N^{[1]})$  and  $(N_{fp} \times N^{[2]})$ , respectively.

From (3.111), (3.112) and (3.115), one is able to obtain the following expression

$$\begin{bmatrix} \tilde{E}_{(:,ip)}^{[1]} & \tilde{E}_{(:,bp)}^{[1]} & \tilde{E}_{(:,fp)}^{[1]} \end{bmatrix} \begin{pmatrix} \tilde{u}_{(ip)}^{[1]} \\ u_b^{[1]} \\ u_\Gamma \end{pmatrix} = RHS^{[1]} \quad (3.117)$$

or

$$\tilde{u}_{(ip)}^{[1]} = A^{[1]} + B^{[1]}u_\Gamma \quad (3.118)$$

where

$$A^{[1]} = \left( \tilde{E}_{(:,ip)}^{[1]} \right)^{-1} \left( RHS^{[1]} - \tilde{E}_{(:,bp)}^{[1]} u_b^{[1]} \right); \quad (3.119)$$

$$B^{[1]} = - \left( \tilde{E}_{(:,ip)}^{[1]} \right)^{-1} \tilde{E}_{(:,fp)}^{[1]}. \quad (3.120)$$

Similarly, from (3.113), (3.114) and (3.115), the interior values of the subdomain  $\Omega_2$  is given by

$$\tilde{u}_{(ip)}^{[2]} = A^{[2]} + B^{[2]}u_\Gamma \quad (3.121)$$

where

$$A^{[2]} = \left( \tilde{E}_{(:,ip)}^{[2]} \right)^{-1} \left( RHS^{[2]} - \tilde{E}_{(:,bp)}^{[2]} u_b^{[2]} \right); \quad (3.122)$$

$$B^{[2]} = - \left( \tilde{E}_{(:,ip)}^{[2]} \right)^{-1} \tilde{E}_{(:,fp)}^{[2]}. \quad (3.123)$$

Equation (3.116) can be expressed as

$$\begin{bmatrix} D_{(:,ip)}^{[1]} & D_{(:,bp)}^{[1]} & D_{(:,fp)}^{[1]} \end{bmatrix} \begin{pmatrix} \tilde{u}_{(ip)}^{[1]} \\ u_b^{[1]} \\ u_\Gamma \end{pmatrix} = \begin{bmatrix} D_{(:,ip)}^{[2]} & D_{(:,bp)}^{[2]} & D_{(:,fp)}^{[2]} \end{bmatrix} \begin{pmatrix} \tilde{u}_{(ip)}^{[2]} \\ u_b^{[2]} \\ u_\Gamma \end{pmatrix}. \quad (3.124)$$

By substituting Equations (3.118) and (3.121) into (3.124), the interface values  $u_\Gamma$  are determined as

$$u_\Gamma = \frac{-D_{(:,ip)}^{[1]}A^{[1]} - D_{(:,bp)}^{[1]}u_b^{[1]} + D_{(:,ip)}^{[2]}A^{[2]} + D_{(:,bp)}^{[2]}u_b^{[2]}}{D_{(:,ip)}^{[1]}B^{[1]} + D_{(:,fp)}^{[1]} - D_{(:,ip)}^{[2]}B^{[2]} - D_{(:,fp)}^{[2]}}. \quad (3.125)$$

By substituting (3.125) into (3.118) and (3.121), one can obtain the subdomain solutions  $\tilde{u}_{(ip)}^{[1]}$  and  $\tilde{u}_{(ip)}^{[2]}$ .

The combination of LMLS-1D-IRBFN and a domain decomposition technique is developed to handle this large scale problem using a PC with 2.99 *GHz* CPU and 3.25 *GB* of RAM. The computational domain is discretised using Cartesian grids as shown in Figure 3.13. The grid convergence study of vorticity distribution on the cylinder surface for *Re* number of 40 is presented in Figure 3.14. It can be seen that the current simulations converge with increasing grid densities. The results obtained for the grids of  $151 \times 151$  and  $167 \times 167$  are in good agreement with those of Kim et al. (2007) and Dennis and Chang (1970). Therefore, the grid of  $151 \times 151$  is then used to investigate the flow field with the other values of *Re* numbers (i.e. 5, 10 and 20). It is noted that when the flow reaches the steady state, a pair of vortices and the separated region behind the cylinder are formed. The length of the wake is measured from the rear of the cylinder to the end of the separated region, while the angle of separation is defined at the point where the vorticity vanishes. Table 3.9 presents the length of the wake behind the cylinder ( $L_{sep}$ ), the separation angle ( $\theta_{sep}$ ) and the drag coefficient ( $C_D$ ) for *Re* numbers of 5, 10, 20 and 40. The comparisons of vorticity and pressure coefficient distribution on the cylinder surface in the case of *Re* numbers of 5, 10, 20 and 40 are given in Figures 3.15 and 3.16, respectively. It can be seen that the present numerical results are in good agreement with other published results. The contours of stream function and vorticity of the flow field around the cylinder are shown in Figure 3.17.

Table 3.9: Flow past a circular cylinder: comparison of the wake length ( $L_{sep}$ ), the separation angle ( $\theta_{sep}$ ) and the drag coefficient ( $C_D$ ) for  $Re = 5, 10, 20$  and  $40$ , using a grid of  $151 \times 151$ .

$Re$	Source	$L_{sep}$	$\theta_{sep}$	$C_D$
5	Dennis and Chang (1970)	-	-	4.116
	Kim et al. (2007)	-	-	4.282
	Present	-	-	4.108
10	Dennis and Chang (1970)	0.265	29.6	2.846
	Ding et al. (2004)	0.252	30.0	3.070
	Kim et al. (2007)	0.281	29.5	2.920
	Present	0.27	30.1	2.829
20	Dennis and Chang (1970)	0.94	43.7	2.045
	Ding et al. (2004)	0.93	44.1	2.180
	Kim et al. (2007)	0.91	43.7	2.017
	Present	0.92	43.6	2.010
40	Dennis and Chang (1970)	2.345	53.8	1.522
	Ding et al. (2004)	2.20	53.5	1.713
	Kim et al. (2007)	2.187	55.1	1.640
	Present	2.31	53.7	1.542

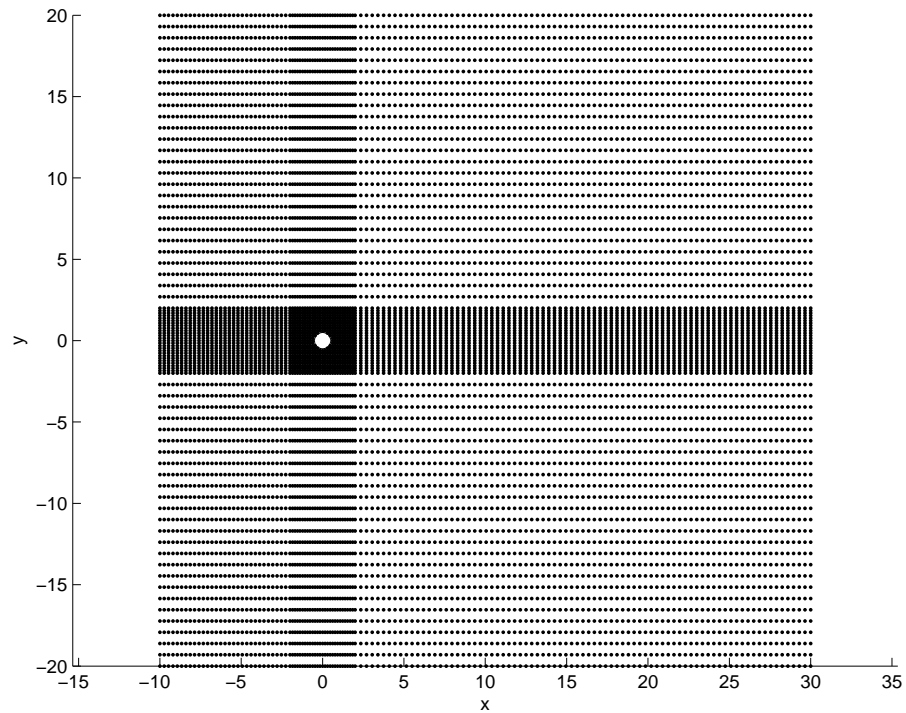
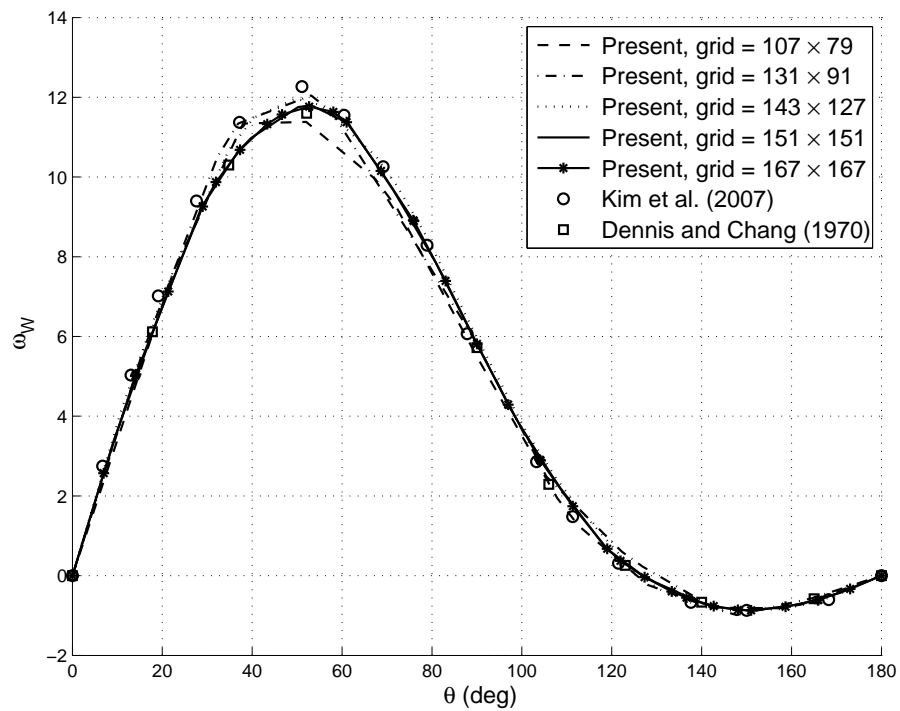


Figure 3.13: Flow past a circular cylinder: grid configuration.

Figure 3.14: Flow past a circular cylinder: grid convergence study,  $Re = 40$ .

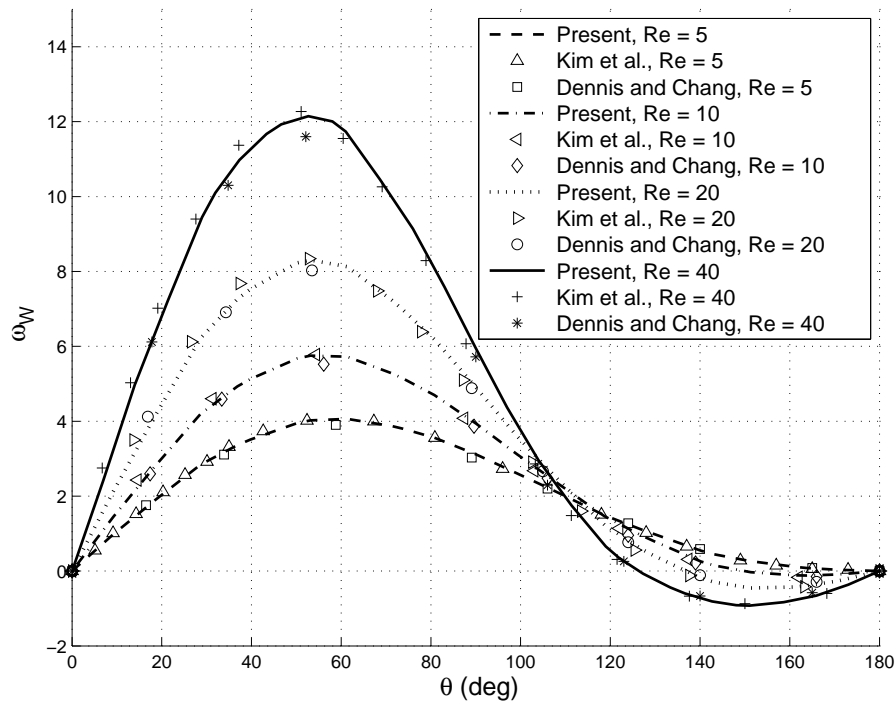


Figure 3.15: Flow past a circular cylinder: comparison of vorticity on the circular cylinder in the cases of  $Re = 5, 10, 20$  and  $40$ , using a grid of  $151 \times 151$ .

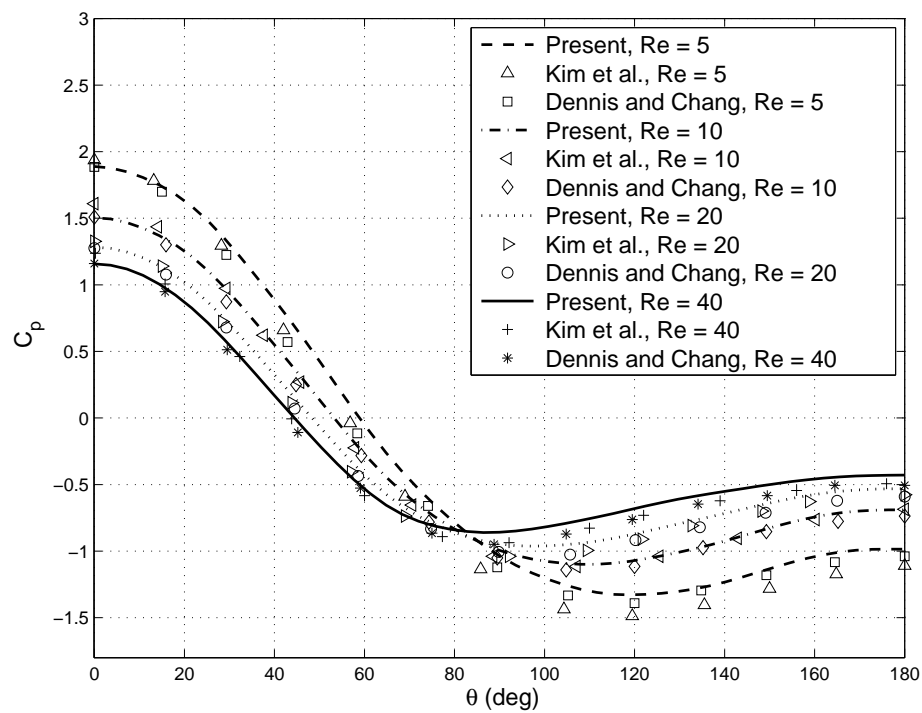


Figure 3.16: Flow past a circular cylinder: comparison of pressure coefficient on the circular cylinder in the cases of  $Re = 5, 10, 20$  and  $40$ , using a grid of  $151 \times 151$ .

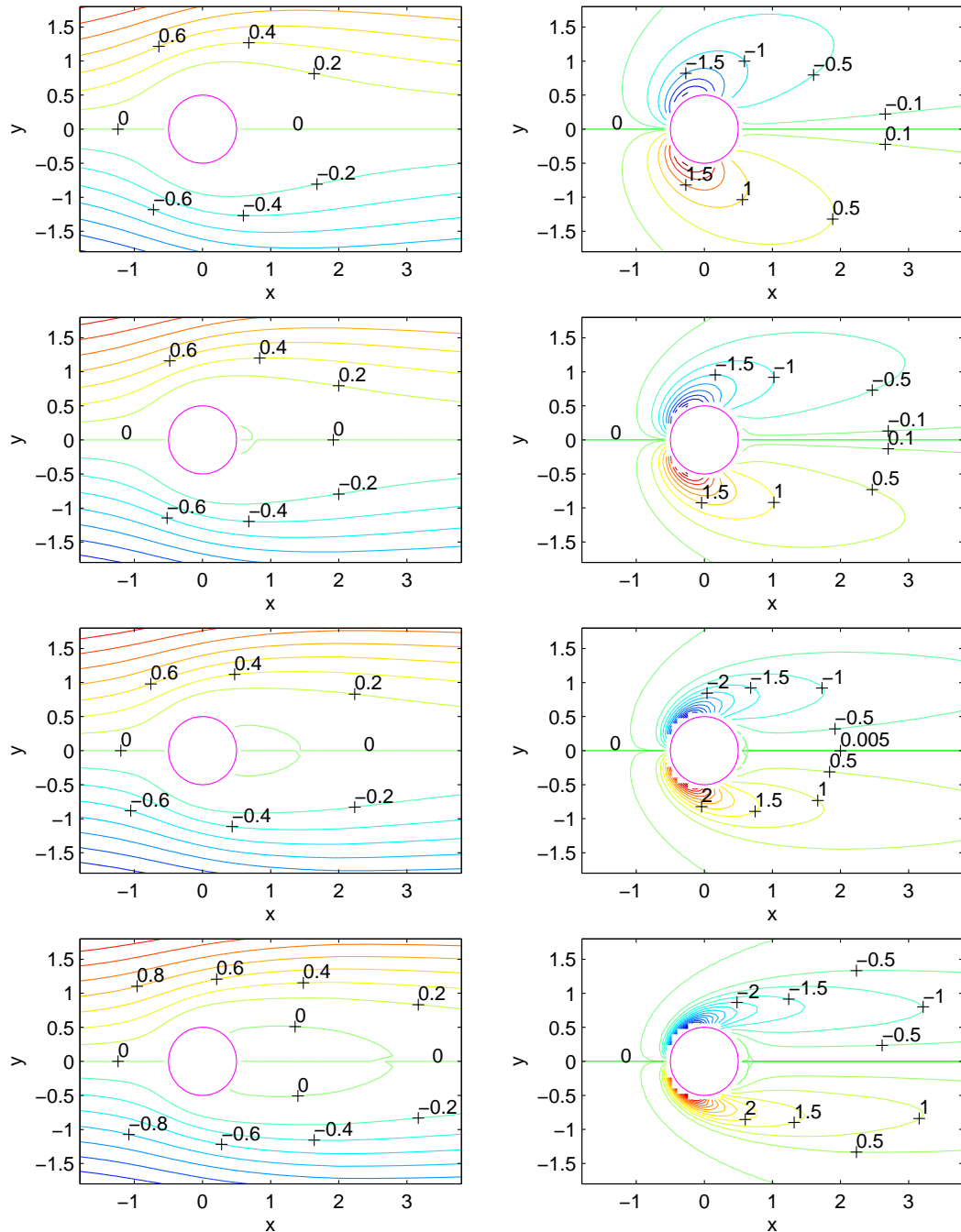


Figure 3.17: Flow past a circular cylinder: contours of stream function (left) and vorticity (right) for the cases of  $Re = 5, 10, 20$  and  $40$ , from top to bottom, using a grid of  $151 \times 151$ .

### 3.8 Concluding remarks

A local MLS-1D-IRBFN method is proposed for solving incompressible viscous flow problems in terms of stream function and vorticity. The present approach is based on the PU concept and incorporates the MLS and 1D-IRBFN methods. The LMLS-1D-IRBFN approach offers the same order of accuracy as the 1D-IRBFN method, while the system matrix is more sparse than that of the 1D-IRBFN, which helps reduce the computational cost significantly as discussed earlier. The LMLS-1D-IRBFN shape function possesses the Kronecker- $\delta$  property which allows an exact imposition of the essential boundary condition. Cartesian grids are used to discretise both rectangular and irregular problem domains. The numerical results for the lid-driven cavity flows at high  $Re$  numbers showed that the calculation of convection terms using the 1D-IRBFN technique are more accurate than the one using the LMLS-1D-IRBFN technique. The combination of the LMLS-1D-IRBFN method and a domain decomposition technique is successfully developed for solving a larger problem. The obtained numerical results for both cases of lid-driven cavity flow and flow past a circular cylinder are in good agreement with other published results available in the literature. The present method can be used to handle problems with irregular domains, while the standard finite difference method cannot be applied directly at the grid points near the boundary of irregular domains. Owing to the use of integrated RBFN for local approximation, the present method appears to be more accurate than the FDM with central-difference scheme. Owing to the use of a fixed Cartesian grid, the present method is expected to be more efficient than the conventional FDM, FVM and FEM when solving problems with moving boundary.

## Chapter 4

# Local MLS-1D-IRBFN method for natural convection in multiply-connected domains

The local moving least square - one dimensional integrated radial basis function network (LMLS-1D-IRBFN) method has been successfully developed for solving problems of steady incompressible viscous flows in Chapter 3. In the present chapter, the LMLS-1D-IRBFN method is further developed for multiply-connected domains and applied to simulate natural convection flows in concentric and eccentric annuli in terms of stream function, vorticity and temperature. Stream function value on the inner boundary is unknown and determined by using the single-valued pressure condition (Lewis, 1979). The method is first verified by the solution of the two-dimensional Poisson equation in a square domain with a circular hole, then applied to solve natural convection flow problems.

## 4.1 Introduction

Natural convection has been investigated both experimentally and numerically by many researchers for its wide applications, including nuclear reactor designs, solar energy systems, cooling of electronic equipments and thermal storage systems. Banerjee et al. (2008) conducted a study of heat transfer in a square enclosure with two discrete heat sources mounted on its bottom wall using finite volume method (FVM). Their work is useful in the design of efficient heat-removal systems in electronics and MEMS applications. Jubran et al. (2004) simulated convective layers on solar pond walls using three-dimensional FVM for solving conservation equations for mass, chemical species, momentum and energy. They investigated the effects of wall tilt angle and salt concentration on the characteristics of the convective layers. Costa and Raimundo (2010) numerically studied a mixed convection in a heated square enclosure with a rotating cylinder within it. They observed that the size of the inner cylinder strongly affects the resulting flow and heat transfer process. Their simulation can be used to model real situations where a rotating shaft is used to control the performance of natural convection in an enclosure.

Kuehn and Goldstein (1976) conducted experimental and theoretical studies to investigate the natural convection within an annulus between horizontal concentric cylinders. Their experimental results showed that the flow is steady for small Rayleigh numbers. Their numerical results were in good agreement with their experimental data. Moukalled and Acharya (1996) studied the natural convection in a annulus between concentric horizontal circular and square cylinders using a control volume-based method. Shu and Zhu (2002) employed the differential quadrature (DQ) method to simulate the natural convection in a concentric annulus between a cold outer square cylinder and a heated inner circular cylinder. The DQ method can yield very accurate numerical results owing to its global approximation. However, the irregular physical domain must be transformed into a regular computational domain, and the governing equations

as well as the boundary conditions are also transformed into relevant forms in the computational space. Šarler and Perko (2004) presented a radial basis function collocation method for solving natural convection problems in porous media in terms of primitive variables. Recently, Kim et al. (2008) employed an immersed boundary method (IBM) based on FVM with non-uniform Cartesian grid distribution for the simulation of natural convection between an inner circular cylinder and an outer square enclosure.

When dealing with incompressible viscous flows in multiply-connected domains using stream function-vorticity formulation, the stream function value on the inner boundaries are unknown and can be determined through a single-valued pressure condition (Lewis, 1979). Tezduyar et al. (1988) proposed a streamline-upwind/Petrov-Galerkin finite element procedure for a computation of two-dimensional fluid flow involving multiply-connected domains based on the vorticity-stream function formulation. The stream function values at the internal boundaries were determined through additional equations obtained by integrating the equation of motion along those boundaries. Shu et al. (2001) applied the DQ method to the natural convective transfer in an eccentric annulus between a circular inner cylinder and a square outer cylinder. In their work, an explicit formulation of the stream function value on the inner cylinder wall was derived from the single-valued pressure condition.

In the past decades, meshfree methods have become a very interesting research topic as they might have certain advantages over conventional element-based methods. Some of their appealing properties are (i) a significant reduction in discretisation complexity and (ii) suitability for solving problems with moving boundaries and complicated geometry. However, global meshfree methods are not suitable for simulating large-scale problems because they produce very dense system matrices, which leads to the ill-conditioning problem, large storage requirement and a long computational time (Kansa, 1990b; Zerroukat et al., 2000; Šarler and Perko, 2004). In order to overcome this disadvantage, local meshfree

methods have been proposed. Shu et al. (2003) presented a local RBF-based differential quadrature method (local RBF-DQ) for a simulation of natural convection in a square cavity. In their study, three layers of orthogonal grid near and including the boundary were generated for the purpose of imposing the Neumann condition for temperature and vorticity on the wall. The derivatives of the field variables in the boundary conditions were then discretised by the conventional one-sided second order finite difference scheme. Ding et al. (2005) employed the local RBF-DQ method for simulation of natural convection in a horizontal eccentric annulus. In their work, the effects of eccentricity and angular position on the flow and thermal fields for medium aspect ratios were studied. The local RBF-DQ method was also used for solving incompressible flow problems including the driven-cavity flow, flow past one isolated cylinder and flow around two staggered circular cylinders (Shu et al., 2005). Šarler and Vertnik (2006) proposed an explicit local radial basis function collocation method for diffusion problems. The method appeared efficient, because it does not deal with a large system of equations like the original Kansa method (Kansa, 1990b). The method was then extended to solve many other problems such as convection-diffusion problems with phase change (Vertnik and Šarler, 2006), a solution of conjugate heat transfer (Divo and Kassab, 2007), and a solution of incompressible turbulent flow (Vertnik and Šarler, 2009). Recently, Yao et al. (2011) presented a comparison of three explicit local meshless methods including a local method of approximate particular solutions (LMAPS), a local direct radial basis function collocation method (LDRBFCM), and a local indirect radial basis function collocation method (LIRBFNCM). Three methods were applied to a simple diffusion equation with Dirichlet jump boundary condition based on both uniform and non-uniform node distributions. Their numerical results showed that all methods have high accuracy and improvement of the accuracies with increasing node density and decreasing time step. For random node arrangement, the LMAPS and the LDRBFCM are more stable than the LDRBFCM. Some other meshfree methods based on local approximations include meshless local Petrov Galerkin method (MLPG) (Atluri and Zhu, 1998), a

point interpolation meshless method based on combining radial and polynomial basis function by Wang and Liu (2002), local multiquadric (LMQ) and local inverse multiquadric (LIMQ) approximation methods by Lee et al. (2003), a moving IRBFN-based Galerkin meshless method proposed by Le et al. (2010).

A different approach for solving PDEs is the so-called Cartesian grid method where the governing equations are discretised by a Cartesian grid which does not conform to the immersed boundaries. This significantly reduces the grid generation cost and has a great potential over the conventional body-fitted methods when solving problems with moving boundaries and complicated geometry. Ye et al. (1999) developed a finite-volume based Cartesian grid method for simulating two-dimensional unsteady, viscous, incompressible flows with complex immersed boundaries. In their method, the immersed boundary is represented by a series of piecewise linear segments. Based on these segments, the control volume near the immersed boundary is reformed into a body-fitted trapezoidal shape. Russell and Wang (2003) presented a Cartesian grid method for solving 2D incompressible viscous flows around multiple moving objects based on stream function-vorticity formulation.

As an alternative to the conventional differentiated radial basis function network (DRBFN) method (Kansa, 1990b), Mai-Duy and Tran-Cong (2001a) proposed the use of integration to construct the RBFN expressions (the IRBFN method) for the approximation of a function and its derivatives and for the solution of PDEs. The numerical results showed that the IRBFN method is more accurate than the DRBFN (Mai-Duy and Tran-Cong, 2001a,b). A one-dimensional integrated radial basis function network (1D-IRBFN) collocation method for the solution of second- and fourth-order PDEs was presented by Mai-Duy and Tanner (2007). Along grid lines, 1D-IRBFN are constructed to satisfy the governing differential equations with boundary conditions in an exact manner. In the 1D-IRBFN method, the Cartesian grids were used to discretise both rectangular and non-rectangular problem domains. The 1D-IRBFN method is much more

efficient than the original IRBFN method reported in Mai-Duy and Tran-Cong (2001a). Le-Cao et al. (2011) employed the 1D-IRBFN method to simulate unsymmetrical flows of a Newtonian fluid in multiply-connected domains using the stream-function and temperature formulation. Ngo-Cong et al. (2011) extended this method to investigate free vibration of composite laminated plates based on first-order shear deformation theory (Chapter 2). Ngo-Cong et al. (2012) proposed a local moving least square - one dimensional integrated radial basis function network method (LMLS-1D-IRBFN) for simulating 2-D steady incompressible viscous flows in terms of stream function and vorticity (Chapter 3). The method is based on the partition of unity framework to incorporate the moving least square and 1D-IRBFN techniques in an approach that produces a very sparse system matrix and offers as a high level of accuracy as that of the 1D-IRBFN. Moreover, LMLS-1D-IRBFN shape function possesses the Kronecker- $\delta$  property which helps impose the essential boundary condition in an exact manner. In this chapter, the LMLS-1D-IRBFN is applied to the solution of the stream-function, vorticity and temperature formulation of the natural convection in concentric and eccentric annuli. For the concentric case, the stream function values at the inner and outer boundaries are taken to be zero. For the eccentric case, the stream function value at the outer boundary is taken to be zero, while the stream function at the inner cylinder is unknown and calculated based on the single-valued pressure condition.

The chapter is organised as follows. The LMLS-1D-IRBFN method is presented in Section 4.2. The governing equations for natural convection flows are given in Section 4.3. Several numerical examples are investigated using the proposed method in Section 4.4. Section 4.5 concludes the chapter.

## 4.2 Local moving least square - one dimensional integrated radial basis function network technique

A schematic outline of the LMLS-1D-IRBFN method is depicted in Figure 4.1. The proposed method with 3-node support domains ( $n = 3$ ) and 5-node local 1D-IRBF networks ( $n_s = 5$ ) is presented here. On an  $x$ -grid line  $[l]$ , a global interpolant for the field variable at a grid point  $x_i$  is sought in the form

$$u(x_i) = \sum_{j=1}^n \bar{\phi}_j(x_i) u^{[j]}(x_i), \quad (4.1)$$

where  $\{\bar{\phi}_j\}_{j=1}^n$  is a set of the partition of unity functions constructed using MLS approximants (Liu, 2003);  $u^{[j]}(x_i)$  the nodal function value obtained from a local interpolant represented by a 1D-IRBF network  $[j]$ ;  $n$  the number of nodes in the support domain of  $x_i$ . In (4.1), MLS approximants are presently based on linear polynomials, which are defined in terms of 1 and  $x$ . It is noted that the MLS shape functions possess a so-called partition of unity properties as follows.

$$\sum_{j=1}^n \bar{\phi}_j(x) = 1. \quad (4.2)$$

Relevant derivatives of  $u$  at  $x_i$  can be obtained by differentiating (4.1)

$$\frac{\partial u(x_i)}{\partial x} = \sum_{j=1}^n \left( \frac{\partial \bar{\phi}_j(x_i)}{\partial x} u^{[j]}(x_i) + \bar{\phi}_j(x_i) \frac{\partial u^{[j]}(x_i)}{\partial x} \right), \quad (4.3)$$

$$\frac{\partial^2 u(x_i)}{\partial x^2} = \sum_{j=1}^n \left( \frac{\partial^2 \bar{\phi}_j(x_i)}{\partial x^2} u^{[j]}(x_i) + 2 \frac{\partial \bar{\phi}_j(x_i)}{\partial x} \frac{\partial u^{[j]}(x_i)}{\partial x} + \bar{\phi}_j(x_i) \frac{\partial^2 u^{[j]}(x_i)}{\partial x^2} \right), \quad (4.4)$$

where the values  $u^{[j]}(x_i)$ ,  $\partial u^{[j]}(x_i)/\partial x$  and  $\partial^2 u^{[j]}(x_i)/\partial x^2$  are calculated from 1D-IRBFN networks with  $n_s$  nodes.

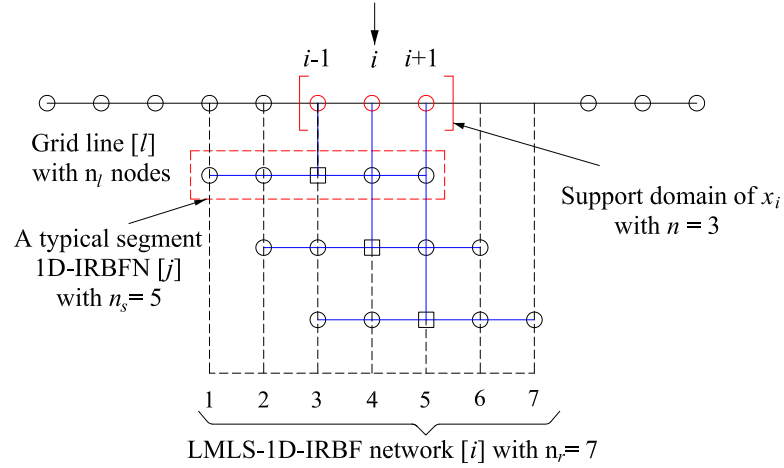


Figure 4.1: LMLS-1D-IRBFN scheme,  $\square$  a typical [j] node.

Full details of the LMLS-1D-IRBFN method can be found in Chapter 3.

### 4.3 Governing equations for natural convection flows

Fluid properties are assumed to be constant except that the density changes with temperature, which is represented by using the Boussinesq approximation. The dimensionless governing equations, expressed in terms of stream function  $\psi$ , vorticity  $\omega$  and temperature  $T$ , are written as

$$\frac{\partial^2 \psi}{\partial x^2} + \frac{\partial^2 \psi}{\partial y^2} = -\omega, \quad (4.5)$$

$$\frac{\partial^2 \omega}{\partial x^2} + \frac{\partial^2 \omega}{\partial y^2} - \frac{1}{\text{Pr}} \frac{\partial \omega}{\partial t} = -Ra \frac{\partial T}{\partial x} + \frac{1}{\text{Pr}} \left( \frac{\partial \psi}{\partial y} \frac{\partial \omega}{\partial x} - \frac{\partial \psi}{\partial x} \frac{\partial \omega}{\partial y} \right), \quad (4.6)$$

$$\frac{\partial^2 T}{\partial x^2} + \frac{\partial^2 T}{\partial y^2} - \frac{\partial T}{\partial t} = \frac{\partial \psi}{\partial y} \frac{\partial T}{\partial x} - \frac{\partial \psi}{\partial x} \frac{\partial T}{\partial y}, \quad (4.7)$$

where  $Pr$  is the Prandtl number defined as  $Pr = \mu C_p / k$ ,  $Ra$  the Rayleigh number defined as  $Ra = (C_p \rho_0 g \beta_0 L^3 \Delta T) / (k \nu)$ ,  $\mu$  the viscosity,  $C_p$  the specific heat at constant pressure,  $k$  thermal conductivity,  $\rho_0$  the reference density,  $g$  the gravitational acceleration,  $\beta_0$  the thermal expansion coefficient,  $L$  the side length of the square outer cylinder,  $\Delta T$  the temperature difference between inner and outer cylinders,  $\nu$  the kinematic viscosity,  $t$  the time, and  $(x, y)^T$  the position vector. The  $x$  and  $y$  components of the velocity vector can be defined in terms of the stream function as

$$u = \frac{\partial \psi}{\partial y}, \quad (4.8)$$

$$v = -\frac{\partial \psi}{\partial x}. \quad (4.9)$$

The computational boundary conditions for vorticity can be computed as

$$\omega_w = -\left( \frac{\partial^2 \psi_w}{\partial x^2} + \frac{\partial^2 \psi_w}{\partial y^2} \right) \quad (4.10)$$

where the subscript  $w$  is used to denote quantities on the boundary. For curved boundaries, a formula reported in (Le-Cao et al., 2009) is employed here to derive the vorticity boundary conditions at boundary points on  $x$ - and  $y$ -grid lines as follows.

$$\omega_w^{(x)} = -\left[ 1 + \left( \frac{t_x}{t_y} \right)^2 \right] \frac{\partial^2 \psi_w}{\partial x^2} - q_y, \quad (4.11)$$

$$\omega_w^{(y)} = -\left[ 1 + \left( \frac{t_y}{t_x} \right)^2 \right] \frac{\partial^2 \psi_w}{\partial y^2} - q_x, \quad (4.12)$$

where  $q_x$  and  $q_y$  are known quantities defined by

$$q_x = -\frac{t_y}{t_x^2} \frac{\partial^2 \psi_w}{\partial y \partial s} + \frac{1}{t_x} \frac{\partial^2 \psi_w}{\partial x \partial s}, \quad (4.13)$$

$$q_y = -\frac{t_x}{t_y^2} \frac{\partial^2 \psi_w}{\partial x \partial s} + \frac{1}{t_y} \frac{\partial^2 \psi_w}{\partial y \partial s}, \quad (4.14)$$

in which  $t_x = \partial x / \partial s$ ,  $t_y = \partial y / \partial s$  and  $s$  is the direction tangential to the curved surface.

Boundary conditions for stream function and temperature are specified in the following examples.

## 4.4 Numerical results and discussion

The present method is applied to obtain the solution of two-dimensional Poisson equation in a square domain with a circular hole, and the natural convection in concentric and eccentric annuli. The problem domains are discretised using Cartesian grids. By using the LMLS-1D-IRBFN method to discretise the left hand side (LHS) of governing equations and the LU decomposition technique to solve the resultant sparse system of simultaneous equations, the computational cost and data storage requirements are reduced. In the analyses of natural convection flows, the diffusion terms are discretised using the LMLS-1D-IRBFN method, whereas the nonlinear convection terms are explicitly calculated using the 1D-IRBFN method. As shown in Chapter 3 (Ngo-Cong et al., 2012), this approach yields more accurate solutions than the one using the LMLS-1D-IRBFN to discretise both diffusion and convection terms. In the following Examples 2-4, computational boundary conditions for vorticity are determined by Equations (4.10)-(4.14).

#### 4.4.1 Example 1: Two-dimensional Poisson equation in a square domain with a circular hole

The present method is first verified through the solution of the following 2D Poisson equation

$$\frac{\partial^2 u}{\partial x^2} + \frac{\partial^2 u}{\partial y^2} = 0, \quad (4.15)$$

defined on a square domain with a square hole as shown in Figure 4.2 and subject to Dirichlet boundary conditions. The problem has the following exact solution

$$u_E = (1/\sinh(\pi)) \sin(\pi x) \sinh(\pi y), \quad (4.16)$$

from which the boundary values of  $u$  can be derived.

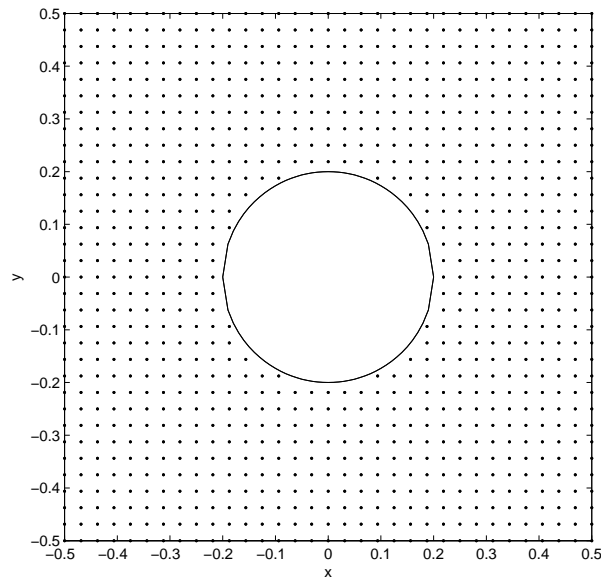


Figure 4.2: A square domain with a circular hole.

It is noted that the accuracy of RBF-based solution depends on the RBF width, small or large values of the RBF width make the response of neuron too peaked or flat, respectively (Haykin, 1999). Figure 4.3 presents the  $\beta$ -adaptivity study

of relative error norm ( $Ne$ ) and condition number ( $cond$ ) in a range of  $4 \leq \beta \leq 10$  by using the LMLS-1D-IRBFN method. It appears that the accuracy increases with increasing value of  $\beta$  for coarse grids. However, the solution becomes unstable at large values of  $\beta$  for dense grids. Therefore, proper values of  $\beta$  are required to obtain good numerical solutions. The condition numbers of the system matrix remains unchanged for different values of  $\beta$  and are slightly different from those of the 1D-IRBFN method.

Table 4.1 describes the grid convergence study of relative error norms ( $Ne$ ), condition number ( $cond$ ) and percentage of nonzero elements of the system matrix ( $\epsilon$ ) of the present method with  $\beta = 6$  in comparison with those of 1D-IRBFN method. Both methods yield highly accurate results and converge well with increasing node density. It is observed that the convergence order of LMLS-1D-IRBFN (error norm of  $O(h^{1.99})$ ) is smaller than that of 1D-IRBFN (error norm of  $O(h^{3.10})$ ), however, the accuracy of former is better than that of the latter at a given grid size. In addition, the present method is more efficient than the 1D-IRBFN method in terms of memory requirements (e.g., 12.6 times for a grid of  $105 \times 105$ ).

Table 4.1: Poisson equation in a square domain with a circular hole subject to Dirichlet boundary conditions: comparison of relative error norm ( $Ne$ ), condition number ( $cond$ ) and percentage of nonzero elements of the system matrix ( $\epsilon$ ), using  $\beta = 1$  for 1D-IRBFN and  $\beta = 6$  for the present method (LMLS-1D-IRBFN).

Grid	$Ne$		$cond$		$\epsilon(\%)$	
	1D-IRBFN	Present	1D-IRBFN	Present	1D-IRBFN	Present
$25 \times 25$	3.38E-05	5.82E-06	3.31E+02	3.32E+02	7.79	2.48
$33 \times 33$	1.34E-05	3.05E-06	3.56E+02	3.74E+02	5.79	1.43
$41 \times 41$	6.65E-06	2.00E-06	5.96E+02	6.06E+02	4.55	0.92
$49 \times 49$	3.87E-06	1.42E-06	9.00E+02	8.97E+02	3.84	0.64
$57 \times 57$	2.38E-06	1.05E-06	1.66E+03	1.68E+03	3.26	0.47
$65 \times 65$	1.58E-06	7.97E-07	2.28E+03	2.38E+03	2.88	0.36
$73 \times 73$	1.09E-06	6.33E-07	2.99E+03	3.07E+03	2.54	0.29
$81 \times 81$	7.89E-07	5.18E-07	4.06E+03	4.17E+03	2.27	0.23
$89 \times 89$	5.90E-07	4.19E-07	4.05E+03	4.10E+03	2.09	0.19
$97 \times 97$	4.48E-07	3.62E-07	4.50E+03	4.54E+03	1.90	0.16
$105 \times 105$	3.53E-07	3.03E-07	6.02E+03	6.30E+03	1.77	0.14

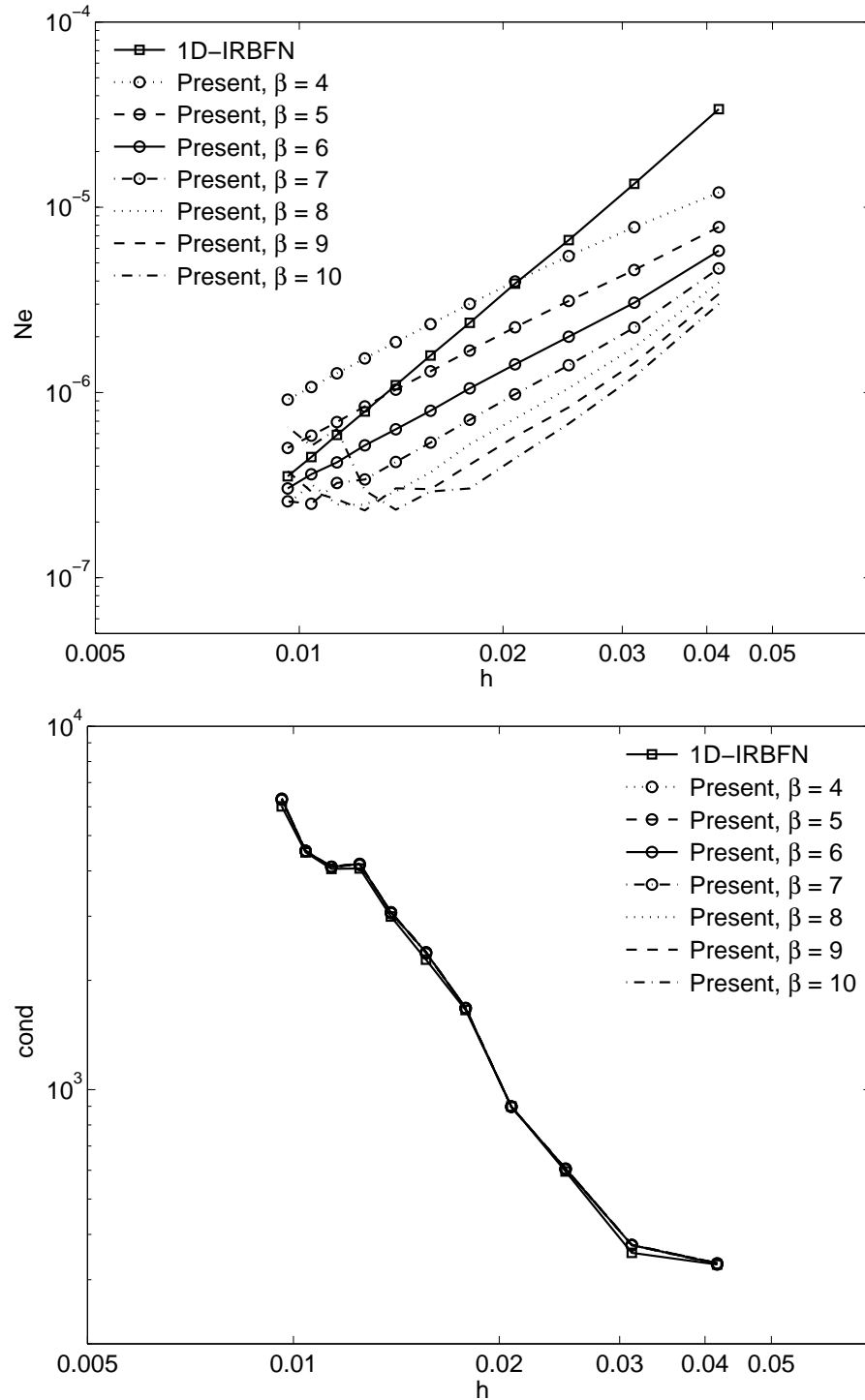


Figure 4.3: Poisson equation in a square domain with a circular hole subject to Dirichlet boundary conditions:  $\beta$ -adaptivity study for the present method (LMLS-1D-IRBFN).

### 4.4.2 Example 2: Concentric annulus between two circular cylinders

The present method is applied to the solution of natural convection in a concentric annulus between two circular cylinders. The problem geometry and boundary conditions are described in Figure 4.4. The parameter values used here are:  $Pr = 0.7$ ,  $L = 1.0$  and  $L/D_i = 0.8$ , where  $L$  is the annulus width, and  $D_i$  the inner cylinder diameter. The average equivalent conductivity is given by

$$\bar{k}_{eq} = \frac{-\ln(D_o/D_i)}{2\pi} \oint \frac{\partial T}{\partial n} ds, \quad (4.17)$$

where  $D_o$  is the diameters of the outer cylinder; and  $n$  the direction normal to the cylinder surfaces.

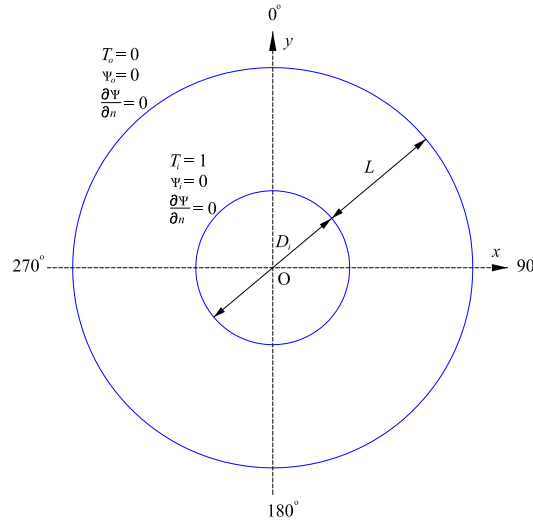


Figure 4.4: Concentric annulus between two circular cylinders: problem geometry and boundary conditions. Angular positions are measured clockwise from the positive  $y$ -axis. Note that computational boundary conditions for vorticity are determined by Equations (4.10)-(4.14).

Table 4.2 shows the grid convergence study of average equivalent conductivity on the outer and inner cylinders for Rayleigh numbers from  $10^2$  to  $7 \times 10^4$ . Three levels of grid density including  $41 \times 41$ ,  $51 \times 51$  and  $61 \times 61$  are considered. The present numerical results are compared with the 1D-IRBFN, FDM and DQM results obtained by Le-Cao et al. (2009); Kuehn and Goldstein (1976); and Shu

(1999), respectively. It can be seen that the present results converge to those reference values with increasing grid density.

Table 4.2: Concentric annulus between two circular cylinders: Grid convergence study of the average equivalent conductivity on the outer and inner cylinders,  $k_{eqo}$  and  $k_{eqi}$ , respectively, for different Rayleigh numbers.

$Ra$	$10^2$	$10^3$	$3 \times 10^3$	$6 \times 10^3$	$10^4$	$5 \times 10^4$	$7 \times 10^4$
Grid	$k_{eqi}$						
$41 \times 41$	1.002	1.083	1.397	1.716	1.983	3.107	3.462
$51 \times 51$	1.001	1.083	1.399	1.719	1.984	3.017	3.288
$61 \times 61$	1.001	1.083	1.398	1.717	1.982	2.983	3.238
1D-IRBFN <sup>a</sup>	1.000	1.083	1.396	1.709	1.975	2.962	3.207
FDM <sup>b</sup>	1.000	1.081	1.404	1.736	2.010	3.024	3.308
DQM <sup>c</sup>	1.001	1.082	1.397	1.715	1.979	2.958	
	$k_{eqo}$						
$41 \times 41$	1.001	1.083	1.399	1.715	1.969	3.264	3.733
$51 \times 51$	1.001	1.083	1.399	1.718	1.979	2.996	3.394
$61 \times 61$	1.001	1.083	1.398	1.717	1.981	2.927	3.218
1D-IRBFN <sup>a</sup>	0.999	1.080	1.393	1.712	1.970	2.942	3.246
FDM <sup>b</sup>	1.002	1.084	1.402	1.735	2.005	2.973	3.226
DQM <sup>c</sup>	1.001	1.082	1.397	1.715	1.979	2.958	

<sup>a</sup> (Le-Cao et al., 2009)

<sup>b</sup> (Kuehn and Goldstein, 1976)

<sup>c</sup> (Shu, 1999)

Figures 4.5 and 4.6 show the influence of Rayleigh number on the equivalent conductivities on the inner and outer the cylinders, respectively. The figures indicate that heat is being convected from the lower portion of the inner cylinder to the top of the outer cylinder.

Figures 4.7 and 4.8 present the contours of temperature and stream function of the flow in the annulus for Rayleigh numbers from  $10^2$  to  $7 \times 10^4$ . Those contours are symmetric with respect to the vertical center line. At low Rayleigh numbers (say  $< 10^2$ ), the flow appears almost symmetric about the horizontal center line since convection is quite small. As the Rayleigh number increases, the center of rotation moves upwards and the temperature distribution become distorted, resulting in an increase in overall heat transfer. The highest local heat flux occurs at the stagnation point while the smallest local heat flux occurs at the separation point. For the inner cylinder, the stagnation point is at the bottom while the separation point is at the top. For the outer cylinder, the stagnation point is at the top while the separation point is at the bottom.

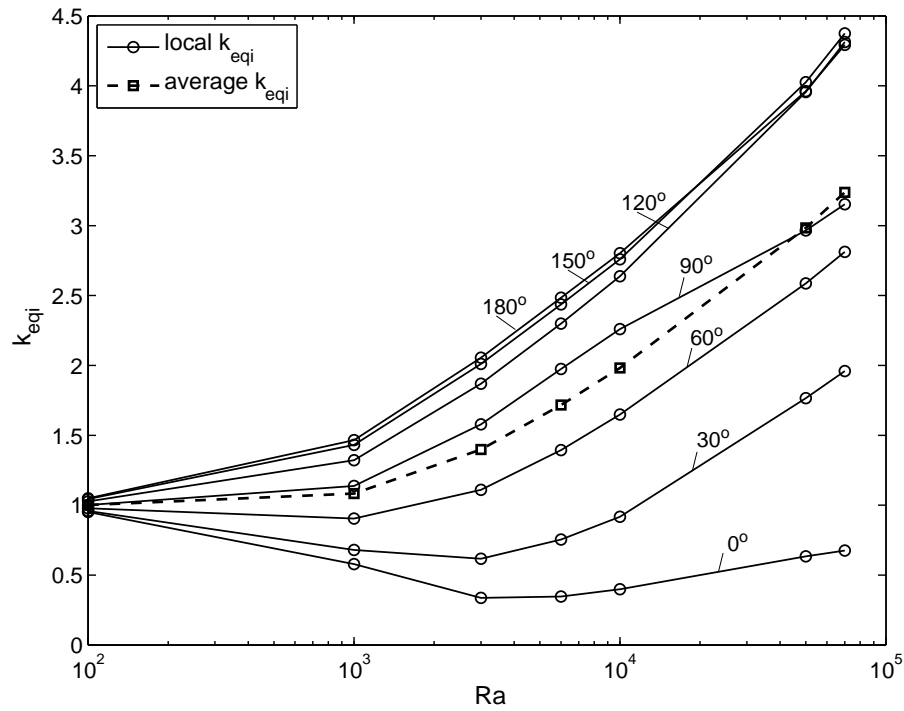


Figure 4.5: Concentric annulus between two circular cylinders: influence of Rayleigh number on local and average equivalent conductivities on the inner cylinders.

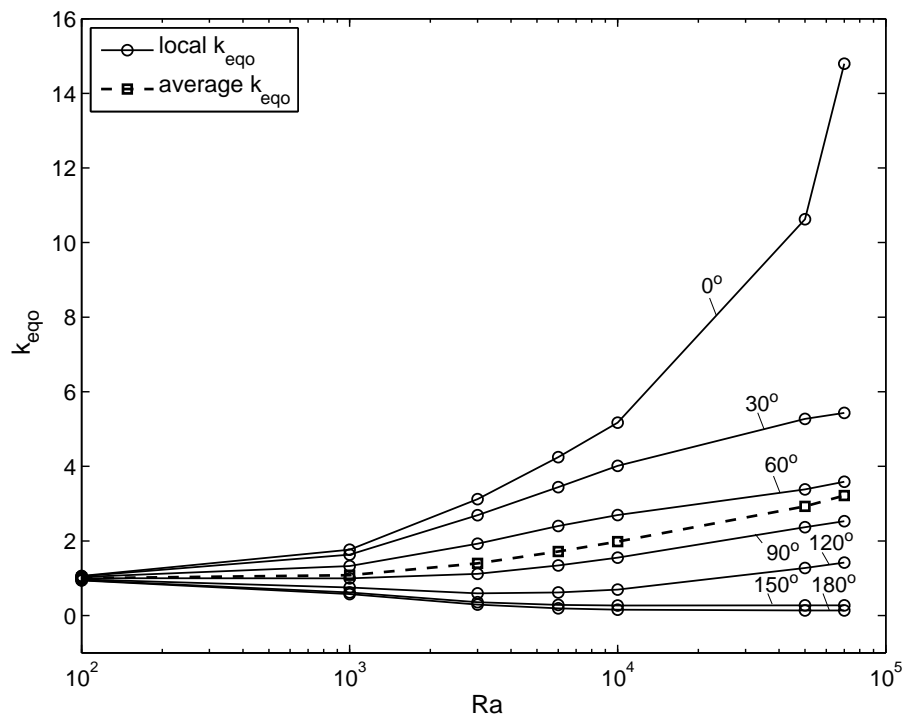


Figure 4.6: Concentric annulus between two circular cylinders: influence of Rayleigh number on local and average equivalent conductivities on the outer cylinders.

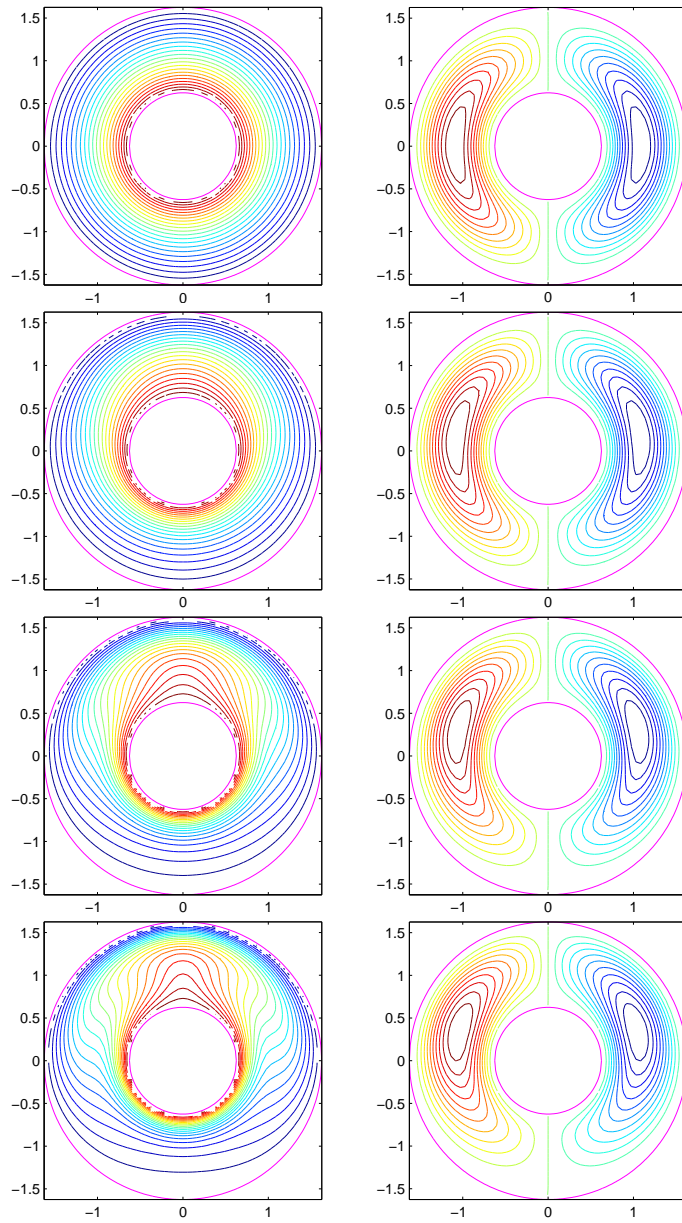


Figure 4.7: Concentric annulus between two circular cylinders: contours of temperature (left) and stream function (right) for different Rayleigh numbers  $Ra = 10^2, 10^3, 3 \times 10^3$  and  $6 \times 10^3$ , from top to bottom, using a grid of  $61 \times 61$ . Each plot contains 21 contour levels varying linearly from the minimum value to the maximum value.

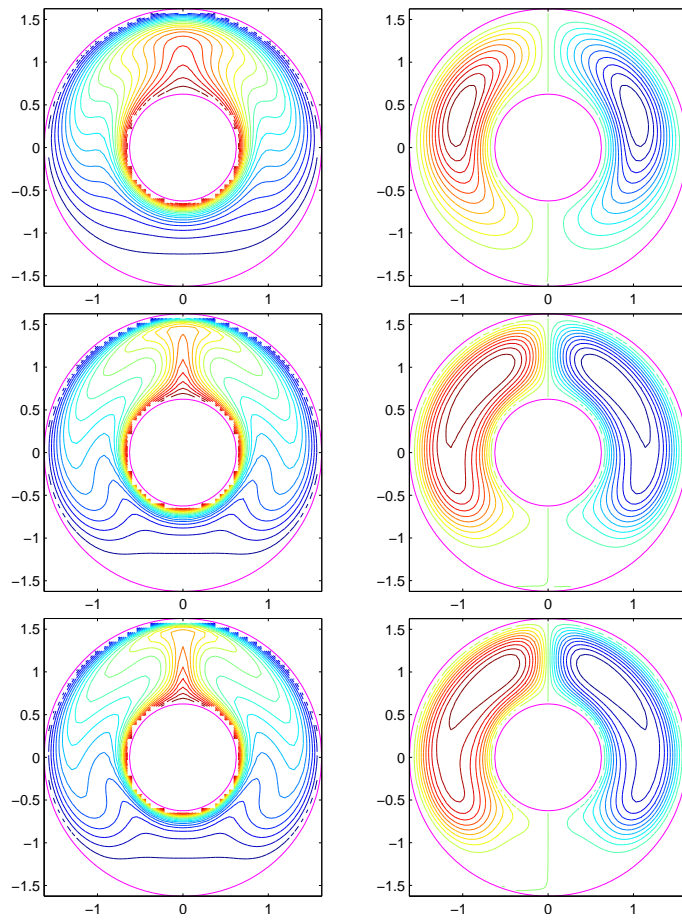


Figure 4.8: Concentric annulus between two circular cylinders: contours of temperature (left) and stream function (right) for different Rayleigh numbers  $Ra = 10^4, 5 \times 10^4$  and  $7 \times 10^4$ , from top to bottom, using a grid of  $61 \times 61$ . Each plot contains 21 contour levels varying linearly from the minimum value to the maximum value.

### 4.4.3 Example 3: Concentric annulus between a square outer cylinder and a circular inner cylinder

This example is concerned with the natural convection in a concentric annulus between a square outer cylinder and a circular inner cylinder. The problem geometry and boundary conditions are described in Figure 4.9. The parameter values used here are:  $Pr = 0.71$  and  $L/2R = 2.5$ , where  $L$  is the side length of the outer square, and  $R$  the radius of the inner cylinder. The average Nusselt number is defined by

$$Nu = -\frac{1}{k} \oint \frac{\partial T}{\partial n} ds, \quad (4.18)$$

where  $k$  is the thermal conductivity.

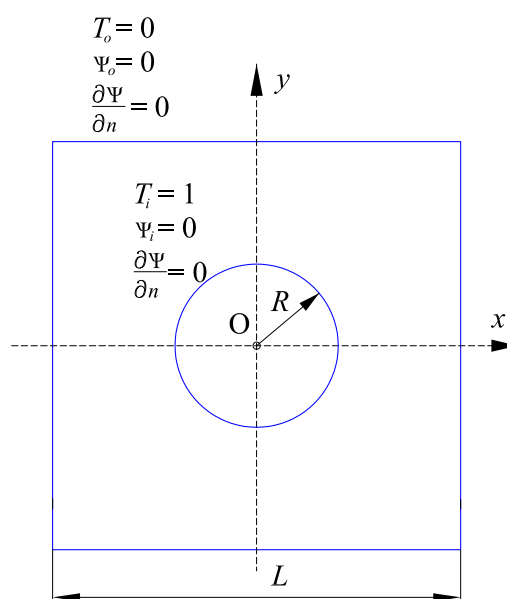


Figure 4.9: Concentric annulus between a square outer cylinder and a circular inner cylinder: problem geometry and boundary conditions. Note that computational boundary conditions for vorticity are determined by Equations (4.10)-(4.14).

Table 4.3 presents the grid convergence study of the average Nusselt number on the inner and the outer cylinders for different Raleigh numbers. Moukalled and Acharya (1996) studied this problem by solving the governing elliptic conserva-

tion equations in a boundary-fitted coordinate system using a control volume-based procedure. The governing equations were solved for only one-half of the physical domain since the flow is symmetric about the vertical axis. In the present study, a whole of the physical domain is considered. Therefore, the average Nusselt numbers obtained are divided by 2 for the purposes of comparison. It can be seen that the present results converge to the 1D-IRBFN (Le-Cao et al., 2009) and FDM (Moukalled and Acharya, 1996) results with increasing grid density.

Table 4.3: Concentric annulus between a square outer cylinder and a circular inner cylinder: Grid convergence study of the average Nusselt number on the inner and outer cylinders,  $Nu_i$  and  $Nu_o$ , respectively, for different Rayleigh numbers.

$Ra$	$10^4$	$5 \times 10^4$	$10^5$	$5 \times 10^5$	$10^6$
Grid	$Nu_i$				
$43 \times 43$	3.23	4.05	4.90	7.58	9.00
$53 \times 53$	3.23	4.05	4.91	7.56	8.94
$63 \times 63$	3.23	4.06	4.92	7.55	8.90
1D-IRBFN <sup>a</sup>	3.21	4.04	4.89	7.51	8.85
FDM <sup>b</sup>	3.24		4.86		8.90
DQM <sup>c</sup>	3.33		5.08		9.37
	$Nu_o$				
$43 \times 43$	3.22	4.03	4.86	7.31	9.15
$53 \times 53$	3.22	4.05	4.89	7.38	8.76
$63 \times 63$	3.23	4.05	4.91	7.43	8.67
1D-IRBFN <sup>a</sup>	3.22	4.04	4.89	7.43	8.70
FDM <sup>b</sup>	3.24		4.86		8.90
DQM <sup>c</sup>	3.33		5.08		9.37

<sup>a</sup> (Le-Cao et al., 2009)  
<sup>b</sup> (Moukalled and Acharya, 1996)  
<sup>c</sup> (Shu and Zhu, 2002)

Figure 4.10 shows the contours of temperature, stream function and vorticity of the flow field inside the enclosure for different Rayleigh numbers. The numerical results obtained are symmetric about the vertical center line. The contours of stream function shows that the flow moves up along the inner cylinder wall and the vertical axis to reach the top of the outer cylinder, and then moves down along the outer cylinder wall. There are boundary layers near the bottom of the inner cylinder and near the top of the outer cylinder, while a flow separation occurs near the top of the inner cylinder which forms a thermal plume. Those behaviours agree well with published results in the literature.

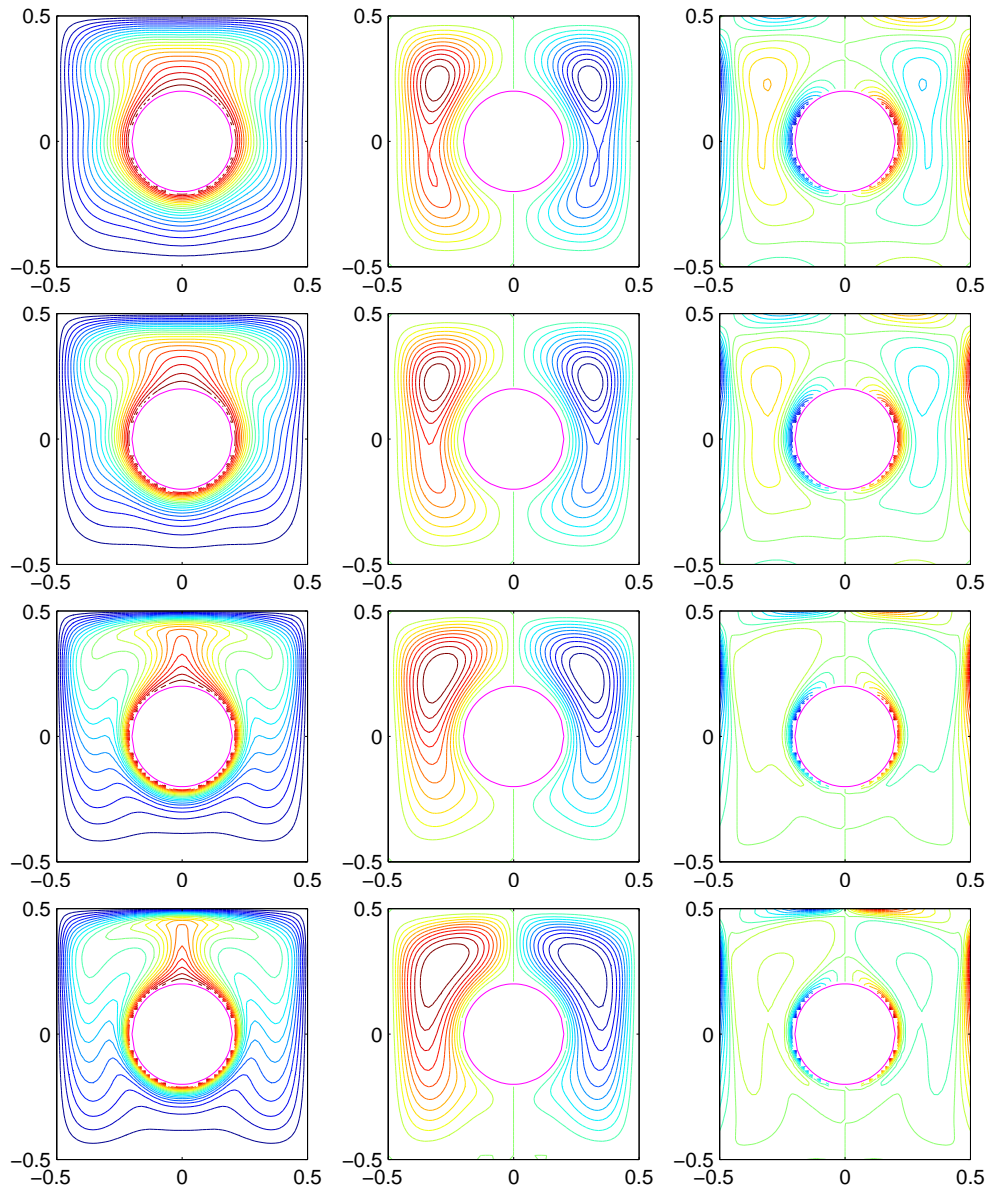


Figure 4.10: Concentric annulus between a square outer cylinder and a circular inner cylinder: contours of temperature (left), stream function (middle) and vorticity (right) for different Rayleigh numbers  $Ra = 5 \times 10^4, 10^5, 5 \times 10^5$  and  $10^6$ , from top to bottom, using a grid of  $63 \times 63$ . Each plot contains 21 contour levels varying linearly from the minimum value to the maximum value.

#### 4.4.4 Example 4: Eccentric annulus between a square outer cylinder and a circular inner cylinder

Natural convection heat transfer between a heated circular cylinder placed eccentrically inside a square cylinder is studied. The stream function value on the outer wall is taken to be zero, while the stream function value on the inner wall ( $\psi_{wall}$ ) is unknown, which can be determined by using a single-valued pressure condition through the following equation.

$$\oint_{\Gamma} \frac{\partial^3 \psi}{\partial y \partial x^2} dx + \oint_{\Gamma} \frac{\partial^3 \psi}{\partial y^3} dx - \oint_{\Gamma} \frac{\partial^3 \psi}{\partial x^3} dy - \oint_{\Gamma} \frac{\partial^3 \psi}{\partial x \partial y^2} dy = 0. \quad (4.19)$$

where  $\Gamma$  is the inner boundary. The reader is referred to the work of Le-Cao et al. (2011) for further details. The geometry and boundary conditions of the present problem are depicted in Figure 4.11, where  $\varphi$  is the angular position of the center of the inner cylinder,  $R$  the radius of the inner cylinder and  $L$  the side length of the outer square. The dimensionless eccentricity is defined by  $\varepsilon_0 = \varepsilon/(L/2 - R)$ , where  $\varepsilon$  is the distance between the centers of the inner and outer cylinders. The simulation is conducted with the parameter values  $Pr = 0.71$ ,  $Ra = 3 \times 10^5$  and  $L/2R = 2.6$ .

The comparison of the maximum stream-function value  $\psi_{max}$ , the stream-function values on the inner cylinder  $\psi_{wall}$  and the average Nusselt number among the present method and the other methods for different values of  $\varepsilon_0$  and  $\varphi$  are shown in Tables 4.4, 4.5 and 4.6, respectively. A grid of  $108 \times 108$  is taken for the cases  $\varepsilon_0 = 0.75$  and  $\varphi = 0, -90, 90$ , while a grid of  $82 \times 82$  is used for the other cases. The present results are in good agreement with those of the MQ-DQ (Ding et al., 2005) and 1D-IRBFN (Le-Cao et al., 2011) methods. The differences of  $\psi_{max}$  between the present method and the MQ-DQ and the 1D-IRBFN are less than 1.0% and 1.9%, respectively. The differences of Nusselt numbers

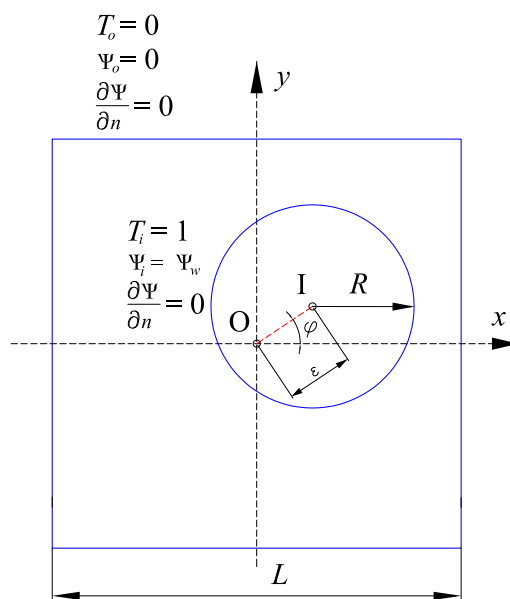


Figure 4.11: Eccentric annulus between a square outer cylinder and a circular inner cylinder: problem geometry and boundary conditions. The angular position  $\varphi$  of the center of the inner cylinder is measured counterclockwise from the positive  $x$ -axis. Note that computational boundary conditions for vorticity are determined by Equations (4.10)-(4.14).

between the present results and the MQ-DQ results are less than 1.4%. The differences of  $\psi_{wall}$  between the present results with the other results are quite large due to the sensitivity in the determination of stream function value on the inner cylinder wall, which is also mentioned by Ding et al. (2005). Figures 4.12, 4.13, 4.14, 4.15, and 4.16 present the contours of temperature, stream function and vorticity of flow field inside the eccentric annuli with different values of  $\varepsilon_0$  and  $\varphi$ . These contours agree well with those in (Ding et al., 2005; Le-Cao et al., 2011).

Table 4.4: Eccentric annulus between a square outer cylinder and a circular inner cylinder: Comparison of the maximum stream-function values  $\psi_{max}$  for different values of  $\varepsilon_0$  and  $\varphi$ .

$\varphi$	$\varepsilon_0$	$\psi_{max}$			
		DQ <sup>a</sup>	MQ-DQ <sup>b</sup>	1D-IRBFN <sup>c</sup>	Present
-90°	0.25	18.67	18.64	18.63	18.64
	0.50	21.43	21.29	21.30	21.34
	0.75	24.07	23.52	23.47	23.68
-45°	0.25	18.84	18.50	18.50	18.53
	0.50	19.75	20.03	20.09	20.11
	0.75	20.65	21.01	21.02	21.06
	0.95	21.68	21.59	21.61	21.63
0°	0.25	17.15	17.00	17.00	17.01
	0.50	18.77	16.97	16.99	16.99
	0.75	16.83	16.84	16.87	16.89
45°	0.25	15.56	15.32	15.31	15.33
	0.50	14.60	14.35	14.23	14.49
	0.75	13.94	13.61	13.52	13.56
	0.95	12.96	12.98	12.91	13.02
90°	0.25	12.55	12.39	12.37	12.41
	0.50	11.32	11.38	11.36	11.41
	0.75	10.26	10.09	10.10	10.11

<sup>a</sup> (Shu et al., 2001)

<sup>b</sup> (Ding et al., 2005)

<sup>c</sup> (Le-Cao et al., 2011)

Table 4.5: Eccentric annulus between a square outer cylinder and a circular inner cylinder: Comparison of the stream-function values on the inner cylinder  $\psi_{wall}$  for different values of  $\varepsilon_0$  and  $\varphi$ .

$\varphi$	$\varepsilon_0$	$\psi_{wall}$		
		DQ <sup>a</sup>	MQ-DQ <sup>b</sup>	Present
-90°	0.25	$< 10^{-4}$	$< 10^{-3}$	$< 10^{-3}$
	0.50	$< 10^{-4}$	$< 10^{-3}$	$< 10^{-3}$
	0.75	$< 10^{-4}$	$< 10^{-3}$	$< 10^{-3}$
-45°	0.25	0.11	0.04	0.02
	0.50	0.47	0.46	0.80
	0.75	1.46	1.46	1.09
	0.95	1.80	1.64	1.80
0°	0.25	0.15	0.20	0.27
	0.50	1.64	0.94	0.97
	0.75	1.05	1.35	1.35
45°	0.25	0.12	0.21	0.09
	0.50	0.84	0.69	1.01
	0.75	1.25	1.19	0.87
	0.95	0.93	1.29	1.43
90°	0.25	$< 10^{-4}$	$< 10^{-3}$	$< 10^{-3}$
	0.50	$< 10^{-4}$	$< 10^{-3}$	$< 10^{-3}$
	0.75	$< 10^{-4}$	$< 10^{-3}$	$< 10^{-3}$

<sup>a</sup> (Shu et al., 2001)

<sup>b</sup> (Ding et al., 2005)

Table 4.6: Eccentric annulus between a square outer cylinder and a circular inner cylinder: Comparison of the average Nusselt number  $Nu$  for different values of  $\varepsilon_0$  and  $\varphi$ .

$\varphi$	$\varepsilon_0$	$Nu$		
		DQ <sup>a</sup>	MQ-DQ <sup>b</sup>	Present
-90°	0.25	6.75	6.74	6.71
	0.50	6.98	6.92	6.88
	0.75	7.95	7.63	7.52
-45°	0.25	6.90	6.64	6.63
	0.50	6.92	6.68	6.62
	0.75	7.06	6.78	6.76
	0.95	7.61	7.29	7.28
0°	0.25	6.73	6.48	6.46
	0.50	6.72	6.42	6.41
	0.75	7.40	7.03	7.03
45°	0.25	6.48	6.29	6.29
	0.50	6.25	6.01	5.99
	0.75	6.23	5.96	5.97
	0.95	6.45	6.36	6.36
90°	0.25	7.05	6.74	6.72
	0.50	6.17	6.15	6.15
	0.75	6.90	6.62	6.62

<sup>a</sup> (Shu et al., 2001)

<sup>b</sup> (Ding et al., 2005)

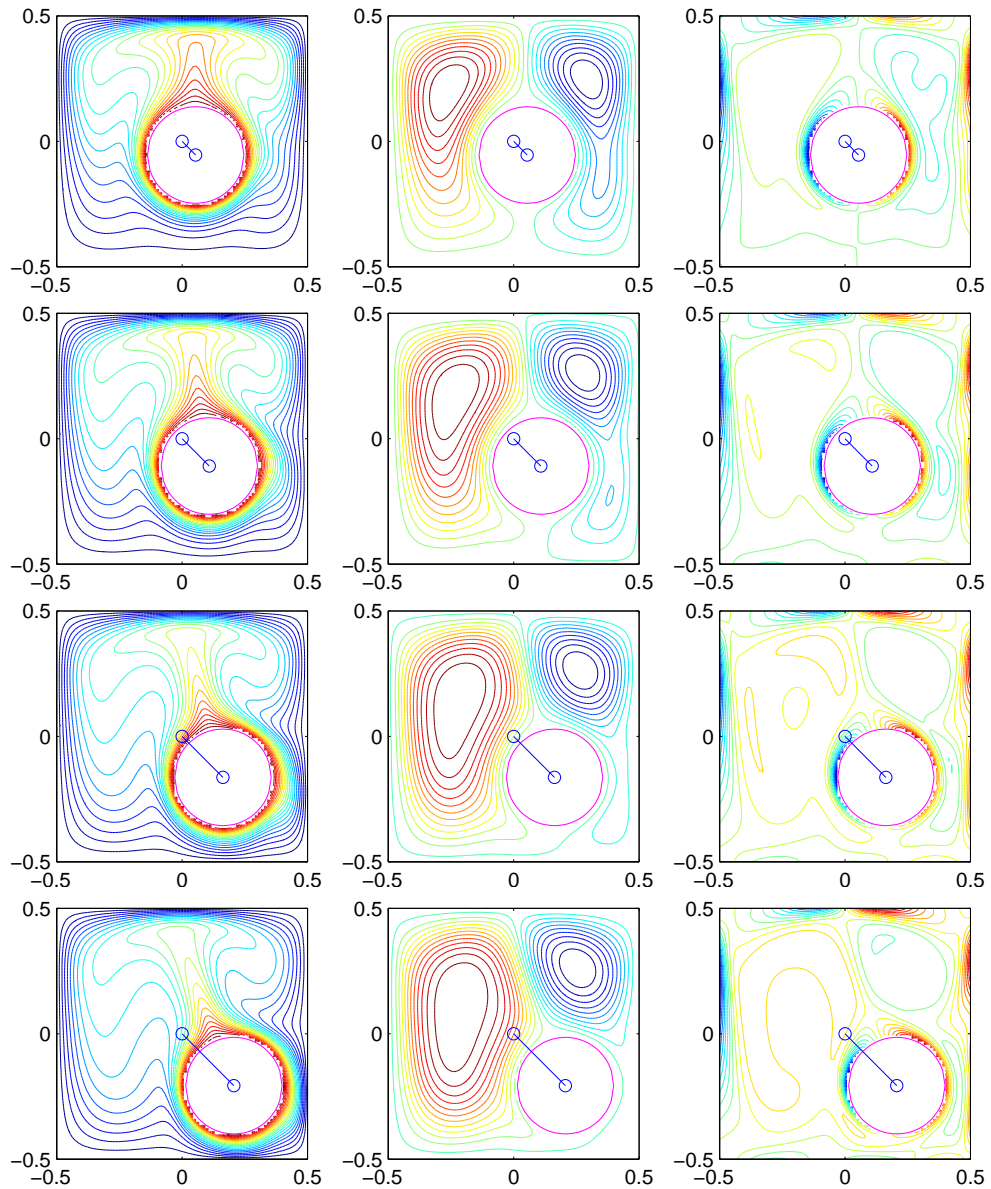


Figure 4.12: Eccentric annulus between a square outer cylinder and a circular inner cylinder: contours of temperature (left), stream function (middle) and vorticity (right) for the cases of  $\varepsilon_0 = 0.25, 0.50, 0.75$  and  $0.95$ , from top to bottom,  $Ra = 3 \times 10^5$ ,  $L/2R = 2.6$ ,  $\varphi = -45^\circ$ , using a grid of  $82 \times 82$ . Each plot contains 21 contour levels varying linearly from the minimum value to the maximum value.

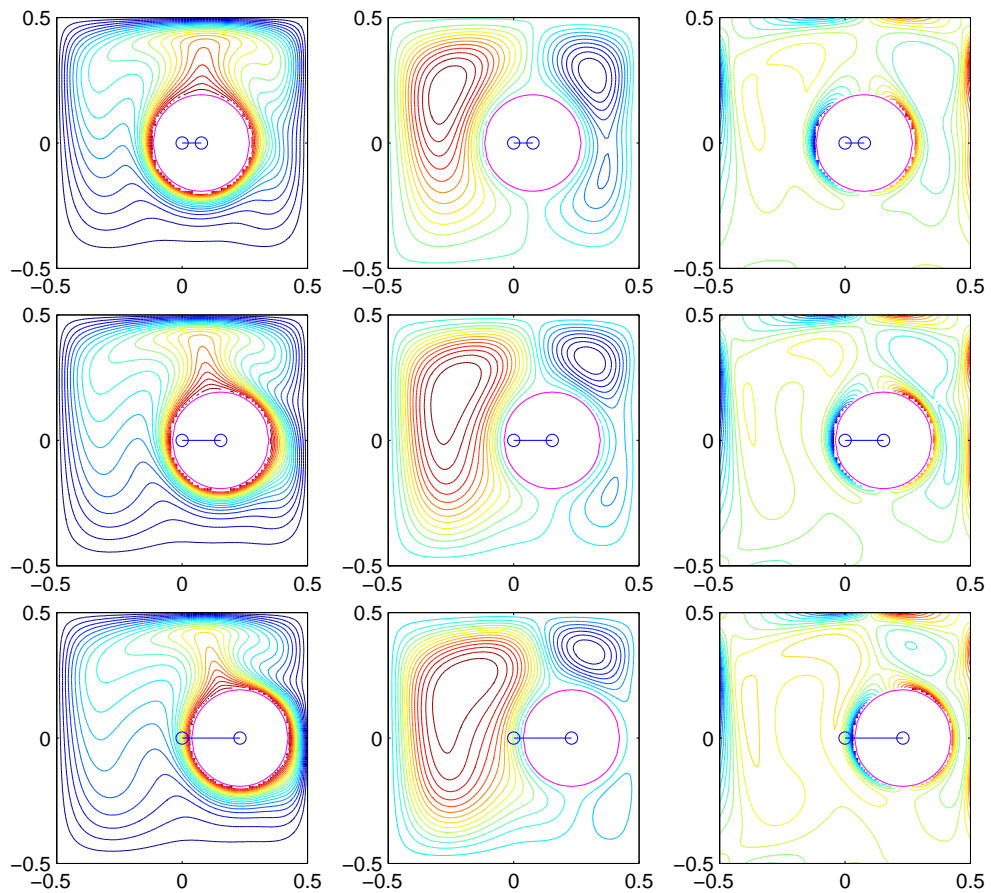


Figure 4.13: Eccentric annulus between a square outer cylinder and a circular inner cylinder: contours of temperature (left), stream function (middle) and vorticity (right) for the cases of  $\varepsilon_0 = 0.25, 0.50$  and  $0.75$ , from top to bottom,  $Ra = 3 \times 10^5$ ,  $L/2R = 2.6$ ,  $\varphi = 0^\circ$ , using a grid of  $108 \times 108$  for the case  $\varepsilon_0 = 0.75$  and a grid of  $82 \times 82$  for the others. Each plot contains 21 contour levels varying linearly from the minimum value to the maximum value.

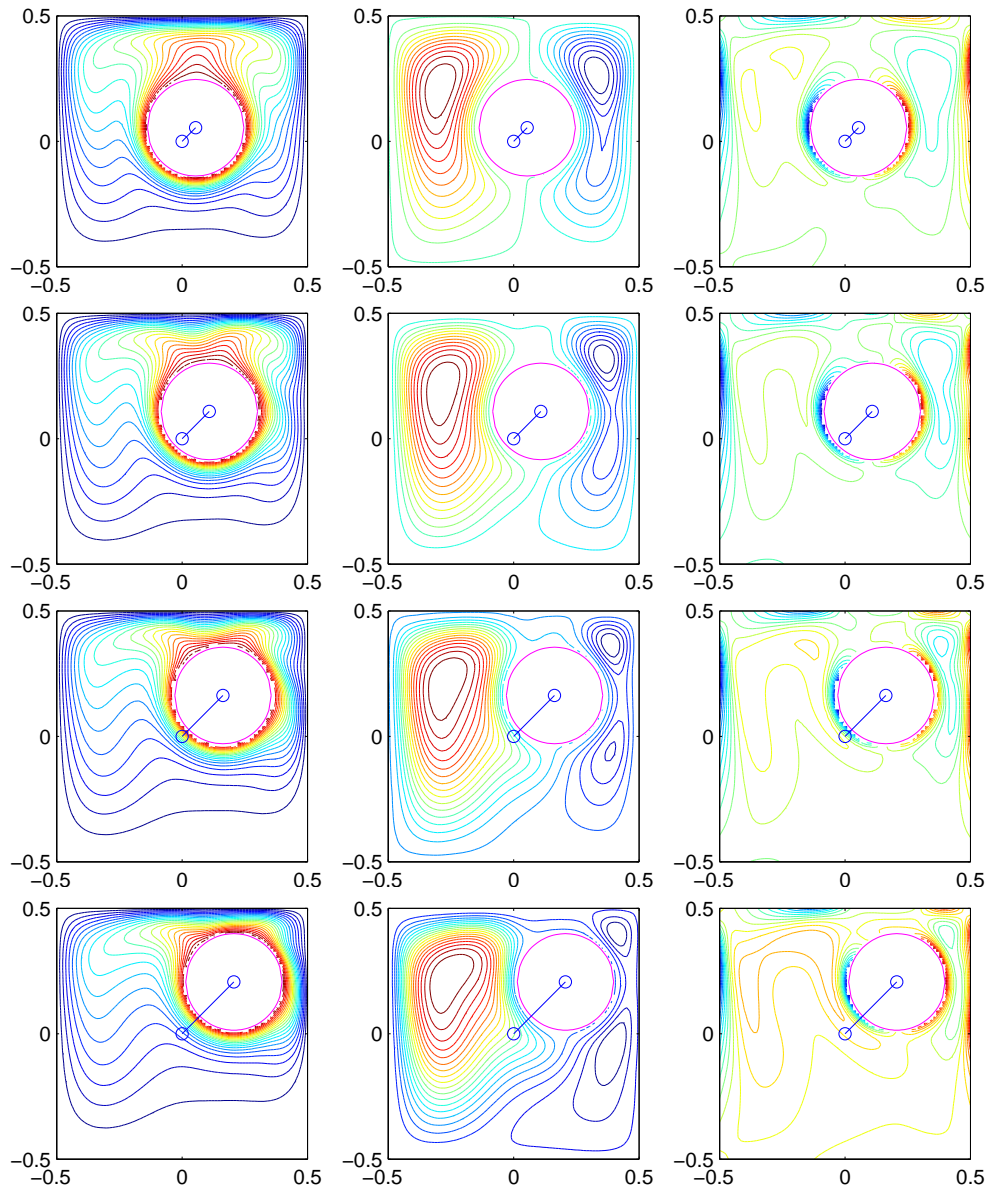


Figure 4.14: Eccentric annulus between a square outer cylinder and a circular inner cylinder: contours of temperature (left), stream function (middle) and vorticity (right) for the cases of  $\varepsilon_0 = 0.25, 0.50, 0.75$  and  $0.95$ , from top to bottom,  $Ra = 3 \times 10^5$ ,  $L/2R = 2.6$ ,  $\varphi = 45^\circ$ , using a grid of  $82 \times 82$ . Each plot contains 21 contour levels varying linearly from the minimum value to the maximum value.

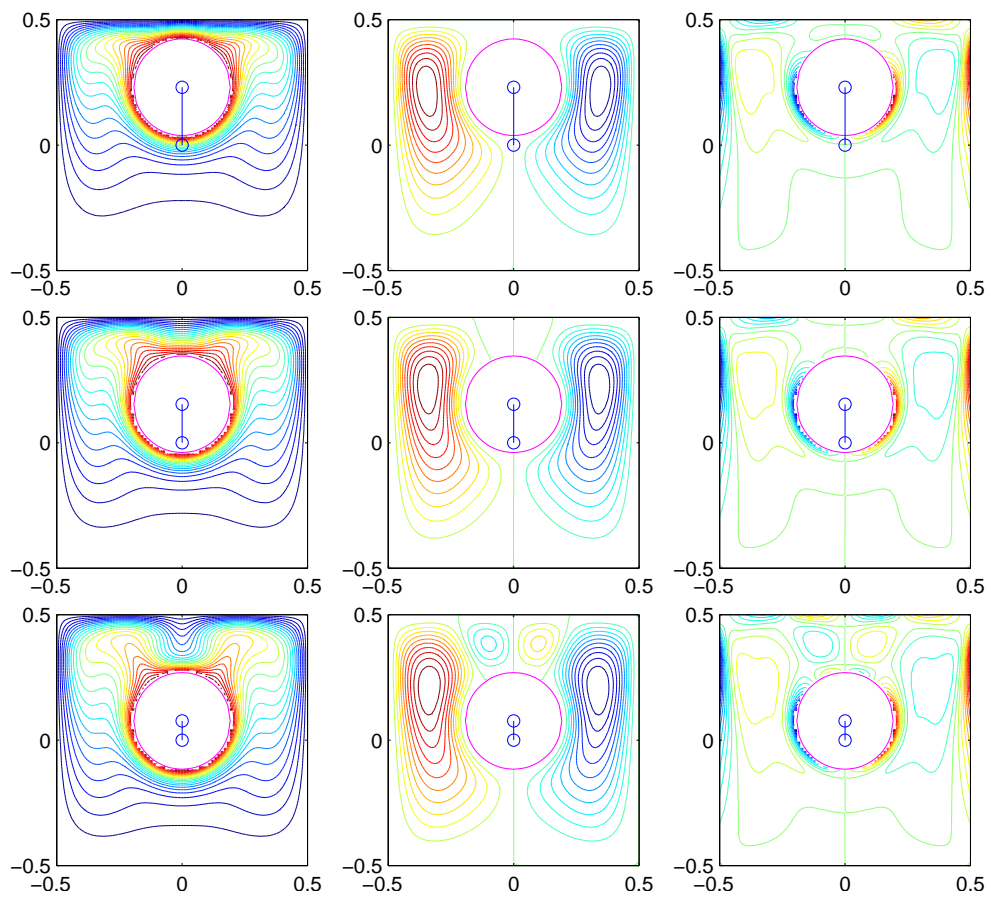


Figure 4.15: Eccentric annulus between a square outer cylinder and a circular inner cylinder: contours of temperature (left), stream function (middle) and vorticity (right) for the cases of  $\varepsilon_0 = 0.75, 0.50$  and  $0.25$ , from top to bottom,  $Ra = 3 \times 10^5$ ,  $L/2R = 2.6$ ,  $\varphi = 90^\circ$ , using a grid of  $108 \times 108$  for the case  $\varepsilon_0 = 0.75$  and a grid of  $82 \times 82$  for the others. Each plot contains 21 contour levels varying linearly from the minimum value to the maximum value.

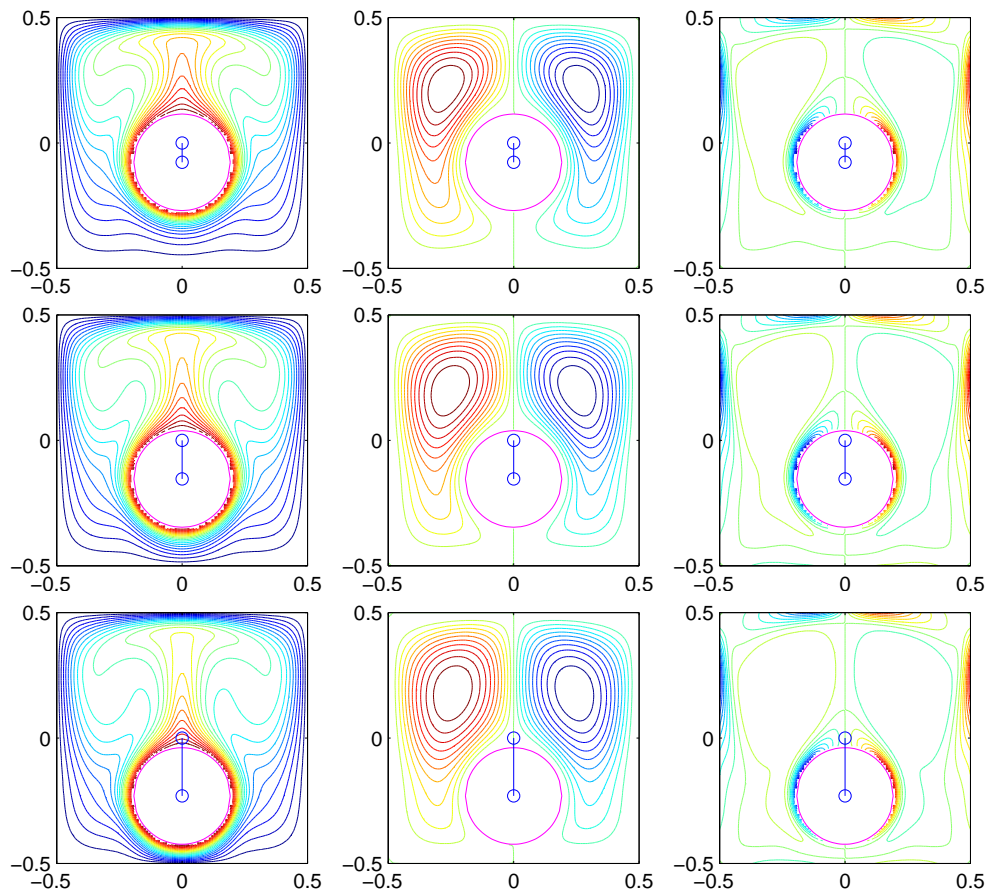


Figure 4.16: Eccentric annulus between a square outer cylinder and a circular inner cylinder: contours of temperature (left), stream function (middle) and vorticity (right) for the cases of  $\varepsilon_0 = 0.25, 0.50$  and  $0.75$ , from top to bottom,  $Ra = 3 \times 10^5$ ,  $L/2R = 2.6$ ,  $\varphi = -90^\circ$ , using a grid of  $108 \times 108$  for the case  $\varepsilon_0 = 0.75$  and a grid of  $82 \times 82$  for the others. Each plot contains 21 contour levels varying linearly from the minimum value to the maximum value.

## 4.5 Concluding remarks

The local MLS-1D-IRBFN method is developed and successfully applied to simulate the natural convection flows in multi-connected domains. The governing equations are formulated in terms of stream function, vorticity and temperature. The unknown stream function value on the inner boundary is determined by using the single-valued pressure condition. The diffusion terms are discretised by using the LMLS-1D-IRBFN while the nonlinear terms are calculated explicitly by using the 1D-IRBFN method. Uniform Cartesian grids are employed to represent all the problem domains. The numerical results showed that the LMLS-1D-IRBFN approximation produces a very sparse system matrix which helps save a lot of memory, while offers a high level of accuracy as that of the 1D-IRBFN method. The numerical results obtained for a wide range of Rayleigh number and various geometry parameters are in good agreement with the numerical data available in the literature.

# Chapter 5

## Local MLS-1D-IRBFN method for unsteady incompressible viscous flows

The local moving least square - one dimensional integrated radial basis function network (LMLS-1D-IRBFN) method has been devised for the analysis of steady incompressible viscous flow in Chapter 3 and natural convection in multiply-connected domains in Chapter 4. The LMLS-1D-IRBFN is now extended to a solution of time-dependent problems such as Burgers' equation, unsteady flow past a square cylinder in a horizontal channel and unsteady flow past a circular cylinder. The present method is combined with a domain decomposition technique to handle large-scale problems. The obtained numerical results compare favourably with other published results in the literature.

## 5.1 Introduction

Time-dependent analysis plays a very important role in the design of diverse engineering products and systems, e.g. in aerospace, automotive, marine and civil applications. In this chapter, a new efficient numerical method is developed for the solution of time-dependent problems and illustrated with examples such as the well-known Burgers' equation, unsteady flows past a square cylinder in a horizontal channel, and unsteady flows past a circular cylinder. Burgers' equation has been studied by many authors to verify their proposed numerical methods because it is the simplest nonlinear equation that includes convection and dissipation terms. Caldwell et al. (1987) presented a moving node finite element method to obtain a solution of Burgers' equation under different prescribed conditions. Iskander and Mohsen (1992) devised new algorithms based on a combination of linearization and splitting-up for solving this equation. Hon and Mao (1998) solved Burgers' equation using multiquadric (MQ) for spatial discretisation and a low order explicit finite difference scheme for temporal discretisation. Their numerical results indicated that the major numerical error is from the time integration instead of the MQ spatial approximation. Hassanien et al. (2005) developed fourth-order finite difference method based on two-level three-point finite difference for solving Burgers' equation. Hashemian and Shodja (2008) proposed a gradient reproducing kernel particle method (GRKPM) for spatial discretisation of Burgers' equation to obtain equivalent nonlinear ordinary differential equations which are then discretised in time by the Gear's method. Hosseini and Hashemi (2011) presented a local-RBF meshless method for solving Burgers' equation with different initial and boundary conditions.

Flows past a circular cylinder have been extensively studied by many researchers to verify their new numerical methods for irregular domains. There is no singularity on a circular cylinder surface and the flow field behind the cylinder contains a variety of fluid dynamic phenomena, which makes the problem inter-

esting as a benchmark. Cheng et al. (2001) applied a discrete vortex method to investigate an unsteady flow past a rotationally oscillating circular cylinder for different values of oscillating amplitude and frequency at a Reynolds number of 200. Based on the numerical results obtained, they provided a map of lock-on and non-lock-on regions which helps to classify the different vortex structure in the wake with respect to the oscillating amplitude and frequency of the cylinder.

For the problem of flow past a square cylinder, singularities occur at the corners of the square cylinder, which poses some challenges in terms of accurate determination of such singularities. In order to obtain a convergent solution, very dense grids are usually generated near the singularities. Davis and Moore (1982) studied unsteady flow past a rectangular cylinder using finite difference method (FDM) with third-order upwind differencing for convection, standard central scheme for diffusion terms and a Leith-type scheme for time integration. Zaki et al. (1994) conducted a numerical study of flow past a fixed square cylinder at various angles of incidence for Reynolds numbers up to 250. Their numerical simulation was based on the stream function-vorticity formulation of the Navier-Stokes equation together with a single-valued pressure condition to make the problem well-posed. Sohankar et al. (1998) presented calculations of unsteady 2-D flows around a square cylinder at different angles of incidence using an incompressible SIMPLEC finite volume code with a non-staggered grid arrangement. The convective terms were discretised using the third-order QUICK differencing scheme, while the diffusive terms were discretised using central differences. Breuer et al. (2000) investigated a confined flow around a square cylinder in a channel with blockage ratio of  $1/8$  by a lattice-Boltzmann automata (LBA) and a finite volume method (FVM). Turki et al. (2003) studied an unsteady flow and heat transfer characteristics in a channel with a heated square cylinder using a control volume finite element method (CVFEM) adapted to a staggered grid. In their work, the influences of blockage ratio, Reynolds number and Richardson number on the flow pattern were investigated. Berrone and Marro (2009) applied a space-time adaptive method to solve unsteady flow

problems including flows over backward facing step and flows past a square cylinder in a channel. Moussaoui et al. (2010) simulated a 2-D flow and heat transfer in a horizontal channel obstructed by an inclined square cylinder using a hybrid scheme with lattice Boltzmann method to determine the velocity field and FDM to solve the energy equation.

Dhiman et al. (2005) investigated influences of blockage ratio, Prandtl number and Peclet number on the flow and heat transfer characteristics of an isolated square cylinder confined in a channel in a 2-D steady flow regime ( $1 \leq Re \leq 45$ ) using semi-explicit FEM on a non-uniform Cartesian grid. The third order QUICK scheme was used to discretise the convection terms, while the second-order central difference scheme was used to discretise the diffusion terms. The semi-explicit FEM was also applied to a steady laminar mixed convection flow across a heated square cylinder in a channel (Dhiman et al., 2008). Sahu et al. (2010) conducted a study of 2-D unsteady flow of power-law fluids past a square cylinder confined in a channel for different values of Reynolds number ( $60 \leq Re \leq 160$ ), blockage ratio ( $\beta_0 = 1/6, 1/4$  and  $1/2$ ) and power-law flow behaviour index ( $0.5 \leq n \leq 1.8$ ) using the semi-explicit FEM. Bouaziz et al. (2010) employed a control volume finite element method (CVFEM) adapted to the staggered grid to study an unsteady laminar flow and heat transfer of power-law fluids in 2-D horizontal plane channel with a heated square cylinder.

In the past decades, some mesh-free and local RBF-based methods have been developed for solving fluid flow problems. Shu et al. (2003) presented a local RBF-based differential quadrature method (local RBF-DQ) for a simulation of natural convection in a square cavity. In their study, three layers of orthogonal grid near and including the boundary were generated for imposing the Neumann condition of temperature and the vorticity on the wall. The derivatives of the field variables in the boundary conditions were then discretised by the conventional one-sided second order finite difference scheme. The local RBF-DQ method was also employed for solving several cases of incompressible flows

including a driven-cavity flow, flow past a cylinder, and flow around two staggered circular cylinders (Shu et al., 2005). Ding et al. (2007) presented the mesh-free least square-based finite difference (MLSFD) method to simulate a flow field around two circular cylinders arranged in tandem and side-by-side. Vertnik and Šarler (2006) presented an explicit local RBF collocation method for diffusion problems. Sanyasiraju and Chandhini (2008) developed a local RBF based gridfree scheme for unsteady incompressible viscous flows in terms of primitive variables. Chen et al. (2008) employed a partition of unity concept (Babuška and Melenk, 1997) to combine the reproducing kernel and RBF approximations to yield a local approximation that enjoys the exponential convergence of RBF and improves the conditioning of the discrete system. Le et al. (2010) proposed a locally supported moving IRBFN-based meshless method for solving various problems including heat transfer, elasticity of both compressible and incompressible materials, and linear static crack problems.

Another approach for solving PDEs is the so-called Cartesian grid method where the governing equations are discretised with a fixed Cartesian grid. This approach significantly reduces the grid generation cost and has a great potential over the conventional body-fitted methods when solving problems with moving boundary and complicated geometry. Udaykumar et al. (2001) presented a Cartesian grid method for computing fluid flows with complex immersed and moving boundaries. The incompressible Navier-Stokes equations are discretised using a second-order FVM, and second-order fractional-step scheme is employed for time integration. Russell and Wang (2003) presented a Cartesian grid method for solving 2-D incompressible viscous flows around multiple moving objects based on stream function-vorticity formulation. Zheng and Zhang (2008) employed an immersed-boundary method to predict the flow structure around a transversely oscillating cylinder. The influences of oscillating frequency on the drag and lift acting on the cylinder were investigated.

As an alternative to the conventional differentiated radial basis function network

(DRBFN) method (Kansa, 1990b), Mai-Duy and Tran-Cong (2001a) proposed the use of integration to construct the RBFN expressions (the IRBFN method) for the approximation of a function and its derivatives and for the solution of PDEs. Numerical results showed that the IRBFN method achieves superior accuracy (Mai-Duy and Tran-Cong, 2001a,b). Mai-Cao and Tran-Cong (2005) developed numerical schemes combining the IRBFN method with different time integration techniques for solving time-dependent parabolic PDEs, hyperbolic PDEs, and advection-diffusion equations. A one-dimensional integrated radial basis function network (1D-IRBFN) collocation method for the solution of second- and fourth-order PDEs was presented by Mai-Duy and Tanner (2007). The 1D-IRBFN method is much more efficient than the original IRBFN method reported in Mai-Duy and Tran-Cong (2001a). Le-Cao et al. (2011) employed the 1D-IRBFN method to simulate unsymmetrical flows of a Newtonian fluid in multiply-connected domains using the stream-function and temperature formulation. Ngo-Cong et al. (2011) extended this method to investigate free vibration of composite laminated plates based on first-order shear deformation theory (Chapter 2). Ngo-Cong et al. (2012) proposed a local moving least square - one dimensional integrated radial basis function network method (LMLS-1D-IRBFN) for simulating 2-D steady incompressible viscous flows in terms of stream function and vorticity (Chapter 3). In the present chapter, we further extend the LMLS-1D-IRBFN method for solving time-dependent problems and demonstrate the new procedure with the simulation of Burgers' equation, unsteady flows past a square cylinder in a horizontal channel, and unsteady flows past a circular cylinder. The present numerical procedure is combined with a domain decomposition technique to handle large-scale problems.

The chapter is organised as follows. The LMLS-1D-IRBFN method is presented in Section 5.2. The governing equations for incompressible viscous flows are given in Section 5.3. Several numerical examples are investigated using the proposed method in Section 5.4. Section 5.5 concludes the chapter.

## 5.2 Local moving least square - one dimensional integrated radial basis function network technique

A schematic outline of the LMLS-1D-IRBFN method is depicted in Figure 5.1. The proposed method with 3-node support domains ( $n = 3$ ) and 5-node local 1D-IRBF networks ( $n_s = 5$ ) is presented here. On an  $x$ -grid line  $[l]$ , a global interpolant for the field variable at a grid point  $x_i$  is sought in the form

$$u(x_i) = \sum_{j=1}^n \bar{\phi}_j(x_i) u^{[j]}(x_i), \quad (5.1)$$

where  $\{\bar{\phi}_j\}_{j=1}^n$  is a set of the partition of unity functions constructed using MLS approximants (Liu, 2003);  $u^{[j]}(x_i)$  the nodal function value obtained from a local interpolant represented by a 1D-IRBF network  $[j]$ ;  $n$  the number of nodes in the support domain of  $x_i$ . In (5.1), MLS approximants are presently based on linear polynomials, which are defined in terms of 1 and  $x$ . It is noted that the MLS shape functions possess a so-called partition of unity properties as follows.

$$\sum_{j=1}^n \bar{\phi}_j(x) = 1. \quad (5.2)$$

Relevant derivatives of  $u$  at  $x_i$  can be obtained by differentiating (5.1)

$$\frac{\partial u(x_i)}{\partial x} = \sum_{j=1}^n \left( \frac{\partial \bar{\phi}_j(x_i)}{\partial x} u^{[j]}(x_i) + \bar{\phi}_j(x_i) \frac{\partial u^{[j]}(x_i)}{\partial x} \right), \quad (5.3)$$

$$\frac{\partial^2 u(x_i)}{\partial x^2} = \sum_{j=1}^n \left( \frac{\partial^2 \bar{\phi}_j(x_i)}{\partial x^2} u^{[j]}(x_i) + 2 \frac{\partial \bar{\phi}_j(x_i)}{\partial x} \frac{\partial u^{[j]}(x_i)}{\partial x} + \bar{\phi}_j(x_i) \frac{\partial^2 u^{[j]}(x_i)}{\partial x^2} \right), \quad (5.4)$$

where the values  $u^{[j]}(x_i)$ ,  $\partial u^{[j]}(x_i)/\partial x$  and  $\partial^2 u^{[j]}(x_i)/\partial x^2$  are calculated from 1D-IRBFN networks with  $n_s$  nodes.

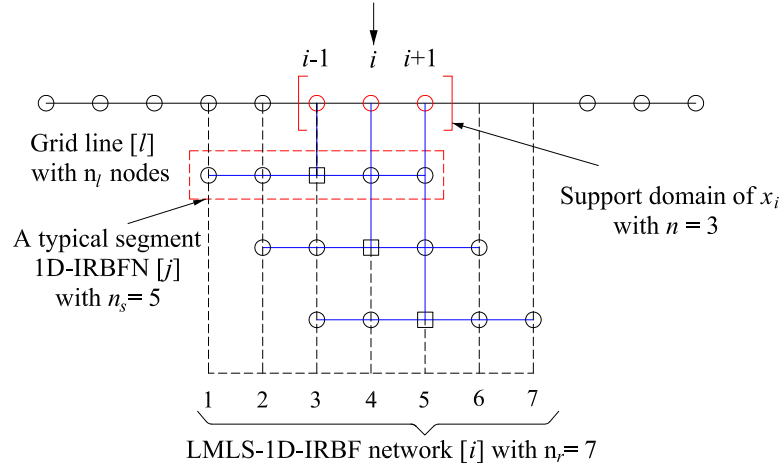


Figure 5.1: LMLS-1D-IRBFN scheme,  $\square$  a typical [j] node.

Full details of the LMLS-1D-IRBFN method can be found in Chapter 3.

### 5.3 Governing equations for 2-D unsteady incompressible viscous flows

The governing equations for 2-D incompressible viscous flows written in terms of stream function  $\psi$  and vorticity  $\omega$  are given by

$$\frac{\partial^2 \psi}{\partial x^2} + \frac{\partial^2 \psi}{\partial y^2} = -\omega, \quad (5.5)$$

$$\frac{1}{Re} \left( \frac{\partial^2 \omega}{\partial x^2} + \frac{\partial^2 \omega}{\partial y^2} \right) = \frac{\partial \omega}{\partial t} + \left( \frac{\partial \psi}{\partial y} \frac{\partial \omega}{\partial x} - \frac{\partial \psi}{\partial x} \frac{\partial \omega}{\partial y} \right), \quad (5.6)$$

where  $Re$  is the Reynolds number,  $t$  the time, and  $(x, y)^T$  the position vector. The  $x$  and  $y$  components of the velocity vector can be defined in terms of the

stream function as

$$u = \frac{\partial \psi}{\partial y}, \quad (5.7)$$

$$v = -\frac{\partial \psi}{\partial x}. \quad (5.8)$$

The computational boundary conditions for vorticity can be computed as

$$\omega_w = -\left(\frac{\partial^2 \psi_w}{\partial x^2} + \frac{\partial^2 \psi_w}{\partial y^2}\right) \quad (5.9)$$

where the subscript  $w$  is used to denote quantities on the boundary. For curved boundaries, a formula reported in (Le-Cao et al., 2009) is employed here to derive the vorticity boundary conditions at boundary points on  $x$ - and  $y$ -grid lines as follows.

$$\omega_w^{(x)} = -\left[1 + \left(\frac{t_x}{t_y}\right)^2\right] \frac{\partial^2 \psi_w}{\partial x^2} - q_y, \quad (5.10)$$

$$\omega_w^{(y)} = -\left[1 + \left(\frac{t_y}{t_x}\right)^2\right] \frac{\partial^2 \psi_w}{\partial y^2} - q_x, \quad (5.11)$$

where  $q_x$  and  $q_y$  are known quantities defined by

$$q_x = -\frac{t_y}{t_x^2} \frac{\partial^2 \psi_w}{\partial y \partial s} + \frac{1}{t_x} \frac{\partial^2 \psi_w}{\partial x \partial s}, \quad (5.12)$$

$$q_y = -\frac{t_x}{t_y^2} \frac{\partial^2 \psi_w}{\partial x \partial s} + \frac{1}{t_y} \frac{\partial^2 \psi_w}{\partial y \partial s}, \quad (5.13)$$

in which  $t_x = \partial x / \partial s$ ,  $t_y = \partial y / \partial s$  and  $s$  is the direction tangential to the curved surface.

Boundary conditions for stream function are specified in the following examples.

## 5.4 Numerical results and discussion

Several time-dependent problems are considered in this section to study the performance of the present numerical procedure. The domains of interest are discretised using Cartesian grids. The simple Euler scheme is used for time integration. For Burgers' equation, the LMLS-1D-IRBFN method is employed to discretise both diffusion and convection terms. For fluid flow problems, the LMLS-1D-IRBFN is used to discretise the diffusion terms while the convection terms are explicitly calculated by using the 1D-IRBFN technique. A domain decomposition technique is employed for solving the fluid flow problems. By using the LMLS-1D-IRBFN method to discretise the left hand side of governing equations and the LU decomposition technique to solve the resultant sparse system of simultaneous equations, the computational cost and data storage requirements are reduced.

### 5.4.1 Example 1: Burgers' equation

The present numerical method is first verified through the solution of Burgers' equation as follows.

$$\frac{\partial u}{\partial t} + u \frac{\partial u}{\partial x} = \frac{1}{Re} \frac{\partial^2 u}{\partial x^2}. \quad (5.14)$$

The diffusion and convection terms in Equation (5.14) are discretised on a uniform grid using LMLS-1D-IRBFN method implicitly and explicitly, respectively.

#### Approximation of shock wave propagation

Consider the Burgers' equation (5.14) defined on a segment  $0 \leq x \leq 1, t \geq 0$  and subject to Dirichlet boundary conditions. The initial and boundary conditions

can be calculated from the following analytical solution (Hassanien et al., 2005; Hosseini and Hashemi, 2011)

$$u_E(x, t) = \frac{[\alpha_0 + \mu_0 + (\mu_0 - \alpha_0) \exp(\eta)]}{1 + \exp(\eta)}, \quad (5.15)$$

where  $\eta = \alpha_0 Re(x - \mu_0 t - \beta_0)$ ,  $\alpha_0 = 0.4$ ,  $\beta_0 = 0.125$ ,  $\mu_0 = 0.6$ ,  $Re = 100$ .

Table 5.1 shows the comparison among the numerical results of LMLS-1D-IRBFN and 1D-IRBFN methods and the exact solution at time  $t = 1.0$  for several time step sizes and using a grid of 61. It can be seen that the accuracy is greatly improved by reducing the time step. Grid convergence studies for both methods with the same time step of  $10^{-3}$  are given in Table 5.2. The numerical results show that the accuracy is not improved much with increasing grid density for both methods, which indicates that the major numerical error is not from the LMLS-1D-IRBFN and 1D-IRBFN spatial approximation, but from the temporal discretisation. It is noted that the LMLS-1D-IRBFN method offers the same level of accuracy as the 1D-IRBFN method.

### Sinusoidal initial condition

Consider the Burgers' Equation (5.14) defined on a segment  $0 \leq x \leq 1, t \geq 0$  and subject to the following Dirichlet boundary conditions and initial condition.

$$u(0, t) = u(1, t) = 0, \quad t > 0, \quad (5.16)$$

$$u(x, 0) = \sin \pi x, \quad 0 \leq x \leq 1. \quad (5.17)$$

The corresponding analytical solution was found by Cole (1951) as follows.

$$u_E(x, t) = \frac{2\pi\varepsilon \sum_{j=1}^{\infty} j k_j \sin(j\pi x) \exp(-j^2 \pi^2 \varepsilon t)}{k_0 + \sum_{j=1}^{\infty} k_j \cos(j\pi x) \exp(-j^2 \pi^2 \varepsilon t)}, \quad (5.18)$$

Table 5.1: Burgers' equations, approximation of shock wave propagation: comparison of numerical results and exact solution at  $t = 1.0$  for  $Re = 100$  and several time step sizes, using a grid of 61. (1) 1D-IRBFN, (2) LMLS-1D-IRBFN

$x$	Exact	$dt = 10^{-2}$		$dt = 10^{-3}$		$dt = 10^{-4}$	
		(1)	(2)	(1)	(2)	(1)	(2)
0.000	1.0000	1.0000	1.0000	1.0000	1.0000	1.0000	1.0000
0.056	1.0000	1.0000	1.0000	1.0000	1.0000	1.0000	1.0000
0.111	1.0000	1.0000	1.0000	1.0000	1.0000	1.0000	1.0000
0.167	1.0000	1.0000	1.0000	1.0000	1.0000	1.0000	1.0000
0.222	0.9998	1.0000	1.0000	0.9999	0.9998	0.9998	0.9998
0.278	0.9978	1.0000	0.9999	0.9983	0.9982	0.9980	0.9979
0.333	0.9801	0.9991	0.9988	0.9829	0.9831	0.9808	0.9810
0.389	0.8473	0.9153	0.9145	0.8545	0.8547	0.8495	0.8496
0.444	0.4518	0.4516	0.4526	0.4533	0.4539	0.4533	0.4539
0.500	0.2379	0.2387	0.2383	0.2382	0.2379	0.2381	0.2379
0.556	0.2043	0.2050	0.2050	0.2044	0.2044	0.2043	0.2043
0.611	0.2005	0.2006	0.2006	0.2005	0.2005	0.2005	0.2005
0.667	0.2001	0.2001	0.2001	0.2001	0.2001	0.2001	0.2001
0.722	0.2000	0.2000	0.2000	0.2000	0.2000	0.2000	0.2000
0.778	0.2000	0.2000	0.2000	0.2000	0.2000	0.2000	0.2000
0.833	0.2000	0.2000	0.2000	0.2000	0.2000	0.2000	0.2000
0.889	0.2000	0.2000	0.2000	0.2000	0.2000	0.2000	0.2000
0.944	0.2000	0.2000	0.2000	0.2000	0.2000	0.2000	0.2000
1.000	0.2000	0.2000	0.2000	0.2000	0.2000	0.2000	0.2000
$Ne$		2.45E-02	2.42E-02	2.75E-03	2.86E-03	9.51E-04	1.12E-03

where  $\varepsilon = 1/Re$ ,  $k_0 = \int_0^1 \exp(-1 - \cos \pi x / 2\pi\varepsilon) dx$ , and

$$k_j = 2 \int_0^1 \cos(j\pi x) \exp(-1 - \cos \pi x / 2\pi\varepsilon) dx.$$

Table 5.3 presents the numerical results at several positions  $x$  and times  $t$  for Reynolds number of 10 and several grid sizes in comparison with the exact solution and the numerical results of Hosseini and Hashemi (2011) who used a local-RBF collocation for spatial discretisation and the explicit Euler scheme for time discretisation, while the corresponding comparison for the case of Reynolds number of 100 is given in Table 5.4. For the purpose of comparison, the same time step is taken to be  $10^{-3}$  in these cases. It can be seen that the present numerical results are slightly more accurate than those of the local-RBF in general.

The numerical results for the case of a large Reynolds number of 10000 at time

Table 5.2: Burgers' equations, approximation of shock wave propagation: grid convergence study of numerical results for  $Re = 100$ ,  $t = 1.0$ , and  $\Delta t = 10^{-3}$ . (1) 1D-IRBFN, (2) LMLS-1D-IRBFN

$x$	Exact	$n_x = 41$		$n_x = 61$		$n_x = 81$	
		(1)	(2)	(1)	(2)	(1)	(2)
0.000	1.0000	1.0000	1.0000	1.0000	1.0000	1.0000	1.0000
0.056	1.0000	1.0000	1.0000	1.0000	1.0000	1.0000	1.0000
0.111	1.0000	1.0000	1.0000	1.0000	1.0000	1.0000	1.0000
0.167	1.0000	1.0000	1.0000	1.0000	1.0000	1.0000	1.0000
0.222	0.9998	0.9999	0.9998	0.9999	0.9998	0.9999	0.9998
0.278	0.9978	0.9983	0.9979	0.9983	0.9982	0.9983	0.9983
0.333	0.9801	0.9829	0.9848	0.9829	0.9831	0.9829	0.9829
0.389	0.8473	0.8546	0.8554	0.8545	0.8547	0.8545	0.8546
0.444	0.4518	0.4534	0.4552	0.4533	0.4539	0.4533	0.4535
0.500	0.2379	0.2381	0.2372	0.2382	0.2379	0.2382	0.2381
0.556	0.2043	0.2044	0.2043	0.2044	0.2044	0.2044	0.2044
0.611	0.2005	0.2005	0.2005	0.2005	0.2005	0.2005	0.2005
0.667	0.2001	0.2001	0.2001	0.2001	0.2001	0.2001	0.2001
0.722	0.2000	0.2000	0.2000	0.2000	0.2000	0.2000	0.2000
0.778	0.2000	0.2000	0.2000	0.2000	0.2000	0.2000	0.2000
0.833	0.2000	0.2000	0.2000	0.2000	0.2000	0.2000	0.2000
0.889	0.2000	0.2000	0.2000	0.2000	0.2000	0.2000	0.2000
0.944	0.2000	0.2000	0.2000	0.2000	0.2000	0.2000	0.2000
1.000	0.2000	0.2000	0.2000	0.2000	0.2000	0.2000	0.2000
$Ne$		2.78E-03	3.48E-03	2.75E-03	2.86E-03	2.75E-03	2.78E-03

$t = 1.0$  are described in Tables 5.5 and 5.6 using the same grid size of 301 and the same time step of  $10^{-4}$  as reported in (Hosseini and Hashemi, 2011). Table 5.5 gives the numerical results at a uniform grid with a grid spacing of  $1/8$  in comparison with the exact solution and the results of other authors, while the corresponding comparison of numerical results at the same grid positions as reported in (Hassanien et al., 2005; Hashemian and Shodja, 2008; Hosseini and Hashemi, 2011) are provided in Table 5.6. Those comparisons show that the present numerical results are in good agreement with the exact and other numerical method solutions.

Table 5.3: Burgers' equations, sinusoidal initial condition: comparison among the numerical results of LMLS-1D-IRBFN and Local-RBF (Hosseini and Hashemi, 2011) and the analytical solution for  $Re = 10$ ,  $\Delta t = 10^{-3}$ .

$x$	$t$	Exact	$n_x = 9$		$n_x = 33$		$n_x = 57$		$n_x = 81$	
			Present	Local-RBF	Present	Local-RBF	Present	Local-RBF	Present	Local-RBF
0.25	0.4	0.30889	0.30820	0.30817	0.30838	0.30821	0.30838	0.30862	0.30839	
	0.6	0.24074	0.24025	0.24026	0.24040	0.24030	0.24040	0.24059	0.24040	
	0.8	0.19568	0.19556	0.19533	0.19543	0.19537	0.19543	0.19560	0.19543	
	1.0	0.16256	0.16291	0.16230	0.16238	0.16234	0.16238	0.16253	0.16238	
0.50	0.4	0.56963	0.57036	0.56861	0.56896	0.56867	0.56896	0.56929	0.56896	
	0.6	0.44721	0.44865	0.44643	0.44670	0.44651	0.44669	0.44701	0.44669	
	0.8	0.35924	0.36150	0.35863	0.35886	0.35871	0.35885	0.35913	0.35885	
	1.0	0.29192	0.29463	0.29142	0.29163	0.29150	0.29162	0.29187	0.29162	
0.75	0.4	0.04021	0.04081	0.04011	0.04020	0.04015	0.04020	0.04025	0.04020	
	0.6	0.62544	0.62926	0.62486	0.62515	0.62496	0.62511	0.62540	0.62511	
	0.8	0.48721	0.49318	0.48646	0.48695	0.48658	0.48691	0.48712	0.48691	
	1.0	0.37392	0.37992	0.37322	0.37371	0.37333	0.37369	0.37385	0.37369	
	3.0	0.28747	0.29251	0.28688	0.28732	0.28698	0.28731	0.28744	0.28731	
	3.0	0.02977	0.03021	0.02970	0.02977	0.02973	0.02977	0.02981	0.02977	

Table 5.4: Burgers' equations, sinusoidal initial condition: comparison among the numerical results of LMLS-1D-IRBFN and Local-RBF (Hosseini and Hashemi, 2011) and the analytical solution for  $Re = 100$ ,  $\Delta t = 10^{-3}$ .

$x$	$t$	Exact	$n_x = 9$		$n_x = 33$		$n_x = 57$		$n_x = 81$	
			Present	Local-RBF	Present	Local-RBF	Present	Local-RBF	Present	Local-RBF
0.25	0.4	0.34191	0.33414	0.33395	0.34114	0.33396	0.34114	0.33794	0.34114	
	0.6	0.26896	0.26353	0.26328	0.26841	0.26328	0.26841	0.26613	0.26841	
	0.8	0.22148	0.21759	0.21722	0.22107	0.21723	0.22107	0.21936	0.22107	
	1.0	0.18819	0.18523	0.18488	0.18787	0.18489	0.18787	0.18655	0.18787	
0.50	0.4	0.07511	0.07416	0.07438	0.07504	0.07438	0.07504	0.07476	0.07504	
	0.6	0.66071	0.64995	0.64907	0.65961	0.64908	0.65961	0.65496	0.65961	
	0.8	0.52942	0.51822	0.51971	0.52848	0.51972	0.52849	0.52461	0.52849	
	1.0	0.43914	0.42785	0.43139	0.43839	0.43140	0.43839	0.43530	0.43839	
0.75	0.4	0.37442	0.36512	0.36820	0.37381	0.36821	0.37381	0.37134	0.37381	
	0.6	0.15018	0.14802	0.14872	0.15003	0.14873	0.15004	0.14947	0.15004	
	0.8	0.91026	0.85640	0.90742	0.91011	0.90749	0.91014	0.90905	0.91015	
	1.0	0.76724	0.65947	0.75810	0.76643	0.75814	0.76643	0.76282	0.76643	
	0.8	0.64740	0.55693	0.63810	0.64651	0.63812	0.64652	0.64284	0.64652	
	1.0	0.55605	0.48796	0.54787	0.55524	0.54789	0.55527	0.55202	0.55527	
	3.0	0.22481	0.20834	0.22261	0.22449	0.22265	0.22459	0.22376	0.22459	

Table 5.5: Burgers' equations, sinusoidal initial condition: comparison among numerical results and exact solution for  $Re = 10000$ ,  $\Delta t = 10^{-4}$ , using a grid of 301.

$x$	Exact	Caldwell, Wanless and Cook (1987)	Iskander and Mohsen (1992)	Hon and Mao (1998)	Present
0.056	0.0422	0.0422	0.0419	0.0424	0.0421
0.111	0.0843	0.0844	0.0839	0.0843	0.0842
0.167	0.1263	0.1266	0.1253	0.1263	0.1263
0.222	0.1684	0.1687	0.1692	0.1684	0.1683
0.278	0.2103	0.2108	0.2034	0.2103	0.2103
0.333	0.2522	0.2527	0.2666	0.2522	0.2521
0.389	0.2939	0.2946	0.2527	0.2939	0.2939
0.444	0.3355	0.3362	0.3966	0.3355	0.3355
0.500	0.3769	0.3778	0.2350	0.3769	0.3769
0.556	0.4182	0.4191	0.5480	0.4182	0.4182
0.611	0.4592	0.4601	0.2578	0.4592	0.4592
0.667	0.5000	0.5009	0.6049	0.4999	0.4999
0.722	0.5404	0.5414	0.6014	0.5404	0.5404
0.778	0.5806	0.5816	0.4630	0.5802	0.5805
0.833	0.6203	0.6213	0.7011	0.6201	0.6202
0.889	0.6596	0.6605	0.6717	0.6600	0.6595
0.944	0.6983	0.6992	0.7261	0.6957	0.6982

Table 5.6: Burgers' equations, sinusoidal initial condition: comparison of numerical results for  $Re = 10000$ ,  $\Delta t = 10^{-4}$ , using a grid of 301.

$x$	Hassanien, Salama and Hosham (2005)	Hashemian and Shodja (2008)	Hosseini and Hashemi (2011)	Present
0.050	0.0379	0.0379	0.0379	0.0379
0.110	0.0834	0.0834	0.0833	0.0834
0.160	0.1213	0.1213	0.1212	0.1213
0.220	0.1667	0.1667	0.1666	0.1667
0.270	0.2044	0.2044	0.2044	0.2044
0.330	0.2469	0.2497	0.2496	0.2496
0.380	0.2872	0.2872	0.2871	0.2872
0.440	0.3322	0.3322	0.3321	0.3322
0.500	0.3769	0.3769	0.3768	0.3769
0.550	0.4140	0.4141	0.4140	0.4140
0.610	0.4584	0.4584	0.4583	0.4583
0.660	0.4951	0.4951	0.4950	0.4950
0.720	0.5388	0.5388	0.5387	0.5388
0.770	0.5749	0.5749	0.5748	0.5749
0.830	0.6179	0.6179	0.6178	0.6179
0.880	0.6533	0.6533	0.6530	0.6532
0.940	0.6952	0.6952	0.6890	0.6941

### 5.4.2 Example 2: Steady and unsteady flows past a square cylinder in a horizontal channel

The steady and unsteady flows past a square cylinder in a horizontal channel are considered here. The present LMLS-1D-IRBFN method is used for discretisation of diffusion terms implicitly, while the 1D-IRBFN method is employed to calculate the convection terms explicitly. The problem geometry and boundary conditions are described in Figure 5.2. Note that computational boundary conditions for vorticity are determined by Equation (5.9). The distances from the inlet and outlet to the center of the square cylinder are taken to be  $L_u = 6.5D$  and  $L_d = 19.5D$ , respectively, where  $D$  is the side length of the square cylinder taken to be 1. Those distances are chosen based on the studies of (Sohankar et al., 1998; Turki et al., 2003; Bouaziz et al., 2010).

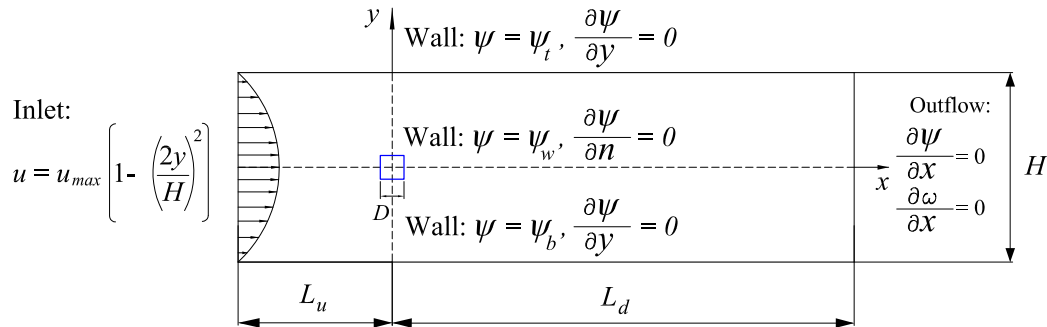


Figure 5.2: Flow past a square cylinder in a channel: geometry and boundary conditions. The blockage ratio is defined as  $\beta_0 = D/H$ . Note that computational boundary conditions for vorticity are determined by Equation (5.9).

A fully developed laminar flow is assumed at the inlet, thus the inlet velocity is described by a parabolic profile as follows.

$$u = u_{max} \left( 1 - \left( \frac{2y}{H} \right)^2 \right) \quad (5.19)$$

where  $u_{max}$  the maximum velocity at the inlet taken to be 1; and  $H$  the height of the channel. The stream function values at the top and bottom walls of the channel ( $\psi_t$  and  $\psi_b$ ) can be determined through Equations 5.7, 5.8 and 5.19.

When solving fluid flow problems involving the vortex shedding, the proper boundary condition at the outlet is a very important issue. A suitable outflow boundary condition allows the flow to exit the domain smoothly and has a minimum effect on the behaviour of the flow field. In the present study, the Neumann boundary conditions of the stream function and vorticity at the outlet are considered. It is noted that the value of stream function on the cylinder wall ( $\psi_w$ ) is equal to zero for the case of steady flows, but it is unknown for the case of unsteady flows. This value  $\psi_w$  varies with respect to time and can be determined by using a single-valued pressure condition (Lewis, 1979; Le-Cao et al., 2011).

The non-overlapping domain decomposition technique (Quarteroni and Valli, 1999) is employed here in order to reduce the size of memory required. The continuity of the stream function and vorticity variables and their first-order derivatives are imposed at the subdomain interfaces. The computational domain is decomposed into 24 subdomains. Each subdomain is represented by a uniform Cartesian grid as shown in Figure 5.3. Fine grids are generated in the domains near the cylinder in order to obtain reliable and accurate numerical results.

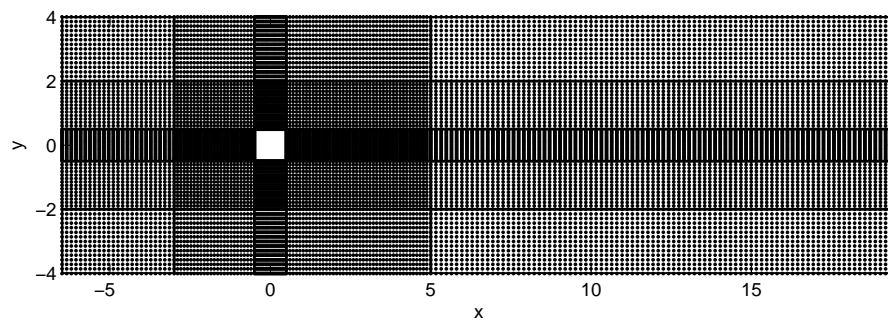


Figure 5.3: Flow past a square cylinder in a channel: grid configuration.

#### *Calculation of drag and lift coefficients*

From the primitive variable formulation, the pressure gradients ( $\partial p/\partial x, \partial p/\partial y$ )

on the square cylinder are given by

$$\frac{\partial p}{\partial x} = \frac{1}{Re} \left( \frac{\partial^2 u}{\partial x^2} + \frac{\partial^2 u}{\partial y^2} \right) - \left( u \frac{\partial u}{\partial x} + v \frac{\partial u}{\partial x} \right), \quad (5.20)$$

$$\frac{\partial p}{\partial y} = \frac{1}{Re} \left( \frac{\partial^2 v}{\partial x^2} + \frac{\partial^2 v}{\partial y^2} \right) - \left( u \frac{\partial v}{\partial x} + v \frac{\partial v}{\partial x} \right), \quad (5.21)$$

where  $Re$  is Reynolds number defined by  $Re = u_{max}D/\nu$ ,  $D$  the side length of the square cylinder,  $\nu$  the kinematic viscosity. For the case of stationary cylinder, the convection terms are equal to zero on the cylinder surface, Equations (5.20) and (5.21) then become

$$\frac{\partial p}{\partial x} = \frac{1}{Re} \left( \frac{\partial^2 u}{\partial x^2} + \frac{\partial^2 u}{\partial y^2} \right), \quad (5.22)$$

$$\frac{\partial p}{\partial y} = \frac{1}{Re} \left( \frac{\partial^2 v}{\partial x^2} + \frac{\partial^2 v}{\partial y^2} \right). \quad (5.23)$$

The vorticity can be determined as

$$\omega = \frac{\partial v}{\partial x} - \frac{\partial u}{\partial y}. \quad (5.24)$$

Making use of (5.24) along the top and the bottom of the square cylinder and differentiating both sides with respect to  $y$  result in

$$\frac{\partial \omega}{\partial y} = -\frac{\partial^2 u}{\partial y^2}. \quad (5.25)$$

From Equations (5.22) and (5.25), the gradients of pressure along the bottom and the top walls are determined as

$$\frac{\partial p}{\partial x} = -\frac{1}{Re} \frac{\partial \omega}{\partial y}. \quad (5.26)$$

In a similar fashion, one can calculate the gradients of pressure along the front and the rear walls as follows.

$$\frac{\partial p}{\partial y} = \frac{1}{Re} \frac{\partial \omega}{\partial x}. \quad (5.27)$$

Integrating Equations (5.26) and (5.27) along the horizontal and vertical walls, respectively, the pressure distribution on the cylinder surface can be determined.

Drag and lift coefficients can be determined as

$$C_D = \frac{F_D}{1/2\rho u_{\max}^2 D}, \quad (5.28)$$

$$C_L = \frac{F_L}{1/2\rho u_{\max}^2 D}, \quad (5.29)$$

where  $\rho$  is fluid density, and the drag  $F_D$  and lift  $F_L$  are defined by

$$F_D = F_{D_p} + F_{D_f}, \quad (5.30)$$

$$F_L = F_{L_p} + F_{L_f}, \quad (5.31)$$

in which

$$F_{D_p} = \int_0^1 (p_f - p_r) dy, \quad (5.32)$$

$$F_{L_p} = \int_0^1 (p_b - p_t) dx, \quad (5.33)$$

$$F_{D_f} = \int_0^1 (\tau_t - \tau_b) dx, \quad (5.34)$$

$$F_{L_f} = \int_0^1 (\tau_r - \tau_f) dy, \quad (5.35)$$

where  $p_f, p_r, p_b,$  and  $p_t$  are values of pressure distribution on the front, rear, bottom and top surfaces of the square cylinder, respectively; and  $\tau_f, \tau_r, \tau_b,$  and  $\tau_t$  are values of shear stress acting on the front, rear, bottom and top surfaces of the square cylinder, respectively, as shown in Figure 5.4.

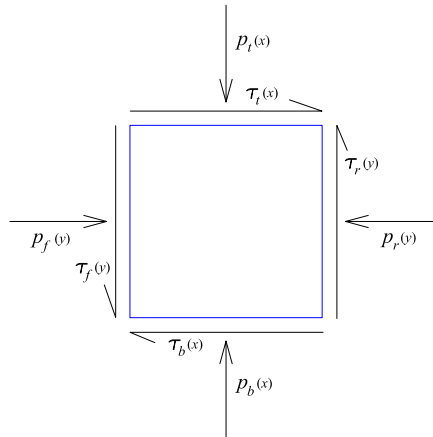


Figure 5.4: Pressure and shear stress acting on the surface of a square cylinder.

### Steady case

A grid independence study for flow past a square cylinder in a channel at Reynolds number of 40 is conducted. The length of recirculation zone  $L_r$  and drag coefficient  $C_D$  for various grid sizes are presented in Table 5.7. The variations of  $L_r$  and  $C_D$  with respect to the number of nodes are described in Figures 5.5 and 5.6. It can be seen that the numerical results are convergent with increasing grid density. The flow parameters  $L_r$  and  $C_D$  for different Reynolds numbers ( $Re \leq 40$ ) using a grid of  $571 \times 351$  are provided in Table 5.8. The present numerical results are in good agreement with the published results of other authors. Contours of stream function and vorticity of the flow field around the square cylinder for small Reynolds numbers are given in Figure 5.7. It appears that the flow separation occurs at the trailing edges of the cylinder and a closed steady recirculation region containing two symmetric vortices forms behind the cylinder. The size of the recirculation region increases with increasing Reynolds number.

Table 5.7: Steady flow past a square cylinder in a channel: grid convergence study of recirculation length  $L_r$  and drag coefficient  $C_D$  for  $Re = 40$ .

Grid	$L_r$	$C_D$
$173 \times 121$	2.37	1.10
$211 \times 151$	2.29	1.31
$281 \times 201$	2.26	1.49
$351 \times 251$	2.25	1.57
$469 \times 301$	2.25	1.75
$493 \times 305$	2.25	1.79
$557 \times 341$	2.27	1.88
$571 \times 351$	2.27	1.89
$599 \times 351$	2.27	1.91
$645 \times 367$	2.27	1.92
$717 \times 377$	2.27	1.91
Breuer et al. (2000)	2.15	1.70
Gupta et al. (2003)	1.90	1.86
Dhiman et al. (2005)	2.17	1.75

Table 5.8: Steady flow past a square cylinder in a channel: comparison of recirculation length  $L_r$  and drag coefficient  $C_D$ , using a grid of  $571 \times 351$ .

$Re$	Source	$L_{sep}$	$C_D$
10	Breuer et al. (2000)	0.49	3.64
	Gupta et al. (2003)	0.40	3.51
	Dhiman et al. (2005)	0.49	3.63
	Present	0.48	3.73
20	Breuer et al. (2000)	1.04	2.50
	Gupta et al. (2003)	0.90	2.45
	Dhiman et al. (2005)	1.05	2.44
	Present	1.06	2.64
30	Breuer et al. (2000)	1.60	2.00
	Gupta et al. (2003)	1.40	2.06
	Dhiman et al. (2005)	1.62	1.99
	Present	1.66	2.15
40	Breuer et al. (2000)	2.15	1.70
	Gupta et al. (2003)	1.90	1.86
	Dhiman et al. (2005)	2.17	1.75
	Present	2.27	1.89

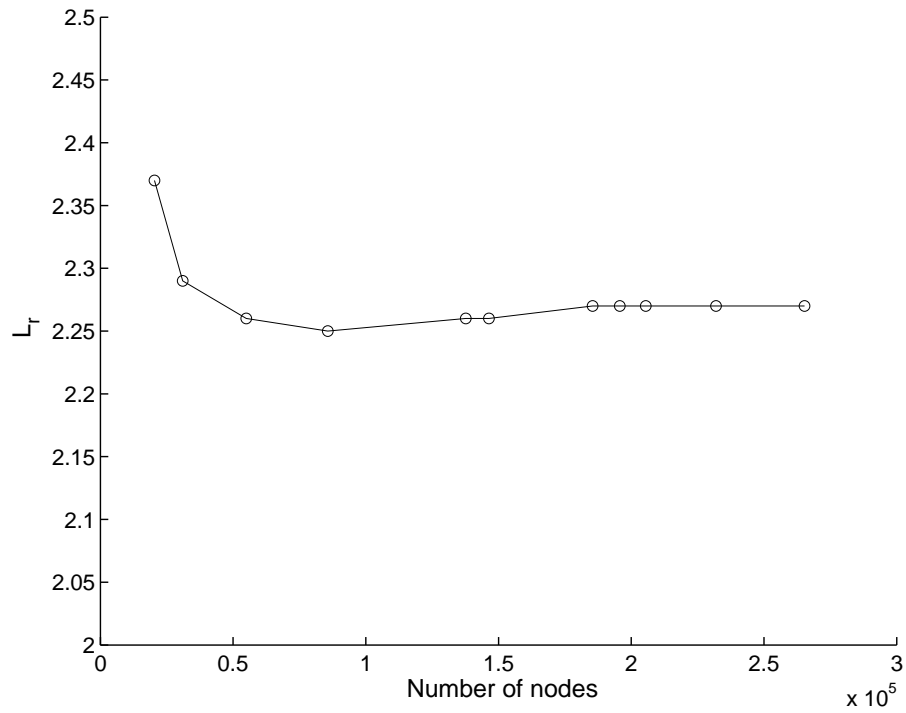


Figure 5.5: Steady flow past a square cylinder in a channel: grid convergence study of recirculation length  $L_r$  for  $Re = 40$ .

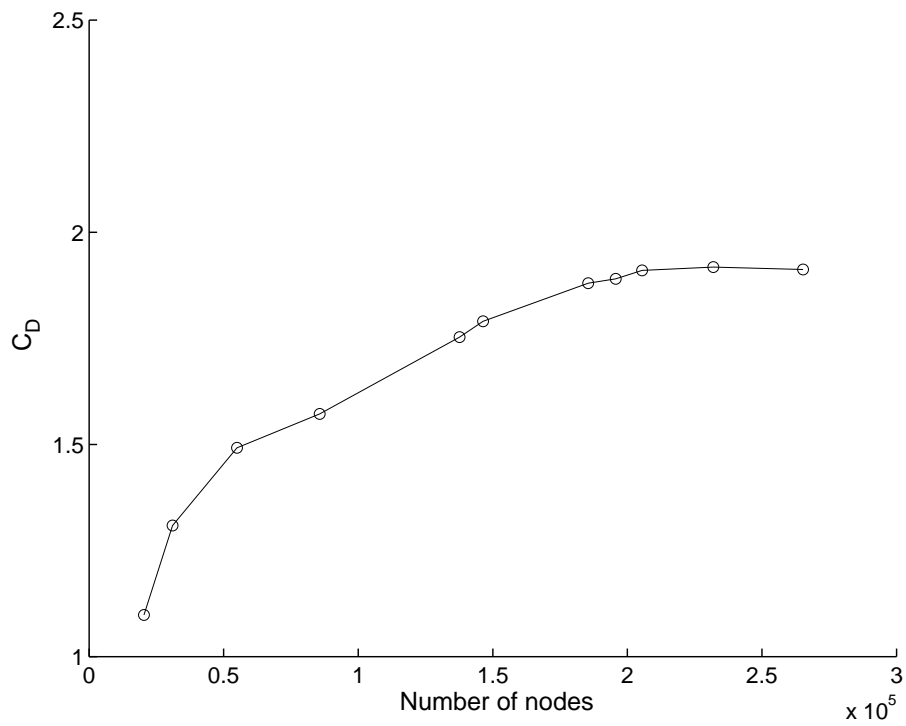


Figure 5.6: Steady flow past a square cylinder in a channel: grid convergence study of drag coefficient  $C_D$  for  $Re = 40$ .

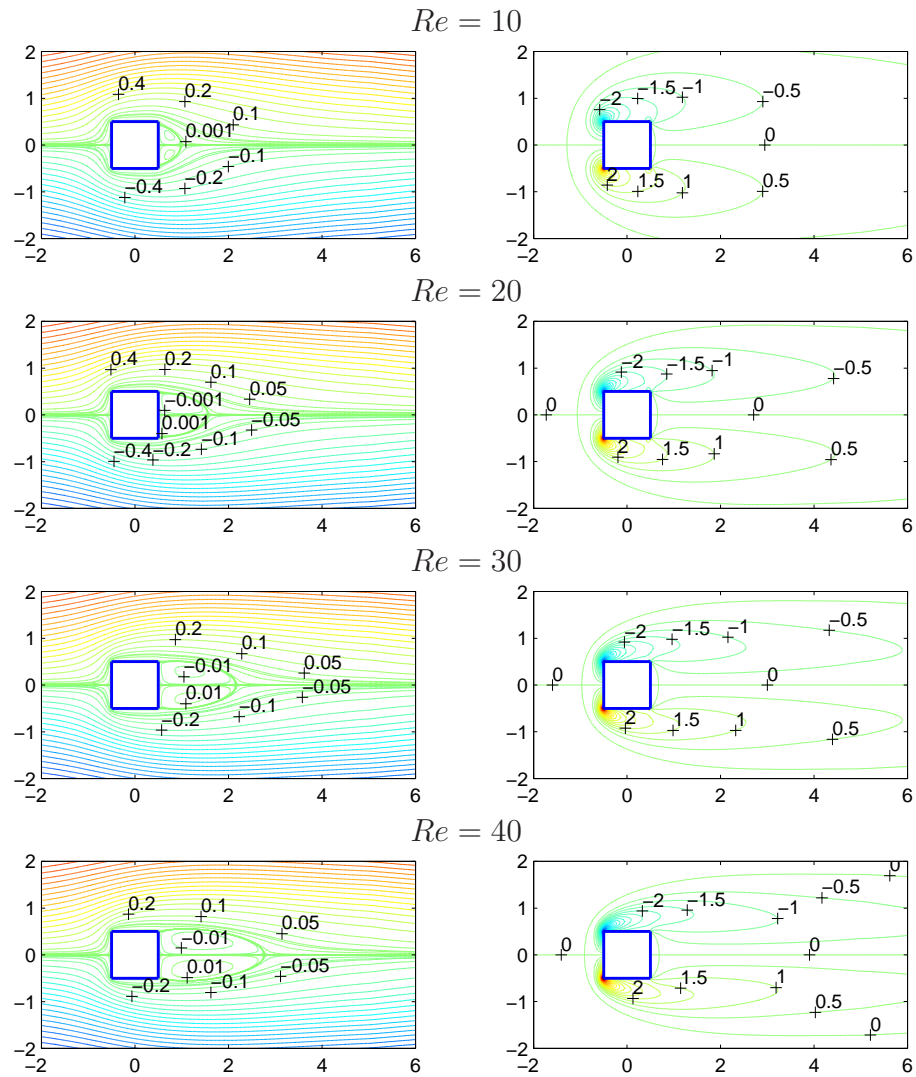


Figure 5.7: Steady flow past a square cylinder in a channel: contours of stream function for different Reynolds numbers, using a grid of  $571 \times 351$ .

### Unsteady case

When the Reynolds number reaches a certain critical value, flow past a square cylinder in a channel becomes unsteady. The critical Reynolds number is a function of the blockage ratio defined in Figure 5.2. Here we do not attempt to search for these critical Reynolds numbers and simply investigate the flow for several values of  $\beta_0$  (1/2, 1/4, and 1/8) and Reynolds numbers ( $60 \leq Re \leq 160$ ). The Strouhal number is calculated based on the frequency of the vortex shedding  $f$ , the cylinder length  $D$  and the maximum inlet velocity  $u_{max}$  as follows.

$$St = \frac{fD}{u_{max}}. \quad (5.36)$$

Time-averaged drag coefficient  $C_{Dm}$  is defined by

$$C_{Dm} = \frac{1}{t_2 - t_1} \int_{t_1}^{t_2} C_D dt, \quad (5.37)$$

where  $t_2 - t_1$  is the period of the vortex shedding.

Figures 5.8 and 5.9 respectively present variations of Strouhal number  $St$  and time-averaged drag coefficient  $C_{Dm}$  with respect to Reynolds number for the case of blockage ratio of 1/8 and using different grids of  $547 \times 331$ ,  $571 \times 351$  and  $645 \times 367$ . The obtained numerical results are compared with the results of FVM (Breuer et al., 2000) both using a non-uniform grid of  $560 \times 340$ , lattice-Boltzmann automata (LBA) method (Breuer et al., 2000) using a uniform grid of  $2000 \times 320$ , space-time adaptive method (STAM) (Berrone and Marro, 2009) and control volume finite element method (CVFEM) (Bouaziz et al., 2010) using a non-uniform grid of  $249 \times 197$ . It can be seen that the present numerical results at three different grids are slightly different and in good agreement with the results of other methods. Figure 5.10 shows variations of drag and lift co-

efficients with respect to time  $t$  for the case of  $Re = 90$ ,  $\beta_0 = 1/8$  and using a grid of  $571 \times 351$ . It can be seen that those coefficients vary periodically after a certain time. The contours of stream function and vorticity for different Reynolds numbers ( $Re = 40, 60, 90$  and  $160$ ) and  $\beta_0 = 1/8$  are depicted in Figures 5.11 and 5.12, respectively. The well-known von Karman vortices generate behind the cylinder periodically when a critical Reynolds number ( $Re \approx 60$ ) is exceeded.

Table 5.9 presents Strouhal number  $St$  and time-averaged drag coefficient  $C_{Dm}$  for several Reynolds numbers ( $60 \leq Re \leq 160$ ) and blockage ratios ( $\beta_0 = 1/2, 1/4$  and  $1/8$ ). It is noted that in the cases of  $\beta_0 = 1/2$  and  $1/4$ , the flow is still steady for  $Re = 60$  and  $80$ . The influences of Reynolds number on the Strouhal number and time-averaged drag coefficient for blockage ratios ( $\beta_0 = 1/2$  and  $1/4$ ) are described in Figures 5.13 and 5.14, respectively. It can be seen that Reynolds number has a very weak influence on the Strouhal number for those cases, and the time-averaged drag coefficient decreases with increasing Reynolds number up to  $160$ . Figures 5.15 and 5.16 presents the contours of stream function and vorticity of flow field around the square cylinder in a channel with blockage ratio of  $1/4$ , while the corresponding contours for the case of blockage ratio of  $1/2$  are given in Figures 5.17 and 5.18. Figures 5.11, 5.15 and 5.17 indicate that the critical Reynolds number (at which the flow becomes unsteady) increases with increasing blockage ratio. For example, at  $Re = 60$ , the flow becomes unsteady in the case of  $\beta_0 = 1/8$ , but is still steady in the case of  $\beta_0 = 1/4$ . At  $Re = 100$ , the flow becomes unsteady in the case of  $\beta_0 = 1/4$ , but remains nearly steady in the case of  $\beta_0 = 1/2$ . The numerical results obtained are in good agreement with those of Sahu et al. (2010) who used the semi-explicit FEM.

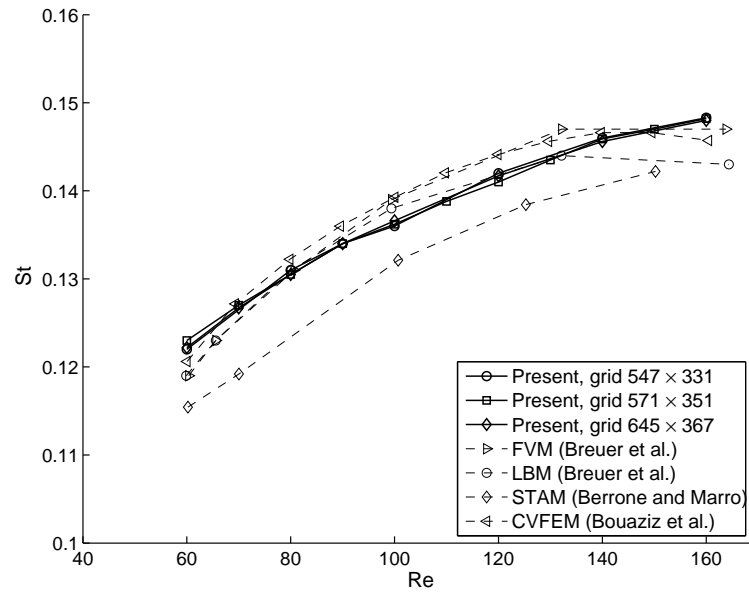


Figure 5.8: Unsteady flow past a square cylinder in a channel (blockage ratio  $\beta_0 = 1/8$ ): variation of Strouhal number  $St$  with respect to Reynolds number  $Re$ , using different grids of  $547 \times 331$ ,  $571 \times 351$  and  $645 \times 367$ ; FVM (Breuer et al., 2000) using a non-uniform grid of  $560 \times 340$ ; LBA (Breuer et al., 2000) using a uniform grid of  $2000 \times 320$ ; STAM (Berrone and Marro, 2009); CVFEM (Bouaziz et al., 2010) using a non-uniform grid of  $249 \times 197$ .

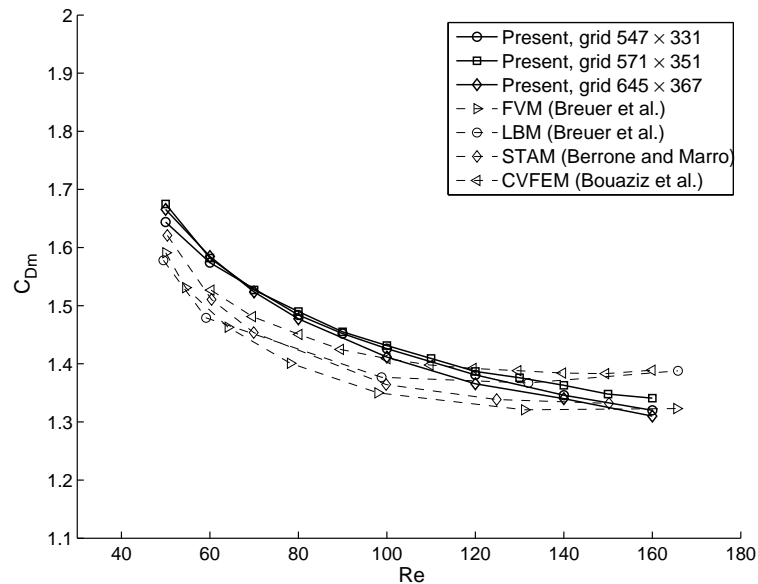


Figure 5.9: Unsteady flow past a square cylinder in a channel (blockage ratio  $\beta_0 = 1/8$ ): variation of time-averaged drag coefficient  $C_{Dm}$  with respect to Reynolds number  $Re$ , using different grids of  $547 \times 331$ ,  $571 \times 351$  and  $645 \times 367$ ; FVM (Breuer et al., 2000) using a non-uniform grid of  $560 \times 340$ ; LBA (Breuer et al., 2000) using a uniform grid of  $2000 \times 320$ ; STAM (Berrone and Marro, 2009); CVFEM (Bouaziz et al., 2010) using a non-uniform grid of  $249 \times 197$ .

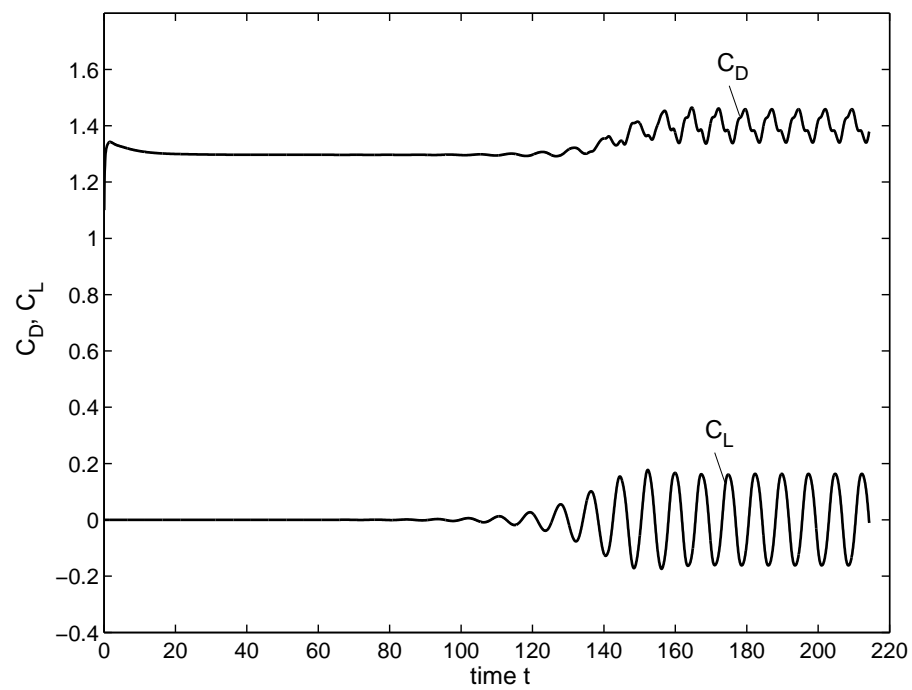


Figure 5.10: Unsteady flow past a square cylinder in a channel (blockage ratio  $\beta_0 = 1/8$ ): variation of drag coefficient  $C_D$  and lift coefficient  $C_L$  with respect to time  $t$  for the case of  $Re = 90$ , using a grid of  $571 \times 351$ .

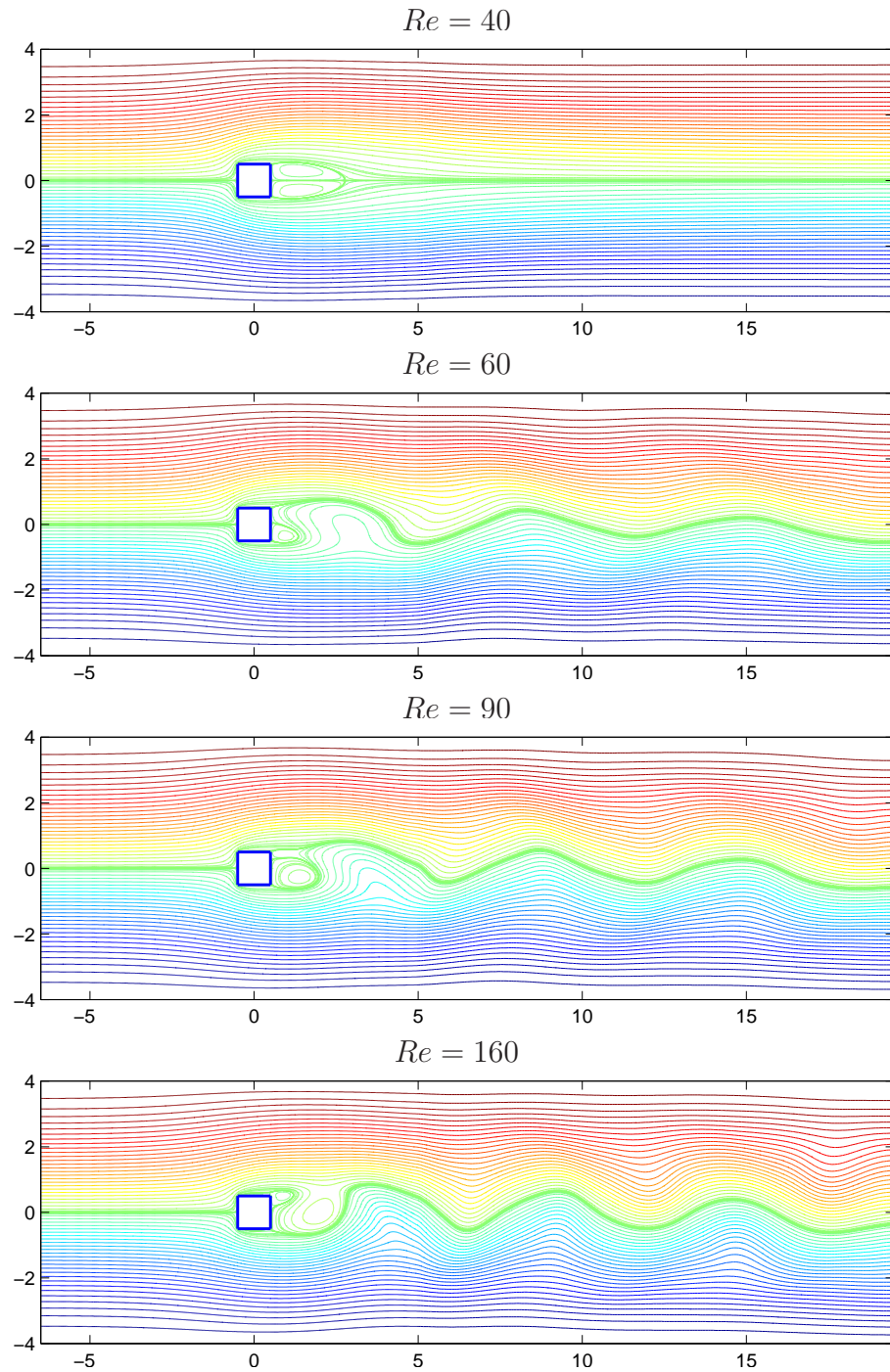


Figure 5.11: Unsteady flow past a square cylinder in a channel (blockage ratio  $\beta_0 = 1/8$ ): Contours of stream function for different Reynolds numbers, using a grid of  $645 \times 367$ .

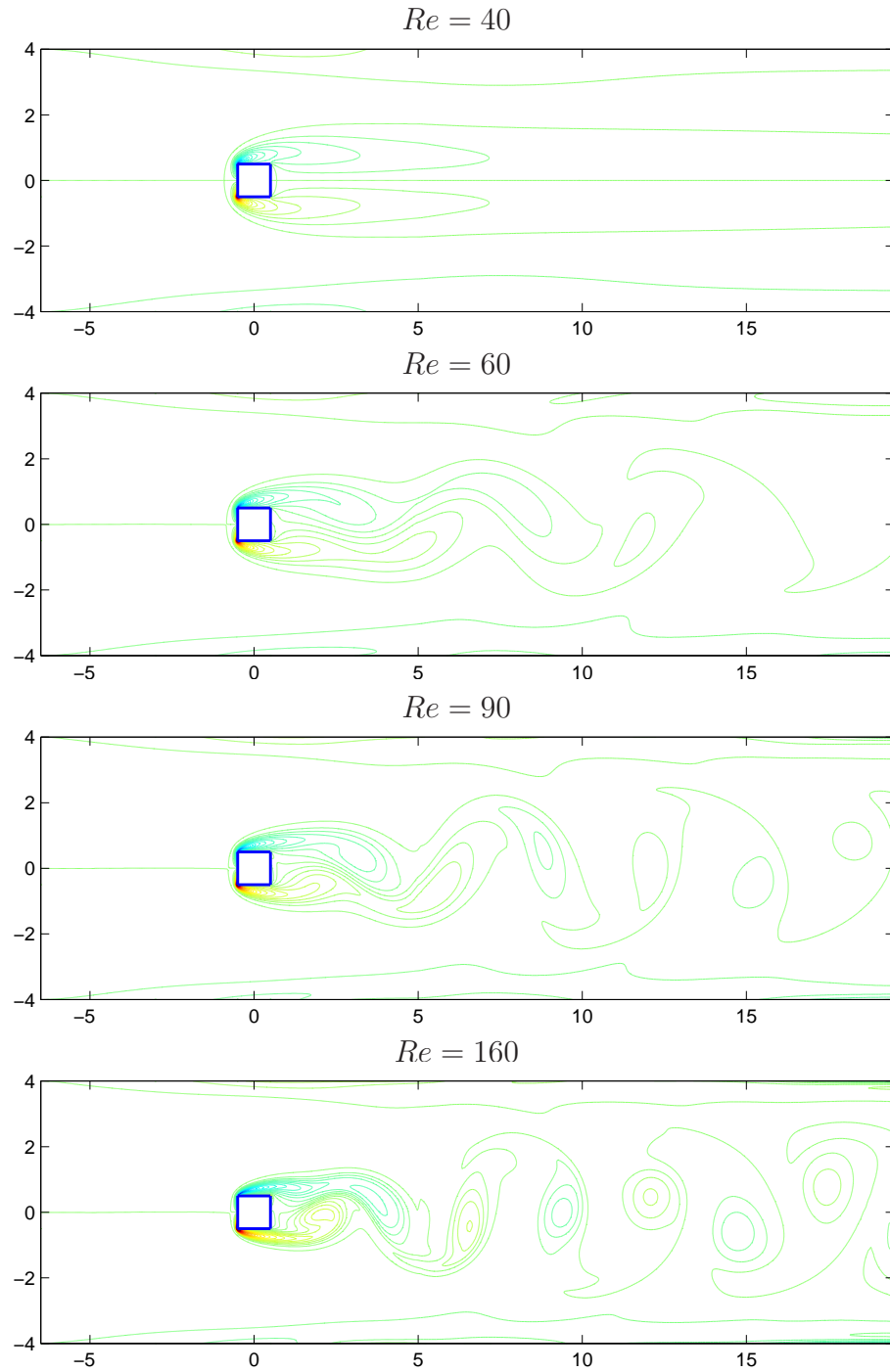


Figure 5.12: Unsteady flow past a square cylinder in a channel (blockage ratio  $\beta_0 = 1/8$ ): Contours of vorticity for different Reynolds numbers, using a grid of  $645 \times 367$ .

Table 5.9: Unsteady flow past a square cylinder in a channel: Strouhal number  $St$  and time-averaged drag coefficient  $C_{Dm}$  for different blockage ratios  $\beta_0 = 1/2, 1/4$  and  $1/8$ , using grids of  $645 \times 191$ ,  $645 \times 271$  and  $645 \times 367$ , respectively. Note that in the case of  $\beta_0 = 1/2, 1/4$ , the flow is still steady for  $Re = 60, 80$

$Re$	$\beta_0 = 1/2$		$\beta_0 = 1/4$		$\beta_0 = 1/8$	
	$St$	$C_{Dm}$	$St$	$C_{Dm}$	$St$	$C_{Dm}$
60	-	7.522	-	1.871	0.122	1.585
80	-	6.237	-	1.634	0.131	1.477
100	0.344	5.396	0.185	1.483	0.137	1.412
120	0.349	4.773	0.192	1.382	0.142	1.366
140	0.352	4.269	0.196	1.303	0.146	1.340
160	0.352	3.850	0.197	1.239	0.148	1.315

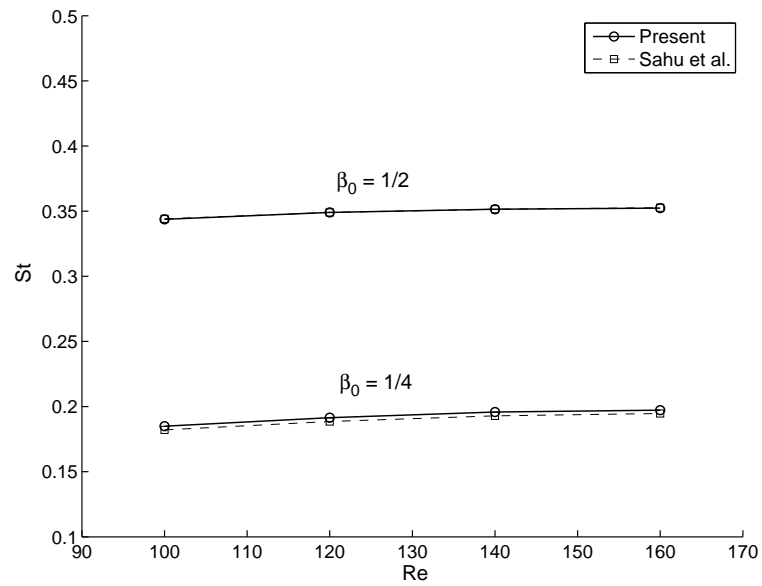


Figure 5.13: Unsteady flow past a square cylinder in a channel: variation of time-averaged drag coefficient  $C_{Dm}$  with respect to Reynolds number  $Re$  for blockage ratios  $\beta_0 = 1/2$  and  $1/4$ , using grids of  $645 \times 191$  and  $645 \times 271$ , respectively;

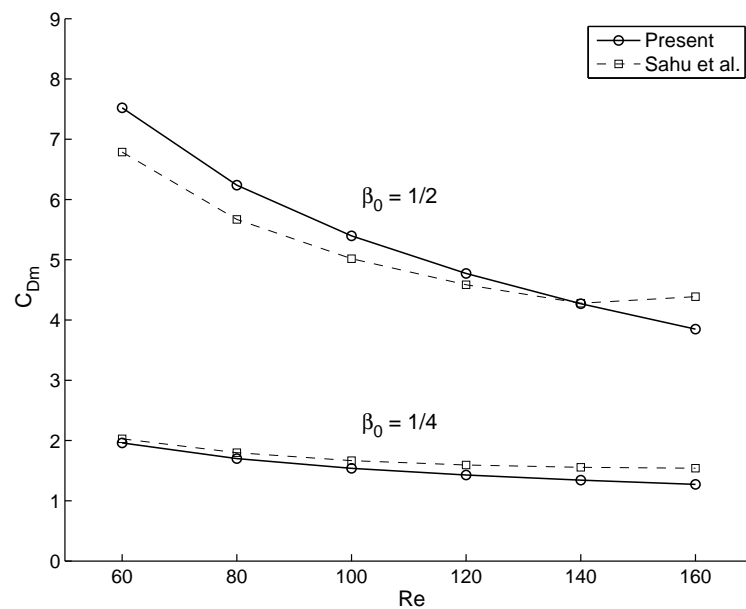


Figure 5.14: Unsteady flow past a square cylinder in a channel: variation of time-averaged drag coefficient  $C_{Dm}$  with respect to Reynolds number  $Re$  for blockage ratios  $\beta_0 = 1/2$  and  $1/4$ , using grids of  $645 \times 191$  and  $645 \times 271$ , respectively;

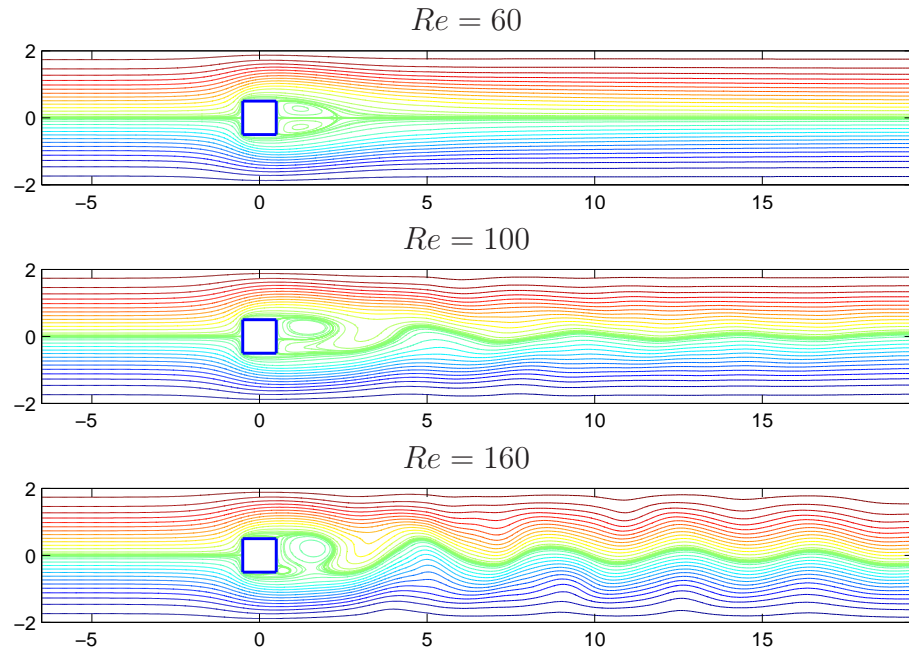


Figure 5.15: Unsteady flow past a square cylinder in a channel: Contours of stream function for different Reynolds numbers ( $\beta_0 = 1/4$ , grid =  $645 \times 271$ ).

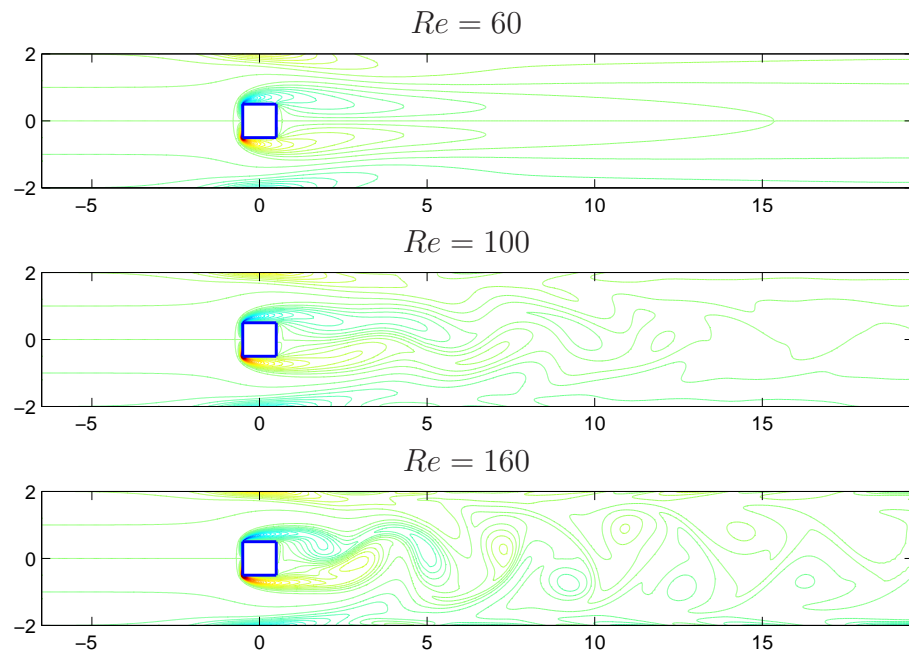


Figure 5.16: Unsteady flow past a square cylinder in a channel: Contours of vorticity for different Reynolds numbers ( $\beta_0 = 1/4$ , grid =  $645 \times 271$ ).

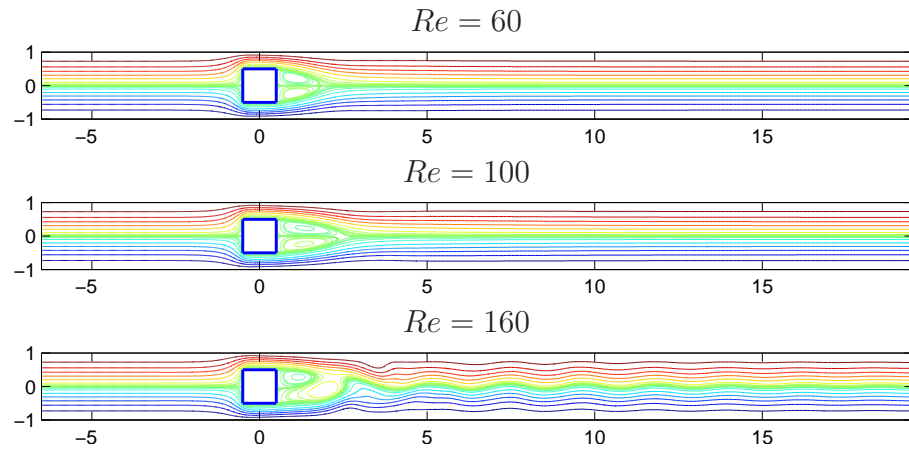


Figure 5.17: Unsteady flow past a square cylinder in a channel: Contours of stream function for different Reynolds numbers ( $\beta_0 = 1/2$ , grid =  $645 \times 191$ ).

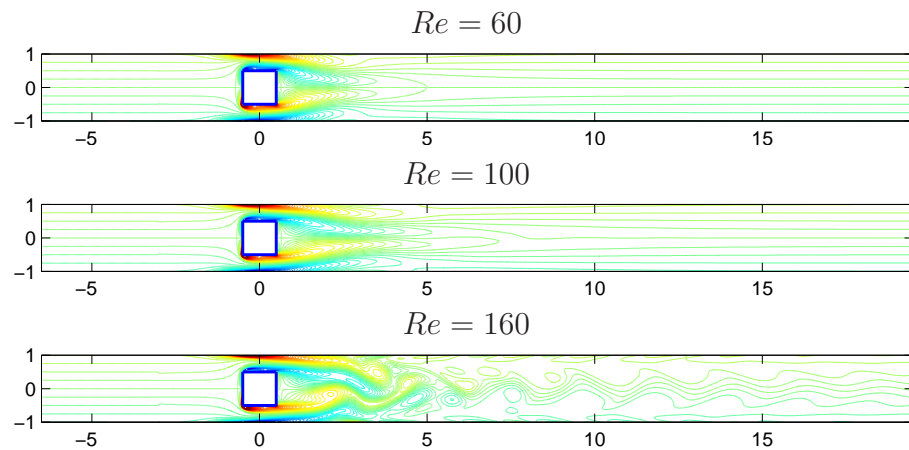


Figure 5.18: Unsteady flow past a square cylinder in a channel: Contours of vorticity for different Reynolds numbers ( $\beta_0 = 1/2$ , grid =  $645 \times 191$ ).

### 5.4.3 Example 3: Unsteady flows past a circular cylinder

The unsteady flow past a circular cylinder at different Reynolds numbers ( $Re = 80, 100$  and  $200$ ) is considered here, where  $Re = U_0 D / \nu$ ,  $U_0$  is the far-field inlet velocity taken to be 1,  $D$  the diameter of the cylinder taken to be 1,  $\nu$  the kinematic viscosity. The same numerical procedure as in Example 2 is employed. The problem geometry and boundary conditions are described in Figure 5.19. Note that computational boundary conditions for vorticity are determined by Equations (5.9)-(5.13). The computational domain is decomposed into 25 subdomains as shown in Figure 5.20. A finer grid is generated in the subdomain containing the circular cylinder. The far-field flow is assumed to behave as a potential flow and the far-field stream function  $\psi^{far}$  can be defined by (Kim et al., 2007)

$$\psi^{far} = U_0 y \left( 1 - \frac{D^2}{4(x^2 + y^2)} \right). \quad (5.38)$$

The boundary conditions for stream function are given by

$$\psi = \psi^{far}, \quad \omega = 0, \quad \text{on } \Gamma_1, \Gamma_2, \Gamma_3 \quad (5.39)$$

$$\frac{\partial \psi}{\partial x} = 0, \quad \frac{\partial \omega}{\partial x} = 0, \quad \text{on } \Gamma_4 \quad (5.40)$$

$$\psi = \psi_w, \quad \frac{\partial \psi}{\partial n} = 0, \quad \text{on } \Gamma_w \quad (5.41)$$

where  $n$  is the direction normal to the cylinder surface;  $\psi_w$  the unknown stream function value on the cylinder wall,  $\Gamma_w$ ; and the subscript  $w$  is used to denote quantities on  $\Gamma_w$ . The value  $\psi_w$  varies with respect to time and can be determined by using a single-valued pressure condition (Lewis, 1979; Le-Cao et al., 2011).

Tables 5.10-5.12 respectively present Strouhal number, drag and lift coefficients for different Reynolds numbers. The present numerical results are in good agreement with the published results of other authors. Figure 5.21 presents

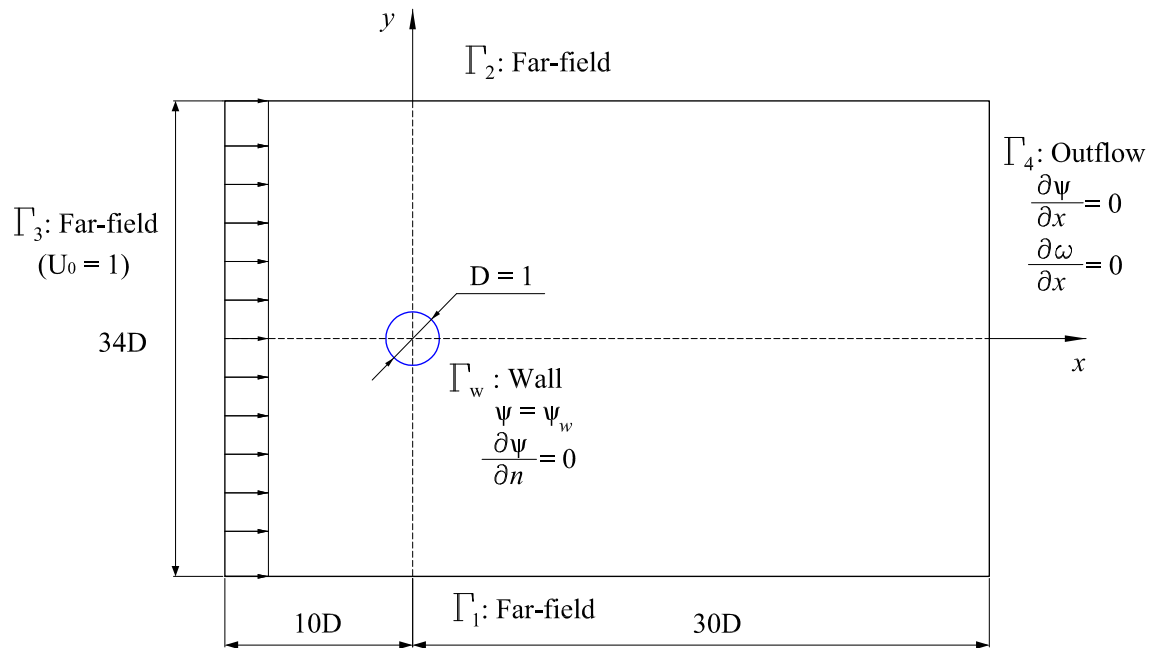


Figure 5.19: Unsteady flow past a circular cylinder: geometry and boundary conditions. Note that computational boundary conditions for vorticity are determined by Equations (5.9)-(5.13).

the variations of drag and lift coefficients with respect to time for  $Re = 100$ . The periodic variations of these coefficients are observed as time goes on. The contours of stream function and vorticity of the flow field around the circular cylinder at different Reynolds numbers are provided in Figures 5.22 and 5.23, respectively. With increasing Reynolds number, the vortex shedding frequency increases and the vortices become smaller.

Table 5.10: Unsteady flow past a circular cylinder: Strouhal number  $St$  for different Reynolds number  $Re = 80, 100$  and  $200$ .

Source	$Re = 80$	$Re = 100$	$Re = 200$
Braza et al. (1986)	-	0.16	0.20
Liu et al. (1998)	-	0.165	0.192
Ding et al. (2004)	-	0.164	0.196
Park et al. (1998)	0.152	0.165	-
Silva et al. (2003)	0.15	0.16	-
Present, $548 \times 379$	0.159	0.168	-
Present, $640 \times 379$	0.151	0.168	0.199

Table 5.11: Unsteady flow past a circular cylinder: Drag coefficient  $C_D$  for different Reynolds number  $Re = 80, 100$  and  $200$ .

Source	$Re = 80$	$Re = 100$	$Re = 200$
Braza et al. (1986)	-	$1.364 \pm 0.015$	$1.40 \pm 0.05$
Liu et al. (1998)	-	$1.350 \pm 0.012$	$1.310 \pm 0.049$
Ding et al. (2004)	-	$1.325 \pm 0.008$	$1.327 \pm 0.045$
Park et al. (1998)	1.35	1.33	-
Silva et al. (2003)	1.4	1.39	-
Present, $548 \times 379$	$1.364 \pm 0.004$	$1.344 \pm 0.012$	-
Present, $640 \times 379$	$1.365 \pm 0.005$	$1.344 \pm 0.012$	$1.295 \pm 0.048$

Table 5.12: Unsteady flow past a circular cylinder: Lift coefficient  $C_L$  for different Reynolds number  $Re = 80, 100$  and  $200$ .

Source	$Re = 80$	$Re = 100$	$Re = 200$
Braza et al. (1986)	-	$\pm 0.25$	$\pm 0.75$
Liu et al. (1998)	-	$\pm 0.339$	$\pm 0.69$
Ding et al. (2004)	-	$\pm 0.28$	$\pm 0.60$
Park et al. (1998)	$\pm 0.245$	$\pm 0.332$	-
Silva et al. (2003)	$\pm 0.235$	-	-
Present, $548 \times 379$	$\pm 0.237$	$\pm 0.344$	-
Present, $640 \times 379$	$\pm 0.245$	$\pm 0.341$	$\pm 0.70$

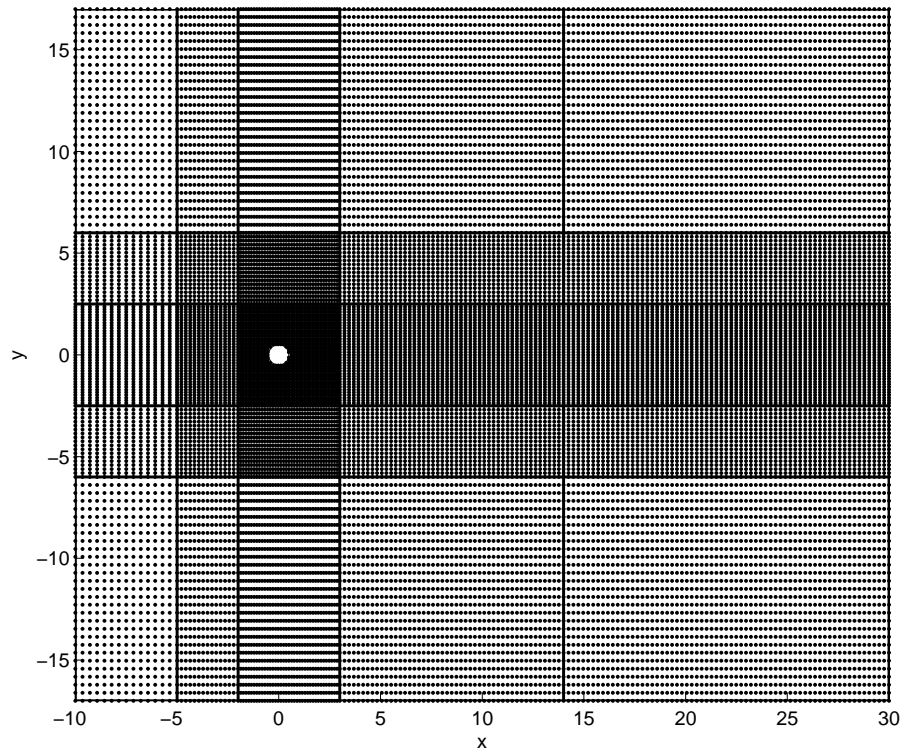
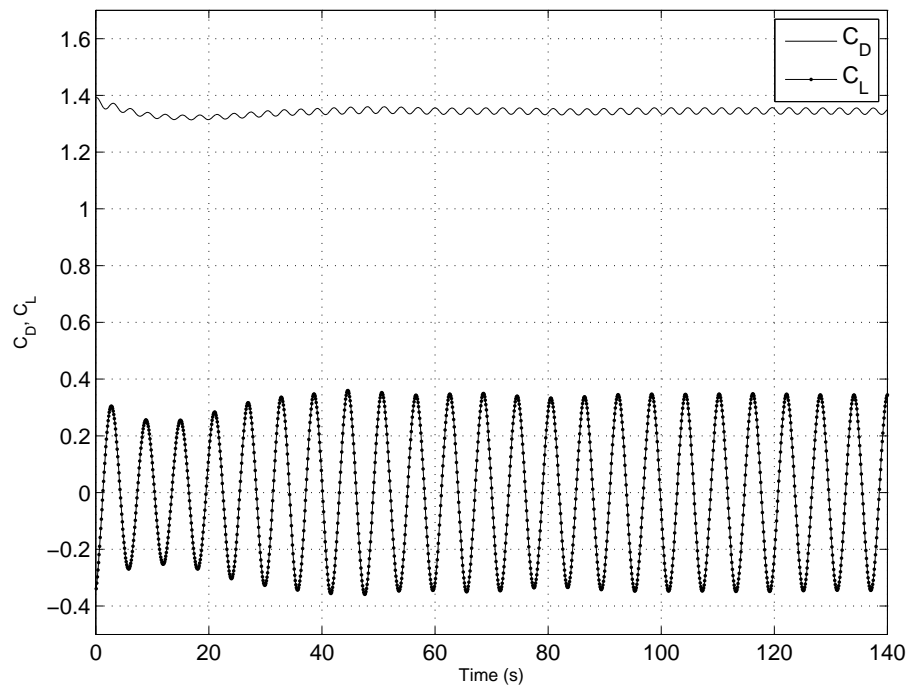


Figure 5.20: Unsteady flow past a circular cylinder: grid configuration.

Figure 5.21: Unsteady flow past a stationary cylinder: drag and lift coefficients  $C_D$  and  $C_L$  with respect to time for  $Re = 100$ , using a grid of  $548 \times 379$ .

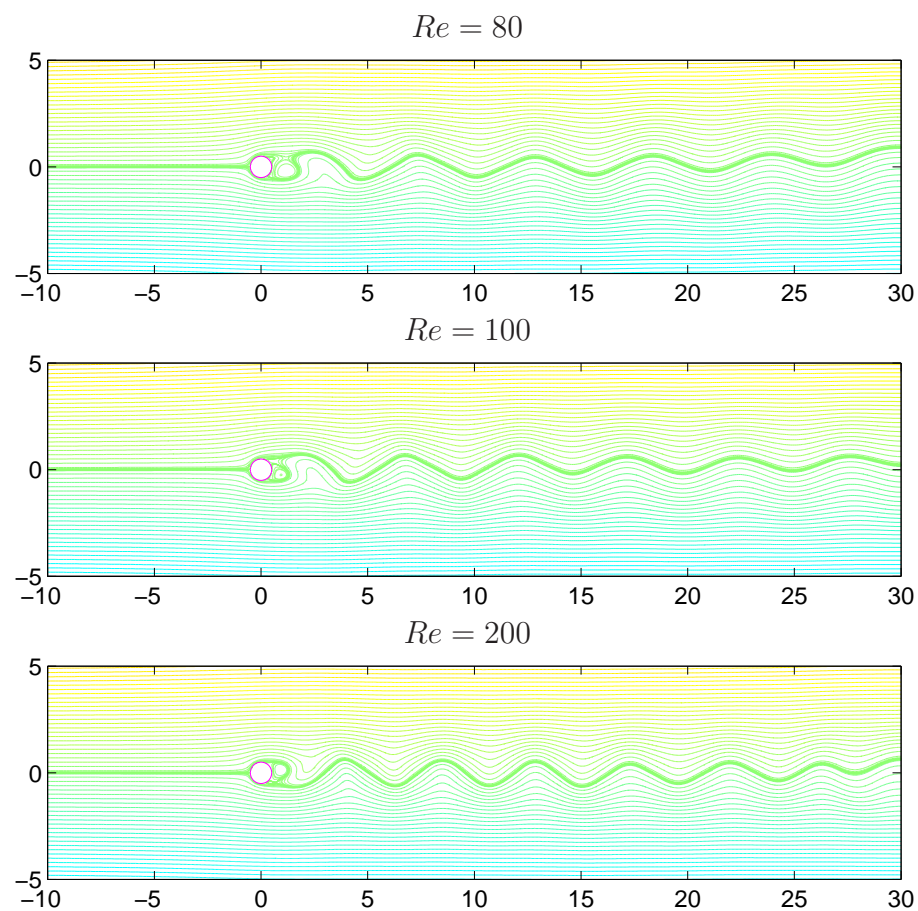


Figure 5.22: Unsteady flow past a circular cylinder: contours of stream function for different Reynolds numbers  $Re = 80, 100$  and  $200$ , using grids of  $548 \times 379$ ,  $548 \times 379$  and  $640 \times 379$ , respectively.

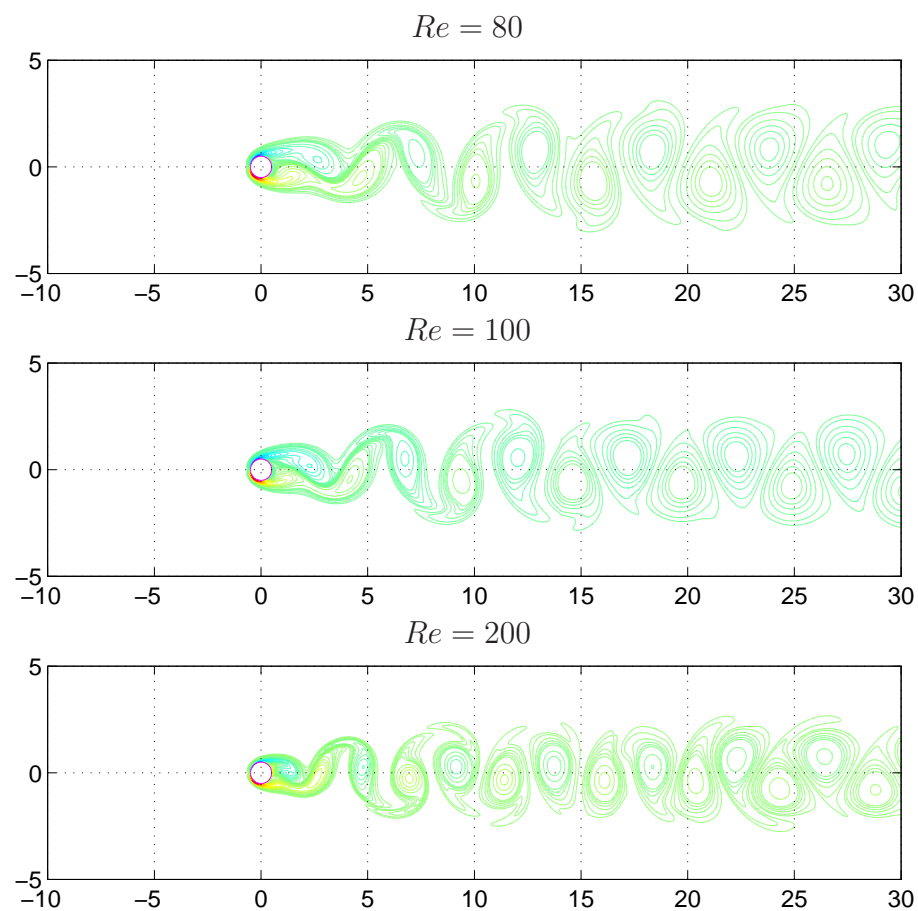


Figure 5.23: Unsteady flow past a circular cylinder: contours of vorticity for different Reynolds numbers  $Re = 80, 100$  and  $200$ , using grids of  $548 \times 379$ ,  $548 \times 379$  and  $640 \times 379$ , respectively.

## 5.5 Concluding remarks

A new numerical procedure based on the local MLS-1D-IRBFN method is presented for time-dependent problems. The numerical results for Burgers' equation indicate that the LMLS-1D-IRBFN approach yields the same level of accuracy as the 1D-IRBFN method, while the system matrix is more sparse than that of the 1D-IRBFN, which helps reduce the computational cost significantly. The LMLS-1D-IRBFN shape function possesses the Kronecker- $\delta$  property which allows an exact imposition of the essential boundary condition. Cartesian grids are employed to discretise both regular and irregular problem domains. The combination of the present numerical procedure and a domain decomposition technique is successfully developed for simulating steady and unsteady flows past a square cylinder in a horizontal channel with different blockage ratios and unsteady flows past a circular cylinder. The influence of blockage ratio on the characteristics of flow past a square cylinder in a channel is investigated for a range of Reynolds numbers ( $60 \leq Re \leq 160$ ) and several blockage ratios ( $\beta_0 = 1/2, 1/4$  and  $1/8$ ). The obtained numerical results indicate that (i) the critical Reynolds number (at which the flow becomes unsteady) increases with increasing blockage ratio; (ii) time-averaged drag coefficient decreases with increasing Reynolds number up to 160; and (iii) the Reynolds number has a very weak influence on the Strouhal number for the cases of  $\beta_0 = 1/2$  and  $1/4$ .

# Chapter 6

## A numerical procedure based on 1D-IRBFN and local MLS-1D-IRBFN methods for fluid-structure interaction analysis

In Chapter 2, the 1D-IRBFN method has been successfully developed for structural analysis of laminated composite plates. In Chapters 3-5, the local moving least square - one dimensional integrated radial basis function network (LMLS-1D-IRBFN) method has been developed and demonstrated with the solution of steady and unsteady fluid flow and natural convection problems where the applicability of the method in multiply-connected domains has been shown. In the present chapter, a new numerical procedure based on the 1D-IRBFN method and LMLS-1D-IRBFN approach is presented for solving fluid-structure interaction (FSI) problems. A combination of Chorin's method and pseudo-time subiterative technique is presented for a transient solution of 2-D incompressible

viscous Navier-Stokes equations in terms of primitive variables. Fluid domains are discretised by using Cartesian grids. The fluid solver is first verified through a solution of mixed convection in a lid-driven cavity with a hot lid and a cold bottom wall. The structural solver is verified with an analytical solution of forced vibration of a beam. The Newmark's method is employed for the forced vibration analysis of the beam based on the Euler-Bernoulli theory. The FSI numerical procedure is then applied to simulate flows in a lid-driven open-cavity with a flexible bottom wall.

## 6.1 Introduction

Fluid-structure interaction (FSI) plays a central role in several engineering problems such as aircraft wing flutter (Dubcova et al., 2008), bridge flutter (Ge and Xiang, 2008), blood flows (Fernández et al., 2007), design of helicopter rotors (Xiong and Yu, 2007). Therefore, FSI analysis is the key for solving those kinds of problems. FSI is a challenge for numerical modelling. To handle FSI problems, one needs to consider the governing equations for fluid and structure, and geometrical compatibility and equilibrium conditions at the interfaces between fluid and structural domains. Some FSI behaviours can converge to a steady-state solution, others can be oscillatory or even unstable.

There are two main approaches for solving FSI problems, including monolithic methods (Rugonyi and Bathe, 2001; Heil, 2004; Liew et al., 2007) and partitioned methods (Farhat and Lesoinne, 1998; Piperno, 1997). Partitioned procedures are usually appropriate for weak interaction between the fluid and the structure while the monolithic procedure is chosen to be effective for solving FSI problems with a strong interaction. In the monolithic approach, the fluid and structural equations are solved simultaneously. This approach may lead to two drawbacks (i) an increase in the number of degrees of freedom (DOFs) and (ii) an ill-conditioned matrix of the coupled equation system. In the par-

tioned approach, the fluid and structural fields are solved separately and the solution variables are transferred at the interfaces of the fluid and structural domains. The major advantage of this approach is the flexibility to choose different solvers for each field. However, the approach introduces a time delay which results in non-physical energy dissipation (Farhat and Lesoinne, 1998). Piperno (1997) introduced coupling staggered procedures with a structural predictor for a transient solution of a supersonic panel flutter using dynamic mesh and finite volume methods (FVM) based on the arbitrary-Lagrangian-Eulerian (ALE) formulation. Their procedures do not satisfy continuity of the structural and fluid grid displacements/velocities at the moving interface, but allow an exact numerical exchange of momentum through the interface.

Recently, a problem of FSI in a lid-driven cavity with a flexible bottom has been studied by several researchers to verify their numerical procedures for the FSI analysis (Förster et al., 2007; Küttler and Wall, 2008; Bathe and Zhang, 2009; Al-Amiri and Khanafer, 2011). Förster et al. (2007) studied this FSI problem and investigated the influence of mass density ratio, structural stiffness, structural predictor and time step size on the instabilities of sequentially staggered FSI simulations where incompressible flows are considered. Bathe and Zhang (2009) presented a numerical procedure to adapt and repair the fluid mesh for solving this FSI problem using the ALE formulation. The fully adaptive solution of transient flow are too expensive and may lead to large computational errors during the time integration. Therefore, they first solved a steady flow in a lid-driven cavity at the maximum velocity of the lid to obtain an adaptive mesh. This mesh is then employed for the transient solution of the FSI system. Al-Amiri and Khanafer (2011) investigated a steady laminar mixed convection heat transfer in a lid-driven cavity with a flexible bottom wall using a finite element formulation based on the Galerkin method of weighted residuals.

As an alternative to the ALE formulation, Eulerian formulations (e.g. Cartesian-based methods) can be used to describe the fluid motion in FSI and mov-

ing boundary problems. Udaykumar et al. (2001) presented a Cartesian grid method for computing fluid flows with complex immersed and moving boundaries. The flow is computed on a fixed Cartesian mesh and the solid boundaries are allowed to move freely through the mesh. The method significantly reduces the grid generation cost and has a great potential over the conventional body-fitted methods when solving problems with moving boundaries and complicated geometry. Šarler and Vertnik (2006) proposed an explicit local radial basis function collocation method for diffusion problems. The method appeared efficient, because it does not deal with a large system of equations like the original collocation multiquadric radial basis function method proposed by Kansa (1990b). Divo and Kassab (2007) developed a localized radial basis function meshless method (LCMM) for a solution of coupled viscous fluid flow and conjugate heat transfer problem. The LCMM was applied to simulate steady and unsteady blood flows in arterial bypass graft geometries (Zahab et al., 2009). Mai-Duy and Tanner (2007) presented a one-dimensional integrated radial basis function network (1D-IRBFN) collocation method for the solution of second- and fourth-order PDEs. Along grid lines, 1D-IRBF networks are constructed to satisfy the governing differential equations with boundary conditions in an exact manner. In the 1D-IRBFN method, the Cartesian grids are used to discretise both rectangular and non-rectangular problem domains. The 1D-IRBFN method is much more efficient than the original IRBFN method reported in Mai-Duy and Tran-Cong (2001a). Ngo-Cong et al. (2011) extended this method to investigate free vibration of composite laminated plates based on first-order shear deformation theory (Chapter 2). Ngo-Cong et al. (2012) proposed a local moving least square - one dimensional integrated radial basis function network method (LMLS-1D-IRBFN) for simulating 2-D incompressible viscous flows in terms of stream function and vorticity (Chapter 3). The method is based on the partition of unity framework to incorporate the moving least square and 1D-IRBFN techniques in an approach that produces a very sparse system matrix and offers as a high level of accuracy as that of the 1D-IRBFN.

The present chapter reports the development of a new numerical procedure based on the 1D-IRBFN and local MLS-1D-IRBFN methods for solving FSI and moving boundary problems such as flows in a lid-driven open-cavity with a flexible bottom wall. The fluid flow is governed by 2-D incompressible viscous Navier-Stokes equations in terms of primitive variables and the motion of the bottom wall is described by using the Euler-Bernoulli theory. The present fluid solver is first verified through a benchmark solution of mixed convection in a lid-driven cavity with a hot moving lid and a cold stationary bottom wall. Torrance et al. (1972) first numerically studied this kind of problem and found that the interaction of the shear driven flow due to the lid motion and natural convection due to the buoyancy effect makes the flow behaviour complicated and different from those driven by the two effects separately. Iwatsu et al. (1993) studied mixed convection in a lid-driven cavity with a hot moving top wall and a cold stationary bottom wall using finite different method (FDM). Sharif (2007) investigated the mixed convection heat transfer in inclined cavities using the FVM with a second-order upwind differencing scheme to discretise convection terms and central differencing scheme to discretise diffusion terms. Recently, Cheng (2011) employed a fourth-order accurate compact form and pseudo time iteration methods for simulations of mixed convection in a 2-D lid-driven cavity using the stream function, vorticity and temperature formulation.

The present chapter is organised as follows. Section 6.2 briefly reproduces the 1D-IRBFN and local MLS-1D-IRBFN techniques. The governing equations for structure, 2-D incompressible viscous flows and FSI are presented in Section 6.3. Section 6.4 describes the discretisation of the governing equations, the details of determination of variable values at “freshly cleared” nodes (defined later in section 6.4.3) and a sequentially staggered algorithm for FSI analysis. Several numerical examples are investigated using the present numerical procedure in Section 6.5. Section 6.6 concludes the chapter.

## 6.2 1D-IRBFN and local MLS-1D-IRBFN methods

The domain of interest is discretised using a Cartesian grid, i.e. an array of straight lines that run parallel to the  $x$ - and  $y$ -axes. The dependent variable  $u$  and its derivatives on each grid line are approximated using 1D-IRBFN and local MLS-1D-IRBFN methods as described in the remainder of this section.

### 6.2.1 1D-IRBFN methods

The 1D-IRBFN methods (Mai-Duy and Tanner, 2007) including 1D-IRBFN-2 and 1D-IRBFN-4 schemes are briefly described here.

#### Second-order 1D-IRBFN (1D-IRBFN-2 scheme)

Consider an  $x$ -grid line, e.g.  $[j]$ , as shown in Figure 6.1. The variation of  $u$  along this line is sought in the IRBF form. The second-order derivative of  $u$  is decomposed into RBFs; the RBF network is then integrated once and twice to obtain the expressions for the first-order derivative of  $u$  and the solution  $u$  itself,

$$\frac{\partial^2 u(x)}{\partial x^2} = \sum_{i=1}^{N_x^{[j]}} w^{(i)} G^{(i)}(x) = \sum_{i=1}^{N_x^{[j]}} w^{(i)} H_{[2]}^{(i)}(x), \quad (6.1)$$

$$\frac{\partial u(x)}{\partial x} = \sum_{i=1}^{N_x^{[j]}} w^{(i)} H_{[1]}^{(i)}(x) + c_1, \quad (6.2)$$

$$u(x) = \sum_{i=1}^{N_x^{[j]}} w^{(i)} H_{[0]}^{(i)}(x) + c_1 x + c_2, \quad (6.3)$$

where  $N_x^{[j]}$  is the number of nodes on the grid line  $[j]$ ;  $\{w^{(i)}\}_{i=1}^{N_x^{[j]}}$  RBF weights to be determined;  $\{G^{(i)}(x)\}_{i=1}^{N_x^{[j]}} = \{H_{[2]}^{(i)}(x)\}_{i=1}^{N_x^{[j]}}$  known RBFs;  $H_{[1]}^{(i)}(x) = \int H_{[2]}^{(i)}(x)dx$ ;  $H_{[0]}^{(i)}(x) = \int H_{[1]}^{(i)}(x)dx$ ; and  $c_1$  and  $c_2$  integration constants which are also unknown. An example of RBF, used in this work, is the multiquadrics  $G^{(i)}(x) = \sqrt{(x - x^{(i)})^2 + a^{(i)2}}$ ,  $a^{(i)}$  is the RBF width determined as  $a^{(k)} = \beta d^{(k)}$ ,  $\beta$  a positive factor, and  $d^{(k)}$  the distance from the  $k^{th}$  center to its nearest neighbour.

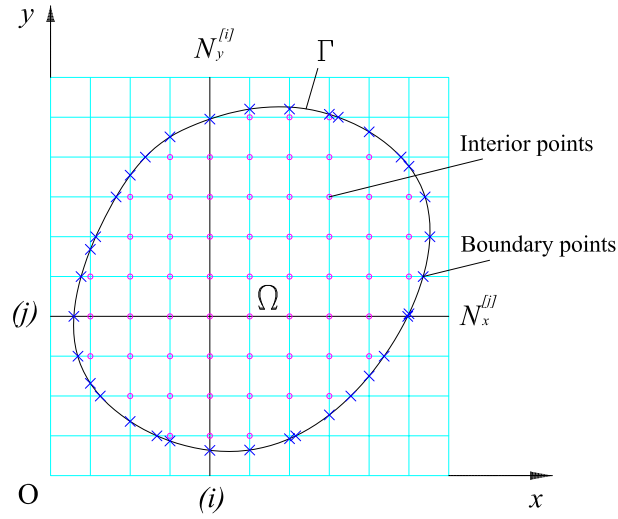


Figure 6.1: Cartesian grid discretisation.

#### Fourth-order 1D-IRBFN (1D-IRBFN-4 scheme)

In the 1D-IRBFN-4 scheme, the fourth-order derivative is decomposed into RBFs. The RBF networks are then integrated to obtain the lower-order deriva-

tives and the function itself,

$$\frac{\partial^4 u(x)}{\partial x^4} = \sum_{i=1}^{N_x^{[j]}} w^{(i)} G^{(i)}(x) = \sum_{i=1}^{N_x^{[j]}} w^{(i)} H_{[4]}^{(i)}(x), \quad (6.4)$$

$$\frac{\partial^3 u(x)}{\partial x^3} = \sum_{i=1}^{N_x^{[j]}} w^{(i)} H_{[3]}^{(i)}(x) + c_1, \quad (6.5)$$

$$\frac{\partial^2 u(x)}{\partial x^2} = \sum_{i=1}^{N_x^{[j]}} w^{(i)} H_{[2]}^{(i)}(x) + c_1 x + c_2, \quad (6.6)$$

$$\frac{\partial u(x)}{\partial x} = \sum_{i=1}^{N_x^{[j]}} w^{(i)} H_{[1]}^{(i)}(x) + \frac{c_1}{2} x^2 + c_2 x + c_3, \quad (6.7)$$

$$u(x) = \sum_{i=1}^{N_x^{[j]}} w^{(i)} H_{[0]}^{(i)}(x) + \frac{c_1}{6} x^3 + \frac{c_2}{2} x^2 + c_3 x + c_4, \quad (6.8)$$

where  $\{G^{(i)}(x)\}_{i=1}^{N_x^{[j]}} = \{H_{[4]}^{(i)}(x)\}_{i=1}^{N_x^{[j]}}$  are known RBFs;  $H_{[3]}^{(i)}(x) = \int H_{[4]}^{(i)}(x) dx$ ;  $H_{[2]}^{(i)}(x) = \int H_{[3]}^{(i)}(x) dx$ ;  $H_{[1]}^{(i)}(x) = \int H_{[2]}^{(i)}(x) dx$ ;  $H_{[0]}^{(i)}(x) = \int H_{[1]}^{(i)}(x) dx$ ; and  $c_1, c_2, c_3$  and  $c_4$  integration constants which are also unknown.

### 6.2.2 Local moving least square - one dimensional integrated radial basis function network technique

A schematic outline of the LMLS-1D-IRBFN method is depicted in Figure 6.2. The proposed method with 3-node support domains ( $n = 3$ ) and 5-node local 1D-IRBF networks ( $n_s = 5$ ) is presented here. On an  $x$ -grid line  $[l]$ , a global interpolant for the field variable at a grid point  $x_i$  is sought in the form

$$u(x_i) = \sum_{j=1}^n \bar{\phi}_j(x_i) u^{[j]}(x_i), \quad (6.9)$$

where  $\{\bar{\phi}_j\}_{j=1}^n$  is a set of the partition of unity functions constructed using MLS approximants (Liu, 2003);  $u^{[j]}(x_i)$  the nodal function value obtained from a local interpolant represented by a 1D-IRBF network  $[j]$ ;  $n$  the number of nodes in

the support domain of  $x_i$ . In (6.9), MLS approximants are presently based on linear polynomials, which are defined in terms of 1 and  $x$ . It is noted that the MLS shape functions possess a so-called partition of unity properties as follows.

$$\sum_{j=1}^n \bar{\phi}_j(x) = 1. \quad (6.10)$$

Relevant derivatives of  $u$  at  $x_i$  can be obtained by differentiating (6.9)

$$\frac{\partial u(x_i)}{\partial x} = \sum_{j=1}^n \left( \frac{\partial \bar{\phi}_j(x_i)}{\partial x} u^{[j]}(x_i) + \bar{\phi}_j(x_i) \frac{\partial u^{[j]}(x_i)}{\partial x} \right), \quad (6.11)$$

$$\frac{\partial^2 u(x_i)}{\partial x^2} = \sum_{j=1}^n \left( \frac{\partial^2 \bar{\phi}_j(x_i)}{\partial x^2} u^{[j]}(x_i) + 2 \frac{\partial \bar{\phi}_j(x_i)}{\partial x} \frac{\partial u^{[j]}(x_i)}{\partial x} + \bar{\phi}_j(x_i) \frac{\partial^2 u^{[j]}(x_i)}{\partial x^2} \right), \quad (6.12)$$

where the values  $u^{[j]}(x_i)$ ,  $\partial u^{[j]}(x_i)/\partial x$  and  $\partial^2 u^{[j]}(x_i)/\partial x^2$  are calculated from 1D-IRBFN networks with  $n_s$  nodes.

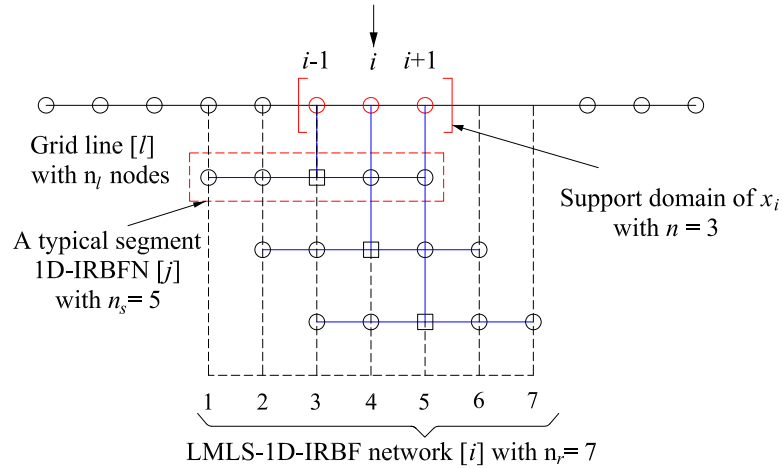


Figure 6.2: LMLS-1D-IRBFN scheme,  $\square$  a typical  $[j]$  node.

Full details of the LMLS-1D-IRBFN method can be found in Chapter 3.

## 6.3 Governing equations for fluid, structure and fluid-structure interaction

In this study, the FSI problem of flow in a lid-driven open-cavity with a flexible bottom wall (Förster et al., 2007; Bathe and Zhang, 2009) is considered. The bottom wall is modelled as a flexible beam using the Euler-Bernoulli beam theory. The fluid is described by the 2-D Navier-Stokes equations of incompressible viscous flow in terms of primitive variables.

### 6.3.1 Governing equations for forced vibration of a beam

The equation of motion for forced lateral vibration of a beam is based on the Euler-Bernoulli beam theory. This is a small-deflection theory and therefore some error will be incurred due to the neglect of the geometric non-linear term when the deflection is actually not small (Spoon and Grant, 2011). Our purpose here is to demonstrate our FSI analysis procedure and we will ignore the non-linear term here for the following reason. As shown later in the numerical results section, the actual maximum central deflection of the beam is about 14.71% of the beam length in the worst case of simply-supported boundary conditions and therefore the error is less than 10% (Spoon and Grant, 2011). In the case of clamped boundary conditions, the error is less than 1.3% since the maximum deflection is about 4.37% of the beam length. The equation of motion is given by (Rao, 2004)

$$EI \frac{\partial^4 w}{\partial x^4} + \rho_s A \frac{\partial^2 w}{\partial t^2} = f(x, t). \quad (6.13)$$

where  $w$  is the lateral deflection of the beam;  $t$  the time;  $E$  Young's modulus;  $I$  the moment of inertia;  $A$  the cross-section area;  $\rho_s$  material density of the beam; and  $f(x, t)$  the external force per unit length of the beam. The boundary conditions for a simply supported or clamped end of a beam are described as

follows.

- Simply supported case:

$$w = 0, \frac{\partial^2 w}{\partial x^2} = 0. \quad (6.14)$$

- Clamped case:

$$w = 0, \frac{\partial w}{\partial x} = 0. \quad (6.15)$$

### 6.3.2 Governing equations for 2-D incompressible viscous flows

The dimensional conservative form of the 2-D Navier-Stokes equations of incompressible viscous flow in terms of primitive variables is written as (Bathe and Zhang, 2009)

$$\frac{\partial u}{\partial x} + \frac{\partial v}{\partial y} = 0, \quad (6.16)$$

$$\rho_f \frac{\partial u}{\partial t} + \rho_f \frac{\partial u^2}{\partial x} + \rho_f \frac{\partial uv}{\partial y} = -\frac{\partial p}{\partial x} + \mu \left[ \frac{\partial^2 u}{\partial x^2} + \frac{\partial^2 u}{\partial y^2} \right], \quad (6.17)$$

$$\rho_f \frac{\partial v}{\partial t} + \rho_f \frac{\partial uv}{\partial x} + \rho_f \frac{\partial v^2}{\partial y} = -\frac{\partial p}{\partial y} + \mu \left[ \frac{\partial^2 v}{\partial x^2} + \frac{\partial^2 v}{\partial y^2} \right], \quad (6.18)$$

where  $u$ ,  $v$  and  $p$  are horizontal velocity, vertical velocity and static pressure of the fluid, respectively;  $\rho_f$  the fluid density; and  $\mu$  the dynamic viscosity of the fluid.

### 6.3.3 Coupled equations for fluid-structure interaction

The geometrical compatibility conditions at the interface  $\Gamma$  between the fluid and structural domains are given by

$$\mathbf{r}^\Gamma(t) = \mathbf{w}^\Gamma(t), \quad (6.19)$$

$$\dot{\mathbf{r}}^\Gamma(t) = \dot{\mathbf{w}}^\Gamma(t), \quad (6.20)$$

where  $\mathbf{r}^\Gamma$  and  $\mathbf{w}^\Gamma$  are the displacement vectors of the fluid and structure at the interface  $\Gamma$ , respectively; and  $\dot{\mathbf{r}}^\Gamma$  and  $\dot{\mathbf{w}}^\Gamma$  the velocity vectors of the fluid and structure at the interface  $\Gamma$ , respectively.

The equilibrium conditions can be described as follows.

$$\mathbf{h}_f^\Gamma(t) + \mathbf{h}_s^\Gamma(t) = \mathbf{0}, \quad (6.21)$$

where  $\mathbf{h}_f^\Gamma$  and  $\mathbf{h}_s^\Gamma$  are the fluid and structure traction vectors acting on the interface  $\Gamma$ , respectively.

## 6.4 Numerical procedures

In this section, the fractional-step projection method proposed by Chorin (1967) is described for solving the system of equations (6.16)-(6.18) with the use of 1D-IRBFN and LMLS-1D-IRBFN methods for spatial discretisation. The combination of the fractional-step projection method and the subiterative technique (Jameson, 1991; Melson et al., 1993) is presented to solve transient flow problems. The details of determination of variable values at “freshly cleared” nodes and a sequentially staggered algorithm for FSI analysis are also given here.

### 6.4.1 Fractional-step projection method (Chorin's method)

- First step: Determine intermediate velocities  $u^*$  and  $v^*$  by ignoring the pressure term and incompressibility. Convection and diffusion terms are discretised explicitly at time level  $(n)$  using the 1D-IRBFN method.

$$\rho_f \frac{u^* - u^{(n)}}{\Delta t} = -\rho_f \frac{\partial(u^{(n)})^2}{\partial x} - \rho_f \frac{\partial u^{(n)} v^{(n)}}{\partial y} + \mu \left[ \frac{\partial^2 u^{(n)}}{\partial x^2} + \frac{\partial^2 u^{(n)}}{\partial y^2} \right], \quad (6.22)$$

$$\rho_f \frac{v^* - v^{(n)}}{\Delta t} = -\rho_f \frac{\partial u^{(n)} v^{(n)}}{\partial x} - \rho_f \frac{\partial (v^{(n)})^2}{\partial y} + \mu \left[ \frac{\partial^2 v^{(n)}}{\partial x^2} + \frac{\partial^2 v^{(n)}}{\partial y^2} \right]. \quad (6.23)$$

- Second step: Solve a Poisson equation for the pressure at time level  $(n+1)$

$$\frac{\partial^2 p^{(n+1)}}{\partial x^2} + \frac{\partial^2 p^{(n+1)}}{\partial y^2} = \frac{\rho_f}{\Delta t} \left( \frac{\partial u^*}{\partial x} + \frac{\partial v^*}{\partial y} \right). \quad (6.24)$$

It is noted that the LHS of (6.24) is discretised using the local MLS-1D-IRBFN method while the RHS is calculated with the 1D-IRBFN method. The process results in a sparse system of equations, which is then economically solved by the LU decomposition technique.

Neumann boundary conditions for pressure are given by

$$\frac{\partial p^{(n+1)}}{\partial x} = \rho_f \frac{u^* - u^{(n)}}{\Delta t}, \quad (6.25)$$

$$\frac{\partial p^{(n+1)}}{\partial y} = \rho_f \frac{v^* - v^{(n)}}{\Delta t}. \quad (6.26)$$

Then, the velocities  $u^{(n+1)}$  and  $v^{(n+1)}$  are determined as

$$u^{(n+1)} = u^* - \frac{\Delta t}{\rho_f} \frac{\partial p^{(n+1)}}{\partial x}, \quad (6.27)$$

$$v^{(n+1)} = v^* - \frac{\Delta t}{\rho_f} \frac{\partial p^{(n+1)}}{\partial y}. \quad (6.28)$$

For irregular domain problems, when determining the derivatives of pressure w.r.t.  $y$  on the curved boundary through Equation (6.26), the values of  $v^*$  on the curved boundary are unknown and can be determined by using a 1D-IRBFN extrapolant from the  $v^*$  values at the interior points as follows.

$$v^*(y_B) = \hat{\mathbf{H}}_B \hat{\mathbf{H}}_I^{-1} \hat{v}_I^*, \quad (6.29)$$

where  $y_B$  is the  $y$ -coordinate of node  $B$  on the curved boundary as shown in Figure 6.3;

$$\hat{v}_I^* = \left( (v^*)^{(1)}, (v^*)^{(2)}, \dots, (v^*)^{(N_y^{[m]}-1)} \right)^T;$$

$$\hat{\mathbf{H}}_B = \left[ \begin{array}{cccccc} H_{[0]}^{(1)}(y_B) & H_{[0]}^{(2)}(y_B) & \dots & H_{[0]}^{(N_y^{[m]}-1)}(y_B) & y_B & 1 \end{array} \right];$$

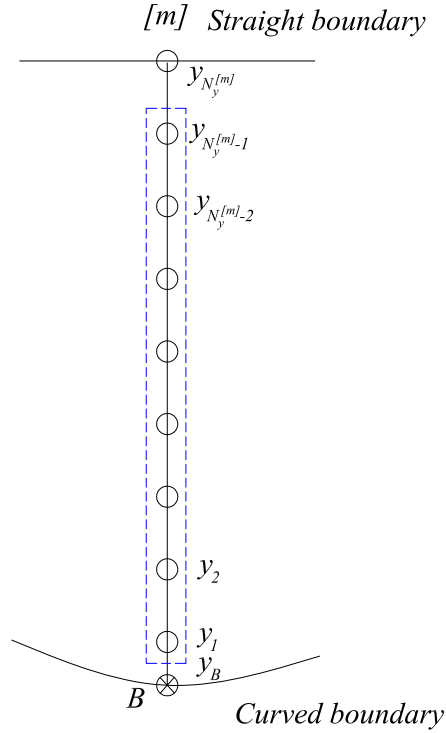
$$\hat{\mathbf{H}}_I = \left[ \begin{array}{cccccc} H_{[0]}^{(1)}(y_1) & H_{[0]}^{(2)}(y_1) & \dots & H_{[0]}^{(N_y^{[m]}-1)}(y_1) & y_1 & 1 \\ H_{[0]}^{(1)}(y_2) & H_{[0]}^{(2)}(y_2) & \dots & H_{[0]}^{(N_y^{[m]}-1)}(y_2) & y_2 & 1 \\ \dots & \dots & \dots & \dots & \dots & \dots \\ H_{[0]}^{(1)}(y_{N_y^{[m]}-1}) & H_{[0]}^{(2)}(y_{N_y^{[m]}-1}) & \dots & H_{[0]}^{(N_y^{[m]}-1)}(y_{N_y^{[m]}-1}) & y_{N_y^{[m]}-1} & 1 \end{array} \right];$$

in which  $N_y^{[m]}$  is the number of grid nodes on the  $y$ -grid line  $[m]$  excluding the node on the curved boundary. The values of  $u^*$  on the curved boundary can be determined in a similar fashion.

#### *Dirichlet boundary condition for pressure*

Making use of Equation (6.3) for pressure values at interior points of an  $x$ -grid line  $[j]$  and Equation (6.2) for first-order derivatives of pressure at the ends of that grid line results in

$$\left( \begin{array}{c} \hat{p}_I \\ \frac{\partial p^{(1)}}{\partial x} \\ \frac{\partial p^{(N_x^{[j]})}}{\partial x} \end{array} \right) = \left[ \begin{array}{c} \hat{\mathbf{H}}_I \\ \hat{\mathbf{K}} \end{array} \right] \left( \begin{array}{c} \hat{w} \\ \hat{c} \end{array} \right), \quad (6.30)$$

Figure 6.3: Configuration to determine  $v^*$  at nodes on a curved boundary.

or

$$\begin{pmatrix} \hat{w} \\ \hat{c} \end{pmatrix} = \begin{bmatrix} \hat{\mathbf{H}}_I \\ \hat{\mathbf{K}} \end{bmatrix}^{-1} \begin{pmatrix} \hat{p}_I \\ \frac{\partial p^{(1)}}{\partial x} \\ \frac{\partial p^{(N_x^{[j]})}}{\partial x} \end{pmatrix}, \quad (6.31)$$

where

$$\begin{aligned} \hat{p}_I &= \left( p^{(2)}, p^{(3)}, \dots, p^{(N_x^{[j]}-1)} \right)^T; \\ \hat{\mathbf{H}}_I &= \begin{bmatrix} H_{[0]}^{(1)}(x_2) & H_{[0]}^{(2)}(x_2) & \dots & H_{[0]}^{(N_x^{[j]})}(x_2) & x_2 & 1 \\ H_{[0]}^{(1)}(x_3) & H_{[0]}^{(2)}(x_3) & \dots & H_{[0]}^{(N_x^{[j]})}(x_3) & x_3 & 1 \\ \dots & \dots & \dots & \dots & \dots & \dots \\ H_{[0]}^{(1)}(x_{N_x^{[j]}-1}) & H_{[0]}^{(2)}(x_{N_x^{[j]}-1}) & \dots & H_{[0]}^{(N_x^{[j]})}(x_{N_x^{[j]}-1}) & x_{N_x^{[j]}-1} & 1 \end{bmatrix}; \\ \hat{\mathbf{K}} &= \begin{bmatrix} H_{[1]}^{(1)}(x_1) & H_{[1]}^{(2)}(x_1) & \dots & H_{[1]}^{(N_x^{[j]})}(x_1) & 1 & 0 \\ H_{[1]}^{(1)}(x_{N_x^{[j]}}) & H_{[1]}^{(2)}(x_{N_x^{[j]}}) & \dots & H_{[1]}^{(N_x^{[j]})}(x_{N_x^{[j]}}) & 1 & 0 \end{bmatrix}; \end{aligned}$$

and  $\partial p^{(1)}/\partial x$  and  $\partial p^{(N_x^{[j]})}/\partial x$  are calculated through Equation (6.25). From Equation (6.3), pressure values at the ends of the  $x$ -grid line  $[j]$  can be defined by

$$\begin{pmatrix} p^{(1)} \\ p^{(N_x^{[j]})} \end{pmatrix} = \hat{\mathbf{H}}_B \begin{pmatrix} \hat{w} \\ \hat{c} \end{pmatrix}, \quad (6.32)$$

where

$$\hat{\mathbf{H}}_B = \begin{bmatrix} H_{[0]}^{(1)}(x_1) & H_{[0]}^{(2)}(x_1) & \dots & H_{[0]}^{(N_x^{[j]})}(x_1) & x_1 & 1 \\ H_{[0]}^{(1)}(x_{N_x^{[j]}}) & H_{[0]}^{(2)}(x_{N_x^{[j]}}) & \dots & H_{[0]}^{(N_x^{[j]})}(x_{N_x^{[j]}}) & x_{N_x^{[j]}} & 1 \end{bmatrix}.$$

By substituting Equation (6.31) into Equation (6.32), the boundary pressure values at both ends of the grid line  $[j]$  are expressed in terms of the values of pressure at interior points and derivatives of pressure at both ends of the grid line  $[j]$  as follows.

$$\begin{pmatrix} p^{(1)} \\ p^{(N_x^{[j]})} \end{pmatrix} = \hat{\mathbf{H}}_B \begin{bmatrix} \hat{\mathbf{H}}_I \\ \hat{\mathbf{K}} \end{bmatrix}^{-1} \begin{pmatrix} \hat{p}_I \\ \frac{\partial p^{(1)}}{\partial x} \\ \frac{\partial p^{(N_x^{[j]})}}{\partial x} \end{pmatrix}. \quad (6.33)$$

The boundary pressure values at both ends of  $y$ -grid lines can be determined in a similar manner.

### 6.4.2 Combination of fractional-step projection method and subiterative technique

In the fractional-step projection method, the RHS of Equations (6.22) and (6.23) are explicitly calculated at time level  $(n)$ . This scheme has severe stability-restricted time-step limitations which leads to a high computational cost when solving moving boundary problems. Jameson (1991) and Melson et al. (1993) presented subiterative techniques within the context of a multigrid methodology

to allow a large physical time step with the use of an explicit code. Rumsey et al. (1996) combined the subiterative technique with an explicit central-difference code and an implicit upwind code for solving unsteady Navier-Stokes equations. The combination of the fractional-step projection method and the subiterative technique are now presented here. The temporal terms of Equations (6.17) and (6.18) are discretised using the backward Euler scheme while the convection and diffusion terms are treated implicitly, which results in

$$\rho_f \frac{u^{(n+1)} - u^{(n)}}{\Delta t} = -\rho_f \frac{\partial(u^{(n+1)})^2}{\partial x} - \rho_f \frac{\partial u^{(n+1)} v^{(n+1)}}{\partial y} - \frac{\partial p^{(n+1)}}{\partial x} + \mu \left[ \frac{\partial^2 u^{(n+1)}}{\partial x^2} + \frac{\partial^2 u^{(n+1)}}{\partial y^2} \right], \quad (6.34)$$

$$\rho_f \frac{v^{(n+1)} - v^{(n)}}{\Delta t} = -\rho_f \frac{\partial u^{(n+1)} v^{(n+1)}}{\partial x} - \rho_f \frac{\partial(v^{(n+1)})^2}{\partial y} - \frac{\partial p^{(n+1)}}{\partial y} + \mu \left[ \frac{\partial^2 v^{(n+1)}}{\partial x^2} + \frac{\partial^2 v^{(n+1)}}{\partial y^2} \right]. \quad (6.35)$$

Pseudo-time derivative terms are added into Equations (6.34) and (6.35) as

$$\rho_f \frac{u^{(n+1)} - u^{(n)}}{\Delta t} + \rho_f \frac{\partial u}{\partial \tau} = -\rho_f \frac{\partial(u^{(n+1)})^2}{\partial x} - \rho_f \frac{\partial u^{(n+1)} v^{(n+1)}}{\partial y} - \frac{\partial p^{(n+1)}}{\partial x} + \mu \left[ \frac{\partial^2 u^{(n+1)}}{\partial x^2} + \frac{\partial^2 u^{(n+1)}}{\partial y^2} \right], \quad (6.36)$$

$$\rho_f \frac{v^{(n+1)} - v^{(n)}}{\Delta t} + \rho_f \frac{\partial v}{\partial \tau} = -\rho_f \frac{\partial u^{(n+1)} v^{(n+1)}}{\partial x} - \rho_f \frac{\partial(v^{(n+1)})^2}{\partial y} - \frac{\partial p^{(n+1)}}{\partial y} + \mu \left[ \frac{\partial^2 v^{(n+1)}}{\partial x^2} + \frac{\partial^2 v^{(n+1)}}{\partial y^2} \right], \quad (6.37)$$

where  $\tau$  is the pseudo time and  $t$  the physical time. The additional terms  $\partial u / \partial \tau$  and  $\partial v / \partial \tau$  are designed in such a way that they vanish when the values of  $u$  and  $v$  approach their correct values at time level  $(n + 1)$  as follows ( $k$  is a

pseudo-time level).

$$\begin{aligned} \rho_f \frac{u^{(n+1)} - u^{(n)}}{\Delta t} + \rho_f \frac{u^{(n+1,k+1)} - u^{(n+1,k)}}{\Delta \tau} &= -\rho_f \frac{\partial(u^{(n+1,k)})^2}{\partial x} - \rho_f \frac{\partial u^{(n+1,k)} v^{(n+1,k)}}{\partial y} \\ &\quad - \frac{\partial p^{(n+1,k+1)}}{\partial x} + \mu \left[ \frac{\partial^2 u^{(n+1,k)}}{\partial x^2} + \frac{\partial^2 u^{(n+1,k)}}{\partial y^2} \right], \end{aligned} \quad (6.38)$$

$$\begin{aligned} \rho_f \frac{v^{(n+1)} - v^{(n)}}{\Delta t} + \rho_f \frac{v^{(n+1,k+1)} - v^{(n+1,k)}}{\Delta \tau} &= -\rho_f \frac{\partial u^{(n+1,k)} v^{(n+1,k)}}{\partial x} - \rho_f \frac{\partial(v^{(n+1,k)})^2}{\partial y} \\ &\quad - \frac{\partial p^{(n+1,k+1)}}{\partial y} + \mu \left[ \frac{\partial^2 v^{(n+1,k)}}{\partial x^2} + \frac{\partial^2 v^{(n+1,k)}}{\partial y^2} \right]. \end{aligned} \quad (6.39)$$

- First step: Determine intermediate velocities  $u^*$  and  $v^*$  by the following equations. The convection and diffusion terms are explicitly calculated at pseudo-time level ( $k$ ) using the 1D-IRBFN method.

$$\begin{aligned} \rho_f \frac{u^* - u^{(n+1,k)}}{\Delta \tau} &= -\rho_f \frac{\partial(u^{(n+1,k)})^2}{\partial x} - \rho_f \frac{\partial u^{(n+1,k)} v^{(n+1,k)}}{\partial y} \\ &\quad + \mu \left[ \frac{\partial^2 u^{(n+1,k)}}{\partial x^2} + \frac{\partial^2 u^{(n+1,k)}}{\partial y^2} \right], \end{aligned} \quad (6.40)$$

$$\begin{aligned} \rho_f \frac{v^* - v^{(n+1,k)}}{\Delta \tau} &= -\rho_f \frac{\partial u^{(n+1,k)} v^{(n+1,k)}}{\partial x} - \rho_f \frac{\partial(v^{(n+1,k)})^2}{\partial y} \\ &\quad + \mu \left[ \frac{\partial^2 v^{(n+1,k)}}{\partial x^2} + \frac{\partial^2 v^{(n+1,k)}}{\partial y^2} \right]. \end{aligned} \quad (6.41)$$

- Second step: Solve a Poisson equation for the pressure  $p^{(n+1,k+1)}$

$$\frac{\partial^2 p^{(n+1,k+1)}}{\partial x^2} + \frac{\partial^2 p^{(n+1,k+1)}}{\partial y^2} = \frac{\rho_f}{\Delta \tau} \left( \frac{\partial u^*}{\partial x} + \frac{\partial v^*}{\partial y} \right), \quad (6.42)$$

The LHS of (6.42) is discretised using the local MLS-1D-IRBFN method while the RHS is calculated with the 1D-IRBFN method. Neumann boundary conditions for pressure are given by

$$\frac{\partial p^{(n+1,k+1)}}{\partial x} = -\rho_f \frac{u^{(n+1,k)} - u^{(n)}}{\Delta t} - \rho_f \frac{u^{(n+1,k)} - u^*}{\Delta \tau}, \quad (6.43)$$

$$\frac{\partial p^{(n+1,k+1)}}{\partial y} = -\rho_f \frac{v^{(n+1,k)} - v^{(n)}}{\Delta t} - \rho_f \frac{v^{(n+1,k)} - v^*}{\Delta \tau}. \quad (6.44)$$

Then, velocities  $u^{(n+1,k+1)}$  and  $v^{(n+1,k+1)}$  are determined as follows.

$$u^{(n+1,k+1)} = k_t \left( -\frac{1}{\rho_f} \frac{\partial p^{(n+1,k+1)}}{\partial x} + \frac{u^{(n)}}{\Delta t} + \frac{u^*}{\Delta \tau} \right), \quad (6.45)$$

$$v^{(n+1,k+1)} = k_t \left( -\frac{1}{\rho_f} \frac{\partial p^{(n+1,k+1)}}{\partial y} + \frac{v^{(n)}}{\Delta t} + \frac{v^*}{\Delta \tau} \right), \quad (6.46)$$

where  $k_t = \frac{\Delta t \Delta \tau}{\Delta t + \Delta \tau}$ .

- Third step: Check convergence criterion for  $u, v$  and  $p$

$$CM_u = \frac{\sqrt{\sum_{i=1}^{N_{ip}} \left( u_i^{(n+1,k+1)} - u_i^{(n+1,k)} \right)^2}}{\sqrt{\sum_{i=1}^{N_{ip}} \left( u_i^{(n+1,k+1)} \right)^2}} < TOL, \quad (6.47)$$

$$CM_v = \frac{\sqrt{\sum_{i=1}^{N_{ip}} \left( v_i^{(n+1,k+1)} - v_i^{(n+1,k)} \right)^2}}{\sqrt{\sum_{i=1}^{N_{ip}} \left( v_i^{(n+1,k+1)} \right)^2}} < TOL, \quad (6.48)$$

$$CM_p = \frac{\sqrt{\sum_{i=1}^{N_{ip}} \left( p_i^{(n+1,k+1)} - p_i^{(n+1,k)} \right)^2}}{\sqrt{\sum_{i=1}^{N_{ip}} \left( p_i^{(n+1,k+1)} \right)^2}} < TOL, \quad (6.49)$$

where  $TOL$  is a given tolerance and presently set to be  $10^{-7}$ ; and  $N_{ip}$  the number of interior points of the fluid domain. If not converged, return to the first step. Otherwise, assign  $u^{(n+1)} = u^{(n+1,k+1)}$ ,  $v^{(n+1)} = v^{(n+1,k+1)}$  and  $p^{(n+1)} = p^{(n+1,k+1)}$ , then advance the physical time  $t$ .

### 6.4.3 Determine variable values at “freshly cleared” nodes

“Freshly cleared” nodes are the nodes that are not inside the fluid domain at time level  $(n)$ , but emerge into the fluid domain at the next time level  $(n+1)$ . We need to have a “guess” value at these nodes, i.e. at pseudo-time level  $k=0$

associated with the real time level  $(n + 1)$ . For this purpose, the technique presented by Udaykumar et al. (2001) to determine values at the “freshly cleared” nodes is employed here. As shown in Figure 6.4, the values at the “freshly cleared” nodes (e.g., a typical node  $A$ ) are interpolated from the information at two interior nodes (nodes  $C$  and  $D$ ), and one node on the boundary (node  $B$ ) through the following interpolant.

$$u^I(y) = a_0 + a_1y + a_2y^2, \quad (6.50)$$

where  $a_0$ ,  $a_1$  and  $a_2$  are coefficients to be determined through the variable values and coordinates of nodes  $B$ ,  $C$  and  $D$ .

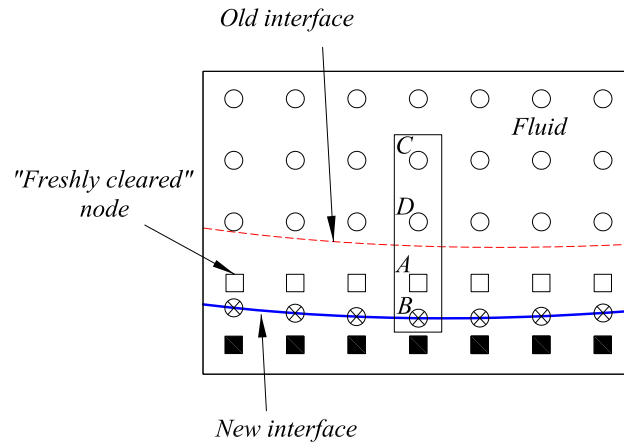


Figure 6.4: Configuration to determine initial values at “freshly cleared” nodes.

#### 6.4.4 Sequential staggered fluid-structure interaction algorithm

The sequentially staggered algorithm (Piperno, 1997; Förster et al., 2007) is used in the present study and described as follows.

- Step 1: At the initial time ( $t = 0s$ ), set the displacement ( $\mathbf{w}$ ) and velocity ( $\dot{\mathbf{w}}$ ) of the bottom wall to be zero.

- Step 2: Calculate a predictor of the structural interface displacement at the new time level ( $w_p^{(n+1)}$ ) using one of the following two approaches (Piperno, 1997; Förster et al., 2007).

- Approach 1: Zeroth order accurate predictor

$$w_p^{(n+1)} = w^{(n)}. \quad (6.51)$$

- Approach 2: First order accurate predictor

$$w_p^{(n+1)} = w^{(n)} + \Delta t \dot{w}. \quad (6.52)$$

Then determine the grid-node system for fluid analysis based on  $w_p^{(n+1)}$ .

- Step 3: Solve the fluid problem to obtain pressure distribution ( $\mathbf{p}^\Gamma$ ) on the bottom wall with the use of  $\dot{\mathbf{w}}$  as a Dirichlet boundary condition for the vertical velocity ( $v$ ) of fluid field.
- Step 4: Solve the structural problem for a new displacement ( $\mathbf{w}$ ) and velocity ( $\dot{\mathbf{w}}$ ) of the bottom wall with consideration of the fluid load  $\mathbf{p}^\Gamma$  (the effect of viscous stress on the displacement of the bottom wall is much smaller than that of the pressure stress and hence neglected here). In the present study, the displacements are restricted to be small, thus there is no distinction between the material coordinates and spatial coordinates.
- Step 5: Advance physical time from level ( $n$ ) to ( $n + 1$ ) and return to Step 2.

Steps 2-5 are repeated until a stable FSI solution is found. The flowchart of the FSI analysis procedure is described in detail as shown in Figure 6.5.

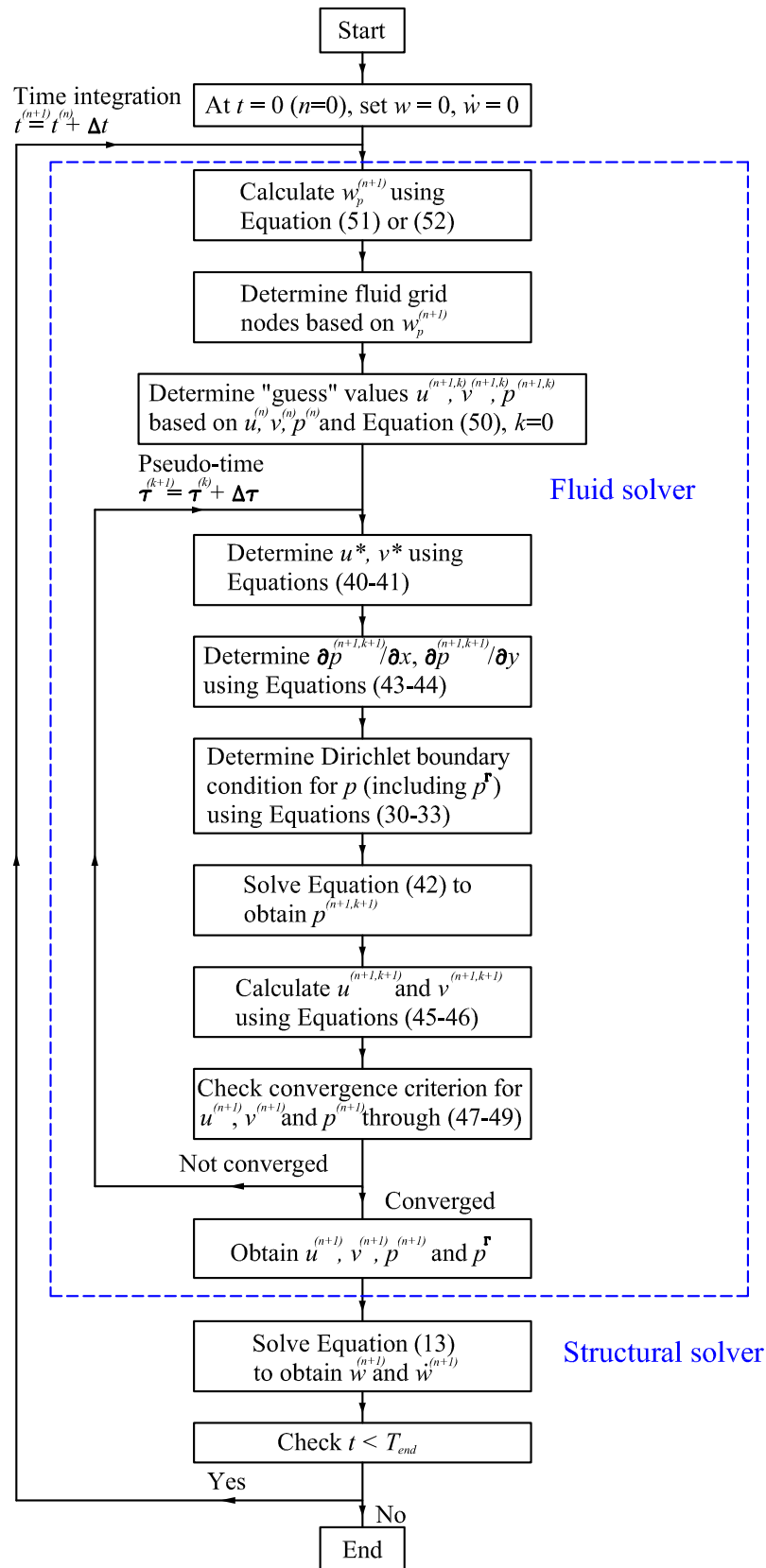


Figure 6.5: Flowchart of the FSI analysis procedure.

## 6.5 Numerical results and discussion

Several examples are considered here to study the performance of the present numerical procedure. The examples are chosen to illustrate various steps of analysis for fluid flow, structural response and ultimately the response in a fluid-structure interaction problem. The domains of interest are discretised using uniform Cartesian grids. By using the LMLS-1D-IRBFN method to discretise the LHS of governing equations and the LU decomposition technique to solve the resultant sparse system of simultaneous equations, the computational cost is reduced.

### 6.5.1 Example 1: Mixed convection in a lid-driven cavity

The fluid solver is first verified through a solution of mixed convection in a lid-driven cavity with a hot moving lid and a cold stationary bottom wall. The problem geometry and boundary conditions are described in Figure 6.6. With the Boussinesq approximation, the dimensionless form of 2-D incompressible Navier-Stokes equations in terms of primitive variables and the energy equation governing the mixed convection in the cavity are written as follows (Iwatsu et al., 1993).

$$\frac{\partial U}{\partial X} + \frac{\partial V}{\partial Y} = 0, \quad (6.53)$$

$$\frac{\partial U}{\partial t'} + \frac{\partial U^2}{\partial X} + \frac{\partial UV}{\partial Y} = -\frac{\partial P}{\partial X} + \frac{1}{Re} \left[ \frac{\partial^2 U}{\partial X^2} + \frac{\partial^2 U}{\partial Y^2} \right], \quad (6.54)$$

$$\frac{\partial V}{\partial t'} + \frac{\partial UV}{\partial X} + \frac{\partial V^2}{\partial Y} = -\frac{\partial P}{\partial Y} + \frac{1}{Re} \left[ \frac{\partial^2 V}{\partial X^2} + \frac{\partial^2 V}{\partial Y^2} \right] + \frac{Gr}{Re^2} \theta, \quad (6.55)$$

$$\frac{\partial \theta}{\partial t'} + \frac{\partial U\theta}{\partial X} + \frac{\partial V\theta}{\partial Y} = \frac{1}{Pr Re} \left[ \frac{\partial^2 \theta}{\partial X^2} + \frac{\partial^2 \theta}{\partial Y^2} \right]. \quad (6.56)$$

The variables in the equations above are nondimensionalised as

$$t' = \frac{t}{H/U_0}, \quad X = \frac{x}{H}, \quad Y = \frac{y}{H},$$

$$U = \frac{u}{U_0}, \quad V = \frac{v}{U_0}, \quad P = \frac{p}{\rho_f U_0^2}, \quad \theta = \frac{T - T_C}{T_H - T_C},$$

where  $H$  is the side length of the square cavity and  $U_0$  velocity of the lid;  $T$  the temperature; and  $T_H$  and  $T_C$  the hot and cold temperatures, respectively.

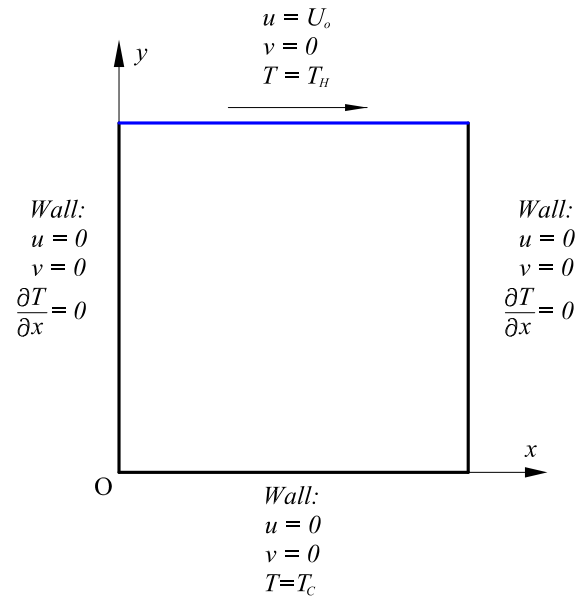


Figure 6.6: Mixed convection in a lid-driven cavity: geometry and boundary conditions.

In these equations, the nondimensionalised parameters are the Reynolds number  $Re = U_0 H / \nu$ , the Prandtl number  $Pr = \nu / \alpha$  ( $Pr$  is set to be 0.71 presently) and the Grashof number  $Gr = Ra / Pr$ , where  $Ra = g \beta (T_H - T_C) H^3 / (\nu \alpha)$ ,  $\nu$  is the kinematic viscosity,  $\alpha$  the thermal diffusivity of the fluid,  $\beta$  the thermal expansion coefficient of the fluid and  $g$  the gravitational acceleration. The Richardson number is defined by  $Ri = Gr / Re^2$  that measures the relative strength of the natural convection and forced convection. If  $Ri \ll 1$  then the forced convection effect is dominant while if  $Ri \gg 1$  then the natural convection effect is dominant.

Table 6.1: Mixed convection in a lid-driven cavity: grid convergence study and comparison of the average Nusselt number ( $Nu$ ) at the top wall for the Grashof number  $Gr = 10^2$ , and several Reynolds numbers  $Re = 100, 400$  and  $1000$ , using the 1D-IRBFN method (Approach 1) and the numerical procedure based on the 1D-IRBFN and local MLS-1D-IRBFN methods (Approach 2).

Grid	$Re = 100$	$Re = 400$	$Re = 1000$
	Approach 1		
$41 \times 41$	1.98	4.13	6.77
$61 \times 61$	1.99	4.08	6.87
$81 \times 81$	2.00	4.05	6.80
$101 \times 101$	2.00	4.04	6.73
	Approach 2		
$41 \times 41$	1.98	4.14	6.89
$61 \times 61$	1.99	4.07	6.89
$81 \times 81$	2.00	4.04	6.80
$101 \times 101$	2.00	4.03	6.72
Iwatsu et al. (1993) (FDM)	1.94	3.84	6.33
Sharif (2007) (FVM)	-	4.05	6.55
Cheng (2011) (FDM)	-	4.14	6.73
Al-Amiri and Khanafer (2011) (FEM)	2.02	4.05	6.45

Table 6.2: Mixed convection in a lid-driven cavity: grid convergence study and comparison of the average Nusselt number ( $Nu$ ) at the top wall for the Grashof number  $Gr = 10^4$ , and several Reynolds numbers  $Re = 100, 400$  and  $1000$ , using the 1D-IRBFN method (Approach 1) and the numerical procedure based on the 1D-IRBFN and local MLS-1D-IRBFN methods (Approach 2).

Grid	$Re = 100$	$Re = 400$	$Re = 1000$
	Approach 1		
$41 \times 41$	1.36	3.87	6.72
$61 \times 61$	1.37	3.83	6.82
$81 \times 81$	1.37	3.80	6.75
$101 \times 101$	1.38	3.79	6.67
	Approach 2		
$41 \times 41$	1.36	3.87	6.83
$61 \times 61$	1.36	3.82	6.83
$81 \times 81$	1.37	3.80	6.74
$101 \times 101$	1.37	3.78	6.67
Iwatsu et al. (1993) (FDM)	1.34	3.62	6.29
Sharif (2007) (FVM)	-	3.82	6.50
Cheng (2011) (FDM)	-	3.90	6.68
Al-Amiri and Khanafer (2011) (FEM)	1.38	3.76	6.56

Table 6.3: Mixed convection in a lid-driven cavity: grid convergence study and comparison of the average Nusselt number ( $Nu$ ) at the top wall for the Grashof number  $Gr = 10^6$ , and several Reynolds numbers  $Re = 100, 400$  and  $1000$ , using the 1D-IRBFN method (Approach 1) and the numerical procedure based on the 1D-IRBFN and local MLS-1D-IRBFN methods (Approach 2).

Grid	$Re = 100$	$Re = 400$	$Re = 1000$
	Approach 1		
$41 \times 41$	1.01	1.24	-
$61 \times 61$	1.01	1.21	1.88
$81 \times 81$	1.01	1.19	1.85
$101 \times 101$	1.01	1.18	1.82
	Approach 2		
$41 \times 41$	1.01	1.25	-
$61 \times 61$	1.01	1.22	1.89
$81 \times 81$	1.01	1.19	1.86
$101 \times 101$	1.01	1.18	1.82
Iwatsu et al. (1993) (FDM)	1.02	1.22	1.77
Sharif (2007) (FVM)	-	1.17	1.81
Cheng (2011) (FDM)	-	1.21	1.75
Al-Amiri and Khanafer (2011) (FEM)	1.02	1.17	1.72

The fractional-step projection method is applied to solve this problem with a time step  $\Delta t' = 10^{-3}$ . Tables 6.1-6.3 describe the grid convergence study of the average Nusselt number at the lid for several Grashof numbers  $Gr = 10^2, 10^4$  and  $10^6$ , and Reynolds numbers  $Re = 100, 400$  and  $1000$ . The LHS of pressure Poisson equation (6.24) is discretised by using 1D-IRBFN method (Approach 1) and LMLS-1D-IRBFN method (Approach 2). The system matrix of Approach 2 is much more sparse than that of Approach 1. The obtained numerical results showed that both approaches yield the same level of accuracy. Approach 2 is used for all other computations in the present study in order to save the computational cost. It can be seen that the converged numerical results are in good agreement with the published results of other authors. The isothermal lines and streamlines of the flow field inside the cavity at several  $Gr$  and  $Re$  numbers are depicted in Figures 6.7-6.9.

For the case  $Gr = 10^2$  (Figure 6.7), the forced convection effect is dominant ( $Ri \ll 1$ ), thus the streamlines of the flow are similar to those of the classical lid-driven cavity case (readers are referred to the work of Ghia et al. (1982) for

$Re = 100, 400$  and  $1000$ . At  $Re = 1000$ , the temperature gradient is steep at the region close to the bottom wall and the lid, while the temperature gradient is small at the center region of the cavity. This indicates that the fluid is well mixed for the bulk of the cavity due to the flow circulation.

For the case  $Gr = 10^4$  (Figure 6.8), the natural convection effect is comparable to the forced convection effect at  $Re = 100$  ( $Ri = 1$ ), while the forced convection effect is still dominant at  $Re = 400$  and  $1000$  ( $Ri \ll 1$ ). Therefore, the flow pattern is quite different at  $Re = 100$ , while remains similar at  $Re = 400$  and  $1000$ , when compared to those of the above case ( $Gr = 10^2$ ).

For the case  $Gr = 10^6$  (Figure 6.9), the natural convection effect is stronger than the forced convection effect. The flow patterns are very different from those of the classical lid-driven cavity case for several Reynolds numbers  $Re = 100, 400$  and  $1000$ . It is observed that the heat conduction is almost uniform for the case  $Re = 100$  and mainly occurs at the bottom and middle regions of the cavity for the cases  $Re = 400$  and  $1000$ .

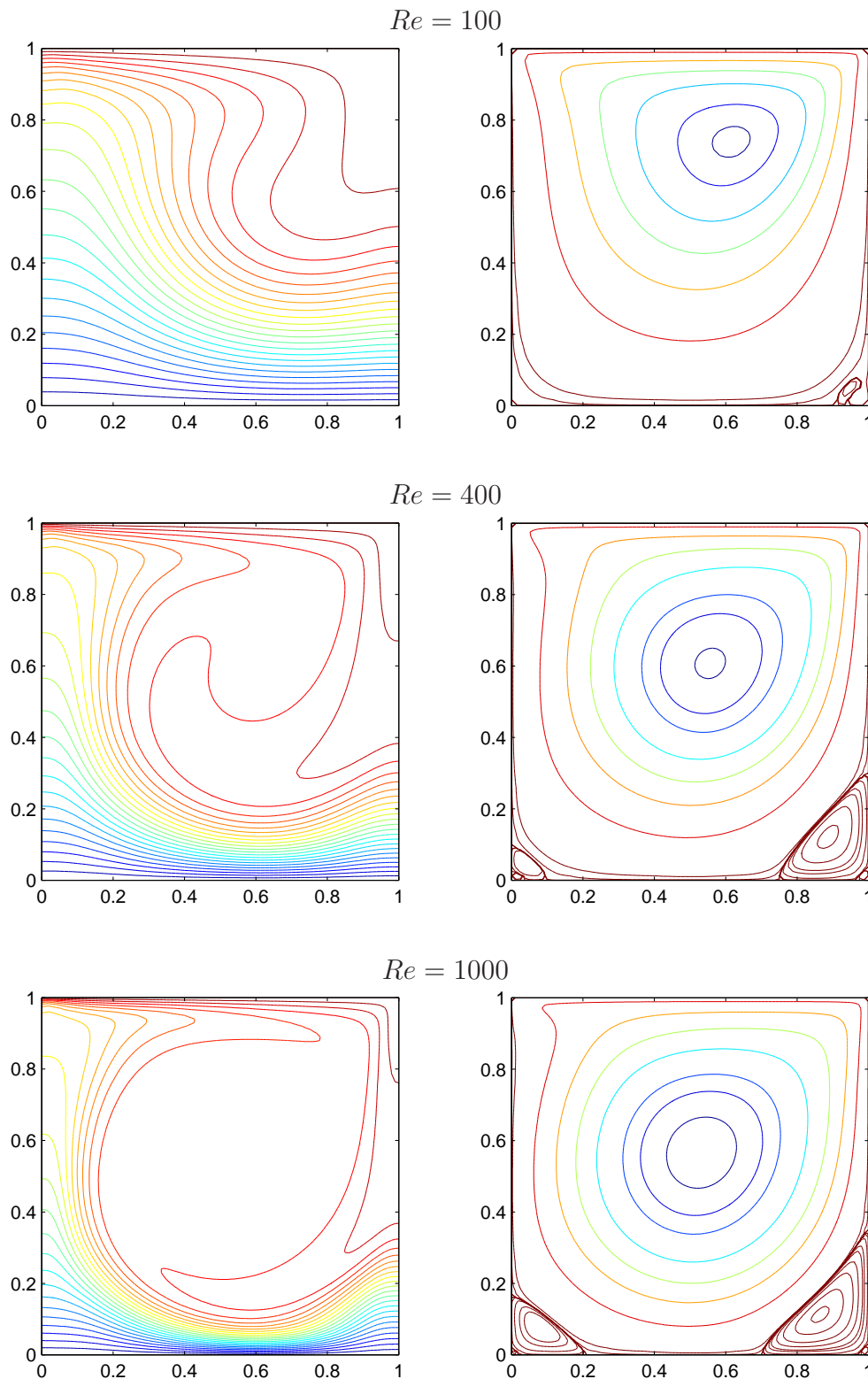


Figure 6.7: Mixed convection in a lid-driven cavity: isothermal lines (left) and streamlines (right) of the flow at  $Gr = 10^2$ , and several Reynolds numbers  $Re = 100, 400$  and  $1000$ , using grids of  $61 \times 61$ ,  $81 \times 81$  and  $101 \times 101$ , respectively. The isothermal values are 25 uniformly distributed values in the range  $[T_C, T_H]$ . The contour values of stream function used here are taken to be the same as those in (Ghia et al., 1982).

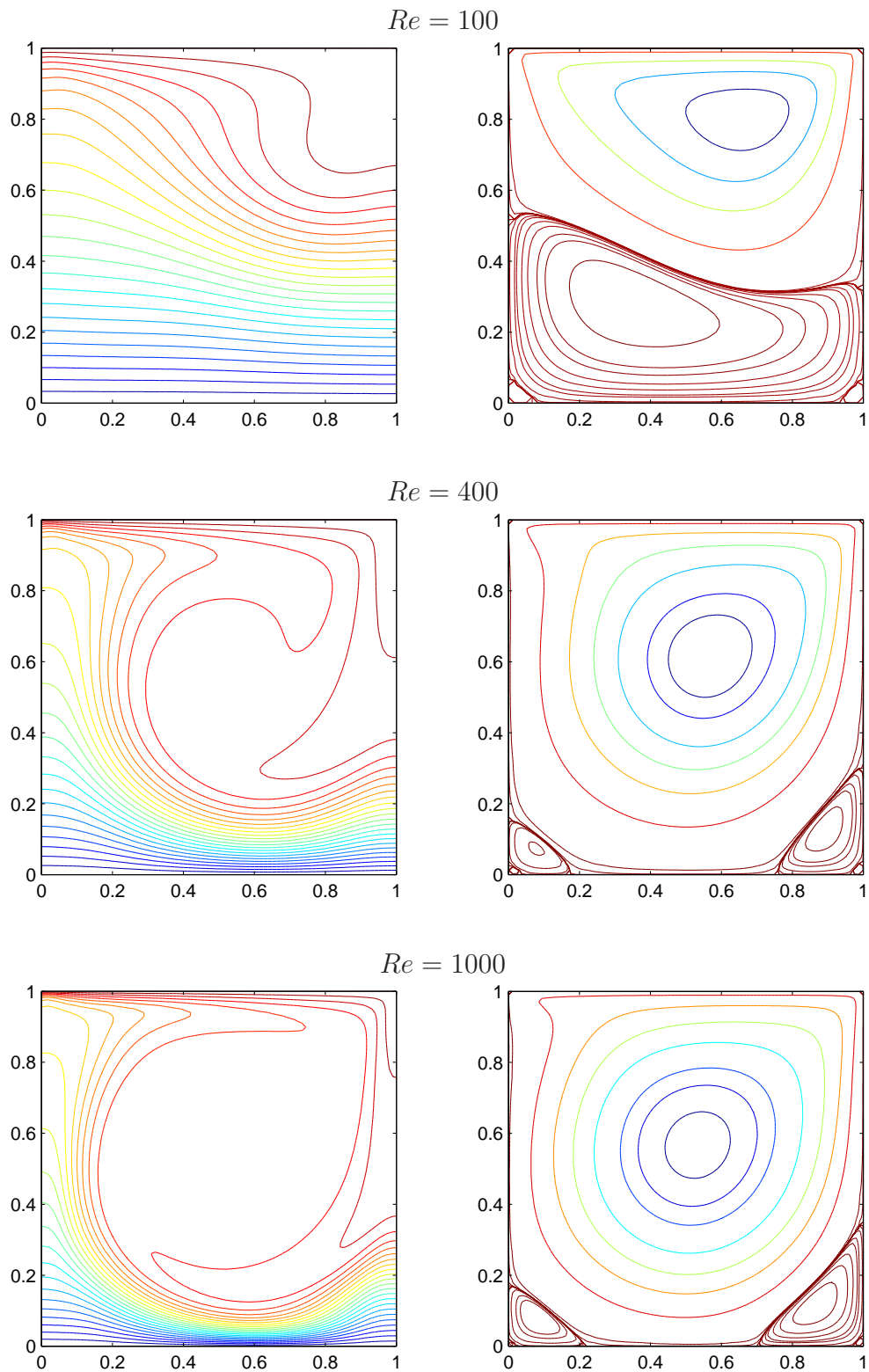


Figure 6.8: Mixed convection in a lid-driven cavity: isothermal lines (left) and streamlines (right) of the flow at  $Gr = 10^4$ , and several Reynolds numbers  $Re = 100, 400$  and  $1000$ , using grids of  $61 \times 61$ ,  $81 \times 81$  and  $101 \times 101$ , respectively. The isothermal values are 25 uniformly distributed values in the range  $[T_C, T_H]$ . The contour values of stream function used here are taken to be the same as those in (Ghia et al., 1982).

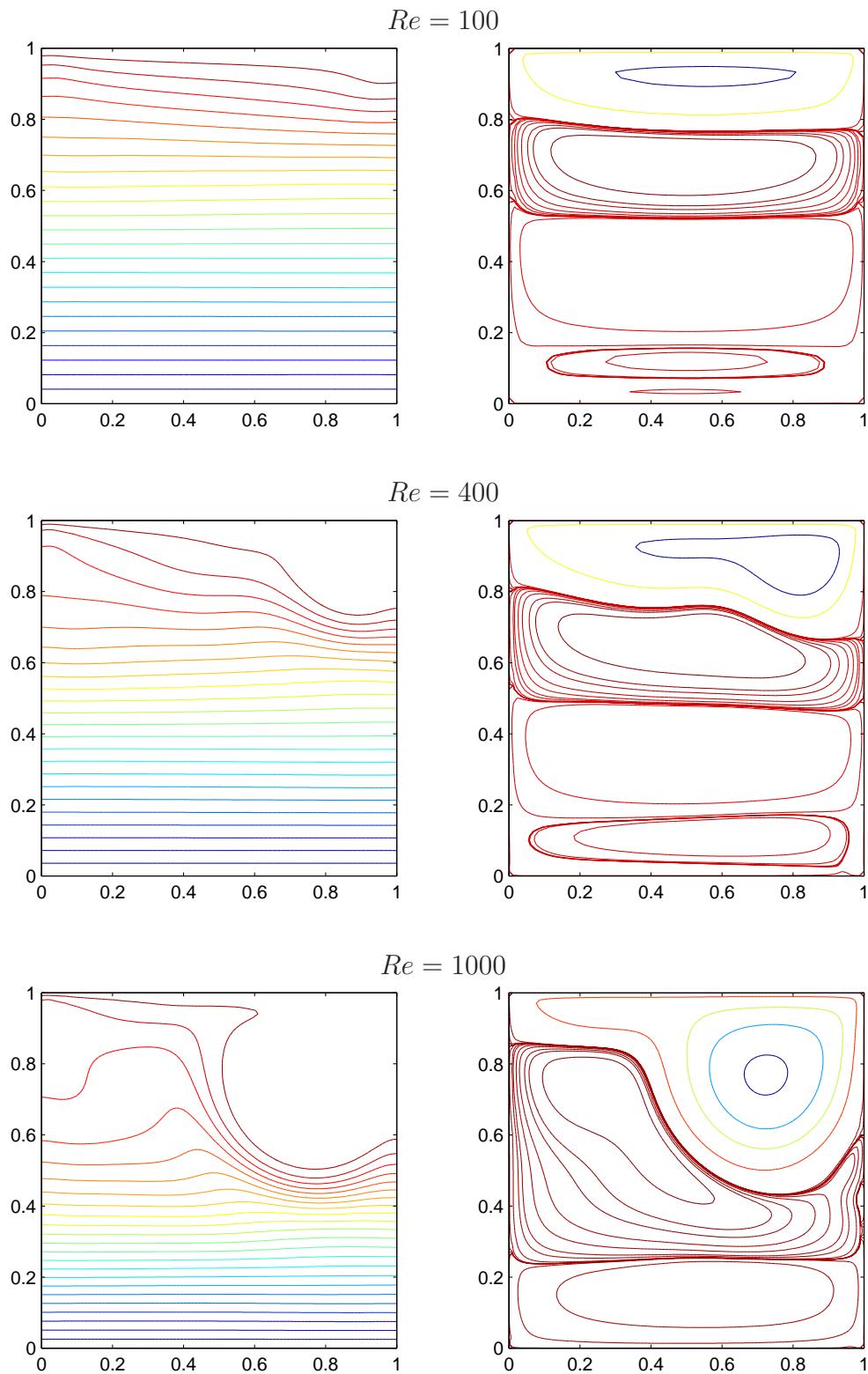


Figure 6.9: Mixed convection in a lid-driven cavity: isothermal lines (left) and streamlines (right) of the flow at  $Gr = 10^6$ , and several Reynolds numbers  $Re = 100, 400$  and  $1000$ , using grids of  $61 \times 61$ ,  $81 \times 81$  and  $101 \times 101$ , respectively. The isothermal values are 25 uniformly distributed values in the range  $[T_C, T_H]$ . The contour values of stream function used here are taken to be the same as those in (Ghia et al., 1982).

### 6.5.2 Example 2: Flow in a lid-driven open-cavity with a prescribed bottom wall motion

The problem geometry and boundary conditions are described in Figure 6.10. The fluid properties and problem geometry used here are: fluid kinematic viscosity  $\nu = 0.01\text{m}^2/\text{s}$ , fluid density  $\rho_f = 1.0\text{kg}/\text{m}^3$ , the side length of the square cavity  $H = 1\text{m}$  and the height of inlet and outlet  $h = 0.1\text{m}$ . The bottom wall motion is given as:  $w = w_0 \cos(\omega_f t - \pi/2)$ , where  $\omega_f = 2\pi/5 \text{ rad}/\text{s}$  and  $w_0 = -0.5(x^2 - x)$ . The lid is sliding from the left to the right in two different manners as follows.

- Case 1:  $U_0 = 1 \text{ m}/\text{s}$ .
- Case 2:  $U_0 = 1 - \cos(\omega_f t) \text{ m}/\text{s}$ .

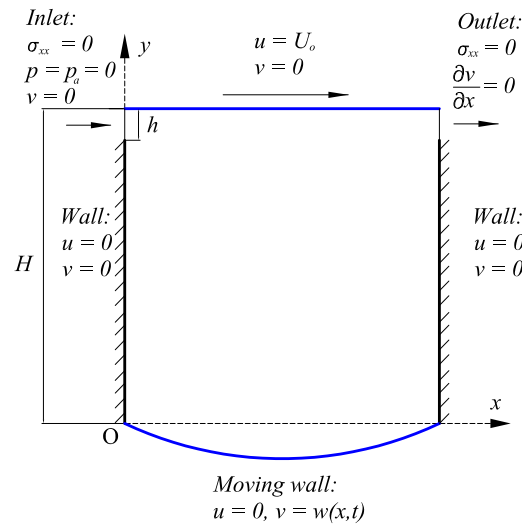


Figure 6.10: Flow in a lid-driven open-cavity with a prescribed bottom wall motion: geometry and boundary conditions.

The combination of the fractional-step projection method and subiterative technique is applied to compute the transient solutions of the flow in the cavity. The grid convergence study is first conducted for the case of stationary bottom wall ( $w = 0$ ) and maximum velocity-loading of the lid ( $U_0 = 2\text{m}/\text{s}$  or  $Re = 200$ ).

Figure 6.11 depicts grid-convergence behaviour of vertical and horizontal velocities along the horizontal and vertical center lines, and static pressure distribution along the stationary bottom wall for the case  $Re = 200$ . Grid convergence is observed and the numerical results obtained are indistinguishable for grids denser than or equal to  $61 \times 61$ . The contours of stream function, velocity magnitude and static pressure of the flow in the cavity for the case  $Re = 200$  are shown in Figure 6.12.

Cartesian grids with a grid spacing of  $1/60$  are employed for the case of prescribed bottom wall motion. As shown in Figure 6.13, the fluid domains are represented by Regions  $A$  and  $B$  for a convex bottom wall, by Regions  $A$ ,  $B_1$  and  $B_2$  for a concave bottom wall. The LHS of pressure Poisson equation (6.42) is discretised through the following strategy. The LMLS-1D-IRBFN method is employed to discretise the term  $\partial^2 p / \partial x^2$  in Region  $A$ , while the 1D-IRBFN is used to discretise that term in Region  $B$  (or Regions  $B_1$  and  $B_2$ ). The discretisation of the term  $\partial^2 p / \partial y^2$  is carried out using the LMLS-1D-IRBFN method.

Figure 6.14 presents the response of static pressure at the mid-point of the bottom wall ( $p_M$ ) with respect to time for Case 1. The physical time step ( $\Delta t$ ) and pseudo time step ( $\Delta \tau$ ) are taken to be  $0.1s$  and  $10^{-3}s$ , respectively. It is noted that this response varies periodically with the same frequency as that of the bottom wall motion ( $= \omega_f / 2\pi$ ). Figure 6.15 shows the contours of stream function, velocity magnitude and static pressure of the flow inside the cavity for several times  $t = 51.5, 52.0, 52.5$  and  $53.0s$  (within one time period) for Case 1. The corresponding numerical results for Case 2 are shown in Figures 6.16 and 6.17.

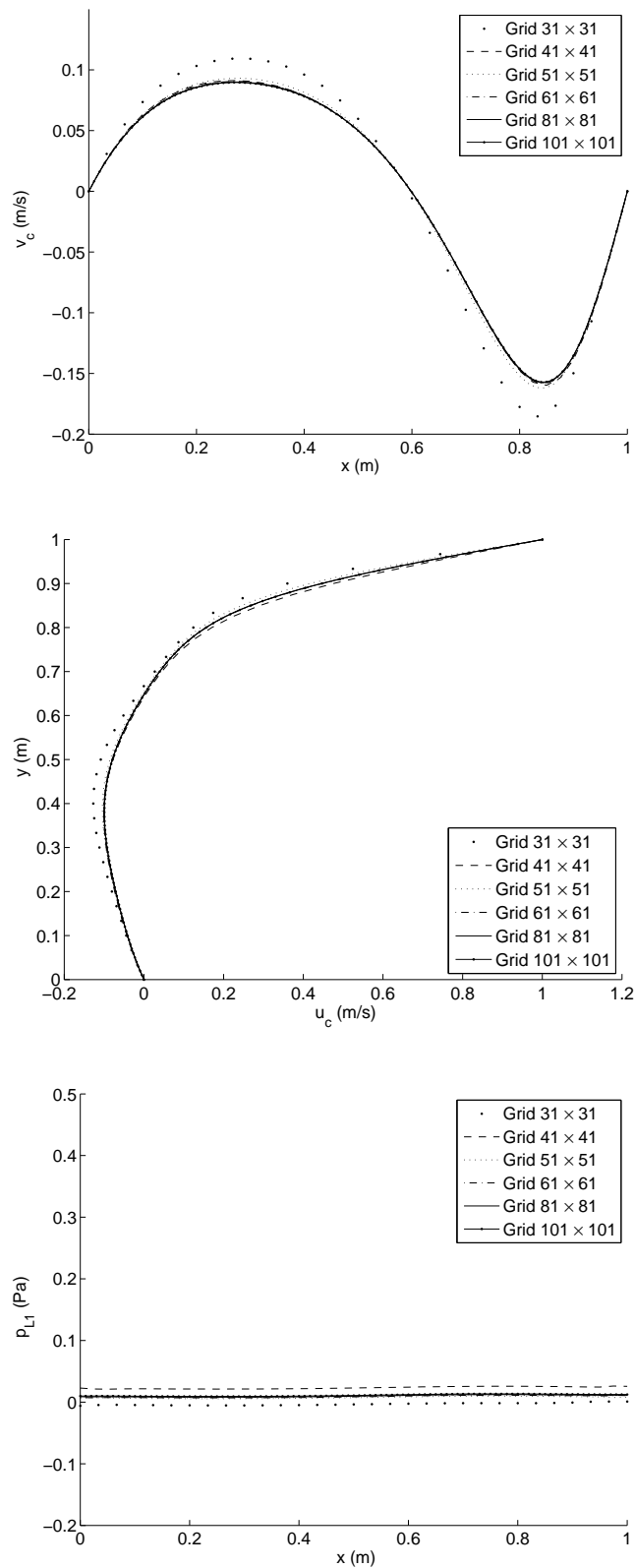


Figure 6.11: Flow in a lid-driven open-cavity with a stationary bottom wall: Grid convergence study of vertical and horizontal velocity profiles along the horizontal and vertical center lines, and static pressure distribution along the bottom wall for  $Re = 200$ .

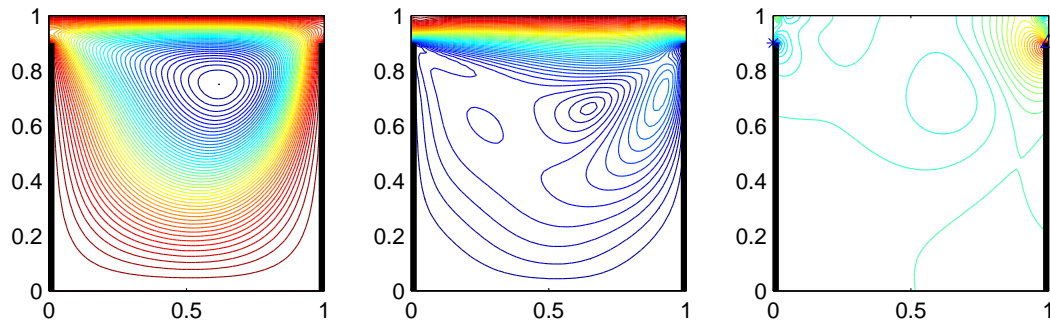


Figure 6.12: Flow in a lid-driven open-cavity with a stationary bottom wall: contours of stream function (left), velocity magnitude (middle) and static pressure (right) of the flow in the cavity for  $Re = 200$ , using a grid of  $61 \times 61$ . Each plot contains 50 contour levels varying linearly from the minimum value to the maximum value.

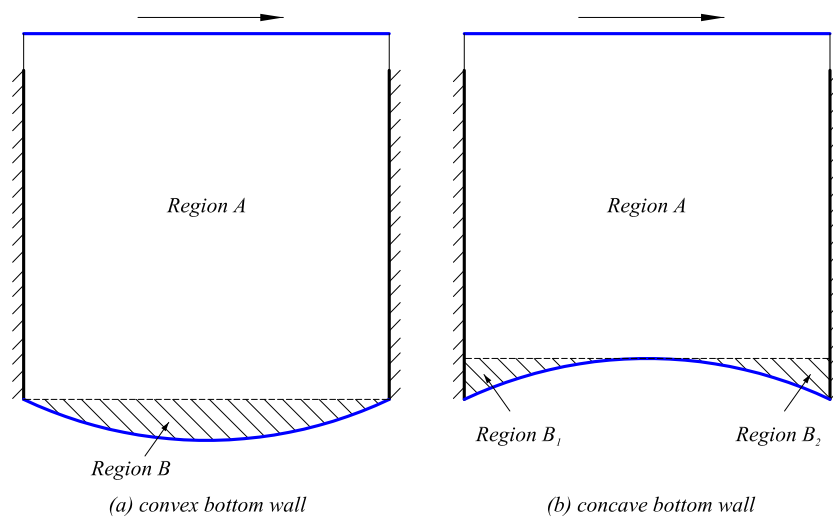


Figure 6.13: Strategy for spatial discretisation using 1D-IRBFN and LMLS-1D-IRBFN methods.

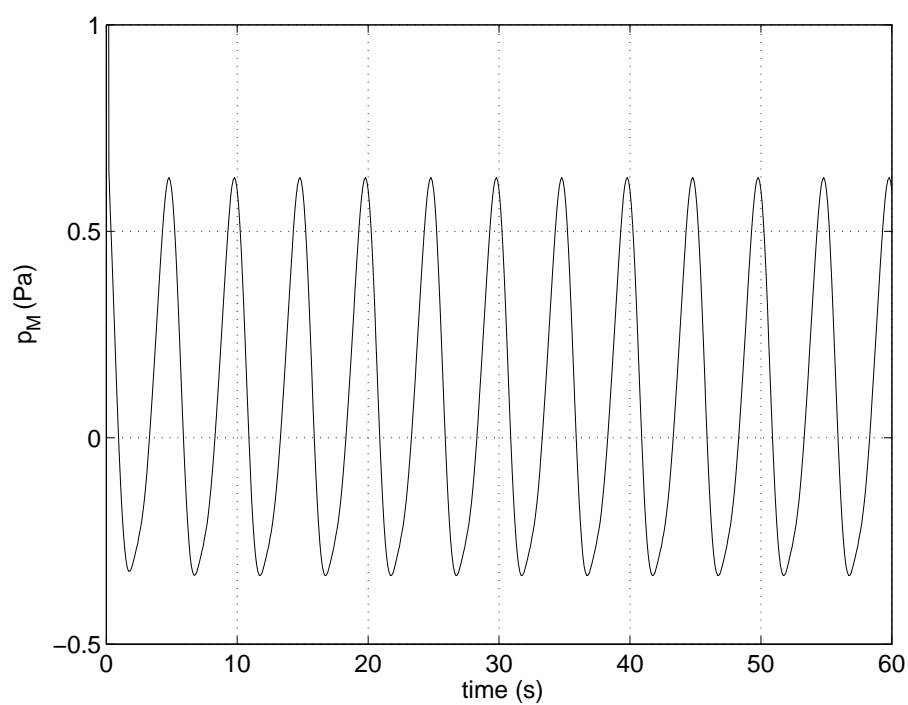


Figure 6.14: Flow in a lid-driven open-cavity with a prescribed bottom wall motion (Case 1): static pressure at the mid-point of the bottom wall with respect to time  $t$ , using a Cartesian grid with a grid spacing of  $1/60$ .

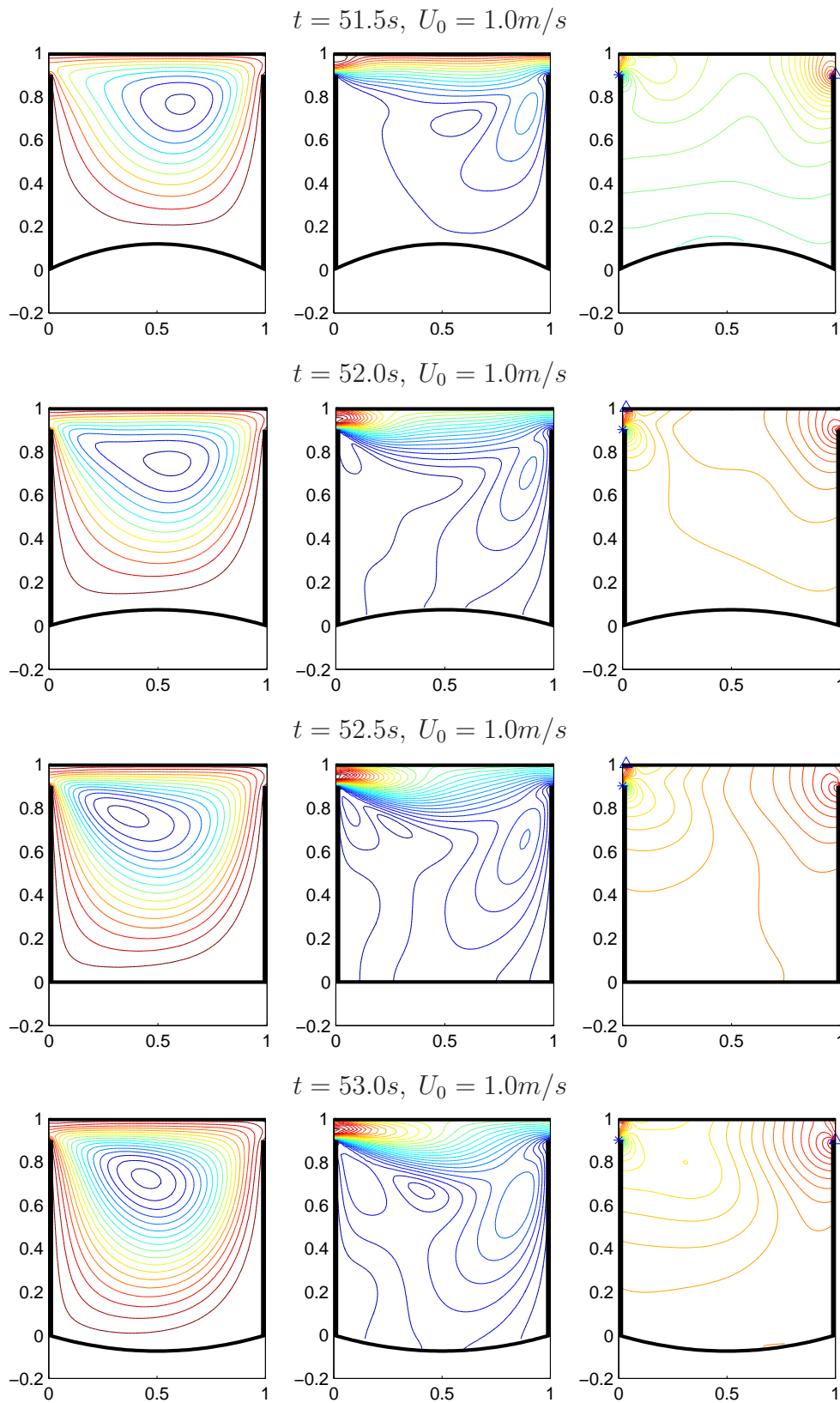


Figure 6.15: Flow in a lid-driven open-cavity with a prescribed bottom wall motion (Case 1): contours of stream function (left), velocity magnitude (middle) and static pressure (right) of the flow for several times  $t = 51.5, 52.0, 52.5$  and  $53.0s$ , from top to bottom, using a Cartesian grid with a grid spacing of  $1/60$ .

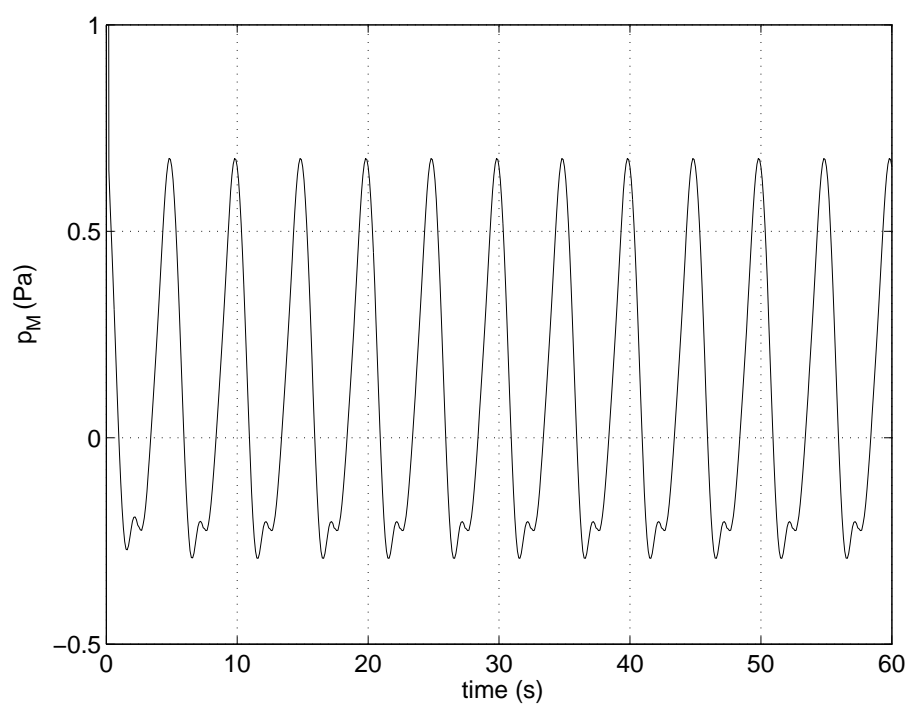


Figure 6.16: Flow in a lid-driven open-cavity with a prescribed bottom wall motion (Case 2): static pressure at the mid-point of the bottom wall with respect to time  $t$ , using a Cartesian grid with a grid spacing of  $1/60$ .

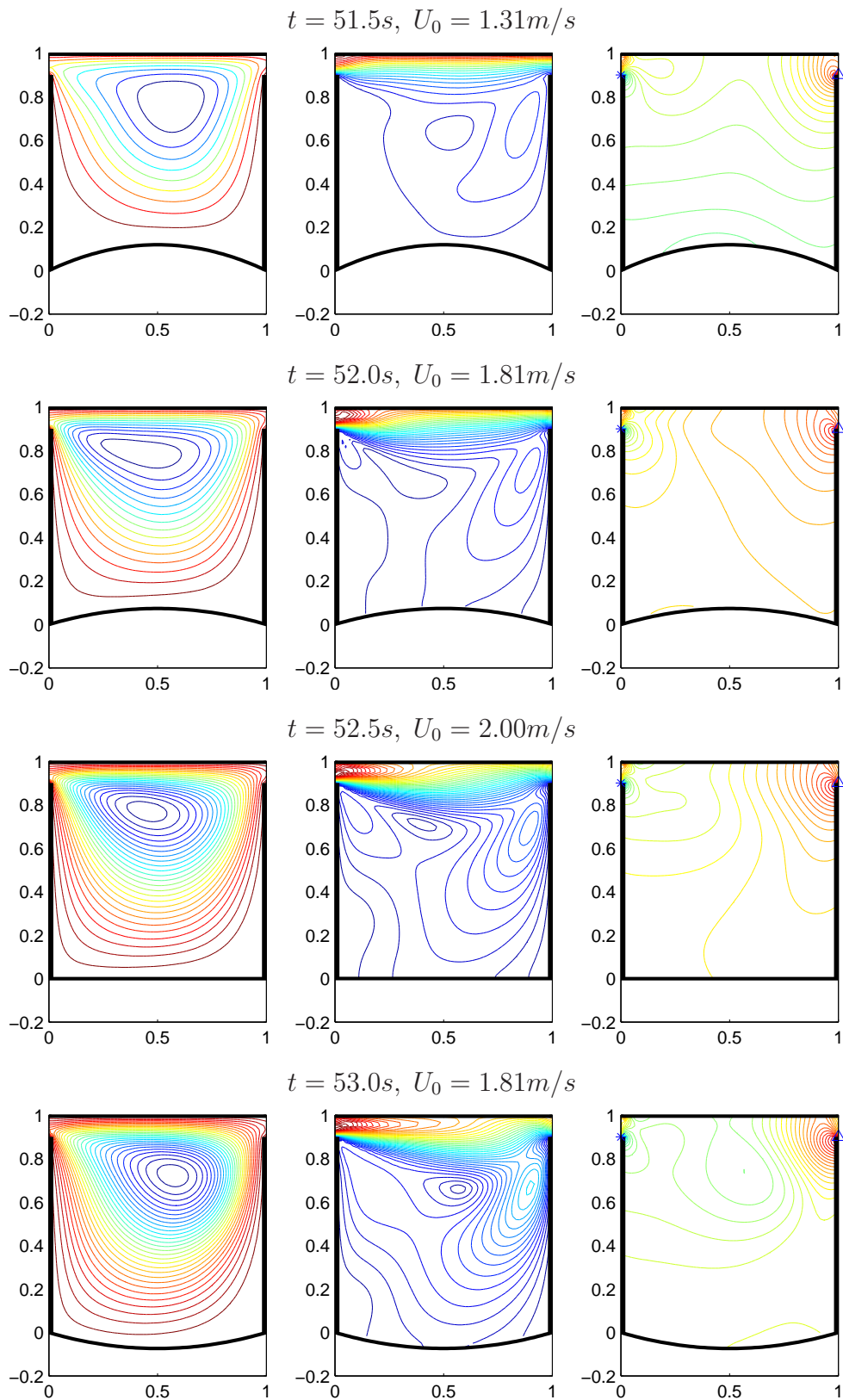


Figure 6.17: Flow in a lid-driven open-cavity with a prescribed bottom wall motion (Case 2): contours of stream function (left), velocity magnitude (middle) and static pressure (right) of the flow for several times  $t = 51.5, 52.0, 52.5$  and  $53.0s$ , from top to bottom, using a Cartesian grid with a grid spacing of  $1/60$ .

### 6.5.3 Example 3: Forced vibration of a simply supported beam

This example deals with the dynamic behaviour of a simply supported beam subject to a harmonic external force  $F(t) = f_0 \sin \omega t$  applied at  $x = a$ , as shown in Figure 6.18 (where  $f_0 = 0.1N$ ,  $\omega = 2\pi/5 \text{ rad/s}$ ,  $a_L = 1m$  and  $a = 0.5m$ ). The problem geometry and material parameters of the beam used here are: the cross-section area  $A = 0.002m^2$ , the moment of inertia  $I = 6.67 \times 10^{-10}m^4$ , Young's modulus  $E = 2.5 \times 10^6 Pa$  and material density  $\rho_s = 500kg/m^3$ . The boundary and initial conditions for the simply supported beam can be described as

$$w = 0, \frac{\partial^2 w}{\partial x^2} = 0, \quad \text{at } x = 0, x = a_L \quad (6.57)$$

$$w = 0, \frac{\partial w}{\partial t} = v_0, \quad \text{at } t = 0 \quad (6.58)$$

where  $v_0$  is the initial velocity of the beam. An analytical solution to this problem can be found in (Rao, 2004).

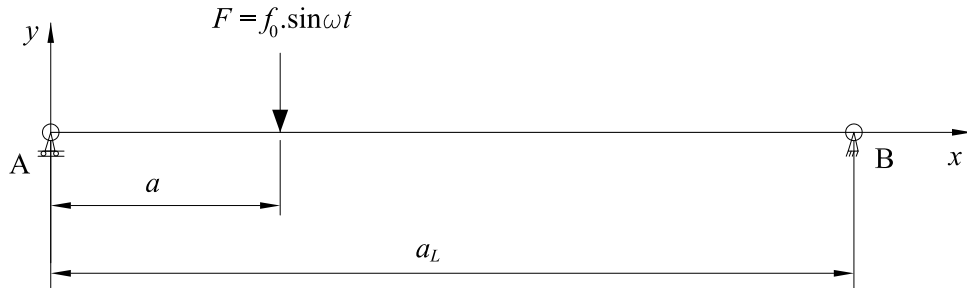


Figure 6.18: Forced vibration of a simply supported beam.

The fully discrete scheme with Newmark's method for temporal discretisation is employed here. The spatial term is discretised by using the 1D-IRBFN-4 scheme based on a uniform grid. Table 6.4 describes the grid convergence study of deflection  $u$  and velocity  $v$  of the beam at time  $t = 14s$ . For a given time step, the accuracy is not improved further when refining the grid to a

certain grid size. However, the accuracy is greatly improved by reducing the time step. This indicates that the major numerical error is not due to the 1D-IRBFN approximation, but due to the temporal discretisation. The steady-state responses of the forced vibration system obtained by the 1D-IRBFN method are in good agreement with the analytical solution as shown in Figure 6.19, using a uniform grid of 61 and time step  $\Delta t = 0.1s$ .

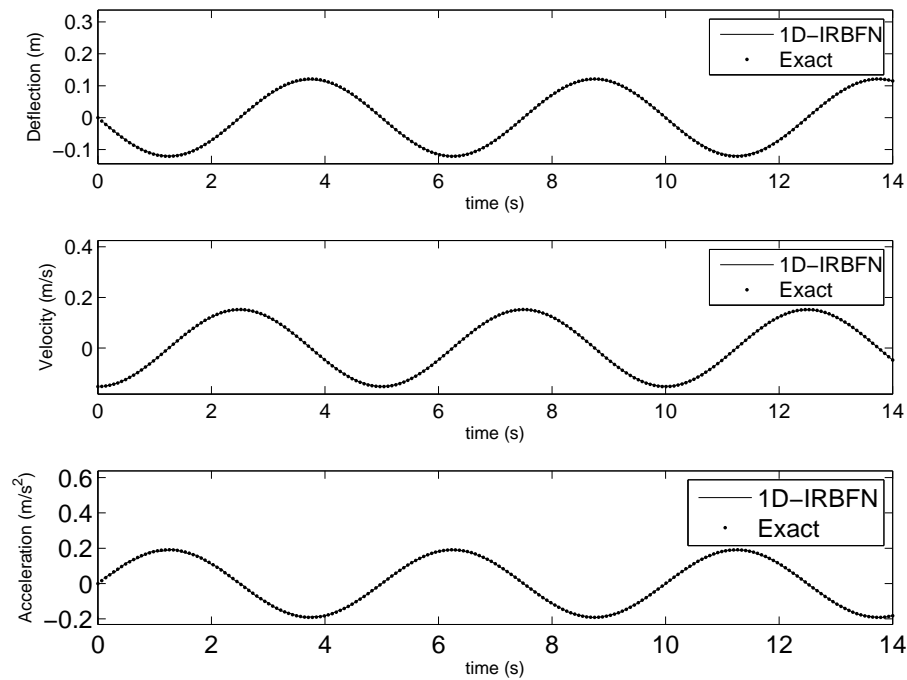


Figure 6.19: Forced vibration of a simply supported beam: steady state response of the mid-point of a simply supported beam, using a uniform grid of 61 and  $\Delta t = 0.1s$ .

Table 6.4: Forced vibration of a simply supported beam: Relative error norms of deflection  $Ne(u)$  and velocity  $Ne(v)$  at time  $t = 14s$ , using several time steps.

Grid	$Ne(u)$			$Ne(v)$		
	$\Delta t = 10^{-1}s$	$\Delta t = 5 \times 10^{-2}s$	$\Delta t = 10^{-2}s$	$\Delta t = 10^{-1}s$	$\Delta t = 5 \times 10^{-2}s$	$\Delta t = 10^{-2}s$
21	1.56E-03	1.53E-03	2.16E-03	6.65E-03	4.69E-03	3.70E-03
31	3.34E-03	1.09E-03	7.05E-04	3.53E-03	2.45E-03	2.76E-03
41	3.29E-03	1.05E-03	6.93E-04	3.63E-03	2.38E-03	2.40E-03
51	3.30E-03	1.06E-03	6.92E-04	3.61E-03	2.34E-03	2.28E-03
61	3.30E-03	1.06E-03	6.91E-04	3.61E-03	2.33E-03	2.21E-03
71	3.30E-03	1.06E-03	6.91E-04	3.61E-03	2.32E-03	2.17E-03

#### 6.5.4 Example 4: Fluid-structure interaction in a lid-driven open-cavity flow with a flexible bottom wall

This example is concerned with a FSI problem of flow in a lid-driven open-cavity with a flexible bottom wall. The problem configuration is similar to that in Example 2 except that the bottom wall motion is now caused by the interaction with the fluid. The lid is sliding from the left to the right at a velocity  $U_0 = 1 - \cos(\omega_f t)$  m/s. The bottom wall is modelled as a flexible beam with two different cases of boundary conditions as follows.

- Case 1: Simply supported at both ends.
- Case 2: Clamped at both ends.

The forced vibration of the bottom wall is governed by Equation (6.13), where  $f(x, t)$  is the fluid static pressure acting on the flexible bottom wall. The geometry and material properties of the bottom wall are taken to be the same as those in Example 3. In Case 1, the predictor of the structural interface displacement at the new time level ( $w_p^{(n+1)}$ ) is computed through Approach 1 (Equation (6.51)) and Approach 2 (Equation (6.52)). Figure 6.20 presents the comparison of deflection of the mid-point of the bottom wall ( $w_M$ ) with respect to time between the two approaches. It appears that both approaches yield almost the same results.

In Case 2, the first order accurate predictor of the bottom wall displacement is used. Figure 6.21 shows the deflection of the mid-point of the clamped bottom wall with respect to time in comparison with that in Case 1. The deflection of the bottom wall is downward for both cases. When the vibration amplitude of the bottom wall is stable, the deflection of its mid-point is equal to  $-0.1342 \pm 0.0129m$  for Case 1 and  $-0.0275 \pm 0.0162m$  for Case 2. As expected, the deflection of the clamped bottom wall is much smaller than that of the simply supported bottom wall of the same geometry and material properties. It is

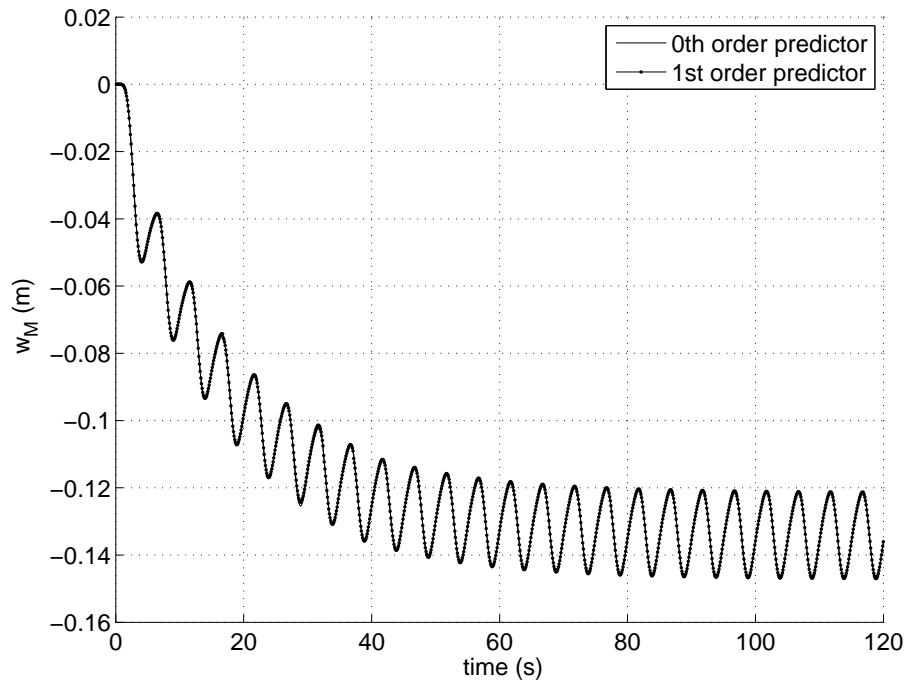


Figure 6.20: Flow in a lid-driven open-cavity with a simply supported flexible bottom wall: deflection of the mid-point of the bottom wall with respect to time  $t$  between two different approaches of predictors, using a Cartesian grid with a grid spacing of  $1/60$ .

noted that the deflection of the bottom wall varies periodically with the same frequency as that of the lid motion. The contours of stream function, velocity magnitude and static pressure of the flow inside the cavity at time  $t = 92.5s$  for Cases 1 and 2 are described in Figures 6.22 and 6.23, respectively.

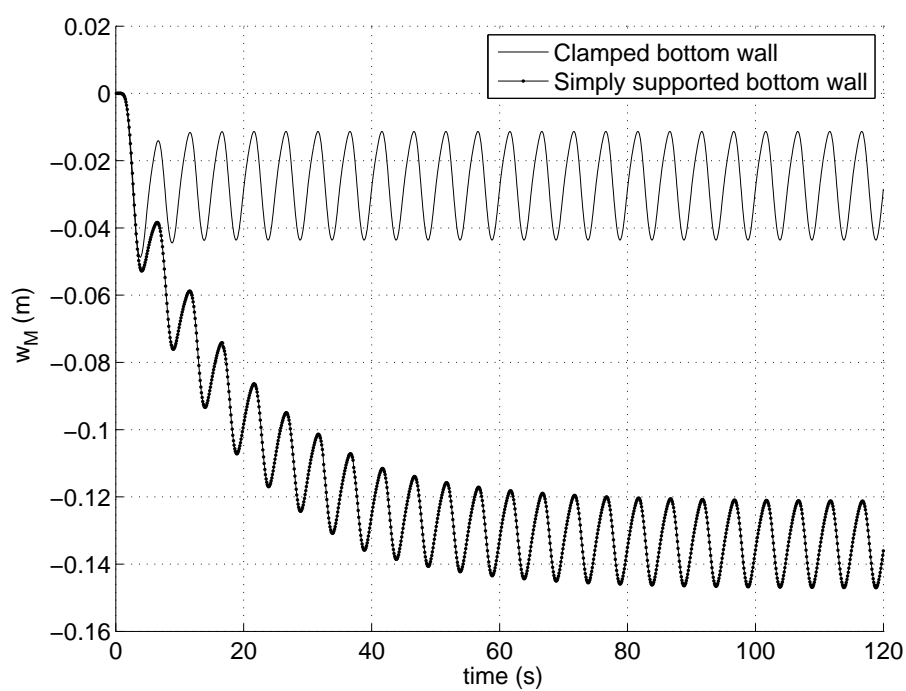


Figure 6.21: Flow in a lid-driven open-cavity with a flexible bottom wall: deflection of the mid-point of the clamped bottom wall with respect to time  $t$  in comparison with the case of simply supported bottom wall, using a Cartesian grid with a grid spacing of  $1/60$ .

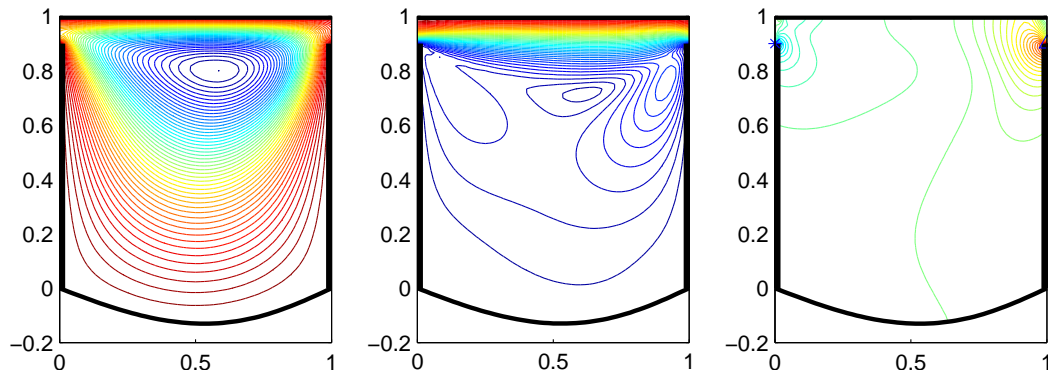


Figure 6.22: Flow in a lid-driven open-cavity with a simply supported flexible bottom wall (Case 1): contours of stream function (left), velocity magnitude (middle) and static pressure (right) of the flow at time  $t = 92.5s$ , using a Cartesian grid with a grid spacing of  $1/60$ . Each plot contains 50 contour levels varying linearly from the minimum value to the maximum value.

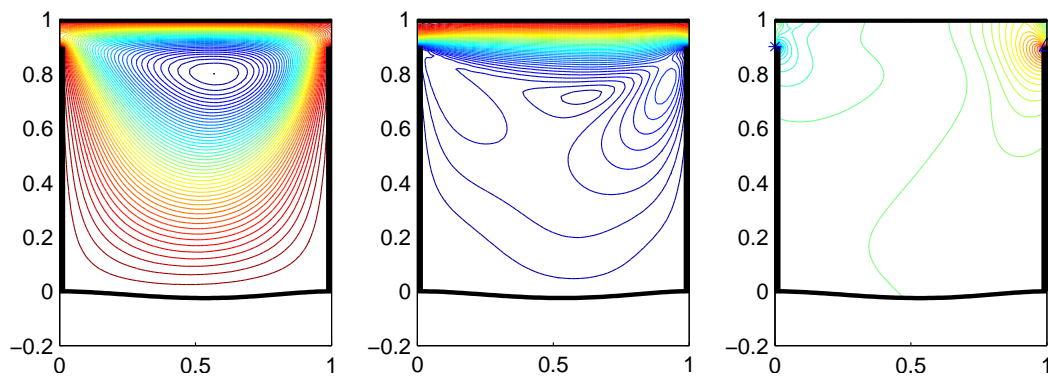


Figure 6.23: Flow in a lid-driven open-cavity with a clamped flexible bottom wall (Case 2): contours of stream function (left), velocity magnitude (middle) and static pressure (right) of the flow at time  $t = 92.5s$ , using a Cartesian grid with a grid spacing of  $1/60$ . Each plot contains 50 contour levels varying linearly from the minimum value to the maximum value.

## 6.6 Concluding remarks

A numerical procedure for FSI analysis based on the 1D-IRBFN and LMLS-1D-IRBF methods is devised and demonstrated with the analysis of the flow inside a lid-driven open-cavity with a flexible bottom wall. A combination of the fractional-step projection method and subiterative technique is presented for solving unsteady incompressible 2-D Navier-Stokes equations in terms of primitive variables, while the Newmark's method is employed for a solution of forced vibration of a beam based on the Euler-Bernoulli theory. The fluid solver is verified through a solution of mixed convection in a lid-driven cavity with a hot moving lid and a cold stationary bottom wall. The numerical results obtained are in good agreement with the published results of other authors. The Cartesian grids are used to discretise both rectangular and irregular fluid domains. The structural analysis solver is successfully verified by comparing the present numerical results with the analytical solution of forced vibration of a simply supported beam. Finally, the proposed numerical procedure is demonstrated with a solution of a fluid-structure interaction system with two different cases of bottom wall boundary conditions. The numerical results show that the bottom wall vibrations reach a steady state after a certain time and the deflection of the clamped bottom wall is much smaller than that of the simply supported bottom wall of the same geometry and material properties.

# Chapter 7

## Conclusions

The outcome of this research project is the successful development of (i) a 1D-IRBFN method for structural analysis of laminated composite plates; (ii) a novel local MLS-1D-IRBFN (or LMLS-1D-IRBFN) method for steady and unsteady incompressible viscous flows and natural convection flows in multiply-connected domains; and (iii) a new numerical procedure based on the 1D-IRBFN and LMLS-1D-IRBFN methods for fluid-structure interaction (FSI) analysis. Cartesian grids are used to discretise both simply and multiply-connected domains with rectangular and non-rectangular shapes. Unlike the conventional differentiated radial basis function network (DRBFNs) method (Kansa, 1990b), IRBFNs are constructed through integration rather than differentiation, which helps to stabilise a numerical solution and provide an effective way to implement derivative boundary conditions.

A development of the 1D-IRBFN method for free vibration of laminated composite plates based on the first order shear deformation theory (FSDT) has been presented in Chapter 2. Plates with various boundary conditions, length-to-width ratios  $a/b$ , thickness-to-length ratios  $t/b$ , and material properties are considered. Numerical results show that faster rates of convergence are obtained for higher  $t/b$  ratios irrespective of  $a/b$  ratios of the rectangular plates. The ef-

fect of boundary conditions on the natural frequencies indicates that higher constraints at the edges yield higher natural frequencies. It is also found that the present method is not only highly accurate but also very stable for a wide range of modulus ratios. The obtained numerical results are in good agreement with the available exact solutions and other published results in the literature.

A development of a novel LMLS-1D-IRBFN technique for steady incompressible viscous flows has been described in Chapter 3. The LMLS-1D-IRBFN approximation is based on the partition of unity concept to incorporate the MLS and 1D-IRBFN methods in a new approach. This approach offers the same order of accuracy as the 1D-IRBFN method, while the system matrix is more sparse than that of the 1D-IRBFN, which helps reduce the computational cost significantly. The LMLS-1D-IRBFN shape function possesses the Kronecker- $\delta$  property which allows an exact imposition of the essential boundary condition. The numerical results for the lid-driven cavity flows at high  $Re$  numbers showed that the calculation of convection terms using the 1D-IRBFN technique are more accurate than the one using the LMLS-1D-IRBFN technique. The LMLS-1D-IRBFN method can be used to handle irregular domain problems such as flow past a circular cylinder, while the standard FDM cannot be applied directly at the grid points near the boundary of irregular domains. Owing to the use of integrated RBFN for local approximation, the present method appears to be more accurate than the FDM with central-difference scheme.

In Chapter 4, the LMLS-1D-IRBFN has been applied to simulate natural convection flows in multiply-connected domains in terms of stream function, vorticity and temperature. The stream function value on the inner boundary is unknown and determined by using the single-valued pressure condition (Lewis, 1979). The numerical procedure is verified through a solution of natural convection flows in concentric and eccentric annuli in terms of stream function, vorticity and temperature. The present numerical results for a wide range of Rayleigh numbers and various geometry parameters are in good agreement with

---

the numerical data available in the literature.

In Chapter 5, the LMLS-1D-IRBFN has been further extended to solve time-dependent problems such as Burgers' equation, unsteady flow past a square cylinder in a horizontal channel and unsteady flow past a circular cylinder. The combination of the LMLS-1D-IRBFN and a domain decomposition technique is successfully developed for solving large-scale fluid flow problems. The present numerical results including Strouhal number, drag and lift coefficients are in good agreement with other published results available in the literature. The influence of blockage ratio on the characteristics of flow past a square cylinder in a channel is investigated for a range of Reynolds numbers ( $60 \leq Re \leq 160$ ) and several blockage ratios ( $\beta_0 = 1/2, 1/4$  and  $1/8$ ). The obtained numerical results indicate that (i) the critical Reynolds number (at which the flow becomes unsteady) increases with increasing blockage ratio; (ii) time-averaged drag coefficient decreases with increasing Reynolds number up to 160; and (iii) the Reynolds number has a very weak influence on the Strouhal number for the cases of  $\beta_0 = 1/2$  and  $1/4$ .

A new numerical procedure based on the 1D-IRBFN and LMLS-1D-IRBFN methods for FSI analysis has been devised and demonstrated with the analysis of the flow inside a lid-driven open-cavity with a flexible bottom wall in Chapter 6. A combination of the fractional-step projection method and subiterative technique is presented for solving unsteady incompressible 2-D Navier-Stokes equations in terms of primitive variables, while the Newmark's method is employed for a solution of forced vibration of a beam based on the Euler-Bernoulli theory. The fluid solver is successfully verified through a solution of mixed convection in a lid-driven cavity with a hot moving lid and a cold stationary bottom wall. The structural analysis solver is successfully verified by comparing the present numerical result with the analytical solution of forced vibration of a simply supported beam. Finally, the proposed numerical procedure is demonstrated with a solution of a fluid-structure interaction system.

In the present research, we limit the analysis to 2-D problems and the fluid is considered to be Newtonian. For future developments, it is possible to extend the present methods to 3-D problems, possibly with non-linear geometric or material behaviours.

# Appendix A

## Basis Functions Used in One-Dimensional Integrated Radial Basis Function Networks Schemes

Multiquadrics radial basis function (MQ-RBF) in one-dimensional form is defined by

$$G^{(i)}(x) = \sqrt{(x - c^{(i)})^2 + a^{(i)2}} \quad (\text{A.1})$$

where  $c^{(i)}$  and  $a^{(i)}$  are the center and width of the  $i^{\text{th}}$  MQ-RBF, respectively. In the present study, the set of centers is chosen to be the same as the set of collocation points, and the RBF width is determined as  $a^{(i)} = \beta d^{(i)}$ ,  $\beta$  is a positive factor, and  $d^{(i)}$  the distance from the  $i^{\text{th}}$  center to its nearest neighbour.

For the 1D-IRBFN-2 scheme, new basis functions obtained from integrating MQ-RBFs are as follows.

$$H_{[1]}^{(i)}(x) = \frac{r}{2}A + \frac{(a^{(i)})^2}{2}B, \quad (\text{A.2})$$

$$H_{[0]}^{(i)}(x) = \left( \frac{r^2}{6} - \frac{(a^{(i)})^2}{3} \right) A + \frac{(a^{(i)})^2 r}{2} B, \quad (\text{A.3})$$

where  $r = x - c^{(i)}$ ,  $A = \sqrt{r^2 + a^{(i)2}}$ , and  $B = \ln(r + A)$ .

For the 1D-IRBFN-4 scheme, new basis functions obtained from integrating MQ-RBFs are as follows.

$$H_{[3]}^{(i)}(x) = \frac{r}{2}A + \frac{(a^{(i)})^2}{2}B, \quad (\text{A.4})$$

$$H_{[2]}^{(i)}(x) = \left( \frac{r^2}{6} - \frac{(a^{(i)})^2}{3} \right) A + \frac{(a^{(i)})^2 r}{2} B, \quad (\text{A.5})$$

$$H_{[1]}^{(i)}(x) = \left( -\frac{13(a^{(i)})^2 r}{48} + \frac{r^3}{24} \right) A + \left( -\frac{(a^{(i)})^4}{16} + \frac{(a^{(i)})^2 r^2}{4} \right) B, \quad (\text{A.6})$$

$$H_{[0]}^{(i)}(x) = \left( \frac{(a^{(i)})^4}{45} - \frac{83(a^{(i)})^2 r^2}{720} + \frac{r^4}{120} \right) A + \left( -\frac{3(a^{(i)})^2 r}{48} + \frac{4(a^{(i)})^2 r^3}{48} \right) B. \quad (\text{A.7})$$

# References

- Agamloh, E. B., Wallace, A. K. and Jouanne, A. V. (2008). Application of fluid-structure interaction of an ocean wave energy extraction device, *Renewable Energy* **33**: 748–757.
- Al-Amiri, A. and Khanafer, K. (2011). Fluid-structure interaction analysis of mixed convection heat transfer in a lid-driven cavity with a flexible bottom wall, *International Journal of Heat and Mass Transfer* **54 (17-18)**: 3826–3836.
- Arzani, H. and Afshar, M. H. (2006). Solving Poisson’s equations by the discrete least squares meshless method, *Boundary Elements and Other Mesh Reduction Methods XXVIII, Skiathos, Greece*, WIT Press, pp. p. 23–32.
- Atluri, S. N. and Zhu, T. (1998). A new Meshless Local Petrov-Galerkin (MLPG) Approach in Computational Mechanics, *Computational Mechanics* **22**: 117–127.
- Babuška, I. (1971). Error-bounds for finite element method, *Numerische Mathematik* **16 (4)**: 322–333.
- Babuška, I. and Melenk, J. M. (1997). The partition of unity method, *International Journal for Numerical Methods in Engineering* **40**: 727–758.
- Banerjee, S., Mukhopadhyay, A., Sen, S. and Ganguly, R. (2008). Natural convection in a bi-heater configuration of passive electronic cooling, *International Journal of Thermal Sciences* **47**: 1516–1527.

- Bathe, K. J. and Zhang, H. (2009). A mesh adaptivity procedure for CFD and fluid-structure interactions, *Computers and Structures* **87**: 604–617.
- Belytschko, T., Lu, Y. Y. and Gu, L. (1994). Element-Free Galerkin Methods, *International Journal for Numerical Methods in Engineering* **37**: 229–256.
- Berrone, S. and Marro, M. (2009). Space-time adaptive simulations for unsteady Navier-Stokes problems, *Computers & Fluids* **38**: 1132–1144.
- Botella, O. and Peyret, R. (1998). Benchmark spectral results on the lid-driven cavity flow, *Computers & Fluids* **27** (4): 421–433.
- Bouaziz, M., Kessentini, S. and Turki, S. (2010). Numerical prediction of flow and heat transfer of power-law fluids in a plane channel with a built-in heated square cylinder, *International Journal of Heat and Mass Transfer* **53**: 5420–5429.
- Braza, M., Chassaing, P. and Ha-Minh, H. (1986). Numerical study and physical analysis of the pressure and velocity fields in the near wake of a circular cylinder, *The Journal of Fluid Mechanics* **165**: 79–130.
- Breuer, M., Bernsdorf, J., Zeiser, T. and Durst, F. (2000). Accurate computations of the laminar flow past a square cylinder based on two different methods: lattice-Boltzmann and finite-volume, *International Journal of Heat and Fluid Flow* **21**: 186–196.
- Brooks, A. N. and Hughes, T. J. R. (1982). Streamline upwind/Petrov-Galerkin formulations for convection dominated flows with particular emphasis on the incompressible Navier-Stokes equations, *Computer Methods in Applied Mechanics and Engineering* **32**: 199–259.
- Bruneau, C. H. and Jouron, C. (1990). An efficient scheme for solving steady incompressible Navier-Stokes equations, *Journal of Computational Physics* **89** (2): 389–413.

- Caldwell, J., Wanless, P. and Cook, A. E. (1987). Solution of Burgers' equation for large Reynolds number using finite elements with moving nodes, *Applied Mathematical Modelling* **11**: 211–227.
- Chen, C. S., Ganesh, M., Golberg, M. A. and Cheng, A. H.-D. (2002). Multilevel Compact Radial Functions based Computational Schemes for Some Elliptic Problems, *Computers & Mathematics with Applications* **43** (3-5): 359–378.
- Chen, J. S., Hu, W. and Hu, H. Y. (2008). Reproducing kernel enhanced local radial basis collocation method, *International Journal for Numerical Methods in Engineering* **75**: 600–627.
- Cheng, M., Liu, G. R. and Lam, K. Y. (2001). Numerical simulation of flow past a rotationally oscillating cylinder, *Computer & Fluids* **30**: 365–392.
- Cheng, T. S. (2011). Characteristics of mixed convection heat transfer in a lid-driven square cavity with various Richardson and Prandtl numbers, *International Journal of Thermal Sciences* **50**: 197–205.
- Chorin, A. J. (1967). A numerical method for solving incompressible viscous flow problems, *Journal of Computational Physics* **2** (1): 12–26.
- Chung, T. J. (2002). *Computational Fluid Dynamics*, Cambridge University Press, Cambridge, United Kingdom.
- Cole, J. D. (1951). On a quasi-linear parabolic equation occurring in aerodynamics, *Quarterly Journal of Applied Mathematics* **9**: 225–236.
- Costa, V. A. F. and Raimundo, A. M. (2010). Steady mixed convection in a differentially heated square enclosure with an active rotating circular cylinder, *International Journal of Heat and Mass Transfer* **53**: 1208–1219.
- Davis, R. W. and Moore, E. F. (1982). A numerical study of vortex shedding from rectangles, *The Journal of Fluid Mechanics* **116**: 475–506.

- Dennis, S. C. R. and Chang, G. Z. (1970). Numerical solutions for steady flow past a circular cylinder at Reynolds number up to 100, *Journal of Fluid Mechanics* **42** (3): 471–489.
- Dhiman, A. K., Chhabra, R. P. and Eswaran, V. (2005). Flow and heat transfer across a confined square cylinder in the steady flow regime: Effect of Peclet number, *International Journal of Heat and Mass Transfer* **48**: 4598–4614.
- Dhiman, A. K., Chhabra, R. P. and Eswaran, V. (2008). Steady mixed convection across a confined square cylinder, *International Communications in Heat and Mass Transfer* **35**: 47–55.
- Ding, H., Shu, C., Yeo, K. S. and Lu, Z. L. (2005). Simulation of natural convection in eccentric annuli between a square outer cylinder and a circular inner cylinder using local MQ-DQ method, *Numerical Heat Transfer, Part A* **47**: 291–313.
- Ding, H., Shu, C., Yeo, K. S. and Xu, D. (2004). Simulation of incompressible viscous flows past a circular cylinder by hybrid FD scheme and meshless least square-based finite difference method, *Computer Methods in Applied Mechanics and Engineering* **193**: 727–744.
- Ding, H., Shu, C., Yeo, K. S. and Xu, D. (2007). Numerical simulation of flows around two circular cylinders by mesh-free least square-based finite difference methods, *International Journal for Numerical Methods in Fluids* **53**: 305–332.
- Divo, E. and Kassab, A. J. (2007). An efficient localized radial basis function meshless method for fluid flow and conjugate heat transfer, *ASME Journal of Heat Transfer* **129**: 124–136.
- Dubcova, L., Feistauer, M., Horacek, J. and Svacek, P. (2008). Numerical simulation of airfoil vibrations induced by turbulent flow, *Journal of Computational and Applied Mathematics* **218**: 34–42.
- Farhat, C. and Lesoinne, M. (1998). Two efficient staggered algorithms for the serial and parallel solution of three-dimensional nonlinear transient aeroe-

- lastic problems, *Computer Methods in Applied Mechanics and Engineering* **182**: 449–515.
- Fernández, M. A., Gerbeau, J.-F. and Grandmont, C. (2007). A projection semi-implicit scheme for the coupling of an elastic structure with an incompressible fluid, *International Journal for Numerical Methods in Engineering* **69**: 794–821.
- Ferreira, A. J. M. and Fasshauer, G. E. (2005). Free Vibration Analysis of Timoshenko Beams and Mindlin Plates by Radial Basis Functions, *International Journal of Computational Methods* **2 (1)**: 15–31.
- Ferreira, A. J. M. and Fasshauer, G. E. (2007). Analysis of Natural Frequencies of Composite Plates by an RBF-Pseudospectral Method, *Composite Structures* **79**: 202–210.
- Ferreira, A. J. M., Roque, C. M. C. and Jorge, R. M. N. (2005). Free Vibration Analysis of Symmetric Laminated Composite Plates by FSDT and Radial Basis Functions, *Computer Methods in Applied Mechanics and Engineering* **194**: 4265–4278.
- Firoozjaee, A. R. and Afshar, M. H. (2011). Steady-state solution of incompressible Navier-Stokes equations using discrete least-squares meshless method, *International Journal for Numerical Methods in Fluids* **67**: 369–382.
- Förster, C., Wall, W. A. and Ramm, E. (2007). Artificial added mass instabilities in sequential staggered coupling of nonlinear structures and incompressible viscous flows, *Computer Methods in Applied Mechanics and Engineering* **196**: 1278–1293.
- Garcia, J. A. and Guruswamy, G. P. (1999). Aeroelastic analysis of transonic wings using Navier-Stokes equations and a nonlinear beam finite element model, *Technical Report AIAA-99-1215*.

- Ge, Y. J. and Xiang, H. F. (2008). Computational models and methods for aerodynamic flutter of long-span bridges, *Journal of Wind Engineering and Industrial Aerodynamics* **96**: 1912–1924.
- Ghia, U., Ghia, K. N. and Shin, C. T. (1982). High-Re solutions for incompressible flow using the Navier-Stokes equations and a multigrid method, *Journal of Computational Physics* **48**: 387–411.
- Glowinski, R. (2003). *Finite Element Methods for Incompressible Viscous Flows*. In Handbook of Numerical Analysis, Vol. 9, North-Holland, Amsterdam.
- Gupta, A. K., Sharma, A., Chhabra, R. P. and Eswaran, V. (2003). Two-dimensional steady flow of a power-law fluid past a square cylinder in a plane channel: Momentum and heat-transfer characteristics, *Industrial & Engineering Chemistry Research* **42**: 5674–5686.
- Guruswamy, G. P. and Byun, C. (1995). Direct coupling of Euler flow equations with plate finite element structures, *AIAA Journal* **33** (2): 375–377.
- Hashemian, A. and Shodja, H. M. (2008). A meshless approach for solution of Burgers' equation, *Journal of Computational and Applied Mathematics* **220**: 226–239.
- Hassanien, I. A., Salama, A. A. and Hosham, H. A. (2005). Fourth-order finite difference method for solving Burgers' equation, *Applied Mathematics and Computation* **170**: 781–800.
- Haykin, S. (1999). *Neural Networks: A Comprehensive Foundation*, Pearson Prentice-Hall, New Jersey.
- Heil, M. (2004). An Efficient Solver for the Fully Coupled Solution of Large-Displacement Fluid-Structure Interaction Problems, *Computer Methods in Applied Mechanics and Engineering* **193**: 1–23.

- Hetherington, J. and Askes, H. (2009). Penalty methods for time domain computational dynamics based on positive and negative inertia, *Computers & Structures* **87**: 1474–1482.
- Ho-Minh, D., Mai-Duy, N. and Tran-Cong, T. (2009). A Galerkin-RBF Approach for the Streamfunction-Vorticity-Temperature Formulation of Natural Convection in 2D Enclosed Domains, *CMES: Computer Modeling in Engineering & Sciences* **44 (3)**: 219–248.
- Hoffmann, K. A. and Chiang, S. T. (2000). *Computational Fluid Dynamics*, Engineering Education System, Kansas.
- Hon, Y. C. and Mao, X. Z. (1998). An efficient numerical scheme for Burgers' equation, *Applied Mathematics and Computation* **97**: 37–50.
- Hosseini, B. and Hashemi, R. (2011). Solution of Burgers' equation using a local-RBF meshless method, *International Journal for Computational Methods in Engineering Science and Mechanics* **12**: 44–58.
- Iskander, L. and Mohsen, A. (1992). Some numerical experiments on splitting of Burgers' equation, *Numerical Methods for Partial Differential Equations* **8**: 267–276.
- Iwatsu, R., Hyun, J. M. and Kuwahara, K. (1993). Mixed convection in a driven cavity with a stable vertical temperature gradient, *International Journal of Heat and Mass Transfer* **36 (6)**: 1601–1608.
- Jameson, A. (1991). Time Dependent Calculations Using Multigrid, with Applications to Unsteady Flows Past Airfoils and Wings, *10th AIAA Computational Fluid Dynamics Conference, Honolulu, Hawaii*, number AIAA 91-1596.
- Jubran, B. A., Al-Abdali, H., Al-Hiddabi, S., Al-Hinai, H. and Zurigat, Y. (2004). Numerical modelling of convective layers in solar ponds, *Solar Energy* **77**: 339–345.

- Kansa, E. J. (1990a). Multiquadrics - A Scattered Data Approximation Scheme with Applications to Computational Fluid-Dynamics - I: Surface Approximations and Partial Derivative Estimates, *Computers & Mathematics with Applications* **19** (8-9): 127–145.
- Kansa, E. J. (1990b). Multiquadrics - A Scattered Data Approximation Scheme with Applications to Computational Fluid-Dynamics - II: Solutions to parabolic, Hyperbolic and Elliptic Partial Differential Equations, *Computers & Mathematics with Applications* **19** (8-9): 147–161.
- Karunasena, W. and Kitipornchai, S. (1997). Free Vibration of Shear-Deformable General Triangular Plates, *Journal of Sound and Vibration* **199** (4): 595–613.
- Karunasena, W., Liew, K. M. and Al-Bermani, F. G. A. (1996). Natural Frequencies of Thick Arbitrary Quadrilateral Plates using the pb-2 Ritz Method, *Journal of Sound and Vibration* **196** (4): 371–385.
- Kim, B. S., Lee, D. S., Ha, M. Y. and Yoon, H. S. (2008). A numerical study of natural convection in a square enclosure with a circular cylinder at different vertical locations, *International Journal of Heat and Mass Transfer* **51**: 1888–1906.
- Kim, Y., Kim, D. W., Jun, S. and Lee, J. H. (2007). Meshfree point collocation method for the stream-vorticity formulation of 2D incompressible Navier-Stokes equations, *Computer Methods in Applied Mechanics and Engineering* **196**: 3095–3109.
- Krysl, P. and Belytschko, T. (2000). An efficient linear-precision partition of unity basis for unstructured meshless methods, *Communications in Numerical Methods in Engineering* **16**: 239–255.
- Kuehn, T. H. and Goldstein, R. J. (1976). An experimental and theoretical study of natural convection in the annulus between horizontal concentric cylinders, *The Journal of Fluid Mechanics* **74** (4): 695–719.

- Küttler, U. and Wall, W. A. (2008). Fixed-point fluid-structure interaction solvers with dynamic relaxation, *Computational Mechanics* **43**: 61–72.
- Le-Cao, K., Mai-Duy, N., Tran, C.-D. and Tran-Cong, T. (2011). Numerical study of stream-function formulation governing flows in multiply-connected domains by integrated RBFs and Cartesian grids, *Computers & Fluids* **44** (1): 32–42.
- Le-Cao, K., Mai-Duy, N. and Tran-Cong, T. (2009). An effective integrated-RBFN Cartesian-grid discretization for the stream function-vorticity-temperature formulation in nonrectangular domains, *Numerical Heat Transfer, Part B* **55**: 480–502.
- Le, P. B. H., Rabczuk, T., Mai-Duy, N. and Tran-Cong, T. (2010). A moving IRBFN-based integration-free meshless method, *CMES: Computer Modeling in Engineering & Sciences* **61** (1): 63–109.
- Lee, C. K., Liu, X. and Fan, S. C. (2003). Local multiquadric approximation for solving boundary value problems, *Computational Mechanics* **30**: 396–409.
- Leonard, B. P. (1979). A stable and accurate convective modelling procedure based on quadratic upstream interpolation, *Computer Methods in Applied Mechanics and Engineering* **19**: 59–98.
- Lewis, E. (1979). Steady flow between a rotating circular cylinder and fixed square cylinder, *The Journal of Fluid Mechanics* **95** (3): 497–513.
- Liew, K. M. (1996). Solving the Vibration of Thick Symmetric Laminates by Reissner/Mindlin Plates Theory and the p-Ritz Method, *Journal of Sound and Vibration* **198** (3): 343–360.
- Liew, K. M. and Chen, X. L. (2004). Buckling of rectangular Mindlin Plates subjected to Partial In-plane Edge loads using the Radial Point Interpolation Method, *International Journal of Solids and Structures* **41**: 1677–1695.

- Liew, K. M., Chen, X. L. and Reddy, J. N. (2004). Mesh-free Radial Basis Function Method for Buckling Analysis of Non-uniformly Loaded Arbitrarily Shaped Shear Deformable Plates, *Computer Methods in Applied Mechanics and Engineering* **193**: 205–224.
- Liew, K. M., Huang, Y. Q. and Reddy, J. N. (2003). Vibration Analysis of Symmetrically Laminated Plates based on FSDT using the Moving Least Squares Differential Quadrature Method, *Computer Methods in Applied Mechanics and Engineering* **192**: 2203–2222.
- Liew, K. M., Hung, K. C. and Lim, M. K. (1993). A Continuum Three-dimensional Vibration Analysis of Thick Rectangular Plates, *International Journal of Solids and Structures* **30 (24)**: 3357–3379.
- Liew, K. M., Hung, K. C. and Lim, M. K. (1994). Three-Dimensional Vibration of Rectangular Plates: Variance of Simple support conditions and influence of In-lane Inertia, *International Journal of Solids and Structures* **31 (23)**: 3233–3247.
- Liew, K. M., Hung, K. C. and Lim, M. K. (1995). Three-Dimensional Vibration of Rectangular Plates: Effects of Thickness and Edge Constraints, *Journal of Sound and Vibration* **182 (5)**: 709–727.
- Liew, K. M., Ng, T. Y., Zhao, X. and Reddy, J. N. (2002). Harmonic reproducing kernel particle method for free vibration of rotating cylindrical shells, *Computer Methods in Applied Mechanics and Engineering* **191**: 4141–4157.
- Liew, K. M. and Teo, T. M. (1999). Three-Dimensional Vibration Analysis of Rectangular Plates based on Differential Quadrature Method, *Journal of Sound and Vibration* **220 (4)**: 577–599.
- Liew, K. M., Wang, J., Ng, T. Y. and Tan, M. J. (2004). Free Vibration and Buckling Analyses Of Shear-Deformable Plates based on FSDT Meshfree Method, *Journal of Sound and Vibration* **276**: 997–1017.

- Liew, K. M., Wang, J., Tan, M. J. and Rajendran, S. (2004). Nonlinear Analysis of Laminated Composite Plates using the Mesh-free kp-Ritz Method based on FSDT, *Computer Methods in Applied Mechanics and Engineering* **193**: 4763–4779.
- Liew, K. M., Wang, W. Q., Zhang, L. X. and He, X. Q. (2007). A Computational Approach for Predicting the Hydroelasticity of Flexible Structures Based on the Pressure Poisson equation, *International journal for Numerical Methods in Engineering* **72**: 1560–1583.
- Lim, C. W., Liew, K. M. and Kitipornchai, S. (1998a). Numerical Aspects for Free Vibration of Thick Plates. Part I: Formulation and Verification, *Computer Methods in Applied Mechanics and Engineering* **156**: 15–29.
- Lim, C. W., Liew, K. M. and Kitipornchai, S. (1998b). Numerical Aspects for Free Vibration of Thick Plates. Part II: Numerical Efficiency and Vibration Frequencies, *Computer Methods in Applied Mechanics and Engineering* **156**: 31–44.
- Lin, H. and Atluri, S. N. (2000). Meshless local Petrov-Galerkin (MLPG) method for convection-diffusion problems, *CMES: Computer Modeling in Engineering & Sciences* **1 (2)**: 45–60.
- Lin, H. and Atluri, S. N. (2001). The meshless local Petrov-Galerkin (MLPG) method for solving incompressible Navier-Stokes equations, *CMES: Computer Modeling in Engineering & Sciences* **2 (2)**: 117–142.
- Liu, C., Zheng, Z. and Sung, C. H. (1998). Preconditioned multigrid methods for unsteady incompressible flows, *Journal of Computational Physics* **139**: 35–57.
- Liu, G. R. (2003). *Meshfree Methods: Moving Beyond the Finite Element Method*, CRC Press, London.
- Liu, G. R. and Gu, Y. T. (2001). A Point Interpolation Method for Two-Dimensional Solids, *International Journal for Numerical Methods in Engineering* **50**: 937–951.

- Liu, G. R., Li, Y. and Dai, K. Y. (2006). A linearly Conforming Radial Point Interpolation Method for Solid Mechanics Problems, *International Journal of Computational Methods* **3** (4): 401–428.
- Liu, G. R., Zhang, G. Y. and Dai, K. Y. (2005). A Linearly Conforming Point Interpolation Method (LC-PIM) for 2D Solid Mechanics Problems, *International Journal of Computational Methods* **2** (4): 645–665.
- Madych, W. R. and Nelson, S. A. (1989). Multivariate interpolation and conditionally positive definite functions, *Approximation Theory and its Applications* **4**: 77–89.
- Mai-Cao, L. and Tran-Cong, T. (2005). A meshless IRBFN-based method for transient problems, *CMES: Computer Modeling in Engineering & Sciences* **7** (2): 149–171.
- Mai-Duy, N., Khennane, A. and Tran-Cong, T. (2007). Computation of Laminated Composite Plates using Integrated Radial Basis Function Networks, *CMC: Computers, Materials & Continua* **5** (1): 63–77.
- Mai-Duy, N. and Tanner, R. I. (2007). A Collocation Method based on One-Dimensional RBF Interpolation Scheme for Solving PDEs, *International Journal of Numerical Methods for Heat & Fluid Flow* **17** (2): 165–186.
- Mai-Duy, N. and Tran-Cong, T. (2001a). Numerical solution of differential equations using multiquadric radial basis function networks, *Neural Networks* **14**: 185–199.
- Mai-Duy, N. and Tran-Cong, T. (2001b). Numerical Solution of Navier-Stokes Equations using Multiquadric Radial Basis Function Networks, *International Journal for Numerical Methods in Fluids* **37**: 65–86.
- Mai-Duy, N. and Tran-Cong, T. (2002). Mesh-free Radial basis function network methods with domain decomposition for approximation of functions and numerical solution of Poisson’s equations, *Engineering Analysis with Boundary Elements* **26**: 133–156.

- Mai-Duy, N. and Tran-Cong, T. (2003a). Approximation of Function and Its Derivatives using Radial Basis Function Networks, *Applied Mathematical Modelling* **27**: 197–220.
- Mai-Duy, N. and Tran-Cong, T. (2003b). Indirect RBFN Method with Thin Plate Splines for Numerical Solution of Differential Equations, *CMES: Computer Modeling in Engineering & Sciences* **4 (1)**: 85–102.
- Mai-Duy, N. and Tran-Cong, T. (2009a). An Integrated-RBF Technique Based on Galerkin Formulation for Elliptic Differential Equations, *Engineering Analysis with Boundary Elements* **33**: 191–199.
- Mai-Duy, N. and Tran-Cong, T. (2009b). Integrated radial-basis-function networks for computing Newtonian and non-Newtonian fluid flows, *Computers & Structures* **87**: 642–650.
- Melson, N. D., Sanetrik, M. D. and Atkins, H. L. (1993). Time-Accurate Navier-Stokes Calculations with Multigrid Acceleration, *11th AIAA Computational Fluid Dynamics Conference, Part 2, Orlando, Florida*, pp. p. 1041–1042.
- Moukalled, F. and Acharya, S. (1996). Natural convection in the annulus between concentric horizontal circular and square cylinders, *Journal of Thermophysics and Heat Transfer* **10 (3)**: 524–531.
- Moussaoui, M. A., Jami, M., Mezrhab, A. and Naji, H. (2010). MRT-Lattice Boltzmann simulation of forced convection in a plane channel with an inclined square cylinder, *International Journal of Thermal Sciences* **49**: 131–142.
- Muralidhar, K. and Sundararajan, T. (1995). *Computational Fluid Flow and Heat Transfer*. In IIT Kanpur Series of Advanced Texts, Narosa Publishing House, New Delhi.
- Nayroles, B., Touzot, G. and Villon, P. (1992). Generalizing the Finite Element Method: Diffuse Approximation and Diffuse Elements, *Computational Mechanics* **10**: 307–318.

- Ngo-Cong, D., Mai-Duy, N., Karunasena, W. and Tran-Cong, T. (2011). Free vibration analysis of laminated composite plates based on FSDT using one-dimensional IRBFN method, *Computers & Structures* **89**: 1–13.
- Ngo-Cong, D., Mai-Duy, N., Karunasena, W. and Tran-Cong, T. (2012). Local Moving Least Square - One-Dimensional IRBFN Technique for Incompressible Viscous Flows, *International Journal for Numerical Methods in Fluids* p. (published online 9/Jan/2012 DOI: 10.1002/flid.3640).
- Nguyen-Van, H., Mai-Duy, N. and Tran-Cong, T. (2008). Free Vibration Analysis of Laminated Plate/Shell Structures Based on FSDT with a Stabilized Nodal-Integrated Quadrilateral Element, *Journal of Sound and Vibration* **313**: 205–223.
- Noor, A. K. and Burton, W. S. (1973). Free Vibration of Multilayered Composite Plates, *AIAA Journal* **11**: 1038–1039.
- Park, J., Kwon, K. and Choi, H. (1998). Numerical solutions of flow past a circular cylinder at Reynolds numbers up to 160, *KSME International Journal* **12 (6)**: 1200–1205.
- Park, J. and Sandberg, I. W. (1991). Universal approximation using radial-basis-function networks, *Neural Computation* **3**: 246–257.
- Park, S. H. and Youn, S. K. (2001). The least-squares meshfree method, *International Journal for Numerical Methods in Engineering* **52**: 997–1012.
- Parolini, N. and Quarteroni, A. (2005). Mathematical models and numerical simulations for the Americas Cup, *Computer Methods in Applied Mechanics and Engineering* **194**: 1001–1026.
- Phan-Thien, N. and Kim, S. (1994). *Microstructures in Elastic Media: Principles and Computational Methods*, Oxford University Press.
- Piperno, S. (1997). Explicit/implicit fluid/structure staggered procedures with

- a structural predictor and fluid subcycling for 2D inviscid aeroelastic simulations, *International Journal for Numerical Methods in Fluids* **25**: 1207–1226.
- Pozrikidis, C. (2002). *A Practical Guide to Boundary Element Methods with The Software Library BEMLIB*, Chapman & Hall/CRC.
- Quarteroni, A. and Valli, A. (1999). *Domain Decomposition Methods for Partial Differential Equations*, Clarendon Press, Oxford.
- Rao, S. S. (2004). *Mechanical Vibrations*, 4th edn, Pearson Prentice Hall, New Jersey.
- Reddy, J. N. (1984). A simple higher-order theory for laminated composite plates, *Journal of Applied Mechanics* **51**: 745–752.
- Reddy, J. N. (1993). *An Introduction to The Finite Element Method*, 2nd edn, McGraw-Hill, Inc., New York, USA.
- Reddy, J. N. (2004). *Mechanics of Laminated Composite Plates and Shells: Theory and Analysis*, CRC Press, London.
- Reddy, J. N. (2006). *An Introduction to The Finite Element Method*, McGraw-Hill, New York.
- Reddy, J. N. and Phan, N. D. (1985). Stability and Vibration of Isotropic, Orthotropic and Laminated Plates according to a Higher-Order Shear Deformation Theory, *Journal of Sound and Vibration* **98**: 157–170.
- Rendall, T. C. S. and Allen, C. B. (2008). Unified fluid-structure interpolation and mesh motion using radial basis functions, *International Journal for Numerical Methods in Engineering* **74**: 1519–1559.
- Roache, P. J. (1998). *Fundamentals of Computational Fluid Dynamics*, Hermosa, New Mexico.
- Rugonyi, S. and Bathe, K. J. (2001). On Finite Element Analysis of Fluid Flows Fully Coupled with Structural Interactions, *CMES: Computer Modeling in Engineering & Sciences* **2 (2)**: 195–212.

- Rumsey, C. L., Sanetrik, M. D., Biedron, R. T., Melson, N. D. and Parlette, E. B. (1996). Efficiency and accuracy of time-accurate turbulent Navier-Stokes computations, *Computers & Fluids* **25** (2): 217–236.
- Russell, D. and Wang, Z. J. (2003). A Cartesian grid method for modeling multiple moving objects in 2D incompressible viscous flow, *Journal of Computational Physics* **191**: 177–205.
- Sahu, A. K., Chhabra, R. P. and Eswaran, V. (2010). Two-dimensional laminar flow of a power-law fluid across a confined square cylinder, *Journal of Non-Newtonian Fluid Mechanics* **165**: 752–763.
- Sanyasiraju, Y. V. S. S. and Chandhini, G. (2008). Local radial basis function based gridfree scheme for unsteady incompressible viscous flows, *Journal of Computational Physics* **227**: 8922–8948.
- Šarler, B. and Perko, J. (2004). Radial basis function collocation method solution of natural convection in porous media, *International Journal of Numerical Methods for Heat & Fluid Flow* **14** (2): 187–212.
- Šarler, B. and Vertnik, R. (2006). Meshfree explicit local radial basis function collocation method for diffusion problems, *Computers and Mathematics with Applications* **51**: 1269–1282.
- Sharif, M. A. R. (2007). Laminar mixed convection in shallow inclined driven cavities with hot moving lid on top and cooled from bottom, *Applied Thermal Engineering* **27**: 1036–1042.
- Shepard, D. (1968). A two dimensional interpolation function for irregularly spaced data, *Proceedings of the 23rd National Conference ACM, ACM, New York*, pp. p. 517–523.
- Shu, C. (1999). Application of differential quadrature method to simulate natural convection in a concentric annulus, *International Journal for Numerical Methods in Fluids* **30**: 977–993.

- Shu, C., Ding, H. and Yeo, K. S. (2003). Local radial basis function-based differential quadrature method and its application to solve two-dimensional incompressible Navier-Stokes equations, *Computer Methods in Applied Mechanics and Engineering* **192**: 941–954.
- Shu, C., Ding, H. and Yeo, K. S. (2005). Computation of Incompressible Navier-Stokes equations by local RBF-based differential quadrature method, *CMES: Computer Modeling in Engineering & Sciences* **7 (2)**: 195–205.
- Shu, C., Xue, H. and Zhu, Y. D. (2001). Numerical study of natural convection in an eccentric annulus between a square outer cylinder and a circular inner cylinder using DQ method, *International Journal of Heat and Mass Transfer* **44**: 3321–3333.
- Shu, C. and Zhu, Y. D. (2002). Efficient computation of natural convection in a concentric annulus between an outer square cylinder and an inner circular cylinder, *International Journal for Numerical Methods in Fluids* **38**: 429–445.
- Silva, A. L. F. L. E., Silveira-Neto, A. and Damasceno, J. J. R. (2003). Numerical simulation of two-dimensional flows over a circular cylinder using the immersed boundary method, *Journal of Computational Physics* **189**: 351–370.
- Sohankar, A., Norberg, C. and Davidson, L. (1998). Low-Reynolds-number flow around a square cylinder at incidence: study of blockage, onset of vortex shedding and outlet boundary condition, *International Journal for Numerical Methods in Fluids* **26**: 39–56.
- Spoon, C. and Grant, W. (2011). Biomechanics of hair cell kinocilia: experimental measurement of kinocilium shaft stiffness and base rotational stiffness with euler-bernoulli and timoshenko beam analysis, *The Journal of Experimental Biology* **214**: 862–870.
- Srinivas, S. and Rao, A. K. (1970). Bending, vibration and buckling of simply

- supported thick orthotropic rectangular plates and laminates, *International Journal of Solids and Structures* **6 (11)**: 1463–1481.
- Stevens, D., Power, H., Lees, M. and Morvan, H. (2009). The use of PDE centres in the local RBF Hermitian method for 3D convective-diffusion problems, *Journal of Computational Physics* **228**: 4606–4624.
- Stevens, D., Power, H. and Morvan, H. (2009). An order-N complexity meshless algorithm for transport-type PDEs, based on local Hermitian interpolation, *Engineering Analysis with Boundary Elements* **33**: 425–441.
- Tanner, R. I. (1985). *Engineering Rheology*, Oxford Engineering Science Series 14.
- Tezduyar, T. E., Glowinski, R. and Liou, J. (1988). Petrov-Galerkin methods on multiply connected domains for the vorticity-stream function formulation of the incompressible Navier-Stokes equations, *International Journal for Numerical Methods in Fluids* **8**: 1269–1290.
- Toro, E. F. (2009). *Riemann Solvers and Numerical Methods for Fluid Dynamics a Practical Introduction*, 3rd edn, Springer, Berlin.
- Torrance, K., Davis, R., Eike, K., Gill, P., Gutman, D., Hsui, A., Lyons, S. and Zien, H. (1972). Cavity flows driven by buoyancy and shear, *Journal of Fluid Mechanics* **51, part 2**: 221–231.
- Tran-Cong, T. (1989). *Boundary element method for some three-dimensional problems in continuum mechanics*, PhD thesis, The University of Sydney, Sydney, Australia.
- Turki, S., Abbassi, H. and Nasrallah, S. B. (2003). Two-dimensional laminar fluid flow and heat transfer in a channel with a built-in heated square cylinder, *International Journal of Thermal Sciences* **42**: 1105–1113.
- Udaykumar, H. S., Mittal, R., Rampungoon, P. and Khanna, A. (2001). A

- sharp interface Cartesian grid method for simulating flows with complex moving boundaries, *Journal of Computational Physics* **174**: 345–380.
- Vertnik, R. and Šarler, B. (2006). Meshless local radial basis function collocation method for convective-diffusive solid-liquid phase change problems, *International Journal of Numerical Methods for Heat and Fluid Flow* **16**: 617–640.
- Vertnik, R. and Šarler, B. (2009). Solution of incompressible turbulent flow by a mesh-free method, *CMES: Computer Modeling in Engineering & Sciences* **44 (1)**: 65–95.
- Vierendeels, J., Dumont, K., Dick, E. and Verdonck, P. (2005). Analysis and Stabilization of Fluid-Structure Interaction Algorithm for Rigid-Body Motion, *AIAA Journal* **43 (12)**: 2549–2557.
- Wang, J. G. and Liu, G. R. (2002). A Point Interpolation Meshless Method based on Radial Basis Function, *International Journal for Numerical Methods in Engineering* **54**: 1623–1648.
- Wendland, H. (1995). Piecewise polynomial, positive definite and compactly supported radial functions of minimal degree, *Advances in Computational Mathematics* **4**: 389–396.
- Wright, G. B. and Fornberg, B. (2006). Scattered node compact finite difference-type formulas generated from radial basis functions, *Journal of Computational Physics* **212**: 99–123.
- Xiong, J. J. and Yu, X. (2007). Helicopter rotor-fuselage aeroelasticity modelling and solution using the partition-iteration method, *Journal of Sound and Vibration* **302**: 821–840.
- Yao, G., Šarler, B. and Chen, C. S. (2011). A comparison of three explicit local meshless methods using radial basis functions, *Engineering Analysis with Boundary Elements* **35**: 600–609.

- Ye, T., Mittal, R., Udaykumar, H. S. and Shyy, W. (1999). An accurate Cartesian grid method for viscous incompressible flows with complex immersed boundaries, *Journal of Computational Physics* **156**: 209–240.
- Zahab, Z. E., Divo, E. and Kassab, A. J. (2009). A localized collocation meshless method (LCMM) for incompressible flows CFD modeling with applications to transient hemodynamics, *Engineering Analysis with Boundary Elements* **33**: 1045–1061.
- Zaki, T. G., Sen, M. and el Hak, M. G. (1994). Numerical and experimental investigation of flow past a freely rotatable square cylinder, *Journal of Fluids and Structures* **8**: 555–582.
- Zerroukat, M., Djidjeli, K. and Charafi, A. (2000). Explicit and implicit meshless methods for linear advection-diffusion-type partial differential equations, *International Journal for Numerical Methods in Engineering* **48**: 19–35.
- Zhang, X. K., Kwon, K. C. and Youn, S. K. (2005). The least-squares meshfree method for the steady incompressible viscous flow, *Journal of Computational Physics* **206**: 182–207.
- Zhao, X., Ng, T. Y. and Liew, K. M. (2004). Free Vibration of Two-Side Simply-Supported Laminated Cylindrical Panels via the Mesh-free kp-Ritz Method, *International Journal of Mechanical Sciences* **46**: 123–142.
- Zheng, Z. C. and Zhang, N. (2008). Frequency effects on lift and drag for flow past an oscillating cylinder, *Journal of Fluids and Structures* **24**: 382–399.